Modeling of Carrier Transport Phenomena at Photocatalytic Semiconductor-Liquid Interfaces

Asif Iqbal

Department of Mining and Materials Engineering
McGill University
Montréal, Québec
Adviser: Professor Kirk H. Bevan

A thesis submitted to McGill University in partial fulfillment of
the requirements of the degree of Doctor of Philosophy

July 2018

Abstract

The conversion of solar energy into a carbon-free chemical form of fuel comprises a key constituent of the economic paradigm based on renewable energy. Throughout the last two decades, the growing and pervasive impact of anthropogenic climate change continue to drive the demand for efficient, eco-friendly and large-scale solar-to-chemical fuel conversion. In the same spirit, solar-assisted water splitting, by utilizing light-absorbing and earth-abundant semiconductors, is of paramount interest as it can delineate a route to low-cost and scalable production of H_2-fuel and possibly serve as the backbone of a renewable economic paradigm. Nevertheless, inadequate understanding of the intricate charge transfer processes governing semiconductor photocatalysis significantly impedes the realization of cost-competitive monolithic photoelectrodes pertaining to solar water splitting in an unassisted fashion. Extensive ongoing research in this direction has outlined critical scientific problems that entail urgent resolution through combined theoretical and experimental efforts.

The research in this dissertation demonstrates numerical modeling of an archetypical semiconductor-aqueous electrolyte junction and theoretically probes the electrostatics and charge transport processes determining interfacial photoelectrochemical performance. Our numerical approach concomitantly incorporates the drift-diffusion methods developed for the solid state semiconductor devices with the Gouy-Chapman-Stern model for aqueous electrolyte. This research, along with the complete numerical description of the system, tackles some of the key numerical problems (boundary conditions) related to the semiclassical modeling of the photocatalytic semiconductor-liquid junctions. To numerically capture both the photovoltage and photocurrent (two of the most commonly measured quantities in typical photoelectrochemical experiments) at semiconductor-liquid interfaces we show that it is necessary to simultaneously solve both the majority and minority carrier transport equations. The solution of the minority carrier transport equation is needed to calculate the interfacial photocurrent and the solution of the majority carrier transport equation is needed to estimate the photovoltage. Throughout this numerical treatment, a floating boundary condition for the electrostatic potential in the bulk and a pseudo-Schottky boundary conditions for the interfacial electron and hole currents must also be imposed to facilitate the band-flattening process brought about by the solar irradiation. In addition, this work also extends the scope of the semiclassical modeling in theoretically exploring the phenomena due to the presence of surface states and bulk trap states. By utilizing a distinct Fermi-level for surface state occupation, this work provides insights regarding the equilibration of surface states and unravels the non-trivial trends in Mott-Schottky analysis. Conversely, computational studies regarding the impact of bulk trapping of the carriers are shown to demonstrate severe degradation of the maximum attainable photovoltage along with poor majority carrier conduction properties. Furthermore, the utility of the methodology, as developed throughout the course of this thesis, is demonstrated by correlating theoretical calculations with experimental measurements reported in the literature. This includes, but is not limited to: computation of the photovoltage, onset and saturation of the photocurrent, interfacial transfer and bulk relaxation of the minority carriers, various generation/recombination processes, impacts of surface states and bulk trap states, Mott-Schottky analysis and capacitance spectroscopy, charge screening at the photoelectrochemical interface, and the suppression of back-reactions. Finally, our results decouple the interfacial transfer of the minority carriers from the recombination at the interface/space charge region, underscore the significance of bulk processes and elucidate possible methods to engineer the mesoscopic transfer process at water splitting electrodes. In general, this work is intended to expand the scope of photocatalytic device design tools and thereby aid the design of the practical photoelectrodes en route to unassisted solar water splitting

Résumé

La conversion de l'énergie solaire en forme de combustible chimique sans carbone constitue un élément clé du paradigme économique que posent les énergies renouvelables. Au cours des deux dernières décennies, les impacts croissants et généralisés provenant des changements climatiques anthropiques sont devenus essentiels à la demande critique pour une conversion de combustible solaire en produit chimique, qui serait à la fois efficace, écologique et produit à grande échelle. Dans cette perspective, la recette scientifique de la séparation de l'eau par voie d'énergie solaire en utilisant des semi conducteurs abondants en terre, qui absorbent la lumière, prend un rôle critique pouvant définir la voie vers une production de H_2 peu coûteuse et évolutive pour ainsi servir de base fondamentale au paradigme économique des renouvelables. Néanmoins, une compréhension inadéquate des processus complexes de transfert de charge contrôlant la photocatalyse à semi-conducteur, entrave considérablement la production des photo-électrodes monolithiques à prix économique, relatif à la séparation de l'eau solaire de manière non assistée. Des recherches approfondies en cours dans cette direction ont mis en évidence des problèmes scientifiques critiques qui demandent une résolution urgente nécessitant des efforts à la fois théoriques et expérimentaux.

Les études de recherche dans cette thèse proposent la modélisation numŕique d'une jonction de diffusion électrolyte archétypique à semi-conducteur aqueux et offre une portée intrigante pour sonder théoriquement l'électrostatique et les processus de transfert de charge qui ainsi peuvent identifier la performance photo-électrochimique interfaciale. Notre approche numérique incorpore de manière concomitante, les méthodes de dérive à diffusion, développées pour les appareils semi-conducteurs à l'état solide ainsi que pour le modèle de Gouy-Chapman-Stern utilisé pour l'électrolyte aqueux. Cette étude, ainsi que la description numérique complète du système, sattaque à certains problèmes numériques fondamentaux (limites de conditions) associés à la modélisation semi-classique des jonctions semi-conductrices photo catalytique-liquide. Afin de capter numériquement et en même temps le photovoltage ainsi que le photocourant (deux des quantités les plus couramment mesurées dans la majorité des essais photo-électrochimiques) aux interfaces semi-conductrices à base liquide, nous démontrons qu'il est nécessaire de résoudre simultanément les formules de transfert de porteurs majoritaires et minoritaires. La solution du calcul de transfert de porteurs minoritaires savère fondamentale pour calculer le photocourant interfacial ainsi que la solution du calcul de transfert de porteurs majoritaires qui savère cruciale pour calculer le photovoltage. Tout au long de ce traitement numérique, une condition limite flottante en masse pour le potentiel électrostatique et pour les conditions limites pseudo-Schottky attribués aux courants d'électrons et trous interfaciaux, doit absolument être appliquée afin de faciliter le processus d'aplatissement des bandes que l'irradiation solaire tend à provoquer. De plus, cette recherche étend également la portée de la modélisation semi-classique en explorant les phénomènes théoriques associés la présence des états de surface et des états de piégeage en masse. En utilisant un différent niveau de Fermi pour l'occupation de l'état de surface, cette recherche fournit des aperçus concernant l'équilibrage des états de surface au niveau de Fermi et dénoue les tendances non-triviales dans l'analyse de Mott-Schottky. Inversement, les calculs concernant l'impact du piégeage en masse des porteurs, présentent une dégradation importante de la photovolte maximale qui est atteignable accompagnée de mauvaises propriétés de conduction provenant de porteurs majoritaires. De plus, les fonctionnalités de la méthodologie développée au cours de cette thèse, sont relevées en corrélant les calculs théoriques avec les mesures expérimentales rapportées dans la littérature. Ceci inclus mais ne se limite pas aux calculs de photovoltage, d'apparition et de saturation du photocourant, de transfert interfacial, de relaxation globale des porteurs minoritaires, des divers processus de génération et de recombinaison, d'états de surface et d'états de piégeage en masse, des analyses Mott-Schottky, de la spectroscopie de capacité, de filtrage de charge à l'interface photo-électrochimique et de la suppression des rétro-réactions. Enfin, nos résultats découplent le transfert interfacial des porteurs minoritaires lors de la recombinaison à la région dinterface et de charge d'espace et soulignent l'importance des processus en masse tout en proposant des nouvelles méthodes pour concevoir le processus de transfert mésoscopique aux électrodes séparatrices de l'eau. En général, ce travail est destiné à élargir la portée des outils de conception des appareils photo-catalytiques et ainsi assister à la conception des photoelectrodes pratiques qui servent au processus de séparation de l'eau solaire, d'une manière non assistée.

Acknowledgements

I would like to express my sincere gratitude to my supervisor Prof. Kirk H. Bevan for his continuous guidance and invaluable support in carrying out my research throughout the entire course of my doctoral study at McGill University. Kirk's critical insights, integrity and work ethics have provided me a role model to pursue scientific research. Moreover, his great advices, motivations and professional character, without a doubt, will continue to inspire my personal life as well as my professional career. I also want to thank him for providing me numerous opportunities that helped develope my professional career as a researcher.

I want to graciously thank to the present and previous members of Bevan Research group (Julien Jamaux, Md. Sazzad Hossain, Zi Wang, Salvador Valtierra, Botong Miao, Shuaishuai Yuan and Yee Wei Foong) for engaging valuable and insightful discussions throughout the span of this research work. I also want to thank all the undergraduate students (Xu Ke, Adnan Yassin Kassab, Ryan Yoo, Jiaxin Zhang, Jeremy Ding, Duta Jaizul-Aziz, Takshi Sachdeva) whom I mentored in different research projects. This extraordinary mentorship experience helped me in many ways to organize my research topics, discussions and critical findings.

I would like to cordially thank my parents, sisters and their families for their unconditional support during my stay at McGill University and Montréal. I cannot thank you all enough for always being with me. I also appreciate the motivation that I received from my friends. Special thanks to my friends Nusrat Haque, Nazmus Sakib and Auria Meher Chowdhury for their thoughtful decisions, precious time and countless support.

Finally, I want to thank McGill Engineering Doctoral Award (MEDA), National Science and Research Council of Canada (NSERC) and Fonds de Recherche du Québec-Nature et Technologies (FRQNT) for their financial support. My sincere gratitude to Mitacs and Lumerical Inc. (Vancouver) to host and financially support

my internship. And of course, thanks a lot to all the respected staffs in the department of Materials Engineering, who have made my doctoral journey a pleasant and memorable one.

To my parents.

Contents

List of Tables

List of Figures

Chapter 1

Introduction

1.1 Objective

The rising societal and environmental costs of fossil fuels have recently driven the worldwide hunt for inexhaustible and carbon-free energy sources.[1–4] This 'as-yet-unknown' source of energy must be abundant, environmentally friendly and replenishable in character in order to reduce our ecological footprint and man-made environmental impact.[1,4] Any solution of this kind is also obliged to meet the energy demand of new eco-friendly economic system, which will be essentially nourished by progressive political stances and green energy policies. As this decade is witnessing the most devastating and pervasive man-made impact on our planet, the need for this green and renewable energy solution is more pronounced than ever.[4] Decades of intensive research has unequivocally directed our search of this 'Holy Grail' of clean energy on the basis of earth-abundant substances and readily available forms of energy (*e.g.*, solar), which can ensure sustainability and offer large-scale and cost-effective energy production.[5,6]

The practical realization of efficient solar-to-chemical fuel production constitutes a long-standing possible solution to assist mankind's journey towards the proposed green and renewable energy paradigm.[5,6] In this regard, the scientific recipe of solar-to-hydrogen generation *via* solar-assisted water splitting requires only cheap ingredients (sunlight, water and earth-abundant metal-oxide semiconductors) to perform the key energy conversion process.[1] An intensive amount of research throughout the last 40 years has robustly delineated the intriguing scope of solar-to-hydrogen generation in mitigating the demand for renewable energy.[1,4–6] Nevertheless, these cumulative research efforts have revealed that efficient solar water splitting is enormously challenging due to our lack of understanding of the relevant fundamental processes. It is now clear that scientists and engineers from different fields need to come together with combined theoretical and experimental efforts to realize the efficient and economical production of solar-H_2.[4]

The objective of this thesis is to comprehend the pivotal charge transfer processes at the semiconductor-liquid interfaces as they pertain to the evolution of H_2 and O_2 *via* solar-assisted water splitting reactions.[7] The method, as presented in this thesis, is based on theoretical modeling, simulation and scientific attempts to correlate the key experimentally observable quantities with the reliable theoretical reproductions. By including the important ingredients of the complete semiconductor water splitting process into the state-of-the-art modeling of semiconductor-liquid junctions, the developed numerical recipe provides an intriguing scope to theoretically probe critical phenomena, such as the generation/recombination of carriers, generation of photovoltage and photocurrent, roles of surface states and bulk trap states, competitive transfer of interfacial carriers that are vulnerable to undesired recombination etcetera. More importantly, theoretical computation of this nature can be directly linked to the state-of-the-art experimental procedures, *e.g.*, measurements of photocurrent, photovoltage and junction capacitance (Mott-Schottky analysis), experimental spectroscopy of carrier relaxation process, and can offer further insights to improve our understanding of the fundamental governing processes en route to solar-to-chemical fuel conversion.

1.2 Organization of the Thesis

The organization of the thesis is based on the published and submitted manuscripts, which are solely developed by utilizing the methodology presented here. The entire discussion is divided into eight chapters. Chapter 1 briefly presents the introductory comments and motivations leading to the research presented in this dissertation. Chapter 2 consists of the literature review covering (1) the aspects of photoelectrochemical water splitting as a form of solar-to-chemical fuel generation (Sections 2.1-2.3); (2) scientific challenges and technological bottlenecks hindering the efficiency of solar-H_2 production (Section 2.4); and (3) a review of theoretical modeling of the photocatalytic semiconductor-liquid junctions with a clear delineation of the limitations of the existing theoretical frameworks (Section 2.5). Chapter 3 presents a thorough discussion on the computational methodology utilized in this thesis. It includes (1) a discussion on the generic semiclassical description of a semiconductor-liquid junction (Sections 3.1-3.2); (2) explanations of the assumptions (Section 3.3); and (3) the details of the numerical formulations of the drift-diffusion equations that are specifically designed/modified to simulate an archetypical semiconductor-liquid junction (Sections 3.4-3.6).

Chapter 4 - 7 are comprised of the published (Chapter 4 - 6) and submitted (Chapter 7) manuscripts in peer-reviewed scientific journals. Chapter 4 presents an elaborate theoretical derivation of the surface states equilibration process at a typical semiconductor-liquid interface. With the aid of the relative rate constants defining the interfacial charge transport, it has been shown that the surface states possess separate non-equilibrium Fermi-level that lies between the respective Fermi-levels of the semiconducting electrode and liquid electrolyte. Furthermore, by incorporating this theory into the numerical computation, Section 4.3 presents theoretical reproduction of the non-trivial phenomena commonly observed through various capacitive measurements (non-linearity, dip and plateau in Mott-Schottky analysis, detrimental and beneficial roles of surface states etc.).

Chapter 5, on the other hand, presents the complete numerical solution of the coupled Poisson-continuity equations at the semiconductor-liquid junctions (Section 5.2). By solving the electrostatics and charge transport in this way, it has been demonstrated that the numerical procedure can simultaneously capture both the photovoltage and photocurrent. In addition, results from the theoretical calculation in Section 5.3 are well-aligned with the experimental results reported in the literature. The pivotal contribution of this work can be identified as the development of the theoretical probing of the charge transport phenomena that determine the overall solar-to-H_2 conversion process.

Chapter 6 presents a scientific analysis on the impact of boundary conditions on simultaneously solving photovoltage and photocurrent at the semiconductor-liquid interfaces. The discussion presented in this chapter provides critical insights on how to numerically replicate the practical photocurrent along with a realistic band diagram of the photocatalytic junctions pertaining solar-assisted water splitting reactions.

Chapter 7 is organized to underscore the impacts of the bulk phenomena in determining the interfacial photoelectrochemical performance of the semiconductor-liquid junctions. Our numerical approach, as presented in this Chapter, includes the dynamics of mobile carrier trapping by the bulk trap states. The key take away from this work can be identified as the theoretical probing of the phenomena, *e.g.* degradation of the maximum of the attainable photovoltage, poor extraction of the majority carrier at the bulk electrode contact and unraveling the low majority carrier conductivity due to the presence of the bulk trap states. The numerical analysis has been linked to the various experimental studies present in the literature. Overall, this work suggests the engineering of the bulk of the semiconductor electrodes along with the more traditional approach of surface modification techniques.

Finally, Chapter 8 summarizes the conclusion obtained from the research work presented in this dissertation. It consists of the contributions to the original knowledge along with the key outcomes obtained from this thesis, the originality of the research findings and intriguing future directions by utilizing the footprint of the research performed throughout this doctoral study.

1.3 Contributions of the Author

The research work, as presented in this thesis, is aimed at the semiclassical modeling of the electrostatics and charge transport phenomena at semiconductor-liquid junctions pertaining solar-assisted water splitting. This thesis contains elaborate descriptions of the computational methodologies that are aptly developed and/or modified to simulate the performance of photoelectrochemical (PEC) devices. Throughout this research, persistent efforts have been given to correlate the theoretically extracted characteristics with those observed in the real-life experiments. The scope of this thesis, along with its original contributions, has been outlined in the following journal publications and submitted manuscript:

1. **Asif Iqbal**, Md. Sazzad Hossain and Kirk H. Bevan, The Role of Relative Rate Constants in Determining Surface State Phenomena at Semiconductor-Liquid Interfaces, *Physical Chemistry Chemical Physics*, 2016, 18, 29466–29477 (Chapter 4).

2. **Asif Iqbal** and Kirk H. Bevan, Simultaneously Solving the Photovoltage and Photocurrent at Semiconductor–Liquid Interfaces, *The Journal of Physical Chemistry C*, 2018, 122 (1), 30–43 (Chapter 5).

3. **Asif Iqbal** and Kirk H. Bevan, The Impact of Boundary Conditions on Calculated Photovoltages and Photocurrents at Photocatalytic Interfaces, *MRS Communications*, 2018, 1–8, DOI: 10.1557/mrc.2018.42 (Chapter 6).

4. **Asif Iqbal**, Shuaishuai Yuan, Zi Wang and Kirk H. Bevan, Impact of Bulk Trapping Phenomena on the Maximum Attainable Photovoltage of Semiconductor-Liquid Interfaces, *The Journal of Physical Chemistry C*, 2018, 122, 42 23878–23889 (Chapter 7).

In all the published manuscripts, the author has derived the relevant theories from the existing semiclassical models of the semiconductor-liquid interfaces. The entire sets of the source codes and simulations have been developed and performed by the author himself. The only exception is the first-principles calculation as presented in Chapter 7, where Shuaishuai Yuan and Zi Wang performed the computations using density functional theory (Section 7.3.2). Throughout the development of these computation models, the author engaged in valuable discussions with Professor Kirk H. Bevan. The idea of the separate Fermi-level for surface states, as presented in Chapter 4, was devised by Professor Kirk H. Bevan, whereas the author deduced the theory and performed all the numerical calculations. Both Professor Kirk H. Bevan and Md. Sazzad Hossain closely participated in the manuscript preparation and internal review. The author deduced all the derivations, simulations and results analysis presented in Chapter 5 and 6, whereas Professor Kirk H. Bevan provided important guidelines, instructions and participated in the writing/reviewing of the manuscripts. Similarly, the idea, derivation and most of the simulation presented in Chapter 7 were performed by the author. Shuaishuai Yuan and Zi Wang computed the DFT analysis and collaborated to prepare the results of polaronic states at the hematite photoanodes in Section 7.3.2. Professor Kirk H. Bevan provided valuable guidelines and participated in the writing/reviewing of the manuscript.

Chapter 2

Literature Review

2.1 Solar-to-Chemical Fuel

The sun offers the largest exploitable source of renewable energy in the form of photons.[1–3] Solar energy is practically inexhaustible and therefore, considered as a key solution of our transition towards a renewable economic paradigm.[1–4] In recent years, the resurgence of solar-fuel research has largely prompted the intention to directly convert solar energy into a storable, eco-friendly chemical form of fuel.[3,4,7–9] Theoretically, the energy of photons from the visible spectrum (ranges between 1 eV to 3 eV) is sufficient to facilitate various reactions synthesizing chemical fuels.[1,3] Furthermore, chemical fuels have the advantage of high energy density and ease of transportation and can serve as the backbone of large-scale energy production.[1,10,11] However, the ultimate scientific formula of solar-to-chemical fuel conversion should incorporate the cheap earth-abundant, non-toxic materials along with the solar energy so that this technology can afford electricity at a comparable price with respect to the cost of the existing fossil fuel based electricity.[1,3–6]

2.2 Artificial Photosynthesis

In this regard, the process of artificial photosynthesis, as inspired by the natural photosynthesis, is one of the possible routes towards the solar conversion to chemical fuel.[4,9] This process utilizes sunlight, water and semiconductors as the key ingredients to perform solar-assisted water splitting reactions to produce hydrogen (H_2) and oxygen (O_2) *via* water reduction and oxidation, respectively.[7–9] Now, H_2 is a storable, green fuel with excellent energy density.[1,10] An informative discussion on H_2 as a chemical fuel has been provided in Chapter 1 of Ref. [10]. However, to find a suitable semiconductor capable of implementing a low-cost but efficient photoconversion route is extremely non-trivial due to the stringent requirements that govern the desired water splitting processes at the typical photocatalytic semiconductor-liquid interfaces.[1,4] Fundamental research on semiconductor photoelectrochemistry, combined with the knowledge of solid state physics, has established the necessary requirements that a semiconductor must satisfy to optimally perform both of the water reduction and oxidation reactions.[1,12–14] These requirements include: (1) suitable semiconductor bandgap and the relevant energetic alignments of the energy levels in semiconductor and liquid phases; (2) facile charge transport between semiconductor and liquid phases; (3) chemical stability of the semiconductor in aqueous environment and (4) the cost of the implementation. For example, to perform solar-to-chemical fuel conversion, the bandgap of the desired semiconductor should range from 1.9 eV to 3.1 eV to ensure optimum absorption of the solar spectrum.[1] In addition, the semiconductor should possess suitable band alignment so that transfer of electrons (for water reduction) and/or holes (for water oxidation) to the liquid environment are energetically viable without the aid of any overpotential. Excellent carrier transport properties inside the semiconductor coupled with the superior interfacial catalytic performance are also crucial to maximize both the semiconductor-assisted solar harvesting as well as the interfacial transfers of the photogenerated carriers. Furthermore, the semiconductor must demonstrate stability against decomposition and corrosion reactions to ensure the durability of the device operation.[1, 13] In practice, any single semiconductor satisfying all of the aforementioned criteria is yet to be realized.[1] This reality, in turn, has directed the recent photocatalysis research towards engineering its underlying properties by nanoscale design,[13–16] surface modification techniques,[17] optimization of the bulk[18, 19] and interfacial carrier transport[20–22] etc. It is now evident that the challenges of efficient artificial photosynthesis need to be solved *via* combined efforts from scientists of all the basic sciences along with engineers from different disciplines.[4]

2.3 Photoelectrochemical (PEC) Water-Splitting

2.3.1 Basics of PEC Operation

The photoelectrochemical (PEC) device, designed to perform the artificial photosynthesis, is at the heart of the technology leading to solar-to-H_2 conversion.[1, 25, 26] Figure 2.1a exhibits a prototype PEC device commonly used in solar-assisted water splitting.[7, 24, 25] To simplify our discussion, in Figure 2.1a, we only consider that an n-type semiconductor is utilized to construct the photoanode (working electrode), whereas a metal electrode is utilized to construct the counter electrode. An exact example of this type of PEC configuration can be found in Ref. [24]. In the literature, wide varieties of practical PEC device configurations, albeit performing the identical water splitting reactions, have been reported.[8, 24, 26–28] Chapter 2 of Ref. [1] provides a brief description of the different types of PEC configurations reported in the literature. Now, in our illustration of the basic PEC configuration, as shown in Figure 2.1a, the oxygen evolution reaction (OER) occurs at the semiconducting photoanode, resulting in the generation of O_2.[29] Conversely, the fuel-generating hydrogen evolution reaction (HER) takes place at the metal counter electrode, giving

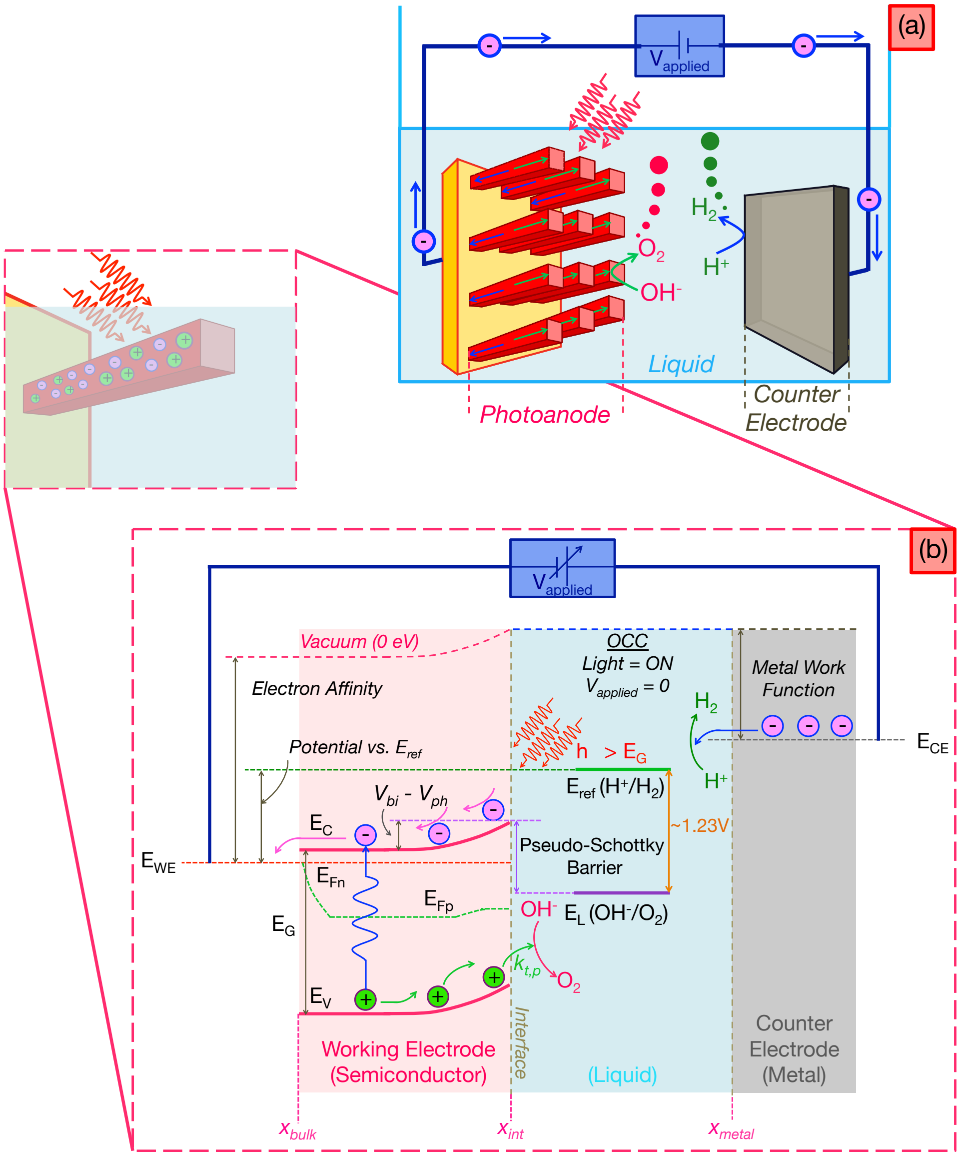

Figure 2.1: (a) A schematic of the standard PEC set-up based on a single semiconductor photoanode.[23,24] Solar-assisted water splitting takes place under illumination and suitably applied external potential ($V_{applied}$). Under the operating conditions, H_2 is bubbled through the metal-counter electrode. The other half of the water splitting reaction occurs at the semiconductor photoanode, where O_2 evolves due to water oxidation reaction. Inset provides an illustration of the interior of the photoelectrode under solar irradiation. The processes of the photogeneration of the electron-hole pairs at the semiconductor bulk and their subsequent separation and transfer are shown in part (b) with the aid of the energy band diagram. The key energy levels in the liquid and the counter electrode are also shown. Details of this band-alignment, e.g., definitions of all the energy levels, open circuit condition (OCC), will be provided in the course of the discussion presented in this chapter.

rise to the formation of H_2.[29] From the electrochemistry literature, we can represent both of the water oxidation and reduction reactions in terms of the respective reaction potentials compared to the potential of a standard electrode scale.[30,31] In this regard, the normal hydrogen electrode (NHE) scale is particularly popular. However, the measurement of NHE is found to be pH dependent.[1] For instance, in an acidic environment, the oxidation (OER) and reduction (HER) reactions of water can be respectively written as[1]

$$2H_2O + 4h^+ \rightleftharpoons 4H^+ + O_2, \quad {E^0}_{ox} = 1.299\text{V } \textit{vs.} \text{ NHE}, \tag{2.1}$$

$$4H^+ + 4e^- \rightleftharpoons 2H_2, \quad {E^0}_{red} = 0.0\text{V } \textit{vs.} \text{ NHE}. \tag{2.2}$$

Using our illustration from Figure 2.1a, ${E^0}_{ox}$ represents the potential of oxygen evolution reaction when the semiconducting photoanode transfers holes (h^+) to the OH^- species. Similarly, ${E^0}_{red}$ represents the potential of the hydrogen evolution reaction when the H^+ species take electrons (e^-) from the metal counter electrode. However, in a basic environment, Eqs. 2.1- 2.2 are respectively written as[1]

$$4OH^- + 4h^+ \rightleftharpoons 2H_2O + O_2, \quad {E^0}_{ox} = 0.401\text{V } \textit{vs.} \text{ NHE}, \tag{2.3}$$

$$4H_2O + 4e^- \rightleftharpoons 2H_2 + 4OH^-, \quad {E^0}_{red} = \text{-}0.828\text{V } \textit{vs.} \text{ NHE}. \tag{2.4}$$

Now, in the case of an aqueous solution with $pH = pH_{liq}$, the potential measurement ($E_{NHE} \mid_{pH_{liq}}$) against NHE scale can be written as[1]

$$E_{NHE} \mid_{pH_{liq}} = E_{NHE} \mid_0 -2.3\frac{k_BT}{q}pH, \tag{2.5}$$

where, $E_{NHE} \mid_0$ is the potential measurement *vs.* NHE at pH = 0, k_B represents the Boltzmann constant, T is the temperature and q is the charge of an electron. To eliminate the pH dependence of the standard electrode scale in PEC measurement, the use of reversible hydrogen electrode (RHE) is extremely useful.[32] In this case, the measurements of RHE (E_{RHE}) at $pH = pH_{liq}$ is expressed as[32]

$$\begin{aligned} E_{RHE} &= E_{NHE}\,|_{pH_{liq}} + 2.3\frac{k_B T}{q} pH_{liq} \\ &= E_{NHE}\,|_0, \end{aligned} \tag{2.6}$$

which is independent of the pH value of the solution.

Figure 2.1b represents the photoanode band diagram along with the key energy levels in the liquid electrolyte and metal counter electrode to fully describe the functionality of a typical PEC device.[7] In this illustration, all the energy levels are referred with respect to E_{ref}, which is a RHE reference scale. In addition, the spatial evolution of the vacuum level (0 eV) – a reference energy widely adopted by the solid state community,[33] is simultaneously drawn for clarity. Here, E_{WE} is the energy of the working electrode (photoanode) and essentially represents the energy of the electron (majority carrier) quasi Fermi-level (E_{Fn}) at the bulk. Similarly, E_{CE} represents the energy of the counter electrode. On the other hand, the liquid contains two electrochemically active redox species, e.g., OH^-/O_2 at 1.23 V *vs.* RHE and H^+/H_2 at E_{ref} or 0 V *vs.* RHE. Considering various practical PEC experiments reported in the literature, the liquid can be characterized as neutral (pH = 7), acidic (pH < 7) or basic (pH > 7) and is deliberately made highly conductive by adding electrochemically inactive supporting electrolyte.[34] Consequently, the semiconductor-liquid (SL) junctions, as presented in Figure 2.1b, exhibits electrostatics similar to the metal-semiconductor (MS) Schottky contacts (see also the discussions in Sections. 2.5.2, 3.3.1 and 3.3.2). Therefore, SL junctions are conventionally treated as pseudo-Schottky contacts in the literature.[32,34,35] Finally, the PEC set-up in Figure 2.1 also allows the application of external excitation in the form of solar irradiation and/or externally applied potential source (denoted by $V_{applied}$).[7]

A comprehensive understanding of the solar-assisted water splitting at a photocatalytic SL interface, such as that shown in Figure 2.1a, can be achieved by perceiving the processes of (i) photogeneration and (ii) separation of electron-hole pairs at the semiconductor interior and subsequent (iii) collection and transportation of the appropriate types of carriers to facilitate the desired electrochemical reaction.[12] In principle, an illuminated semiconductor photoelectrode exhibits the photogeneration of electron-hole pairs (EHPs) if the incident photon possesses energy higher than the semiconductor bandgap (E_G).[1,36] Under the influence of the electric field ($\vec{E}_{field}$), which exists at the space charge region (SCR) of the semiconducting electrode, the photogenerated EHPs (see Figure 2.1b) can be separated and directed oppositely.[36] As a result of this preferential movement of the separated EHPs, photogenerated holes (minority carriers) are collected at the anodic semiconductor-liquid interface, whereas the photogenerated electrons are swept towards the semiconductor bulk and subsequently transferred to the metal counter electrode *via* the external wire. Now, as illustrated in Figure 2.1b, the interfacial holes can oxidize water and generate O_2 (see eqs. 2.1 or 2.3) at the photoanode. Conversely, the electrons at the metal counter electrode can reduce water to produce H_2 (see eqs. 2.2 or 2.5).[1]

2.3.2 Oxygen Evolution Reaction *vs.* Hydrogen Evolution Reaction

The archetypical PEC set-ups performing complete water-splitting reactions demonstrate evolutions of H_2 and O_2 respectively at the cathodes and anodes. Nevertheless, the overall rate of water-splitting is critically set by the reaction characterized by the slowest reaction dynamics. Intensive amount of research during the last 40 years has unambiguously attributed OER at the photoanodes to limit the rate and efficiency of the complete solar assisted water-splitting.[37] OER is notoriously slow due to its complex reaction process requiring the transfer of four interfacial holes to complete the reaction.[38] In practical water splitting environment, the extraordinaryly sluggish kinetics of OER require large anodic overpotential to proceed and can lead up to 85% of the efficiency loss.[29,39] However, on the other hand, numerous experimental results on HER at the photocathodes have demonstrated the fast reaction mechanism leading an appreciable amount of current at equilibrium HER potential.[29,37,39] Consequently, though the goal of artificial photosynthesis is to perform complete water splitting, however, a large amount of the research and design efforts in the last two decades have been deliberately directed to the electrochemistry of OER.[37] Untill today, the understanding/optimization of the photoanodes performing OER remains as the long-standing challenge in improving the efficiency of solar-assisted water splitting reactions.[37]

2.3.3 Materials for Photoelectrochemistry and Photocatalysis

The exclusive search for suitable materials for performing OER (photoanodes) and/or HER (photocathodes) has been one of the key ingredients outlining the state-of-the-art PEC research. In last 40 years, a wide variety of semiconductors along with different configurations of the PEC devices have been proposed and tested for PEC-based water-splitting applications. The list of prospective semiconductors include: elementary semiconductors (Si),[40–44] compound semiconductors (Ta_3N_5,[45] WSe_2,[46,47] WS_2,[48] etc.), III - nitride/ III - V semiconductors,[14,44,49–52] oxide-semiconductors (TiO_2,[23] Hematite (α-Fe_2O_3),[53] WO_3[54] $BiVO_4$,[55] Cu_2O[56] etc). It is certainly a daunting task to review all of the key references available in the literature. Interested readers are referred to the expert in Ref. [13], Ref. [57, Chapter 1] and Ref. [37, Chapter 8] (for metal oxide-semiconductors) and Ref. [14], Ref. [57, Chapter 3-4] and Ref. [37, Chapter 9] (for III - nitride/ III - V semiconductors).

PEC-based water splitting scheme has the advantages of generating H_2 and O_2 at separate sites (respectively, at the cathode and anode).[57] Ideally, a prospective material for PEC application should efficiently perform both of the OER and HER without any externally applied potential ($V_{applied} = 0$). Nonetheless, this expectation is far from being practical due to the stringent conditions that a semiconductor must satisfy (see the discussion in Section 2.2). Therefore, the practical PEC devices incorporating complex designs (such as tandem cells) and separate materials for photoanodes and photocathodes are commonly found in the literature.[1,8] Now, in terms of the development of efficient water-reduction photocathode, several key materials have already demonstrated appreciable performance.[2,12] This includes, but is not limited to: p-Si (E_G ∼1.1 eV) with combination of Pt and NiMo catalysts,[40–42] p-WSe_2 (E_G ∼1.2 eV),[46,47] p-WS_2 (E_G ∼1.4 eV),[48] and p-Cu_2O (E_G ∼2 eV).[56] Conversely, the slow kinetics of water oxidation process along with the corrosive electrolyte environment make the search for anodic material extremely non-trivial.[12] For instance, most of the non-oxide semiconductors (Si, GaAs, GaP, InP, CdS) are prone to photocorrosion and exhibit diminishing performance once brought into contact with the aqueous solutions.[12,13,57] Thus, despite of demonstrating reasonable anodic performance, the adaptation of non-oxide semiconductors as a photoanode material still remains technologically unclear. The oxide-semiconductors, on the other hand, display superior stability in electrolyte solution.[57] However, their performance is strongly limited by the inherently poor light harvesting and charge transfer properties.[13,57] Thereby, a single material performing durable and efficient OER has yet to be found.

Now, the oxide-semiconductors are particularly important due to their low-cost synthetic procedure, which can outline cost-effective solar-H_2 generation – the ultimate goal of pursuing solar-to-chemical fuel conversion.[5,6,37] In this regard, the incorporation of TiO_2, α-Fe_2O_3, $BiVO_4$ and WO_3 as photoanode materials is of paramount importance.[13,37,57] In fact, the first demonstration of semiconductor water splitting by Fujishima *et al.* was performed on TiO_2 photoanode.[23] TiO_2 is cheap, chemically stable in a wide range of pH and by far the most studied material for photoelectrochemical and photocatalytic applications.[13,58] However, due to its large bandgap (∼3 eV), TiO_2 mostly absorbs the ultraviolet spectrum and is only able to harvest 5% of the solar spectrum (wavelength $\leq$ 410 nm).[57,59,60] Thus the research efforts are primarily directed to engineer the optical absorption of TiO_2 to incorporate the visible spectrum.[13] In addition, TiO_2 photoanode is characterized by short hole diffusion distance of ∼10 nm and low absorption coefficient (α) – meaning that the photogenerated holes are created at a distance larger than the hole diffusion length beneath the surface and vulnerable to the bulk recombination.[61]

On the other hand, α-Fe_2O_3 has a highly suitable bandgap of ∼ 2.1 eV with a possibility of absorbing 17% of the visible part of the solar spectrum (wavelength $\leq$ 590 nm).[57,59,60] In terms of chemical stability, hematite is found to be relatively stable in nonacidic pH.[13,57] Nonetheless, the anodic performance of hematite is highly suppressed by the hostile environment of the interior that allows only 2-4 nm of hole diffusion length in bare hematite.[62,63] Consequently, the photo-activity of the hematite electrodes are only detectable at potential $\geq$ 0.9 V *vs.* RHE.[53] Finally, $BiVO_4$ (bandgap ∼ 2.4 eV, wavelength $\leq$ 520 nm) and WO_3 (bandgap ∼ 2.7 eV, wavelength $\leq$ 460 nm) are also relatively stable in aqueous solutions and demonstrate photo-activity at potential $\geq$ 0.7 V *vs.* RHE and at potential $\geq$ 0.5 V *vs.* RHE, respectively.[57,64] Both of these materials suffer from low absorption coefficients, while $BiVO_4$ is also characterized by poor charge transport and WO_3 demonstrates unfavourable band alignments with respect to the liquid energy levels.[57,65]

2.3.4 Understanding of the Anodic Process: “The Key”

All the scientific data available today clearly show that the performance of state-of-the-art photoanodes are far shy of the predicted maximum.[59] For instance, using Murphy’s calculation (as presented in Ref. [59]), the theoretical maximum of photocurrent supported by a hematite photoanode can be estimated as 12.6 mA cm^{-2}, which is well above even compared to the best performing hematite electrodes in the literature.[21] Similar observations in other prospective anodic materials strongly suggest the demand of urgent scientific investigation to comprehend the complete anodic process, starting from the incidence of the photons on the semiconductor photoelectrodes to the electrochemistry of OER that is driven by the notoriously sluggish rate of hole transfer at the photocatalytic interface. Current observations/trends of the scientific explorations towards this direction are pressing the need of a combined interdisciplinary knowledge, which is based on experiments involving semiconductor photoelectrochemistry, theoretical modeling of solid state physics and the in-depth understanding of catalytic procedures.[4] Though the solution of this critical problem is still unclear as the scientists are exploring the existing/new avenues of development, it has been unambiguously agreed that the remedy will come *via* systematic and collaborative theoretical and experimental efforts.[4]

2.3.5 Towards Unassisted Solar Water Splitting

The accurate energetic band diagram representation of a photoelectrochemical SL junction, as presented in Figure 2.1b, reveals important electrostatics and charge transfer processes of the junction leading to the desired photoelectrochemical reactions (OER and HER).[1,2,37] Therefore, it is customary to draw the reliable band-alignment to depict the solar-to-H_2 production capability of any arbitrary photocatalytic SL junction. Here, we will also use energy band diagrams to develop our understanding of the photocatalytic SL junctions. Now, to begin, let us consider the

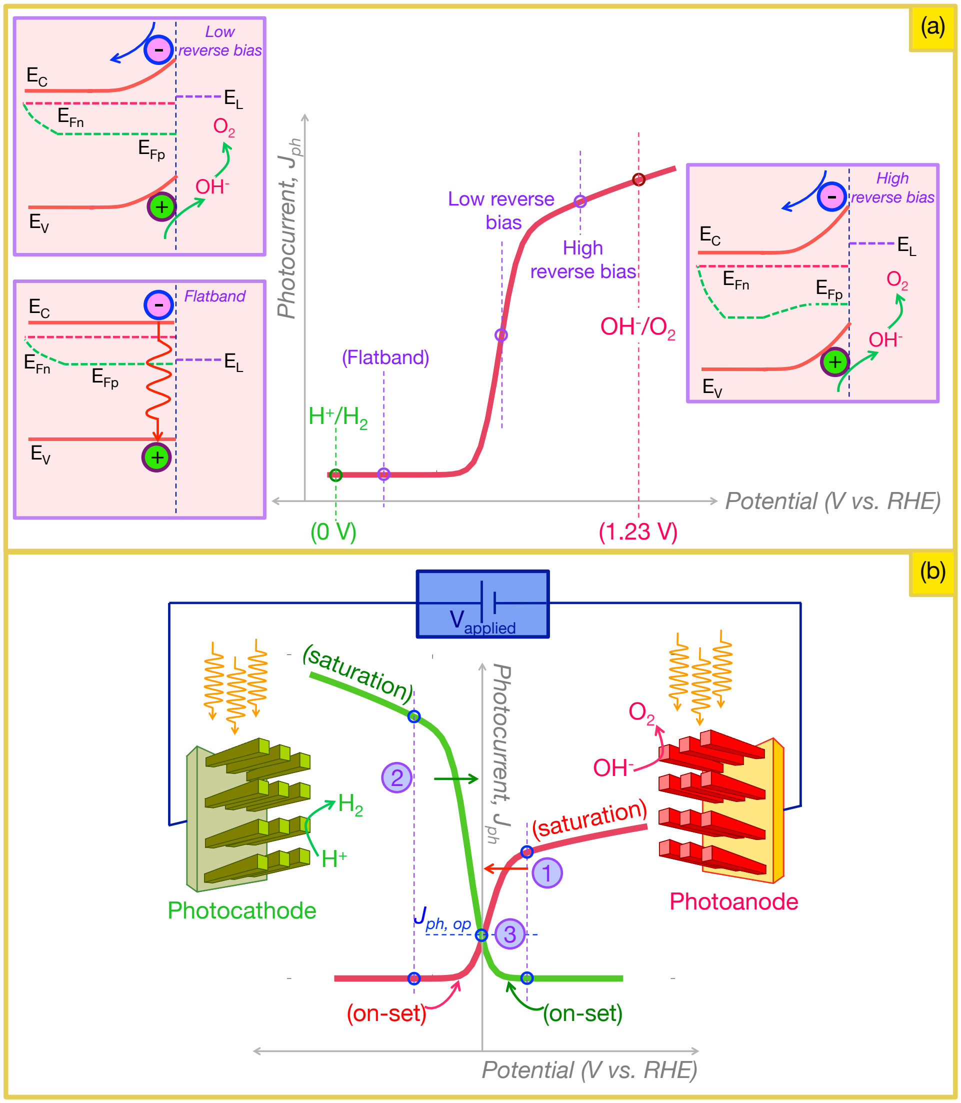

Figure 2.2: (a) Typical J-V characteristic of an anodic PEC junction (as presented in Figure 2.1b) along with the band diagram schematics of the n-type photoanode to demonstrate the influence of $V_{applied}$. The potential of HER (0 V *vs.* RHE) and OER (1.23 V *vs.* RHE) are marked as well. The insets illustrate the restoration of the $\vec{E}_{field}$ by gradually increasing the reverse potential (from the flatband condition). (b) Schematics of J-V characteristics of a photoanode and a photocathode drawn together to display the optimization of the operating photocurrent at a PEC device performing the complete water splitting. Here, the operating photocurrents from both of the electrodes are optimized at the cross-over point (J_{op}) – delineating the equal currents from the respective electrochemical reactions (HER at photocathode and OER at photoanode). Therefore, the design objective of a PEC device generally aimed at increasing J_{op} by simultaneously shifting the photoanode curve towards the cathodic direction (left on the potential axis) and the photocathode curve towards the anodic direction (right on the potential axis).

schematic band diagram in Figure 2.1b. It is imperative to understand that the illustrated band diagram in Figure 2.1b is drawn for the open circuit condition (OCC) at the illuminated SL junctions, meaning that the photocatalytic SL junction exhibits zero net photocurrent ($J_{ph} \approx 0$).[21,36,66,67] Under illuminated OCC, the semiconductor is only exposed to the solar irradiation and the applied external potential ($V_{applied}$) is reduced to zero. The hole concentration is increased at the semiconductor interior due to the photogeneration of EHPs (as depicted by the separate hole quasi Fermi level or E_{Fp}) and the junction exhibits the formation of the photovoltage (V_{ph}).[21,67] Now, the photovoltage is characterized by the flattening of the semiconductor bands under illumination. For instance, from the drawing in Figure 2.1b, the band-flattening process can be seen as the lowering of the band bending to V_{bi} - V_{ph}.[21,36] Here, V_{bi} represents the built-in potential of the SL junction under equilibrium and dark conditions ($V_{applied} = 0$ and without illumination). Nevertheless, the band diagram picture of the SL junction can be changed under the circumstances of externally applied reverse or forward potentials, by respectively increasing or decreasing the semiconductor band bending (see Ref. [37, Chapter 6 and 9]). In the case of the photoanode depicted in Figure 2.1b, the application of a forward bias pushes the bands upwards and the semiconductor approaches towards the flat-band condition. In contrast, reverse bias increases the band bending by pushing the bands in the downward direction.[1,34,36]

To delve more deeply, the influence of the applied external potential on semiconductor band bending is shown *via* a series of schematics in Figure 2.2a along with a sketch of the commonly observed photocurrent at the water-oxidation photoanodes.[2,12,37] As can be seen, the electrode operated at the flat-band condition displays perfect flattening of its bands and its Fermi-level is located cathodic of the water-oxidation potential at 1.23 V *vs.* RHE. Due to the absence of a preferential field ($\vec{E}_{field} \approx 0$) inside of the semiconductor, the separation of EHPs is highly inefficient and thus the amount of photogenerated holes reaching at the SL interface (p_s)

is significantly low.[37] This situation becomes worse if the semiconductor has a relative low absorption coefficient (α) as the photogenerated EHPs are then created deep inside of the semiconductor, well beneath of the surface.[57] Overall, at flatband condition, most of the photogenerated carriers undergo various forms of detrimental recombination processes (see Sec. 2.4 for details of these processes). This limits the photocurrent driven by the interfacial hole transfer around the flatband potential and is displayed as a negligible amount of photocurrent in Figure 2.2a. The negligible photocurrent at flatband condition is also commonly observed in almost every practical PEC experiment.[68–70] However, the solar harvesting of the photogenerated holes (minority carriers) can be improved with the application of the reverse bias, which in turn, restores the $\vec{E}_{field}$ and thus aides the efficient separation of the photogenerated EHPs.[69] The gradual increase of the band bending under reverse bias is also shown in Figure 2.2a. It is crucial to comprehend the trends of a typical photocurrent curve that undergoes the on-set (zero/low photocurrent), transition (moderate photocurrent) and saturation (high photocurrent) as the potential of the photoanode moves anodic of the flatband potential.[37]

At this point, from our discussion of SL junctions, it is clear that the relative alignment of the semiconductor electrode and the key energy levels can be modulated by the external excitation (illumination and applied potential). Consequently, it is also imperative to perceive what constitutes the fundamental design goal of any state-of-the-art PEC device development to conduct efficient solar-to-chemical fuel conversion. To further elaborate, let us simultaneously consider the photocurrent plots of both of the photoanode and photocathode as juxtaposed in Figure 2.2b.[2,12] If the PEC system operates at a potential close to water oxidation potential of 1.23 V *vs.* RHE (① in Figure 2.2b), the current due to oxygen evolution reaction at the photoanode would be high, while the current due to hydrogen evolution reaction at the photocathode (comprised of a p-type semiconductor) would be extremely low. On the other extreme, bringing the operating potential close to the water reduction potential of 0 V *vs.* RHE (② in Figure 2.2b) would highly improve the current at the photocathode, albeit in exchange of a poorly performing photoanode. Hence, the general design objective is aimed at shifting the photoanode curve (marked in red) towards cathodic direction and the photocathode curve (marked in green) towards the anodic direction to guarantee that the potential marking the current-crossover point can offer an optimal operation for both of the electrodes by engaging considerable amount of electrochemical reactions at the respective sites.[2] This is illustrated *via* point ③ in Figure 2.2b representing the optimized photocurrent (J_{op}). Now, the term "unassisted" solar water-splitting is coined to delineate the idea of obtaining high J_{op} when the crucial potential shifts (as marked in red and green arrows in Figure 2.2b) are brought about by only using solar irradiation through efficient generation of the photovoltage (with $V_{applied} = 0$). The implementation of a PEC device in this unassisted fashion arguably sets the target of the state-of-the-art PEC design.[2,21] Consequently, the efficient generation of V_{ph} in a PEC set-up is absolutely pivotal in accomplishing the goal of solar-assisted water splitting.[71] Nevertheless, the different recombination processes at the semiconductor bulk/interface, along with the complex nature of the interfacial charge transport, severely impede the realization of this goal. Therefore, practical implementation of unassisted solar water splitting is considered as one of the hardest challenges preventing our journey towards the renewable energy paradigm.[4,12,20–22]

2.4 Practical Challenges and Bottlenecks

2.4.1 Generation and Recombination Processes

To delve deeper, let us consider Figure 2.3a-b providing the detailed illustration of the impact of photovoltage along with the key generation-recombination processes

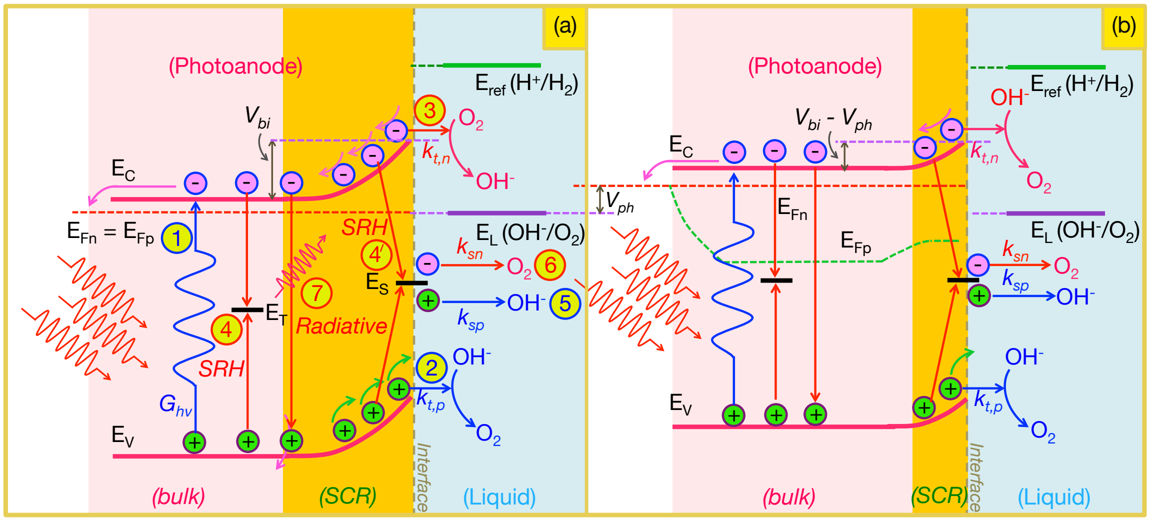

Figure 2.3: Various charge transfer processes at a typical n-type semiconductor-aqueous electrolyte junction pertaining O_2 evolution. The schematic band diagram in (a) represents the situation at the instant when the first stroke of the sunlight is incident on the SL junction. Each process can be identified as either beneficial (marked in blue) or detrimental (marked in red) in terms of the yield of solar to O_2 evolution reaction. For instance, processes depicted by 1, 2 and 5 (namely, photogeneration of carriers, direct and indirect interfacial transfers of valence band holes, respectively) are considered to be the beneficial processes. All other processes, conversely, can hinder the anodic performance either by annihilating the photogenerated holes (processes 4 and 7) or by reversing the product of the electrochemical reaction (processes 3 and 6). These undesirable processes include: the reduction of O_2 by direct interfacial electron transfer (process 3) and indirect surface-mediated electron transfer (process 6), the SRH recombination of free carriers *via* bulk and surface trap states (process 4 and 4′, respectively) and the radiative recombination of the carriers (process 7). The complex mutual interaction of these charge transfer processes ultimately sets the extent of band flattening due to the generation of photovoltage. As can be seen in (b), under a steady rate of illumination, the anodic SL junction demonstrates a partial flattening of its band.

commonly present at the interior and interface of an anodic SL junction.[12,21,37] However, our discussion, with appropriate modifications, is also equally applicable to photocathodes performing HER. Now, at equilibrium, a typical anodic SL junction demonstrates a perfect alignment of all the Fermi levels, if the photoanode only transfers electrons/holes to the OH^-/O_2 redox species in the liquid (see also Sections 3.3.3 and 3.3.4).[72] Figure 2.3a represents the energetics of the SL junction under this dark equilibrium (also known as the dark OCC), when the electrode-electrolyte system demonstrates a flat Fermi level ($E_{Fn} = E_{Fp} = E_L$). Further details of this equilibration process are provided in Section 3.3. In addition, Figure 2.3a can also be considered as the picture of the anodic SL junctions at the instant of solar excitation when the band bending of the semiconductor remains equal to the built-in potential (V_{bi}) of the relaxed electrode. Now, in a generic manner, we can categorize different processes at the typical SL junctions (see Figure 2.3) as beneficial (marked in blue) or detrimental (marked in red) in the context of the unassisted solar water splitting – the ultimate goal of the PEC device development. For instance, under a steady rate of photon incidence ($G_{h\nu}$), semiconducting electrode exhibits the generation of electron-hole pairs if the energy of the photons $\geq E_G$ (marked as ①). As discussed earlier in Section 2.3.1, the photogenerated electrons and holes are separated and subsequently directed in opposite directions under the influence of the electric field at the semiconductor SCR. Afterwards, the accumulated holes at the SL interface can be transferred to the OH^- species at an interfacial transfer rate of $k_{t,p}$ and thus, complete the desired oxidation reaction (marked as ②). Furthermore, the interfacial transfer of electrons to the liquid, if any, can be regarded as an unwanted backward reaction (see ③ in Figure 2.2a), lowering the yield of oxygen evolution reaction at the photoanode (see Section 3.3.3).[72]

Now, in the most usual case, semiconductor electrodes contain bulk and interfacial trap states, located at energy (E_T) intermediate of the bandgap.[1,33,34,36] These states are considered as detrimental recombination centres, reducing the available free carriers in the conduction and valence bands. The dynamics of this trap-assisted recombination is described by the Shockley-Read-Hall (SRH) recombination and illustrated as ④ in Figure 2.2a.[73] It is also important to note that the recombination assisted by surface states (E_S) is also commonly represented in literature by equivalent SRH expression.[74–77] However, the role of surface states in terms of the performance of the anodic OER reaction is still unclear and of paramount interest in the current PEC research.[22,78–82] This is primarily due to the dual role played by surface states to either hinder[22,78–80] or facilitate[81,82] the interfacial charge transfer process. In a classical description, the surface states, similar to the bulk trap states, also act as recombination centres and annihilate solar-harvested minority carrier population *via* recombination (as depicted by ④′ in Figure 2.2a).[22,78–80] Nonetheless, there are experimental evidences of beneficial surface-mediated reactions at the photocatalytic SL interfaces.[81,82] For instance, with a sufficiently fast rate of surface-mediated hole transfer (k_{sp}) in Figure 2.3a, surface trapped holes can avoid the undesired interfacial recombination and perform OER *via* the interfacial transfer from the surface states (presented as ⑤ in Figure 2.3a). Similarly, as shown by ⑥, surface states can also transfer electrons and facilitate the undesired oxygen reduction reaction (ORR)[29] by reversing the product of OER. Finally, the direct band-to-band radiative recombination (process ⑦ in Figure 2.3a) is also possible and can reduce the available photogenerated EHPs.[33,83]

2.4.2 Generation of Photovoltage

As described earlier in Section 2.3.5, at any PEC set-up, we can exploit the photovoltage to incorporate the necessary cathodic shift of the J-V characteristics of a typical photoanode (see the red arrow in Figure 2.2b). This is also true for photocathodes, where the goal is to shift the J-V characteristics towards the anodic direction (green arrow in Figure 2.2b). In both cases, photovoltage generation is absolutely pivotal to meet-up the design goal of complete water splitting PEC devices.[2,12,21] In the literature of solar-assisted water splitting, the photovoltage is considered as a thermodynamic quantity arising due to the net electron-hole pair generation at the interior of the semiconducting materials under solar illumination.[67] The net effect of photovoltage on the overall energetics of SL junction is seen in Figure 2.3b. V_{ph} effectively flattens the semiconductor bands and acts as a forward bias, solely brought about by the solar irradiation. Consequently, splitting of quasi Fermi-levels of electrons and holes are simultaneously observable. Refs. [67], [84] and [85] provide expert's discussion on the role of photovoltage in overall PEC performance. Also, Section 5.2.3 of Chapter 5 of this thesis contains an in-depth description of the generation of photovoltage at a stereotypical photocatalytic SL junctions. Finally, Chapters 5-7 contain extensive discussion on the significance of photovoltage generation (equivalent to the semiconductor band-flattening under illuminated condition) to accomplish the ulitimate design goal of unassisted solar water splitting.

2.4.3 Degradation of Photovoltage and Retarded On-set of Photocurrent

At the semiconductor-liquid junctions, the maximum possible value of photovoltage ($V_{ph|max}$) is generally set by the extent of the built-in potential and exhibited by a complete flattening of the semiconductor bands under solar irradiation (see Ref. [36, Chapter 10]). However, our schematics of an SL junction at illuminated OCC, as presented in Figure 2.1b and Figure 2.3b, depict the degradation in the generation of photovoltage by illustrating a partial band flattening ($V_{ph} < V_{bi}$) – a situation when the band bending is reduced but not completely eliminated under sufficient photoexcitation. This situation can be worsened by reducing $V_{ph} \sim 0$ under certain circumstances. For instance, experimental results on hematite electrode by

Sivula *et al.* show the complete absence of the photovoltage (corresponding to zero photocurrent) unless the electrode undergoes high temperature (800 °C) annealing.[53] Moreover, under the partial band flattening or inefficient generation of V_{ph}, the practical PEC devices demonstrate retarded on-set of photocurrent – an issue that directly hinders the unassisted solar water splitting.[21] Under these circumstances, large overpotential (reverse bias) must be applied to see considerable amount of photocurrent.

Numerous studies in literature attributed the surface and bulk recombination processes as the principal cause behind both of the degradation of photovoltage and retarded on-set of photocurrent.[12, 19–21, 53] Recently, the nanostructuring of the electrodes along with different surface and bulk modification techniques have gained considerable amount of attention due to the corresponding improvement of the photocurrent response and photovoltage generation.[17] Nonetheless, the fundamental understanding and effective mitigation of the detrimental processes causing performance degradation have yet to be determined. Moreover, the role of catalysts and/or dopants to overcome the limits of the practical photoelectrodes has not been explored completely.[86] It is evident that further theoretical and experimental studies providing fundamental insights of the photocatalytic SL junctions are essential to engineer PEC devices and enhance the corresponding solar-to-H_2 (STH) conversion efficiency.

2.5 Modeling of Semiconductor-Liquid Junctions

2.5.1 A Brief History

Analytical Approach

The history of theoretical modeling of the electrostatics and charge transport phenomena at the SL junctions can be dated back to 1977 when Butler first treated a semiconductor-electrolyte junction as a metal-semiconductor (MS) Schottky contact and analytically derived the J-V characteristics of WO_3 photoanode.[35] Butler's derivation was based on Gartner's (1959) original analytical derivation of the photogenetation and the subsequent interfacial collection of carriers at a reverse-biased Schottky contact.[87] At the same timeline, Wilson (1977) published his model on photoexcited electrodes in an electrochemical cell.[88] This work marked the first demonstration of the inclusion of the surface recombination and the interfacial transfer of the minority carriers *via* transfer/recombination velocity. The concept of recombination velocity was originally introduced at the simulation of MS contact by Crowell and Sze (1966) in the wake of semiconductor device modeling development.[89] Using different charge transfer velocities for n-TiO_2 photoanode, Wilson was able to show the competition between the unwanted surface recombination and the beneficial interfacial charge transport – a critical observation generally found to be true for the state-of-the-art photo-active SL junctions.[21,65] Later, a refined analytical model was proposed by Reiss (1978).[90] However, all of these analytical models for semiconductor photoelectrodes disregarded the critical SCR recombination (see Ref. [37, Chapter 1]). The effects of SCR recombination were first considered by Reichman (1980).[91] This approach demonstrated the retarded on-set of the photocurrent response, commonly observed in PEC experiments, by including the SCR recombination.[37,91] Later, El Guibaly and Colbow, in a series of papers, also included SCR recombination and further refined the analytical J-V model for the photoelectrodes utilized in PEC setups.[92–94] It is clear that this early stage of modeling of SL junction was mainly focused on the ideal J-V characteristics of earth abundant oxide-semiconductors (WO_3[35] and TiO_2[88]) with wide bandgaps. Afterwards, Peter *et al.*, in a series of papers, developed analytical models considering the charging/discharging effects of the surface states.[95–98] The most important take away from Refs. [95]-[98] was the explanation of the transient processes widely observed in the chopped light-based voltammograms.[37] Recently, Peter also presented a simplified yet effective phenomenological model[66] to compute the energetics and kinetics of photocatalytic SL junction, which has been utilized in few experimental studies with some success.[62,99] Finally, along with this long list of analytical attempts to model the SL junctions, it is also worthwhile to mention the theoretical works performed by the Lewis group (1992)[72] and Salvador (1999)[67] covering the critical insights on the mathematical treatment of the physical processes at the practical PEC systems. Refs. [72] and [67] discussed fundamentals of formation of quasi Fermi-levels, generation of photovoltage, kinetics of chemical reactions etc., and untill today, are serving as the references of the relevant assumptions utilized in the state-of-the-art modeling of photocatalytic SL junctions.

Numerical Approach

Over the last two decades, the modeling of photocatalytic SL junctions has been mostly spurred by the scope of the computer-aided numerical simulation.[32,82,100–119] The enormous success of numerical simulation in the development of the modern-era semiconductor devices has been continuously motivating scientists to implement similar simulation techniques for the typical SL junctions.[120–122] Numerical modeling of the standard photo-active SL junctions can offer an intriguing scope to probe the fundamental physical processes governing the photoelectrochemistry/photocatalysis and potentially open new avenues to engineer the performance of PEC devices. The ultimate goals of the numerical simulation of SL junction are (1) to model the charge transport and band diagram electrostatics of the semiconductor electrodes (including all the processes as presented in Figure 2.3); (2) to calculate the kinetics of photo-driven electrochemical reactions and surface catalytic processes; and (3) to determine the charge screening and ions distributions inside of the liquid environment. In addition, the numerical approach should be highly adaptable with facile implementation so that the results can be reliably reproducible by the experts of this field. A particular important modeling framework is comprised of the complete solution of the coupled drift-diffusion (Poisson-continuity) equations (see Refs. [120, Chapter 6] and [122, Chapter 4]). The coupled solution of semiconductor drift-diffusion equations can provide insights on charge transport and band bending electrostatics.[122] This, in turn, can be further utilized to engineer the band alignment and generation-recombination processes inside of the photoelectrodes used in PEC applications. Along with this direction, the numerical study presented by Lewis and co-workers (1999) is regarded as one of the earliest efforts to incorporate basic semiconductor equations in the simulation of J-V characteristics of semiconductor photoelectrodes.[100] Cass *et al.* also presented separate numerical studies using the similar sets of equations (2003).[101,102] Very recently, Cendula *et al.* (2014) demonstrated the numerical calculation of the band diagram picture of PEC cells performing water splitting.[32] However, Ref. [32] only considered the light induced modulation of the minority carrier concentration – an assumption that is unable to capture the critical process of photovoltage generation (see Ref. [37, Chapter 1]). Bertoluzzi *et al.* (2016)[82] and Shi *et al.* (2016)[103] also presented results by solving drift-diffusion equations with an aim at understanding the surface recombination process at the photocatalytic interfaces. Two other recent numerical studies towards this direction were performed by Foley *et al.* (2012)[107] and Gaudy *et al.* (2015)[109] using available commercial software.

Furthermore, Boettcher and co-workers have directed their work to the simulation of electrocatalyst-coated semiconducting electrodes for PEC applications.[105,106] The main contribution of these works is the numerical implementation of the adaptive and metallic electrocatalyst layers generally used in catalyzed photoelectrodes. A relevant discussion can be found in Refs. [37, Chapter 7], [105] and [106]. Also, throughout the last two decades, Bisquert and co-workers presented several original works on the capacitive modeling of SL junctions with an aim at correlating theoretical results with the practical observations from the standard impedance spectroscopy (IS) experiments.[81,82,123–126] These works also explored the crucial role surface states charging/discharging[81, 82, 124, 127] and attempted to model the cyclic voltammetry measurements.[125, 126] Finally, existing modeling literature also demonstrated the scope of density functional theory (DFT) to numerically determine the optical and electronic properties of the prospective materials for PEC applications,[110–112] effects of doping,[113–115] relevant band-alignment at the SL interfaces[116, 117] and the performance of water splitting catalysts.[118, 119] However, in general, DFT calculations are computationally expensive. Using the current computational resources, it is a daunting task to perform comprehensive numerical simulation of photoelectrodes, even with a dimension of $\sim$ 10 nm. One particular intriguing scope of DFT analysis in PEC device modeling would be the electrochemical characterization and analysis of the Stern layer located at the SL interface (see discussion in Section 3.1 for details).[116]

2.5.2 Limitations of the Existing Models

Our discussion from Section 2.5.1 clearly establishes the modeling of carrier transport phenomena at the photocatalytic SL junctions as a relatively old problem of the modern photoelectrochemistry. Despite the appreciable amount of analytical and numerical works in this area, the utilization of the existing models with the experimental results in a collaborative manner has demonstrated limited success. This is, of course, partly because of the inherently complicated picture of the practical SL interfaces that makes the theoretical modeling very challenging (see Figure 2.3). More discussion on the electrostatic picture of the SL interface is also provided in Section 3.1 of Chapter 3. Overall, despite of the persistent efforts, a systematic implementation of the numerical models (with robust assumptions) capturing the fundamental processes of artificial photosynthesis has not been fully developed yet. As the concluding part of this chapter, we will now visit some key limitations of the existing models as well as few essential features that need to be considered in the future development of the comprehensive simulation tools for this exciting field of research.

Complete Solution of Drift-Diffusion Equations at Illuminated SL Junction

The complete solution of the drift-diffusion model (coupled Poisson equation with electron and hole continuity equations) is a proven theoretical procedure to probe the pivotal band diagram energetics and charge transport kinetics in the semiconducting materials (see also Section 3.2.1).[33, 120–122] When applying at an SL junction, the combined drift-diffusion model appears to be more complicated as the semiconducting electrode is characterized by the electronic 'band' conduction (due to the movements of the conduction band electrons and valence band holes), whereas the liquid is characterized by the ionic conduction.[1, 25, 34, 36] Hence, at the SL junctions, the conventional current-continuity equations have to be solved only inside of the semiconductor (Eqs. 3.1a - 3.1d). However, the electrostatic potential, the other key energetics that is computed from the Poisson equation, spans throughout the entire SL junction and must be calculated accordingly. Furthermore, as the semiconductor and liquid systems can be considered as dielectric media with widely different dielectric constants (ε_{sc} and ε_L, respectively), it is also important to consider the impact of the spatially varying dielectric constant while solving the Poisson equation in a unified fashion (Eqs. 3.1a and 3.10). For instance, hematite has a bulk dielectric constant of $\varepsilon_{sc} \sim 32$, whereas the bulk water is characterized by a dielectric constant of $\varepsilon_L \sim 80$.[128, 129] Due to these inherent complexities of the semiclassical description of a typical SL junction, the existing drift-diffusion solutions in the literature consider only the semiconductor electrode resides in the computational domain by assuming constant/negligible potential distribution in the liquid.[32, 82, 100–103] In addition, the inclusion of all the key generation-recombination processes (as presented in Section 2.4.1) in the full solution of drift-diffusion equations is also important to accurately predict the PEC-performance. This requirement can make the numerical implementation and the subsequent convergence criteria mathematically difficult to satisfy. For example, Refs. [32], [82] and [103] only assume bulk/SCR radiative recombination and do not include the critical process of SRH recombination into account. This, in other words, greatly simplifies the overall computation. Finally, the boundary conditions of the drift-diffusion model should be imposed according to the physical processes of the SL junctions by clearly comprehending their impact on the calculated results – a crucial issue often ignored in the state-of-the-art SL junctions modeling literature.[32, 82, 103]

Calculation of the Photovolatge

Generation of photovoltage is the key to perform unassisted solar-to-H_2 conversion (see Section 2.4.2). The effect of V_{ph} can be seen as the semiconductor band-flattening brought about by the solar irradiation, which is commonly observed/measured *via* different experimental flatband techniques (see Ref. [130, Chapter 6]). The notions of V_{ph} – flattening of semiconductor bands and cathodic/anodic shift of J-V characteristics of photoanode/photocathode,[21, 67, 84] so far have not been implemented in the existing computational frameworks in the literature.[32, 82, 103]

Pinning/Unpinning of the Semiconductor Bands

The conventional procedure to simulate the charge transport at a photocatalytic SL junction assumes the existence of a pseudo Schottky-type contact at the interface, so that the junction electrostatics closely emulate those of a metal-semiconductor Schottky contact (details are given in Sections 3.3.2 and 5.1).[32, 35, 103] The basis of this assumption can be easily perceived by analyzing the parameters reported in numerous PEC experiments. For instance, by taking the practical hematite-based PEC set-up by Le Formal *et al.*,[68] a simple calculation shows that the concentration of liquid ions ($\sim 3 \times 10^{20}$ cm^{-3}) are substantially higher than the maximum available free electrons ($\sim 10^{19}$-10^{20} cm^{-3}) in the conduction band. Consequently, at a usual PEC set-up, the electrode exhibits higher screening length compared to the liquid side and any change in the junction potential mostly appears as a change of potential in the semiconductor side.[1,34,36] This situation, which is electrostatically equivalent to the MS junctions, is known as the band-level pinning (BLP) of the semiconductor electrodes, where the relative positions of the semiconductor bands with respect to the liquid Fermi-level are independent of the applied potential. Nevertheless, the electrode can deviate from this ideal BLP picture of the interface by unpinning its bands during the events of surface state charging/discharging, high concentration of semiconductor doping or large applied potential. All of these practical scenarios underscore the significance to model the SL junction in such a way so that the potential drop at the liquid side ($\Delta\phi_L$), if needed, can also change at the event of unpinning of semiconductor bands (see our discussion in Section 3.2.2). However, the state-of-the-art SL junction simulations fail to capture the band-level unpinning as they forcibly assume that the SL junction maintains BLP throughout its operation.[32,82,100–103]

Role of Surface States

It has been experimentally well-established that surface states (SSs) play a critical role in determining the ultimate PEC performance at the stereotypical SL junctions.[65,71,81,85] Effects of surface states are often experimentally linked with band-level unpinning, retarded on-set of photocurrent with reduced photovoltage and intensive interfacial recombination.[21,65] Various surface modification techniques and superior geometrical design led by nanostructuring of the electrodes are considered as the potential remedies to eliminate detrimental impact of SS.[17,20,79] On the other hand, recent observations have also attributed the indirect electron/hole transfer to the liquid *via* SS as beneficial as it yields in the solar-to-chemical fuel conversion.[81,82] Needless to say, it is immensely important for a realistic model to capture the dual role of SS-dynamics, which of course does not fully exist in the current SL junction modeling literature. Moreover, earlier research also brought intriguing issues regarding the equilibration process of SS at an SL junction.[131,132] So far, the equilibration of SS at the SL junctions (and thus the occupational statistics of SS) is poorly understood, as SS can be equilibrated with either the semiconductor or the liquid.[131,132] Overall, a numerical description of SS occupational statistics, which is capable of probing/exploring the dual role of SS in photocatalytic SL interfaces would be pivotal as a future work. Moreover, directly correlating the theoretical results with the experimental observations can also be utterly useful to improve our understanding of the critical processes related with SS.

Impact of the Bulk/SCR Trap States on Interfacial Photocurrent

Similar to the surface states, the bulk/SCR trap states also adversely affect the interfacial photocurrent. This is due to the poor bulk-transport characteristics and the inefficient generation of V_{ph}.[53] To better understand, let us consider again the case of oxide-semiconductor based photoanodes.[13] These materials are characterized by the low absorption coefficients (as discussed in Section 2.3.3), elucidating that the photogenerated carriers are mostly created at the bulk region of the electrodes.[57] That being said, now if the electrode contains bulk trap states, most of the EHPs will undergo bulk recombination and the yield of solar water-splitting will be severely reduced. Sivula *et al.*[53] showed that the hematite electrodes are reluctant to exhibit photocurrent generation (and the subsequent solar-harvesting) without the essential high temperature annealing process, which presumably enhances the bulk transport properties. This observation has been widely reported in the literature.[12,22,60,133] In the same direction, Ref. [19] demonstrated the performance degradation by the formation of the 'dead-layer' at the bulk hematite due to the large number of intermediate trap states. Therefore, it is imperative for any numerical model exploring SL junction characteristics to take account the impacts of the bulk/SCR trap states in the overall PEC performance.

Role of Catalysts: Enhancement of Reaction Kinetics or SCR Thermodynamics?

Electrocatalysts are widely utilized to improve the photocatalytic performance of the semiconductor electrodes. Recent experimental studies by Wang and co-workers aptly pointed out the seemingly different strategies played by the electrocatalysts in improving the PEC performance.[21] Subsequently, the concepts of kinetic catalysts (that enhance the reaction kinetics and thus work as traditional catalysts) and thermodynamic catalysts (that enhance the band diagram electrostatics of the SL junctions) have recently emerged in the field of photoelectrochemistry. A particular example can be the role of cobalt-phosphate (Co-Pi) onto hematite photoanode.[86] An experimental study by Klahr *et al.*[134] proposed that Co-Pi, when deposited on hematite, enhances the hole transfer kinetics (kinetic catalyst). Conversely, Barroso *et al.*,[78] using a similar PEC set-up, speculated that the enhancement arises due to the improved band bending (thermodynamic catalyst). Clearly, these observations urge to pursue more theoretical and experimental research towards this direction.

Modeling of the SL Junctions with Corrosion and Mixed Reactions

Ideally, OER constitutes the desired reaction at the photoanodes, whereas HER is the desired reaction at the photocathodes, as illustrated in Figure 2.1b.[7,13,72] Practical PEC systems, however, can deviate from this ideal situation and exhibit mixed electrochemical activities (performing both OER and HER).[72] Moreover, the photocorrosion and self-oxidation of the electrodes can further complicate the electrochemical activities of the photocatalytic SL interfaces (see Ref. [34, Chapter 8] and Ref. [1, Chapter 2]). Though the possibility of the mixed reaction is vaguely outlined in the existing modeling literature due to the inherent complexities of the associated processes, the inclusion of the mixed electrochemical reaction along with the effects of corrosive degradation of the semiconductor (chemical instability) need to be considered in the future models utilized in efficient PEC devices designing.[72]

Modeling of the Liquid Electrolyte

As mentioned earlier that the usual approximation of SL junction simulation assumes that the entire potential drop occurs at the semiconductor-part of the junction and then analytically or numerically calculates the electrostatic potential only inside the electrode.[1,34,36] This oversimplified approximation is unable to capture any change in liquid potential and thus undermines the practical situation of band-level unpinning.[21,34] In order to overcome this limitation, it is imperative to include liquid electrostatics to the combined numerical solution. Along the same direction, it is also crucial to differentiate between electrochemically active and inactive ions in the liquid.[34] Overall, the inclusion of liquid models can manifest the impact of the supporting electrolyte, role of redox-active species, finite-ion size as well as demonstrate the charge screening process and how the charge conservation is satisfied.

Modeling of the Stern Layer

Now, very close to the interface, electrochemically active ions undergo adsorption and desorption processes (also illustrated in Figure 3.1).[1] Ideally, these ions are mainly immobile in character and form a densely packed layer, known as Helmholtz or Stern layer (see Section 3.1 for details).[135,136] In theory, the processes in the Stern layer are usually modeled using analytical expressions.[135–137] In this regard, the application of semiclassical treatment still remains largely unclear. In terms of numerical analysis, so far, the first-principles approach (DFT calculation) seems to be effective in theoretically probing the impacts of the Stern layer (potential jump, constituents of the Stern layer and so on).[116]

Chapter 3

Theory

3.1 Semiconductor-Liquid Interface

In the most generic case, when a semiconductor is immersed in an aqueous electrolyte, charge transfer between solid and liquid phases starts to occur and as a result, a charged interface (analogous to the electrical double layer) is formed almost instantaneously.[1,34,36,129,136] The driving force facilitating this fundamental charge transfer process is the difference between the Fermi levels of both sides of the interface.[25,34] Under any external perturbation in the form of sunlight and/or applied potential, the extent of charged interface would change accordingly (see Ref [1, Chapter 2]). Nevertheless, the overall picture of a semiconductor-liquid interface, as shown in Figure 3.1, remains the same. Here, Figure 3.1 represents a schematic of the spatial charge distribution at a typical anodic SL junction pertaining OER. The electrostatics of any SL interface must obey the fundamental law of charge conservation, meaning that the charge in the semiconductor electrode (Q_{solid}) must be balanced by the equal amount of oppositely signed liquid charge (Q_{liquid}). However, it is also important to understand that the electrical conduction mechanisms on both sides of the interface are very different as the semiconductor is characterized by electronic 'band' conduction, whereas, the liquid exhibits ionic conduction (see Ref. [34, Chapter 3]). In addition, the picture of a realistic SL junction often becomes overwhelmingly complicated due to the presence of the surface and bulk trap states in semiconductor, adsorption of H^+ and OH^- species *via* the protonation/deprotonation reactions at the liquid part of the interface and the slow kinetics of O_2 evolution.[1]

3.1.1 Charge inside of the Semiconductor

The contribution of the net semiconductor charge (Q_{solid}) comes from: (1) the freely moving electrons/holes respectively located at the conduction/valence bands; (2) ionized donors/acceptors; and (3) charge from the trapped electrons and holes in the intermediate bandgap states located at the surface or the bulk of the semiconductor.[33,83,138] The interaction of these different contributions can be seen as the exposed charge in the semiconductor space charge region (SCR), just beneath the SL interface (from $x = x_{int}$ to $x = x_{SCR}$ in Figure 3.1).[1,34,36] In this case, the depleted photoanode (n-type semiconductor) exhibits its net SCR charge comprised of the positively charged ionized donors (N_D^+) along with the photogenerated holes located either at the valence band (free) or the surface states (trapped). Conversely, the bulk of the semiconductor is characterized by a flat electrostatic potential profile, indicating the locally balanced charge distributions in the interior of the semiconductor.[33] However, this picture of the semiconducting electrode (Figure 3.1) is obviously simplified as the photogenerated electrons in the conduction band and the carriers trapped by the bulk trap states can also contribute to the net semiconductor charge in a practical semiconductor photoelectrode. As we will see later in this Chapter that the numerical technique developed in this thesis can take into account of all of these charge contributions in the overall computation.

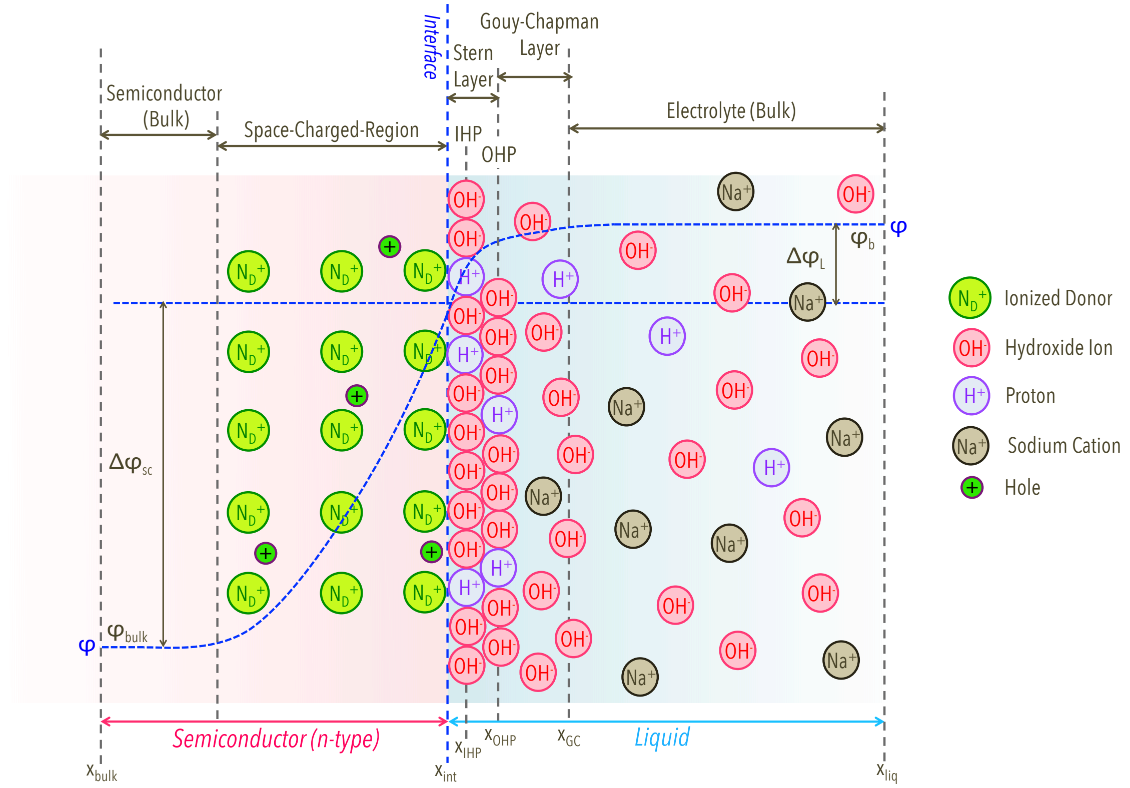

Figure 3.1: Physical picture of an anodic SL junction with the corresponding illustrations of Q_{solid} (on the left) and Q_{liquid} (on the right), where $Q_{solid} + Q_{liquid} = 0$ and $x = x_{int}$ marks the location of the SL interface. Here, the illustration portrays a hematite photoanode immersed in an aqueous solution of pH $= 13.6$, similar to the one presented in Ref. [68]. In general, the screening length in semiconductor usually spans much longer than that of the electrolyte (not drawn in scale here). As can be seen, Q_{solid} at the SCR is primarily comprised of the ionized donors (N_D^+) and photogenerated holes. Nevertheless, SCR in a practical photoanode also contains photogenerated electrons, which is not shown here. Q_{liquid}, on the other hand, is comprised of (1) diffusively distributed ions from liquid bulk ($x = x_{liq}$) up to the extent of outer Helmholtz plane ($x = x_{OHP}$); and (2) specifically adsorbed ions on the inner Helmholtz plane ($x = x_{IHP}$). The spans of Stern layer and diffusive Gouy-Chapman layer are also shown for convenience. In addition, charge neutrality exists in both of the semiconductor-bulk and liquid-bulk. Finally, a typical distribution of electrostatic potential (ϕ) throughout the junction is also exhibited. Here, $\Delta\phi_{sc}$ and $\Delta\phi_L$ are respectively the potential drops in the semiconductor and liquid and $\phi = \Delta\phi_{sc} + \Delta\phi_L$.

3.1.2 Charge inside the Liquid

Conversely, the contribution of the net liquid charge (Q_{liquid}) comes from: (1) electrochemically active ions and (2) electrochemically inactive ions (supporting electrolyte).[34] To further delve, let us begin by the generic picture of the liquid-part of the SL interface, situated from $x = x_{int}$ to $x = x_{liq}$ in Figure 3.1.[135–137] In a usual liquid environment, the movement of the ions in the liquid (charge particles) results in the flow of electricity. However, the experimentally measured value of ionic mobility falls close to 10^{-4} $cm^2V^{-1}s^{-1}$, which is 5 - 6 orders of magnitude lower compared to the electron or hole mobilities in typical semiconductors.[34] To fix this mismatch in conductivity, high concentration (> 0.1 M) of supporting electrolyte is usually added to the solution and the conductivity of the liquid is increased substantially. However, the selection of the supporting electrolyte should be such that the constituent ions are unable to participate in any form of charge transfer reaction with the electrode under the normal PEC operating conditions.[34] Consequently, they are treated as electrochemcially inactive species solely contributing in the charge screening process. Now, the other species in the liquid (H^+ and OH^-, in our case), of course, are electrochemically active and capable of exchanging electrons/holes with the electrode along with their contribution in the overall screening process. In the usual description of the liquid-part of the interface, the distribution of Q_{liquid} can be divided into a diffusive 'Gouy-Chapman' layer and a compact 'Stern' layer hosting the absorption/desorption events.[135–137] According to the Gouy-Chapman model of the liquid,[139,140] the solution is considered to be a dielectric continuum, embedded with different point-ions representing both the electrochemically active and inactive species (see Chapter 5 of Ref. [137]). These ions are distributed under the influence of the varying electrostatic potential by following the Boltzmann statistics.[135,136] The net results of this process can be seen by the formation of a diffusive layer close to the SL interface, as illustrated in Figure 3.1 (from $x = x_{OHP}$ to $x = x_{GC}$). Now, these ions can diffusively approach the physical SL interface up to a certain distance of $x = x_{OHP}$, known as the outer Helmholtz plane (OHP) and then undergo the adsorption process on the inner Helmholtz plane (IHP) at $x = x_{IHP}$ and participate in the inner sphere electrochemical reaction.[135–137] The formation of these two compact layers (IHP and OHP) was first envisioned by Helmholtz[141] and later considered by Stern[142] in the combined Gouy-Chapman-Stern (GCS) model of electrode-electrolyte interface. Together, the compact layer, as shown in Figure 3.1, is often referred as the Stern or Helmholtz layer in the literature.[135, 136]

3.2 Semiclassical Modeling of Semiconductor-Liquid Junctions

Our objective in this section is to formalize the mathematical description of the electrostatics and charge transport phenomena at a generic SL junction, such as that illustrated in Figure 3.1. In this regard, we will begin by separately visiting the relevant semiclassical treatments of the semiconductor photoelectrodes and aqueous electrolytes. Furthermore, the necessary assumptions will be introduced to clearly delineate the linkage between theoretical and practical PEC systems with an additional understanding of the scope and limitations of the models presented in this dissertation. Afterwards, the combined mathematical models, capable of simulating the SL junctions, will be introduced along with the developed boundary conditions.

3.2.1 Semiconductor Drift-Diffusion Equations

Traditionally, the conventional method to simulate and/or model the electrostatics and charge transfer process in semiconducting materials corresponds to the solution of the drift-diffusion equations.[33, 120–122] Drift-diffusion (DD) model, as a semiclassical approach, is immensely popular to numerically calculate physics related to semiconductors and widely used in the commercial solid state device simulation softwares. In 1 D, the complete drift-diffusion model is based on the following set of equations[120–122]

$$\text{Current equation (electron):} \qquad J_n = qn\mu_n E_{field} + k_B T \mu_n \frac{dn}{dx}, \tag{3.1a}$$

$$\text{Current equation (hole):} \quad J_p = qp\mu_p E_{field} - k_B T \mu_p \frac{dp}{dx}, \tag{3.1b}$$

$$\text{Continuity equation (electron):} \quad \frac{dn}{dt} = \frac{1}{q}\frac{dJ_n}{dx} + G_n - R_n, \tag{3.1c}$$

$$\text{Continuity equation (hole):} \quad \frac{dp}{dt} = -\frac{1}{q}\frac{dJ_p}{dx} + G_p - R_p, \tag{3.1d}$$

$$\text{Poisson equation:} \quad \frac{d^2\phi}{dx^2} = -\frac{1}{\varepsilon_{sc}}\left[\rho_{sc} + \rho_{ss} + \rho_T\right], \quad x_{bulk} \leq\ x\ \leq\ x_{int}. \tag{3.1e}$$

Here, the current due to electron flow is given by J_n, whereas the current due to hole movement is given by J_p, n and p respectively represent the electron and hole concentrations, μ_n and μ_p are respectively the electron and hole mobilities. G_n and G_p take into account of all the electron and hole generation processes whereas, R_n and R_p take into account of all the electron and hole recombination processes, respectively and ε_{sc} represents the dielectric constant of the semiconducting material. As can be seen from Eqs. 3.1a- 3.1b, the electron and hole *current equations* explicitly express the contribution of both drift and diffusion components of the respective carrier flow (see Ref. [122, Chapter 4]). To understand, drift is the motion of the charged particles in response to an applied electric field (E_{field}). Thereby, $qn\mu_n E_{field}$ represents the electron drift current. Similarly, $qp\mu_p E_{field}$ represents the hole drift current. Diffusion currents, on the other hand, arise due to the movement of the carriers because of the concentration gradient and are respectively given by $k_B T \mu_n \frac{dn}{dx}$ for electrons and $-k_B T \mu_p \frac{dp}{dx}$ for holes.[122]

Continuity equations (see Eqs. 3.1c- 3.1d) describe a basic concept – any change in the carrier density over time is due to the difference between the incoming and outgoing flux of carriers plus the net carrier generation at the interior of the material.[122] Here, $[G_n - R_n]$ and $[G_p - R_p]$ respectively represent the net generation rates of electrons and holes. In numerical simulations, current and continuity equations are combined and the resultant form of the equation is utilized to solve for the electron and hole distributions. It is also imperative to understand that all the simulations presented in this thesis are performed at steady-state conditions ($^{dn}/_{dt} = {}^{dp}/_{dt} = 0$), meaning that the solutions are time-independent.[120–122]

Now, the final piece of the combined drift-diffusion model of semiconductor is the *Poisson equation* (Eq. 3.1e), which determines the distribution of the electrostatic potential (ϕ) from the charge density inside the material.[33,120–122] In the context of the photoanode drawn in our illustration of SL junction in Figure 3.1, this represents the calculation of ϕ from $x = x_{bulk}$ to $x = x_{int}$. Eq. 3.1e explicitly shows the charge contributions from crystalline semiconductor ($\rho_{sc} \rightarrow$ free carriers and ionized dopants), surface states (ρ_{ss}) and bulk trap states (ρ_T). Here, ρ_{sc} takes into account of the charges due to the freely moving electrons (n) and holes (p) respectively in the conduction and valence band along with the ionized donors (N_D^+) and acceptors (N_A^-) and expressed as[122]

$$\rho_{sc} = N_D^+ - N_A^- + p - n, \tag{3.2}$$

where,[33]

$$n = n_i e^{\left[{}^{(E_{Fn} - E_i)}/_{V_T}\right]}, \tag{3.3}$$

$$p = n_i e^{\left[{}^{(E_i - E_{Fp})}/_{V_T}\right]}. \tag{3.4}$$

Here, $V_T = {}^{k_BT}/_q$ is the thermal voltage, E_i represents the intrinsic Fermi-level given by $E_i = {}^{(E_C + E_V)}/_2 + \frac{1}{2}k_BT \ln\left({}^{N_V}/_{N_C}\right)$, N_V and N_C are the effective density of states in the valence and conduction bands, respectively.[33] Clearly, ρ_{sc} models the charge distribution in a semiconductor without any surface or bulk trap states and thereby, ρ_{sc} is referred here as the charge from the crystalline semiconductors. However, in the case of practical semiconductor photoelectrodes, intermediate bandgap states (trap states) are originated due to the unpassivated dangling bonds, impurities, intrinsic defects or surface reaction intermediates and can effectively trap the conduction band electrons and valence band holes.[125, 143] For instance, it is speculated that the intermediate Fe=O complexes, generated from the first step of the water oxidation process on the surface of hematite photoanode, energetically lie inside the bandgap and act like surface states.[127, 144] Surface states can also be originated due to the various forms of irregularities in the surface morphology of the photoelectrodes.[65, 143, 145, 146] Similar to the surface states, the intermediate bandgap states at the semiconductor-bulk can also participate in overall charge conservation process by trapping and detrapping the freely available electrons and holes (see Ref. [33, Chapter 5]). In this regard, a relevant example in semiconductor water splitting application would be the bulk hematite trap states at the fluorine-doped tin oxide (FTO)/hematite interface, leading to the generation of the notorious 'dead-layer'.[19, 147–149] These bulk trap states are believed to be formed due to the lattice mismatch between FTO and hematite.[19, 149, 150] In our description of the Poisson equation (Eq. 3.1e), ρ_{ss} and ρ_T respectively model the charge contributions from the surface and bulk trap states (see Section 3.4 for numerical details).

3.2.2 Semiclassical Modeling of Liquid Electrolyte

Potential Distribution in Electrolyte

Let us now consider the remaining part of the electrostatic potential (ϕ) that is distributed inside the liquid from $x = x_{int}$ to $x = x_{liq}$, as shown in Figure 3.1. At an ideal PEC set-up, the total potential drop ($\Delta\phi_L$) in the liquid is generally assumed to be relatively small and constant with respect to the total potential drop in the semiconductor ($\Delta\phi_{sc}$).[1, 34, 36] This ideal situation, where the potential drop in the liquid is neglected in the computation ($\Delta\phi_L \ll \Delta\phi_{sc}$ and $\Delta\phi_L \approx 0$), has been widely adopted in the state-of-the-art numerical and analytical models when solving for the electrostatics of SL junctions (see also Section 2.5.1).[35,100,101] In a practical PEC environment, however, $\Delta\phi_L$ can range from few meV to 0.5 eV and hence cannot be ignored for accuracy.[1] For instance, using the first-principles calculation on GaN-water and ZnO-water junctions, Kharche *et al.*[116] demonstrated a liquid potential drop ~ 0.5 eV that can certainly impact the critical energy level alignments at the SL junctions. Cendula *et al.*,[32] in their semiclassical modeling of SL junction, considered a constant $\Delta\phi_L$ computed from an analytical expression and then searched for the numerical solution of ϕ only inside of the semiconductor (from $x = x_{bulk}$ to $x = x_{int}$, in the context of Figure 3.1). This procedure is unable to capture the change in $\Delta\phi_L$ at the event of so called 'band level unpinning' – commonly observed in practical photoelectrodes with surface states, high doping density or large applied potential (see Section 2.5.2). Thus, it is imperative to simultaneously consider the evolution of the potential drop in the liquid with an aim at accurately capturing the overall electrostatics of the SL junctions.

Gouy-Chapmann-Stern (GCS) Model

A complete description of the liquid potential can be given by the Gouy-Chapmann-Stern (GCS) model, as introduced in our discussion in Section 3.1. In practice, due to the high concentration of supporting electrolyte and the densely packed adsorbed species (in the Stern layer), the overall charge screening length inside the liquid-part of the interface spans a very short distance from the physical SL interface.[1] According to the Gouy-Chapman theory, ions in the electrolyte can approach the interface by following the Boltzmann distribution and subsequently, participate in the screening of the counter charges located at the electrode (Q_{solid}, in our case).[135–137] In other words, the spatial distribution of any ions in the liquid can be modeled by Boltzmann-type expression.[137] For example, the concentrations of electrochemically inactive cation (n^{+}) and anion (n^{-}) from the supporting electrolyte can be expressed as[137]

$$n_{+} \;=\; c^{+}_{sup}e^{[\,-\,z\,(\phi\,-\,\phi_b)/V_T]} \tag{3.5}$$

and

$$n_{-} \;=\; c^{-}_{sup}e^{[z\,(\phi\,-\,\phi_b)/V_T]}. \tag{3.6}$$

Here, c^{+}_{sup} and c^{-}_{sup} respectively are the bulk concentrations of the cation and anion of the supporting electrolyte, ϕ_b is the electrostatic potential in the bulk of the liquid (at $x \;=\; x_{liq}$), z denotes the charge number of the ion. Similarly, the concentrations of electrochemically active H^{+} ($c_{H^{+}}$) and OH^{-} ($c_{OH^{-}}$) species can be expressed as[137]

$$c_{H^{+}} \;=\; c^{0}_{H^{+}}e^{[\,-\,(\phi\,-\,\phi_b)/V_T]} \tag{3.7}$$

and

$$c_{OH^{-}} \;=\; c^{0}_{OH^{-}}e^{[\,(\phi\,-\,\phi_b)/V_T]}, \tag{3.8}$$

where, $c^{0}_{H^{+}}$ and $c^{0}_{OH^{-}}$ represent the bulk concentrations of H^{+} and OH^{-} species, respectively. Finally, the total charge contribution of the diffuse layer (ρ_L) can be computed as[137]

$$\rho_L \;= zn_{+} - zn_{-} + c_{H^{+}} - c_{OH^{-}}. \tag{3.9}$$

Eq. 3.9 along with Eqs. 3.5 - 3.8 provide a semiclassical description of the charge distribution process in the liquid electrolyte from $x \;=\; x_{liq}$ (liquid bulk) to $x \;=\; x_{OHP}$ (outer Helmholtz layer). However, the subsequent adsorption and desorption processes of H^{+} and OH^{-} species on the IHP cannot be described by the Boltzmann-type distribution, rather they are determined by the surface protonation and deprotonation reactions (see Ref. [1, Chapter 2]). The impact of these processes can be seen as the net adsorbed charge (ρ_{ad}) in the Stern layer.[136] Unlike the charge in the diffusive layer of the liquid, the charges in the Stern layers are immobile and strongly adsorbed on inner Helmholtz plane.[135] Finally, by combining ρ_L and ρ_{ad}, the electrostatic potential in the liquid can also be computed from the Poisson equation given by (similar to Eq. 3.1e)

$$\frac{d^2\phi}{dx^2} = -\frac{1}{\varepsilon_L}\left[\rho_L + \rho_{ad}\right], \quad x_{int} \leq \ x \ \leq \ x_{liq}. \tag{3.10}$$

Here, ε_L refers to the dielectric constant of the liquid. In the case of bulk water, $\varepsilon_L \approx 80$.[1]

3.3 Assumptions

3.3.1 Supporting Electrolyte

Throughout our model development, as presented in this thesis, we have considered the existence of the electrochemically inactive supporting electrolyte in the solution.[34] As a generic implementation, our model takes into consideration of both the cations (n_+) and anions (n_-) from the supporting electrolyte that are deliberately added to the liquid to achieve sufficient electrical conduction in the PEC set-up. Similar to the practical PEC set-up, we also assume that the ions from the supporting electrolyte can effectively screen the exposed charge in the semiconductor without participating in any electron transfer with the electrode. To elaborate, let us revisit the practical liquid environment as presented by Le Formal *et al.*[68] and also utilized in the simulation of hematite photoanode in Chapters 5 and 6. Here, the solution consists of 10 mL of 1 M NaOH (pH = 13.6) and the PEC set-up is investigated for oxidative water splitting reaction at an n-type hematite electrode with doping concentration (N_D)$\sim 10^{19}$ - 10^{20} cm^{-3}.[68] Hence, the liquid contains OH^-, H^+ and Na^+ species, among which OH^- and H^+ are respectively considered as electrochemically active to photoanode and Pt-counter electrode and whereas, Na^+ constitutes an electrochemically inactive cation (n_+) from the supporting electrolyte. In this particular case, the anionic contribution from the supporting electrolyte is considered to be zero ($n_- \approx 0$).

3.3.2 SL Junction as an Adaptive Pseudo-Schottky Contact

As we discussed in Section 2.5.2, the conventional models of the SL junctions as pseudo Schottky-contacts implicitly assume that the semiconductor bands are pinned (BLP), which is certainly not the practical case when surface states charging/discharging takes place.[21,57] Rather, a more realistic approach should also allow the semiconductor bands to be unpinned when it is appropriate. That being said, the Poisson equation implemented in this thesis (see Section 3.4) can model the required adaptivity of the SL Schottky junctions. In this way, the potential on the liquid side is solely calculated from the extent of screening charge and thereby, the SL junction represents an 'adaptive' pseudo-Schottky contact on the basis of the evolution of the exposed charges. This assumption of the adaptive Schottky contact makes our model suitable to simulate oxide-semiconductors ($\alpha$$-$$Fe_2O_3$, TiO_2, $BiVO_4$ etc.), which are severely affected by band-level unpinning.[57]

3.3.3 Electrochemical Activity at the Interface

Throughout this thesis, our consideration of the PEC cells are essentially photosynthetic cells, where current flow yields in chemical fuel production *via* chemical reactions (see Figure 3.2).[7,72] Photosynthetic cells are different than regenerative cells – another form of the PEC cell, where current flow yields no net chemical change of the electrolyte.[7] As explained in Refs. [72] and [7] , in the water splitting photosynthetic cells, the species (OH^-/O_2) involved in the anodic reaction at the photoanode are not the same as the species (H^+/H_2) involved in the cathodic reaction at the photocathode or metal counter electrode. Figure 3.2 illus-

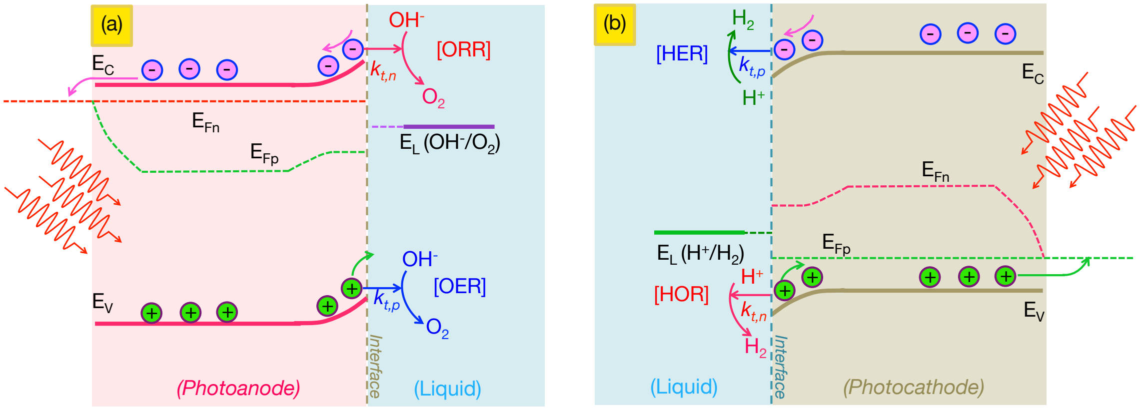

Figure 3.2: Electrochemical activities at (a) an anodic semiconductor-aqueous junction and (b) cathodic semiconductor-aqueous junction (photosynthetic cells). For example, at the photoanode (part a), OER is assumed as the forward reaction, where holes from the valence band participate in oxidation of OH^- species. Conversely, ORR is considered as the backward reaction reversing the yield of the forward reaction by reducing O_2 at the surface of the photoanode *via* conduction band electron transfer. In this case, the liquid Fermi-level (E_L) is determined by OH^-/O_2 species. Similarly, HER and HOR are respectively assumed as the forward and reverse reactions occurring at a photocathode and liquid Fermi-level is determined by H^+/H_2 species.

trates the assumed electrochemical activity of the photocatalytic anodic SL interface (part a) as well as that of the photocatalytic cathodic SL interface (part b) considered in the present work. In this case, we have assumed that the photoanode is only capable of exchanging electrons/holes with OH^-/O_2 redox species. Hence, OER ($H_2O + 2h^+ \rightarrow {}^1\!/\!{}_2O_2 + 2H^+$) is considered as the forward reaction, whereas the oxygen reduction reaction (ORR: ${}^1\!/\!{}_2O_2 + 2H^+ + 2e^- \rightarrow H_2O$) is considered as the reverse reaction at the photoanode.[29,72,151] In the counter-electrode, electrochemical reactions solely consist of HER as the forward reaction ($2H^+ + 2e^- \rightarrow H_2$) and hydrogen oxidation reaction (HOR: $H_2 \rightarrow 2H^+ + 2e^-$) as the reverse reaction.[29] Thus, our assumed set-up of the electrochemical activity perfectly emulates the common situation in the practical water splitting cells, where O_2 is evolved in the photoanode and H_2 is collected in the compartment containing counter-electrode.[7,72]

Though we have considered ORR as the only reverse reaction at the photoanode, it is also possible for the conduction band electrons to reduce the water and produce H_2.[72] In this case, the mixed reaction (as discussed in Section 2.5.2), occurring at the SL interface, would certainly make the computation more complex. As the main objective of this thesis is to model/explore the performance of the rate determinant anodic OER at the photoanode, we discarded the possibility of a mixed reaction, *e.g.*, anodic H_2 production, corrosion of the photoanodes in our computation.[1,34] Moreover, the picture of the anodic SL interface, even only assuming OER/ORR, can become complex if the semiconductor is oxidized by the evolved O_2. Nonetheless, we can rule out the self-oxidation of the oxide-semiconductor-based photoanodes due to the fact that these materials are already in their oxidized forms and practically demonstrate superior chemical stability in the aqueous solution (see also the discussion in Section 2.3.3).[13,57]

3.3.4 Liquid Fermi-level

In general, the liquid Fermi-level (E_L) is determined by the electrochemically active species participating in electron/hole transfers with the electrode, as presented in Figure 3.2.[34,151] Therefore, by considering the assumption of interfacial electrochemical activity from our discussion in Section 3.3.3, the liquid Fermi-level at an anodic SL interface is solely determined by the OH^-/O_2 species as we have considered that the photoanode is only capable of exchanging electrons/holes with OH^-/O_2 species. This approximation is widely utilized in presenting the anodic SL junctions electrostatics in the literature.[32,152] Imposing this assumption on a photoanode guarantees the existence of an equilibrium situation under dark condition, where the Fermi-levels of electrons and holes are equal and perfectly aligned with the liquid Fermi-level ($E_{Fn} = E_{Fp} = E_L$, in Figure 2.3a). Conversely, to model the water reduction reaction on photocathode, we consider HER/HOR as the only electrochemcial reactions at the photocathode, meaning E_L at the cathodic SL junction is entirely determined by the H^+/H_2 species. Nevertheless, both of the situations in photoanode and photocathode need to be replaced by a more complicated non-equilibrium situation (even under dark) if the respective electrode is prone to corrosion and/or demonstrates mixed reactions (see the discussion in Section 3.3.3).

3.3.5 Finite-Size of Ions and Helmholtz Layer Charge

Now, the widely common 'point-ion' approximation in GCS theory becomes gradually invalid when the ions start to approach each other more closely so that the finite-size of the ions cannot be ignored anymore. Using a simple cubic packing of the ions with effective diameter of a, a back-of-the-envelope calculation sets the upper limit of the allowable concentration of a species, $c_{max} = [a^3 \times N_{avg}]^{-1}$.[135] Here, N_{avg} is the Avogadro's number (6.022×10^{23} mol^{-1}). Now, c_{max} effectively limits the maximum surface potential as[135,153,154]

$$\Delta\phi_{L|max} = -\frac{k_B T}{zq} log\left[a^3 N_{avg} c_\infty\right], \tag{3.11}$$

where, c_∞ is the bulk concentration of the species in the liquid under consideration.[135] Now, the assumptions considered in the GCS model would work if the liquid potential ($\Delta\phi_L$) $\leq$ $\Delta\phi_{L|max}$ – delineating the limit for the so called 'point-ion' concept.[137] In general, this constraint can severely limit the application of the simple GCS model, specifically at the metal-electrolyte junctions where all the potential drop occurs in the liquid side.[153,154] Conversely, in the case of an SL junction (see Section 3.2.2), the potential drop inside the liquid remains relatively small (up to 0.5 eV) and thereby, the GCS model is valid up to some extent under normal PEC operating conditions.[1] To better comprehend this, let us consider OH^- ions in an aqueous solution of pH = 7 and with the ionic radii of 1.52 $\mathring{A}$.[155] Therefore, using $c_\infty = c^0_{OH^-} = 10^{-7}$ M and

$a = 3.04$ $\mathring{A}$ in Eq. 3.11, $\Delta\phi_{L|_{max}}$ can be estimated as ≈ 0.522 V. However, if the concentration of OH$^-$ species is elevated to $c^0_{OH^-} = 1$ M (pH = 14), $\Delta\phi_{L|_{max}} \approx 0.1$ V. As expected, high electrolyte concentration can limit the validity of GCS theory as the maximum allowable surface potential gradually becomes smaller. Overall, the calculation of $\Delta\phi_L$ should be checked with respect to $\Delta\phi_{L|_{max}}$ to guarantee the validity of the GCS model.

Furthermore, being a semiclassical approach, the methodology presented in this thesis cannot capture the adsorption/desorption processes at the inner Helmholtz plane (equivalent to the computation of ρ_{ad}). One possible way to compute ρ_{ad} would be the atomistic first-principles calculation.[116] Up to now, the determination of ρ_{ad} with a detailed probing of IHP phenomena remains unclear, to a large degree, in the context of any theory.[137] Nevertheless, the combined Poisson equation, as developed in Section 3.4 of this Chapter, also considers ρ_{ad} in its generic formulation. This means, if ρ_{ad} can be estimated from the atomistic models and subsequently, is supplied as an input of the combined Poisson equation, then our model can take the effects of ρ_{ad} into account along with other contributions of the exposed charges and estimate the potential distribution.

3.4 Formulation of the Numerical Grid

In numerical simulation of the SL junctions, the solutions of the coupled semiclassical transport equations (Poisson-continuity equations) are sought in a discretized grid, such as that shown in Figure 3.3. In this regard, the set of transport equations, as introduced in Section 3.2, needs to be discretized along with the necessary boundary conditions. To understand this, let us begin by revising the space vector as shown in Figures 3.1. Clearly, Figure 3.3 presents the discretized version of the same space vector. All the critical points along the x-axis are also shown for convenience. As a

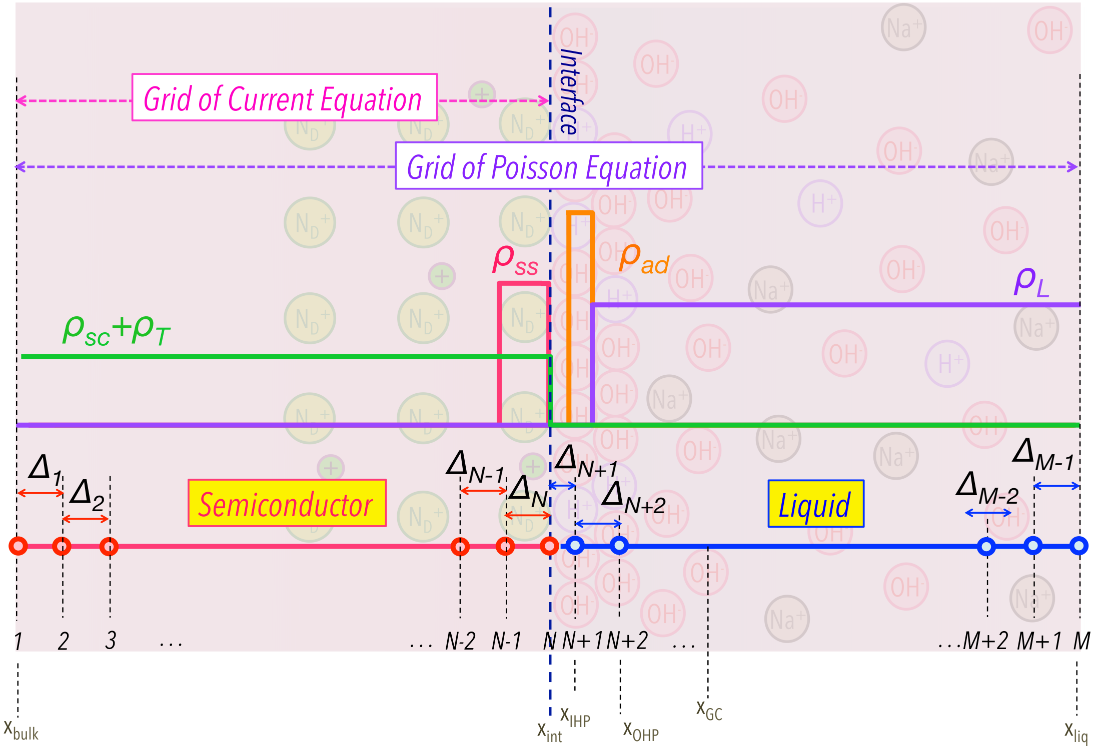

Figure 3.3: An illustration of the discretized grid utilized in the formulation of the discretized versions of the transport equations. The grid is characterized by the non-uniformly spaced grid points with spacings of Δ_i, where i = [1 : M-1]. As can be seen, grid points i = [1 : N] are located in the electrode, whereas the rest of the grid points are placed in the liquid (i = [N+1 : M]). The spans of all the different charge contributions, as described in Sections 3.2.1 and 3.2.2, are also drawn for ease of comprehension. Finally, the extents of the solutions of both the Poisson equation and current equations are also shown in purple and pink, respectively.

part of the generic implementation scheme, we have considered non-uniform spacing of the grid points as the default discretization technique. Here, Δ_i represents the spacing between two consecutive grid points i and $i + 1$, where i can be any value from [1 : M-1]. Also, grid points [1 : N] are located in the semiconductor, grid points [N+1 : M] are placed in the liquid and i = N marks the physical location of the SL interface. Discretizing the x-grid in a non-uniform fashion comes with the advantages of fast and efficient computation albeit with the cost of complexity in the numerical formulation. Some of the notable features of the discretized grid in Figure 3.3 include:

- Illustrations of the spans of charges in semiconductor such as $\rho_{sc} + \rho_T$ in green and ρ_{ss} in red. Also, $\rho_{sc}+\rho_T+\rho_{ss}$ can only have non-zero values when $i = [1 : \text{N}]$ (inside of the semiconductor). Otherwise, $\rho_{sc} + \rho_T + \rho_{ss}$ reduces to zero for grid points $i = [\text{N+1} : \text{M}]$ (in the liquid).

- Similarly, the spans of liquid charges are also shown. In this case, span of the diffusive, mobile ions (ρ_L) is depicted in purple and the span of the specifically adsorbed charges (ρ_{ad}) is marked in orange. Here, $\rho_L + \rho_{ad}$ is non-zero only when $i = [\text{N+1} : \text{M}]$ or i is in the liquid.

- The search for the solution of the electrostatic potential by numerically solving combined Poisson equation (Eqs. 3.1e and 3.10) covers the entire grid ($i = [1 : \text{M}]$).

- Grid points $i = 1$ and $i = \text{M}$ mark the two boundary points for discretized Poisson equation.

- Both of the electron and hole continuity equations are solved only inside of the semiconductor or $i = [1 : \text{N}]$.

- Grid points $i = 1$ and $i = \text{N}$ present the two boundary points for electron and hole continuity equations.

3.5 Combined Poisson Equation of the SL Junctions

In order to develop the discretized form of the combined Poisson equation, the usual starting point should be the descriptions of Poisson equations in semiconductor (Eq. 3.1e) and liquid (Eq. 3.10). However, the expressions in Eqs. 3.1e and 3.10

cannot be coupled in their present forms due to the spatially varying dielectric constant along the SL junction. To resolve this issue, a more convenient starting point would be the generic Gauss equation, where Eq. 3.1e is expressed as

$$\frac{d}{dx}\left[\varepsilon_{sc}E_{field}\right] = \left[\rho_{sc} + \rho_{ss} + \rho_{T}\right], \quad x_{bulk} \leq \ x \ \leq \ x_{int} \tag{3.12}$$

and Eq. 3.10 is expressed as

$$\frac{d}{dx}\left[\varepsilon_{L}E_{field}\right] = \left[\rho_{L} + \rho_{ad}\right]. \quad x_{int} \leq \ x \ \leq \ x_{liq}. \tag{3.13}$$

Together, a combined Gauss equation in 1 D can be written as

$$\frac{d}{dx}\left[\varepsilon E_{field}\right] = \left[\rho_{sc} + \rho_{ss} + \rho_{T} + \rho_{L} + \rho_{ad}\right], \quad x_{bulk} \leq \ x \ \leq \ x_{liq}. \tag{3.14}$$

Here, ε is the varying dielectric constant along the x-axis, $E_{field} = -\frac{d\phi}{dx}$, $Q_{solid} = \rho_{sc} + \rho_{ss} + \rho_{T}$ and $Q_{liquid} = \rho_{L} + \rho_{ad}$. Therefore, Eq. 3.14 can be rewritten as

$$\varepsilon\frac{d^2\phi}{dx^2} \ + \frac{d\varepsilon}{dx}\frac{d\phi}{dx} \ = \ -\left[\rho_{sc} + \rho_{ss} + \rho_{trap} + \rho_{ad} + \rho_{L}\right]. \tag{3.15}$$

Eq. 3.15 is the combined Poisson equation that needs to be discretized and solved using suitable numerical techniques. In this regard, we will be using Gummel technique implemented by the finite-difference (FD) scheme to perform the discretization and subsequent computation of Eq. 3.15.[120–122, 156]

3.5.1 Formulation of the Charges in Semiconductor

Conventionally, the electrostatic potential and all the energy levels in a semiconductor are drawn by considering the transport of electrons as the default charge carrier.[33] For example, an upward bending at an SL interface (see Figure 2.1) represents an energy barrier impeding the electron transport from the bulk towards the liquid side. However, ϕ in the Poisson equation (such as in Eq. 3.15) is assumed to be the electrostatic potential experienced by the positively charged carriers. Therefore, it is customary in the state-of-the-art semiconductor simulation to assume a relationship such as $\phi = -E_i$, which can directly link the semiconductor band bending potential with the computed potential from the Poisson solver. Here, $\phi = -E_i$ means that the electrostatic potential calculated by solving Poisson equation equals to the negative of the semiconductor intrinsic Fermi-level (E_i) (see Ref.[122, Chapter 4]). That being said, we will now derive the necessary expressions suitable for the self-consistent solution of the Poisson equation. While solving the Poisson equation in a self-consistent manner, the iteration always starts from an initial guess of ϕ and then goes on slowly updating $\phi = \phi + \delta\phi$ in each iteration step.[120] Here, $\delta\phi$ is the deviation between to consecutive solutions of ϕ and assumed to be small compared to V_T. Now, using ϕ = -E_i, $\phi = \phi + \delta\phi$ and $\delta\phi \ll V_T$, Eq. 3.3 can be rewritten as[122]

$$\begin{aligned} n &= n_i e^{\left[(E_{Fn}\,+\,\phi)/V_T\right]}, \\ &= n_i e^{\left[(E_{Fn}\,+\,\phi\,+\,\delta\phi)/V_T\right]}, \\ &= n e^{[\delta\phi/V_T]}, \\ &\approx n\left(1+\frac{\delta\phi}{V_T}\right). \end{aligned} \tag{3.16}$$

Here, we use $e^{[\delta\phi/V_T]} \approx [1 + {}^{\delta\phi}/V_T]$. Similarly, Eq. 3.4 can be rewritten as[122]

$$\begin{aligned} p &= n_i e^{\left[-\,(\phi\,+\,E_{Fp})/V_T\right]}, \\ &= n_i e^{\left[-\,(\phi\,+\,\delta\phi\,+\,E_{Fp})/V_T\right]}, \\ &= p e^{[-\delta\phi/V_T]}, \\ &\approx p\left(1-\frac{\delta\phi}{V_T}\right), \end{aligned} \tag{3.17}$$

where, $e^{[-\delta\phi/V_T]} \approx [1 - \delta\phi/V_T]$. Finally, using Eq. 3.2, the contribution of the crystalline semiconductor can be approximated as

$$\rho_{sc} \;\approx\; N_D^+ - N_A^- + p\left(1 - \frac{\delta\phi}{V_T}\right) - n\left(1 + \frac{\delta\phi}{V_T}\right). \tag{3.18}$$

On the other hand, the computations of ρ_{ss} and ρ_T depend on the characteristics (donor- or acceptor-type) of the intermediate trap states. For example, donor-type trap states are considered neutral when filled by electrons, whereas empty donor-states are positively charged.[143] Therefore, the charge from the donor-type surface states ($\rho_{ss|D}$) can be computed by

$$\rho_{ss|D} \;=\int_{E_V^+}^{E_C^-} N_{s|D}(1 - f_{s|D})dE, \tag{3.19}$$

where, $N_{s|D}$ and $f_{s|D}$ are respectively the distribution of donor-type surface states and probability of these states to be occupied by electrons. E_V^+ and E_C^- respectively represent an energy just above the valence band edge and an energy just below the conduction band edge. Furthermore, $f_{s|D}$ is determined *via* the corresponding Fermi-distribution given as

$$f_{s|D} \;=\; \frac{1}{1 + e^{[E_s \,-\, E_{Fs|D}]/k_BT}}. \tag{3.20}$$

Here, $E_{Fs|D}$ is the Fermi-level of the distribution of donor-type surface states and E_s represents the energy of the surface states. The details of the determination of $E_{Fs|D}$ at a photocatalytic SL interface will be a topic of discussion in Chapter 4 of this thesis. Conversely, the acceptor-type states are negatively charged when filled by electrons, whereas they remain charge neutral if the states are empty.[143] Thus bringing the similar treatment as presented for donor-type surface states, the charge due to acceptor-type surface states ($\rho_{ss|A}$) can be expressed as

$$\rho_{ss|A} = -\int_{E_V^+}^{E_C^-} N_{s|A}(f_{s|A})dE, \tag{3.21}$$

Here, $N_{s|A}$ and $f_{s|A}$ are the density of acceptor-type surface states and probability of these states being occupied by electrons, respectively. Finally, $f_{s|A}$ can be given by Fermi-Dirac distribution of

$$f_{s|A} = \frac{1}{1 + e^{\left[E_s - E_{Fs|A}\right]/k_B T}}, \tag{3.22}$$

where, $E_{Fs|A}$ is the Fermi-level of the distribution of acceptor-type surface states determining the electron occupation probability. Now, the total charge contribution from an ensemble of donor- and acceptor-type surface states can be written as

$$\rho_{ss} = \rho_{ss|D} + \rho_{ss|A}. \tag{3.23}$$

Likewise, the charge contribution from bulk/SCR trap states can also be computed by separately considering the donor- and acceptor-type character of the trap states, and expressed as[138]

$$\rho_T = \rho_{T|D} + \rho_{T|A}. \tag{3.24}$$

Here, the charge contributions from the donor- and acceptor-type trap states are respectively given by[33]

$$\rho_{T|D} = \int_{E_V^+}^{E_C^-} g_{T|D}\,(1 - f)dE, \tag{3.25a}$$

$$\rho_{T|A} = -\int_{E_V^+}^{E_C^-} g_{T|A}\,f dE, \tag{3.25b}$$

where, $g_{T|D}$ and $g_{T|A}$ are the distributions of donor- and acceptor-type of bulk/SCR trap states, respectively. Also, f denotes the Fermi-distribution given by $f = \frac{1}{1+e^{[E_T - E_F]/V_T}}$, where E_T is the location of the trap states and E_F is the Fermi-level of the majority carrier of the semiconductor (see Chapter 5 of Ref. [138]). The details of the computation of ρ_T will be a subject of discussion in Chapter 7 of this thesis.

3.5.2 Formulation of the Charges in Liquid

Following a similar procedure, as presented in Section 3.5.1, we can also derive suitable expressions representing different charge contributions in the liquid. For instance, Eq. 3.5 can be rewritten as

$$\begin{aligned} n_+ &= c_{sup}^{+} e^{\left[-z\,(\phi - \phi_b)/V_T\right]}, \\ &= c_{sup}^{+} e^{\left[-z\,(\phi + \delta\phi - \phi_b)/V_T\right]}, \\ &= n_+ e^{\left[-z\delta\phi/V_T\right]}, \\ &\approx n_+ \left(1 - z\frac{\delta\phi}{V_T}\right). \end{aligned} \tag{3.26}$$

Here, we again utilized $\phi = \phi + \delta\phi$ and $\delta\phi \ll V_T$. Likewise, Eqs. 3.6, 3.7 and 3.8 are respectively expressed as

$$n_- = c_{sup}^{-} e^{\left[z\,(\phi - \phi_{bulk})/V_T\right]} \approx n_- \left(1 + z\frac{\delta\phi}{V_T}\right), \tag{3.27}$$

$$c_{H^+} = c_{H^+}^{0} e^{\left[-(\phi - \phi_{bulk})/V_T\right]} \approx c_{H^+} \left(1 - \frac{\delta\phi}{V_T}\right) \tag{3.28}$$

and

$$c_{OH^-} = c_{OH^-}^{0} e^{\left[(\phi - \phi_{bulk})/V_T\right]} \approx c_{OH^-} \left(1 + \frac{\delta\phi}{V_T}\right). \tag{3.29}$$

Therefore, Eq. 3.9 can be written as

$$\rho_L \approx zn_+\left(1 - z\frac{\delta\phi}{V_T}\right) - zn_-\left(1 + z\frac{\delta\phi}{V_T}\right) + c_{H^+}\left(1 - \frac{\delta\phi}{V_T}\right) - c_{OH^-}\left(1 + \frac{\delta\phi}{V_T}\right). \quad (3.30)$$

Finally, as discussed in Section 3.3.5, the theoretical determination of ρ_{ad} on IHP still remains largely unclear.[137] Yet, we consider ρ_{ad} in the expression of the generic Poisson equation so that the impact of adsorption/desorption phenomena can also be aptly included in the future models/extensions towards this direction.

3.5.3 Discretized From of the Combined Poisson Equation

With all the essential expressions of charge contributions at our hand, we can resume our derivation of the combined Poisson equation and rewrite Eq. 3.15 as

$$\begin{aligned}\varepsilon\frac{d^2}{dx^2}\left[\phi + \delta\phi\right] + \frac{d\varepsilon}{dx}\frac{d}{dx}\left[\phi + \delta\phi\right] = \\ -\left[N_D^+ - N_A^- + p - n + \rho_{ss} + \rho_T + zn_+ - zn_- + c_{H^+} - c_{OH^-} + \rho_{ad}\right] \\ + \frac{\delta\phi}{V_T}\left[p + n + z^2n_+ + z^2n_- + c_{H^+} + c_{OH^-}\right].\end{aligned} \quad (3.31)$$

Here, we again use $\phi = \phi + \delta\phi$. Now, if we assume

$$Q' = \left[N_D^+ - N_A^- + p - n + \rho_{ss} + \rho_T + zn_+ - zn_- + c_{H^+} - c_{OH^-} + \rho_{ad}\right], \quad (3.32)$$

and

$$Q'' = \left[p + n + z^2n_+ + z^2n_- + c_{H^+} + c_{OH^-}\right], \quad (3.33)$$

then Eq. 3.31 can be expressed as

$$\varepsilon\frac{d^2}{dx^2}\left[\phi + \delta\phi\right] + \frac{d\varepsilon}{dx}\frac{d}{dx}\left[\phi + \delta\phi\right] = -Q' + \frac{\delta\phi}{V_T}Q''. \quad (3.34)$$

Finally, Eq. 3.34 can be rearranged into

$$\left[\varepsilon\frac{d^2}{dx^2}+\frac{d\varepsilon}{dx}\frac{d}{dx}-\frac{Q''}{V_T}\right]\delta\phi=-\left[\varepsilon\frac{d^2}{dx^2}+\frac{d\varepsilon}{dx}\frac{d}{dx}\right]\phi-Q'. \tag{3.35}$$

At this point, our final goal is to discretize Eq. 3.35 and construct the equivalent matrix representation. Now, at a non-uniformly discretized grid, such as that shown in Figure 3.3, differential operators $\frac{d}{dx}$ and $\frac{d^2}{dx^2}$ in Eq. 3.35 can be written as their respective difference operators given by[120]

$$\left[\frac{d}{dx}\right]_i \rightarrow \begin{bmatrix} -\frac{1}{\Delta_i} \\ \\ \frac{1}{\Delta_i} \end{bmatrix}^{\top} \tag{3.36}$$

and

$$\left[\frac{d^2}{dx^2}\right]_i \rightarrow \begin{bmatrix} \frac{2}{\Delta_{i-1}(\Delta_{i-1}+\Delta_i)} \\ -\left(\frac{2}{\Delta_{i-1}(\Delta_{i-1}+\Delta_i)}+\frac{2}{\Delta_i(\Delta_{i-1}+\Delta_i)}\right) \\ \frac{2}{\Delta_i(\Delta_{i-1}+\Delta_i)} \end{bmatrix}^{\top} \tag{3.37}$$

where, i = 2, 3, . . . , M-1 and i = 1 and i = M are the two boundary points and will be handled along with the boundary conditions (see discussion in Section 3.5.5). Also, $\top$ stands for the transpose of the matrix. Now, with Eqs. 3.33, 3.36 and 3.37, the left-hand-side of Eq. 3.35 can be written into the corresponding Matrices as

$$\left[\varepsilon\frac{d^2}{dx^2}+\frac{d\varepsilon}{dx}\frac{d}{dx}-\frac{Q''}{V_T}\right]\delta\phi \;=\; \overline{\boldsymbol{\Lambda}}\;\overline{\boldsymbol{\delta\Phi}}. \tag{3.38}$$

Here,

$$\bar{\boldsymbol{\Lambda}} \;=\; \begin{bmatrix} \lambda_{11} & \lambda_{12} & \lambda_{13} & \dots & \lambda_{1M} \\ \lambda_{21} & \lambda_{22} & \lambda_{23} & \dots & \lambda_{2M} \\ \vdots & \vdots & \vdots & \ddots & \vdots \\ \lambda_{M1} & \lambda_{M2} & \lambda_{M3} & \dots & \lambda_{MM} \end{bmatrix} \tag{3.39}$$

and

$$\overline{\boldsymbol{\delta\Phi}} = \begin{bmatrix} \delta\phi_1 \\ \delta\phi_2 \\ \vdots \\ \delta\phi_M \end{bmatrix}. \tag{3.40}$$

As can be seen from Eq. 3.39, $\bar{\boldsymbol{\Lambda}}$ is an M×M matrix with the following features:

- Centre diagonal elements:
  $\lambda_{i,i} = -\varepsilon_i \left[\frac{2}{\Delta_{i-1}(\Delta_{i-1}+\Delta_i)} + \frac{2}{\Delta_i(\Delta_{i-1}+\Delta_i)}\right] - \frac{1}{\Delta_i^2}\left[\varepsilon_{i+1} - \varepsilon_i\right] - \frac{Q_i''}{V_T}$, $i = 2, 3, \ldots,$ M-1.
- Diagonal elements below centre diagonal:
  $\lambda_{i,i-1} = \varepsilon_i \left[\frac{2}{\Delta_{i-1}(\Delta_{i-1}+\Delta_i)}\right]$, $i = 2, 3, \ldots,$ M-1.
- Diagonal elements above centre diagonal:
  $\lambda_{i,i+1} = \varepsilon_i \left[\frac{2}{\Delta_i(\Delta_{i-1}+\Delta_i)}\right] + \frac{1}{\Delta_i^2}\left[\varepsilon_{i+1} - \varepsilon_i\right]$, $i = 2, 3, \ldots,$ M-1.
- Elements of $\overline{\boldsymbol{\Lambda}}(1,:)$ and $\overline{\boldsymbol{\Lambda}}(M,:)$ respectively constitute the boundary conditions at $i = 1$ and $i = M$ and is discussed in Section. 3.5.5.
- All other elements are zero.

In addition, $\overline{\boldsymbol{\delta\Phi}}$ is an M×1 column vector (see Eq. 3.40). Similarly, the right hand side of Eq. 3.35 can be expressed as

$$-\left[\varepsilon\frac{d^2}{dx^2} + \frac{d\varepsilon}{dx}\frac{d}{dx}\right]\phi - Q' = \overline{\boldsymbol{\Upsilon}}\,\overline{\boldsymbol{\Phi}} - \overline{\boldsymbol{Q'}}, \tag{3.41}$$

where,

$$\bar{\boldsymbol{\Upsilon}} = \begin{bmatrix} \gamma_{11} & \gamma_{12} & \gamma_{13} & \cdots & \gamma_{1M} \\ \gamma_{21} & \gamma_{22} & \gamma_{23} & \cdots & \gamma_{2M} \\ \vdots & \vdots & \vdots & \ddots & \vdots \\ \gamma_{M1} & \gamma_{M2} & \gamma_{M3} & \cdots & \gamma_{MM} \end{bmatrix}, \tag{3.42}$$

$$\overline{\boldsymbol{\Phi}} = \begin{bmatrix} \phi_1 \\ \phi_2 \\ \vdots \\ \phi_M \end{bmatrix} \tag{3.43}$$

and

$$\overline{\boldsymbol{Q'}} = \begin{bmatrix} Q'_1 \\ Q'_2 \\ \vdots \\ Q'_M \end{bmatrix}. \tag{3.44}$$

Again, $\bar{\boldsymbol{\Upsilon}}$ in Eq. 3.42 is an M×M matrix with the following elements:

- Centre diagonal elements:

  $\gamma_{i,i} = \varepsilon_i \left[\frac{2}{\Delta_{i-1}(\Delta_{i-1}+\Delta_i)} + \frac{2}{\Delta_i(\Delta_{i-1}+\Delta_i)}\right] + \frac{1}{\Delta_i^2}\left[\varepsilon_{i+1} - \varepsilon_i\right]$, i = 2, 3, ..., M-1.

- Diagonal elements below centre diagonal:

  $\gamma_{i,i-1} = -\varepsilon_i \left[\frac{2}{\Delta_{i-1}(\Delta_{i-1}+\Delta_i)}\right]$, i = 2, 3, ..., M-1.

- Diagonal elements above centre diagonal:

  $\gamma_{i,i+1} = -\varepsilon_i \left[\frac{2}{\Delta_i(\Delta_{i-1}+\Delta_i)}\right] - \frac{1}{\Delta_i^2}\left[\varepsilon_{i+1} - \varepsilon_i\right]$, i = 2, 3, ..., M-1.

- Elements of $\overline{\boldsymbol{\Upsilon}}(1,:)$ and $\overline{\boldsymbol{\Upsilon}}(M,:)$ respectively constitute the boundary conditions at $i = 1$ and $i = M$ and is discussed in Section. 3.5.5.

- All other elements are zero.

Furthermore, both $\overline{\boldsymbol{\Phi}}$ (Eq. 3.43) and $\overline{\boldsymbol{Q'}}$ (Eq. 3.44) are M×1 column vectors. Finally, the combined Poisson equation from Eq. 3.35 can be written in its matrix form as

$$\overline{\boldsymbol{\Lambda}}\ \overline{\boldsymbol{\delta\Phi}} = \overline{\boldsymbol{\Upsilon}}\ \overline{\boldsymbol{\Phi}} - \overline{\boldsymbol{Q'}}. \tag{3.45}$$

3.5.4 Self-Consistent Solution of the Combined Poisson Equation

The self-consistent solution of Eq. 3.45 can be computed by implementing the Gummel iterative technique that includes the following steps:[122]

(1) Start with an initial guess for the electrostatic potential $\overline{\boldsymbol{\Phi}}$ (Eq. 3.43).

(2) Compute all the elements of $\overline{\boldsymbol{\Lambda}}$ (Eq. 3.39), $\overline{\boldsymbol{\Upsilon}}$ (Eq. 3.42) and $\overline{\boldsymbol{Q'}}$ (Eq. 3.44). The computations of the matrix elements at the boundaries ($i = 1$ and M) are discussed in detail in the upcoming Section 3.5.5.

(3) Compute $\overline{\boldsymbol{\delta\Phi}}$ using the following expression (by rearranging Eq. 3.45)

$$\overline{\boldsymbol{\delta\Phi}} \;=\; \overline{\boldsymbol{\Lambda}}^{-\mathbf{1}}\left[\overline{\boldsymbol{\Upsilon}}\;\overline{\boldsymbol{\Phi}} - \overline{\boldsymbol{Q'}}\right]. \tag{3.46}$$

(4) Update potential calculation by $\overline{\boldsymbol{\Phi}}\mid_{\boldsymbol{new}} = \overline{\boldsymbol{\Phi}} + \beta\overline{\boldsymbol{\delta\Phi}}$, where β is a mixing factor.

(5) In case, when $\mid \overline{\boldsymbol{\delta\Phi}} \mid <$ tolerance, $\overline{\boldsymbol{\Phi}}$ is assumed to be the converged solution. Otherwise, use $\overline{\boldsymbol{\Phi}} \;=\; \overline{\boldsymbol{\Phi}}\mid_{\boldsymbol{new}}$ and repeat from step (2).

3.5.5 Boundary Conditions for Poisson Equation

Dirichlet Boundary Condition

In this section, we will see how to formulate different boundary conditions to self-consistently solve the combined Poisson equation in Eq. 3.45. At this point, it is important to realize that the element of the column matrix $\overline{\boldsymbol{\delta\Phi}}$ (Eq. 3.40) refer to the deviations between two consecutive iterations (assuming $\beta = 1$). Ideally, when the numerical solution of ϕ converges to the exact solution, all the elements of $\overline{\boldsymbol{\delta\Phi}}$ should be reduced to zero, or $\delta\Phi \mid_i \rightarrow 0$ for $i = [1 : \mathrm{M}]$. This situation can be utilized to implement a Dirichlet-type (constant) boundary condition on ϕ. A Dirichlet-type boundary condition is usually imposed when the value of the variable is known beforehand.[120,121] In the case of an SL junction, the relevant examples consist of the potentials at the grid-points $i = 1$ (at $x = x_{bulk}$) and $i =$ M (at $x = x_{liq}$) that are directly attached to the external bias source ($V_{applied}$). For the sake of our discussion, let us assume that ϕ at the node $i = 1$ ($\phi\mid_{i=1}$) has a value of ϕ_{bulk}, which is known in advance. That being said, we guarantee that $\delta\phi\mid_{i=1}$ reduces to zero as $\phi\mid_{i=1} = \phi_{bulk}$ is the exact solution. Equivalently, this condition can be implemented by

- $\overline{\mathbf{\Lambda}}(1,:) = [\ 1,\ 0,\ 0,\ \ldots,\ 0]$.
- $\overline{\mathbf{\Upsilon}}(1,:) = [\ 0,\ 0,\ 0,\ \ldots,\ 0]$, $\overline{\mathbf{\Phi}}(1) = \phi_{bulk}$ and $\overline{\boldsymbol{Q'}}(1) = [0]$.

Therefore, $\overline{\boldsymbol{\delta\Phi}}(1) = [0]$ as $[\overline{\mathbf{\Upsilon}}(1,:)\overline{\mathbf{\Phi}} - \overline{\boldsymbol{Q'}}(1)] = [0]$ in Eq. 3.46. Likewise, a Dirichlet boundary condition at $i =$ M can be formulated by making

- $\overline{\mathbf{\Lambda}}(M,:) = [\ 0,\ 0,\ 0,\ \ldots,\ 1]$.
- $\overline{\mathbf{\Upsilon}}(M,:) = [\ 0,\ 0,\ 0,\ \ldots,\ 0]$, $\overline{\mathbf{\Phi}}(M) = \phi_b$ and $\overline{\boldsymbol{Q'}}(M) = [0]$.

Also, recall that ϕ_b refers to the potential in the bulk of the liquid (see Section 3.2.2). Finally, $[\overline{\mathbf{\Upsilon}}(M,:)\overline{\mathbf{\Phi}} - \overline{\boldsymbol{Q'}}(M)] = [0]$ and therefore, from Eq. 3.46, we find $\overline{\boldsymbol{\delta\Phi}}(\mathrm{M}) = [0]$.

Neumann Boundary Condition

A Neumann or floating boundary condition is imposed when the derivative of the variable, rather than its exact value, is available.[120,121] In the case of the combined Poisson equation at the SL junction, it means $\frac{d\phi}{dx}$ (or equivalently E_{field}) is known beforehand. Now, being a grid point at the bulk of the semiconductor, the boundary point at $i = 1$ guarantees the vanishing E_{field} or $\frac{d\phi}{dx} = 0$. Alternatively, it means $\overline{\mathbf{\Phi}}(1) = \overline{\mathbf{\Phi}}(2)$ or $\overline{\boldsymbol{\delta\Phi}}(1) = \overline{\boldsymbol{\delta\Phi}}(2)$. Now, this can be implemented by

- $\overline{\mathbf{\Lambda}}(1,:) = [\ 1,\ \text{-}1,\ 0,\ \ldots,\ 0]$.

- $\overline{\boldsymbol{\Upsilon}}(1,:) = [\ 0,\ 0,\ 0,\ \ldots,\ 0]$, $\overline{\boldsymbol{\Phi}}(1) = \overline{\boldsymbol{\Phi}}(2)$ and $\overline{\boldsymbol{Q'}}(1) = [0]$.

Therefore, Eq. 3.46 becomes $[\overline{\boldsymbol{\Upsilon}}(1,:)\overline{\boldsymbol{\Phi}} - \overline{\boldsymbol{Q'}}(1)] = [0]$ and consequently $\overline{\boldsymbol{\delta\Phi}}(1) = \overline{\boldsymbol{\delta\Phi}}(2)$. Following a similar procedure for the other boundary point at $i =$ M, a Neumann-type boundary condition can be implemented as well. In this case, we consider

- $\overline{\boldsymbol{\Lambda}}(M,:) = [\ 0,\ 0,\ \ldots,\ \text{-}1,\ 1]$.
- $\overline{\boldsymbol{\Upsilon}}(M,:) = [\ 0,\ 0,\ 0,\ \ldots,\ 0]$, $\overline{\boldsymbol{\Phi}}(M-1) = \overline{\boldsymbol{\Phi}}(M)$ and $\overline{\boldsymbol{Q'}}(M) = [0]$.

In the end, Eq. 3.46 becomes $[\overline{\boldsymbol{\Upsilon}}(M,:)\overline{\boldsymbol{\Phi}} - \overline{\boldsymbol{Q'}}(M)] = [0]$ and consequently, $\overline{\boldsymbol{\delta\Phi}}(M) = \overline{\boldsymbol{\delta\Phi}}(M-\ 1)$ (Neumann).

3.6 Continuity Equations at the SL Junctions

To extract the valuable electrostatics and charge transport properties, the standard numerical recipe requires the simultaneous solution of the electron and hole current-continuity equations (Eqs. 3.1a-d) along with Poisson's equation (Eq. 3.1e).[120–122] In Section 3.5.3, we have demonstrated a step-by-step procedure to derive the numerical analog of Poisson equation given by Eq. 3.45 in the span of the entire SL junction as shown in Figure 3.3. In this Section, our goal is to derive the discrete versions of the electron and hole current-continuity equations. Nevertheless, the solution grid for continuity equations only extends inside of the electrode that hosts the photo-generated electrons and holes. In the context of Figure. 3.3, the concentrations of electrons (n) and holes (p) will be sought within $i =$ [1 : N], where $i = 1$ and $i =$ N constitute two boundary points.

Similar to our treatment of the combined Poisson equation (derivation of Eq. 3.45 from Eq. 3.15), both of the sets of current-continuity equations (Eqs. 3.1a-d) need to be aptly discretized and converted into suitable matrices to facilitate the numerical calculation. Now, Scharfetter-Gummel (SG) scheme provides an optimum way to discretize Eqs. 3.1a-d and is commonly implemented in the numerical simulation of semiconductor devices.[120–122,157] The details of the SG discretization scheme of SL junctions and the subsequent derivations of the electron and hole continuity equations will be a subject of discussion in Chapter 5 of this thesis. Therefore, in this section, our goal will be to demonstrate a step-by-step procedure to construct the equivalent matrices by utilizing the final discretized versions of the electron and hole continuity equations from Chapter 5.

3.6.1 Discretized Versions of Continuity Equations

Section 5.2.1 of Chapter 5 provides the discretized versions of the electron and hole current-continuity equations by utilizing the footprint of standard SG scheme (see also Refs. [120, Chapter 6] and [122, Chapter 4]). For instance, the final discretized version of the coupled current (Eq. 3.1a) and continuity (Eq. 3.1c) equations of electrons is expressed as (Eq. 5.9 in Section 5.2.1)

$$\begin{aligned}&\frac{\mu_{n|i-1/2}}{\Delta_{i-1}}\left[n_{i-1}B\left(\frac{\phi_{i-1}-\phi_i}{V_T}\right)-n_iB\left(\frac{\phi_i-\phi_{i-1}}{V_T}\right)\right]\\&+\frac{\mu_{n|i+1/2}}{\Delta_i}\left[n_{i+1}B\left(\frac{\phi_{i+1}-\phi_i}{V_T}\right)-n_iB\left(\frac{\phi_i-\phi_{i+1}}{V_T}\right)\right]\\&=\frac{(\Delta_{i-1}+\Delta_i)}{2V_T}\left(R_{n|i}-G_{n|i}\right).\end{aligned}\tag{3.47}$$

Likewise, the discretized representation of the coupled current (Eq. 3.1b) and continuity (Eq. 3.1d) equations of holes is given by (Eq. 5.10 in Section 5.2.1)

$$\begin{aligned}&\frac{\mu_{p|i-1/2}}{\Delta_{i-1}}\left[p_{i-1}B\left(\frac{\phi_i-\phi_{i-1}}{V_T}\right)-p_iB\left(\frac{\phi_{i-1}-\phi_i}{V_T}\right)\right]\\&+\frac{\mu_{p|i+1/2}}{\Delta_i}\left[p_{i+1}B\left(\frac{\phi_i-\phi_{i+1}}{V_T}\right)-p_iB\left(\frac{\phi_{i+1}-\phi_i}{V_T}\right)\right]\\&=\frac{(\Delta_{i-1}+\Delta_i)}{2V_T}\left(R_{p|i}-G_{p|i}\right).\end{aligned}\tag{3.48}$$

Here, i represents any node on the discretized grid inside the semiconductor except at the boundaries. That being said, i can be any point inside [2 : N-1] in Figure. 3.3. This can be easily perceived by looking at Eqs. 3.47 and 3.48, where the carrier concentration at grid-point i is coupled with those of its neighbouring points $i-1$ and $i+1$ (a three-point description). Hence, the expressions in Eqs. 3.47 and 3.48 are applicable to the bulk points when i = [2 : N-1]. Moreover, B stands for Bernoulli function defined as $B(x) = {}^{x}/_{[e^x - 1]}$.[120] Finally, all other variables have already been defined in the course of our discussion as presented in this Chapter.

3.6.2 Discretized Boundary Conditions of Continuity Equations

Boundary Conditions at SL interface (i = N)

The situation at the photoelectrochemically active SL interface is much more intricate and generally solved *via* Neumann boundary condition. To understand, we can start again by treating the SL interfaces as pseudo-Schottky contacts (see Section 3.3.2).[1,32,34–36] Now, the presence of a Schottky-type contact at the interface allows us to write the interfacial electron and hole currents in a similar fashion of those at the MS contacts[158,159] and finally expressed as[32,34,36]

$$J_{n|int} = -qv_{t,n}(n_s - n_{s0}), \tag{3.49}$$

$$J_{p|int} = qv_{t,p}(p_s - p_{s0}). \tag{3.50}$$

Here, $J_{n|int}$ and $J_{p|int}$ represent the interfacial currents respectively due to the electrons and holes transfers at the typical SL junctions. In other words, $J_{n|N} = J_{n|int}$ and $J_{p|N} = J_{p|int}$. A step-by-step procedure to discretize Eqs. 3.49 and 3.50 is provided in Section 5.2.3 of Chapter 5. Therefore, to construct the required matrices *via* SG scheme, here we are directly utilizing the final discretized forms of Eqs. 3.49 and 3.50 from Section 5.2.3 as

$$\frac{\mu_{n|N-1/2}}{\Delta_{N-1}}\left[n_{N-1}B\left(\frac{\phi_{N-1}-\phi_N}{V_T}\right)-n_NB\left(\frac{\phi_N-\phi_{N-1}}{V_T}\right)\right]=\frac{\Delta_{N-1}}{V_T}\left(R_{n|N}-G_{n|N}\right), \tag{3.51}$$

and

$$\frac{\mu_{p|N-1/2}}{\Delta_{N-1}}\left[p_{N-1}B\left(\frac{\phi_N-\phi_{N-1}}{V_T}\right)-p_NB\left(\frac{\phi_{N-1}-\phi_N}{V_T}\right)\right]=\frac{\Delta_{N-1}}{V_T}\left(R_{p|N}-G_{p|N}\right), \tag{3.52}$$

where, $R_{n|N}$ and $G_{n|N}$ respectively accumulate all the possible interfacial recombination and generation processes.

Boundary Conditions at Semiconductor Bulk ($i = 1$)

As the semiconductor bulk is generally characterized by a quasi-neutral region, it is commonly assumed that the concentrations of electrons and holes at the bulk remain the same as their equilibrium concentrations, which are respectively given as n_{bulk} and p_{bulk}.[33] This, in turn, means that the grid point $i = 1$ in Figure 3.3 represents Dirichlet-type boundary conditions for both the electron and hole continuity equations and are expressed as

$$n_1 = n_{bulk}, \tag{3.53}$$

$$p_1 = p_{bulk}, \tag{3.54}$$

However, the semiconductor bulk can also experience carrier extraction and back recombination (as presented in Ref. [70]) and alternatively, the boundary conditions on carrier concentrations can also be given by Neumann-type conditions.[32,103] Similar to our treatment of the boundary conditions of continuity equations at an SL interface, we can define electron and hole currents at the bulk of the semiconductor by utilizing electron and hole extraction/recombination velocities (respectively given as $v_{r,n}$ and $v_{r,p}$). Consequently, the electron and hole currents at the back contact are given as

$$J_{n|bulk} = qv_{r,n}(n_b - n_{b0}), \tag{3.55}$$

$$J_{p|bulk} = -qv_{r,p}(p_b - p_{b0}). \tag{3.56}$$

Here, $J_{n|1} = J_{n|bulk}$ and $J_{p|1} = J_{p|bulk}$ and we define that the positive current flows from the bulk towards the SL interface (in accordance to the current definitions used in Eqs. 3.49 and 3.50). Also n_b and p_b respectively are the bulk concentrations of electron and hole populations under non-equilibrium conditions, whereas n_{b0} and p_{b0} respectively are the electron and hole concentrations in the bulk under equilibrium condition. Finally, by using the SG scheme, the discretized versions of Eqs. 3.55 and 3.56 can be obtained as (for details, see Section 5.2.3)

$$\frac{\mu_{n|1\frac{1}{2}}}{\Delta_1}\left[-n_1 B\left(\frac{\phi_1 - \phi_2}{V_T}\right) + n_2 B\left(\frac{\phi_2 - \phi_1}{V_T}\right)\right] = \frac{\Delta_1}{V_T}\left(R_{n|1} - G_{p|1}\right), \tag{3.57}$$

and

$$\frac{\mu_{p|1\frac{1}{2}}}{\Delta_1}\left[-p_1 B\left(\frac{\phi_2 - \phi_1}{V_T}\right) + p_2 B\left(\frac{\phi_1 - \phi_2}{V_T}\right)\right] = \frac{\Delta_1}{V_T}\left(R_{p|1} - G_{p|1}\right), \tag{3.58}$$

where, $R_{n|1}$ and $G_{n|1}$ respectively accumulate all the possible bulk recombination and generation processes.

3.6.3 Numerical Solution of Carrier Concentrations

At this point, we can now construct the necessary matrices to numerically compute n and p – the ultimate goal of solving the current-continuity equations for electrons and holes (Eqs. 3.1a-d).

Concentration of Electrons

In the numerical computation of the electrons concentration, Eq 3.47 serves as the basic building block of the corresponding matrix representation. In addition, Eqs 3.53 and 3.51 serve as the two boundary conditions located respectively at $i = 1$ and $i =$ N. Together Eqs. 3.47, 3.53 and 3.51 can be expressed as

$$\overline{\boldsymbol{Z_n}}\,\overline{\boldsymbol{n}} \;=\; \overline{\boldsymbol{U_n}}, \tag{3.59}$$

where,

$$\overline{\boldsymbol{Z_n}} \;=\; \begin{bmatrix} z_{n|_{11}} & z_{n|_{12}} & z_{n|_{13}} & \cdots & z_{n|_{1N}} \\ z_{n|_{21}} & z_{n|_{22}} & z_{n|_{23}} & \cdots & z_{n|_{2N}} \\ \vdots & \vdots & \vdots & \ddots & \vdots \\ z_{n|_{N1}} & z_{n|_{N2}} & z_{n|_{N3}} & \cdots & z_{n|_{NN}} \end{bmatrix}, \tag{3.60}$$

$$\overline{\boldsymbol{n}} \;=\; \begin{bmatrix} n_1 \\ n_2 \\ \vdots \\ n_N \end{bmatrix} \tag{3.61}$$

and

$$\overline{\boldsymbol{U_n}} = \begin{bmatrix} u_{n1} \\ u_{n2} \\ \vdots \\ u_{nN} \end{bmatrix} \tag{3.62}$$

Now, as can be seen from Eq. 3.60, $\bar{\boldsymbol{Z}}_{\boldsymbol{n}}$ is an N×N matrix with the following features:

- Centre diagonal elements:

  $z_{n|_{i,i}} = -\left[\frac{\mu_{n|i-1/2}}{\Delta_{i-1}} B\left(\frac{\phi_i - \phi_{i-1}}{V_T}\right) + \frac{\mu_{n|i+1/2}}{\Delta_i} B\left(\frac{\phi_i - \phi_{i+1}}{V_T}\right)\right]$, $i = 2,\ 3,\ \ldots,$ N-1.

- Diagonal elements below centre diagonal:
  $z_{n|_{i,i-1}} = \frac{\mu_{n|i-1/2}}{\Delta_{i-1}} B\left(\frac{\phi_{i-1}-\phi_i}{V_T}\right)$, $i = 2, 3, \ldots,$ N-1.

- Diagonal elements above centre diagonal:
  $z_{n|_{i,i+1}} = \frac{\mu_{n|i+1/2}}{\Delta_{i}} B\left(\frac{\phi_{i+1}-\phi_i}{V_T}\right)$, $i = 2, 3, \ldots,$ N-1.

- Element implementing the Dirichlet boundary condition at $i = 1$: $z_{n|_{11}} = 1$.

- Element implementing the Neumann boundary condition at $i = 1$:
  $z_{n|_{11}} = -\frac{\mu_{n|1\frac{1}{2}}}{\Delta_1}\left[B\left(\frac{\phi_1-\phi_2}{V_T}\right)\right]$ and $z_{n|_{12}} = \frac{\mu_{n|1\frac{1}{2}}}{\Delta_1}\left[B\left(\frac{\phi_2-\phi_1}{V_T}\right)\right]$.

- Elements implementing the Neumann boundary condition at $i =$ N:
  $z_{n|_{NN-1}} = \frac{\mu_{n|N-1/2}}{\Delta_{N-1}}\left[B\left(\frac{\phi_{N-1}-\phi_N}{V_T}\right)\right]$ and $z_{n|_{NN}} = -\frac{\mu_{n|N-1/2}}{\Delta_{N-1}}\left[B\left(\frac{\phi_N-\phi_{N-1}}{V_T}\right)\right]$.

- All other elements are zero.

In addition, $\overline{\boldsymbol{n}}$ and $\overline{\boldsymbol{U_n}}$ can be identified as N×1 column vectors (see Eq. 3.61 and 3.62). The elements of $\overline{\boldsymbol{n}}$ constitute the spatial values of electron concentrations that are under determination, whereas the elements of the $\overline{\boldsymbol{U_n}}$ vector are:

- Non-boundary elements: $u_{ni} = \frac{(\Delta_{i-1}+\Delta_i)}{2V_T}\left(R_{n|i} - G_{n|i}\right)$, $i = 2, 3, \ldots,$ N-1.

- Boundary element at $i = 1$: $u_{n1} = n_{bulk}$.

- Boundary element at $i = 1$: $u_{n1} = \frac{\Delta_1}{V_T}\left(R_{n|1} - G_{n|1}\right)$.

- Boundary element at $i =$ N: $u_{nN} = \frac{\Delta_{N-1}}{V_T}\left(R_{n|N} - G_{n|N}\right)$.

Finally, n can be computed by rearranging Eq. 3.59 as

$$\overline{\boldsymbol{n}} = \overline{\boldsymbol{Z_n}}^{\boldsymbol{-1}}\left[\,\overline{\boldsymbol{U_n}}\,\right]. \tag{3.63}$$

Concentration of Holes

Similar to the case of the electron continuity equation, by utilizing Eqs. 3.48, 3.54 and 3.52, the hole continuity equation can be rewritten as

$$\overline{\boldsymbol{Z_p}}\,\overline{\boldsymbol{p}} \;=\; \overline{\boldsymbol{U_p}}, \tag{3.64}$$

where,

$$\overline{\boldsymbol{Z_p}} \;=\; \begin{bmatrix} z_{p|_{11}} & z_{p|_{12}} & z_{p|_{13}} & \cdots & z_{p|_{1N}} \\ z_{p|_{21}} & z_{p|_{22}} & z_{p|_{23}} & \cdots & z_{p|_{2N}} \\ \vdots & \vdots & \vdots & \ddots & \vdots \\ z_{p|_{N1}} & z_{p|_{N2}} & z_{p|_{N3}} & \cdots & z_{p|_{NN}} \end{bmatrix}, \tag{3.65}$$

$$\overline{\boldsymbol{p}} \;=\; \begin{bmatrix} p_1 \\ p_2 \\ \vdots \\ p_N \end{bmatrix} \tag{3.66}$$

and

$$\overline{\boldsymbol{U_p}} = \begin{bmatrix} u_{p1} \\ u_{p2} \\ \vdots \\ u_{pN} \end{bmatrix}. \tag{3.67}$$

Here, $\overline{\boldsymbol{Z_p}}$ is an N×N matrix with the following features:

- Centre diagonal elements:
  $z_{p|_{i,i}} = -\left[\frac{\mu_{p|i-1/2}}{\Delta_{i-1}} B\left(\frac{\phi_{i-1}-\phi_i}{V_T}\right) + \frac{\mu_{p|i+1/2}}{\Delta_i} B\left(\frac{\phi_{i+1}-\phi_i}{V_T}\right)\right]$, $i = 2, 3, \ldots,$ N-1.
- Diagonal elements below centre diagonal:
  $z_{p|_{i,i-1}} = \frac{\mu_{p|i-1/2}}{\Delta_{i-1}} B\left(\frac{\phi_i-\phi_{i-1}}{V_T}\right)$, $i = 2, 3, \ldots,$ N-1.

- Diagonal elements above centre diagonal:
  $z_{p|_{i,i+1}} = \frac{\mu_{p|i+1/2}}{\Delta_i} B\left(\frac{\phi_i - \phi_{i+1}}{V_T}\right)$, i = 2, 3, ..., N-1.

- Element implementing the Dirichlet boundary condition at $i = 1$: $z_{p|_{11}} = 1$.

- Element implementing the Neumann boundary condition at $i = 1$:
  $z_{p|_{11}} = -\frac{\mu_{p|1\frac{1}{2}}}{\Delta_1}\left[B\left(\frac{\phi_2-\phi_1}{V_T}\right)\right]$ and $z_{p|_{12}} = \frac{\mu_{p|1\frac{1}{2}}}{\Delta_1}\left[B\left(\frac{\phi_1-\phi_2}{V_T}\right)\right]$.

- Elements implementing the Neumann boundary condition at i = N:
  $z_{p|_{NN-1}} = \frac{\mu_{p|N-1/2}}{\Delta_{N-1}}\left[B\left(\frac{\phi_N-\phi_{N-1}}{V_T}\right)\right]$ and $z_{p|_{NN}} = -\frac{\mu_{p|N-1/2}}{\Delta_{N-1}}\left[B\left(\frac{\phi_{N-1}-\phi_N}{V_T}\right)\right]$.

- All other elements are zero.

Moreover, $\overline{\boldsymbol{p}}$ is an N×1 column vector (see Eq. 3.66) representing the spatial values of hole concentrations that are under determination. As can be seen from Eq. 3.67, $\overline{\boldsymbol{U_p}}$ is also an N×1 column vector with the following elements:

- Non-boundary elements: $u_{pi} = \frac{(\Delta_{i-1}+\Delta_i)}{2V_T}\left(R_{p|i} - G_{p|i}\right)$, i = 2, 3, ..., N-1.

- Boundary element at $i = 1$: $u_{p1} = p_{bulk}$.

- Boundary element at $i = 1$: $u_{p1} = \frac{\Delta_1}{V_T}\left(R_{p|1} - G_{p|1}\right)$.

- Boundary element at i = N: $u_{pN} = \frac{\Delta_{N-1}}{V_T}\left(R_{p|N} - G_{p|N}\right)$.

Finally, p can be computed by rearranging Eq. 3.64 as

$$\overline{\boldsymbol{p}} = \overline{\boldsymbol{Z_p}}^{-\mathbf{1}}\left[\, \overline{\boldsymbol{U_p}} \,\right]. \tag{3.68}$$

Chapter 4

The Role of Relative Rate Constants in Determining Surface State Phenomena at Semiconductor-Liquid Interfaces

---

This chapter presents an elaborate theoretical derivation of the occupational dynamics of the surface states at the semiconductor-liquid junctions. By utilizing the rate constants characterizing different surface states-assisted charge transfer processes, it has been shown that the surface states possess a distinct Fermi-level that lies in between the respective Fermi-levels of the semiconductor electrode and the aqueous electrolyte. Importantly, if the charge transfer to the liquid *via* the surface states occurs slowly, the Fermi-level of the surface states equilibrates with the Fermi-level of the semiconducting electrode and the junction deviates from the ideal 'band edge pinning' picture of the interface. Conversely, if the charge transfer to the liquid *via* the surface states happens fast, the Fermi-level of the surface states approaches the

Fermi-level of the aqueous electrolyte and contributes to the yield of interfacial electrochemical reaction by indirectly transferring charges to the liquid. Furthermore, by incorporating this theory into the numerical computation, the theoretical results present reproductions of the non-trivial phenomena often observed through various capacitive measurements (*e.g.*, non-linearity, dip and plateau in Mott-Schottky analysis, low and high frequency capacitive responses, detrimental and beneficial roles of surface states).

This Chapter has been published as: **Asif Iqbal**, Md. Sazzad Hossain and Kirk H. Bevan, The Role of Relative Rate Constants in Determining Surface State Phenomena at Semiconductor-Liquid Interfaces, *Physical Chemistry Chemical Physics*, 2016, 18, 29466–29477.

Abstract

In this work, we present a theoretical study of surface state occupation statistics at semiconductor-liquid interfaces, as it pertains to the evolution of H_2 and O_2 through water splitting. Our approach combines semiclassical charge transport and electrostatics at the semiconductor-liquid junction, with a master rate equation describing surface state mediated electron/hole transfer. As a model system we have studied the TiO_2-water junction in the absence of illumination, where it is shown that surface states might not always equilibrate with the semiconductor. Non-trivial electrostatics, for example, including a shifting of the Mott-Schottky plateau in capacitive measurements are explored when deep-level surface states partially equilibrate with the liquid. We also endeavor to explain observations of non-linearity present in Mott-Schottky plots, as it pertains to surface state occupation statistics. In general, it is intended that the results of this work will serve to further the use and development of quantitative device modeling techniques in the description of H_2 evolution at semiconductor-liquid junctions.

4.1 Introduction

The extensive ongoing research into semiconducting materials utilized in water splitting is spurred by their inherent ability to generate free carriers (electrons and holes) by absorbing freely available solar energy.[1,4,34,160,161] Moreover, through controlled doping the electric field at a semiconductor-water interface may be engineered. This enables the efficient separation of electrons and holes, leading to water oxidation (OH^-/O_2) at semiconductor photoanodes and reduction (H^+/H_2) at semiconductor photocathodes.[1] However, light driven carrier generation within a semiconductor is coupled with the parasitic process of recombination.[33] It is generally believed that surface states (SS) present at the interface often act as an effective recombination centre for photogenerated carries and thereby hinder the process of efficient electron/hole transfer to electroactive species at the semiconductor-liquid interface.[78,79]However, this depicts only a part of the actual dynamics. Indeed, the presence of surface states often facilitates charge transfer between a semiconductor and electroactive species present at the interface.[81] Due to this dual role, the impact of surface states in water splitting has gained considerable research interest.[17,162,163] Recently, Bisquert *et al.* demonstrated[81] that water oxidation at Fe_2O_3 occurs primarily by surface-trap-mediated hole transfer, rather than direct hole transfer from the valence band. Similarly, improved photocatalytic activity has been reported for TiO_2 by deliberately introducing donor/acceptor type band gap states using metallic (Fi,[164] Ni,[165] V[166] or Cr[167]) and non-metallic (C,[168] N[169] or S[170]) dopants, respectively. On the other hand, recent studies have also attributed enhancements in the water splitting performance of Fe_2O_3 to various surface treatments that reduce or passivate surface states.[21,54,71,78,79] Indeed, since the entire process of water splitting is an "inner-sphere" electrochemical reaction, one may argue that surface states formed via reaction intermediates and products during chemisorption play a crucial role in water splitting that deserves deeper investigation.[171]

However, understanding all of the complex phenomena due to SS at the semiconductor-water interface is a long term community wide effort. In this work we explore how the dynamics of SS electron/hole capture and emission processes in the absence of illumination ("dark condition") impacts upon SS occupation statistics. In particular, we examine the degree to which a surface state equilibrates with either the semiconductor or the liquid under various conditions.[131,132] As a quantitative measure of surface state occupation we utilize the concept of a surface state Fermi-level. The idea of a separate intermediate Fermi-level for surface states present at semiconductor-liquid junctions was qualitatively proposed in earlier work.[131] Later, Bisquert *et al.* quantitatively examined the deviation of a SS Fermi-level from the semiconductor Fermi level.[132] Theoretically, surface states can equilibrate entirely either with the semiconductor or with the liquid, or at an intermediate position between these two limits.[131] Crucially, the equilibration of surface states has a direct impact on the availability of electrons and holes during intermediate water splitting reaction steps. Therefore, it is important to develop quantitative models that can provide a deeper understanding of SS-mediated charge transfer processes.

In this work we present a master rate equation based description of surface state occupation statistics, incorporating charge exchange with both the valence and conduction bands as well as the liquid. This master equation approach is combined with a semiclassical treatment of mesoscale semiconductor transport[33] coupled with a non-linear Poisson description of the electrostatics present across the semiconductor-water junction. In this manner, SS-mediated charge transfer is captured self-consistently by calculating the Fermi level dependence upon all the different charge transfer rates present at the interface. Depending on the relative values of the various rate constants, we demonstrate that SS-mediated charge transfer with the liquid is likely to be more prominent for deep-level SS present on wide band gap semiconductors. Moreover, our method produces significantly different electrostatics from commonly predicted

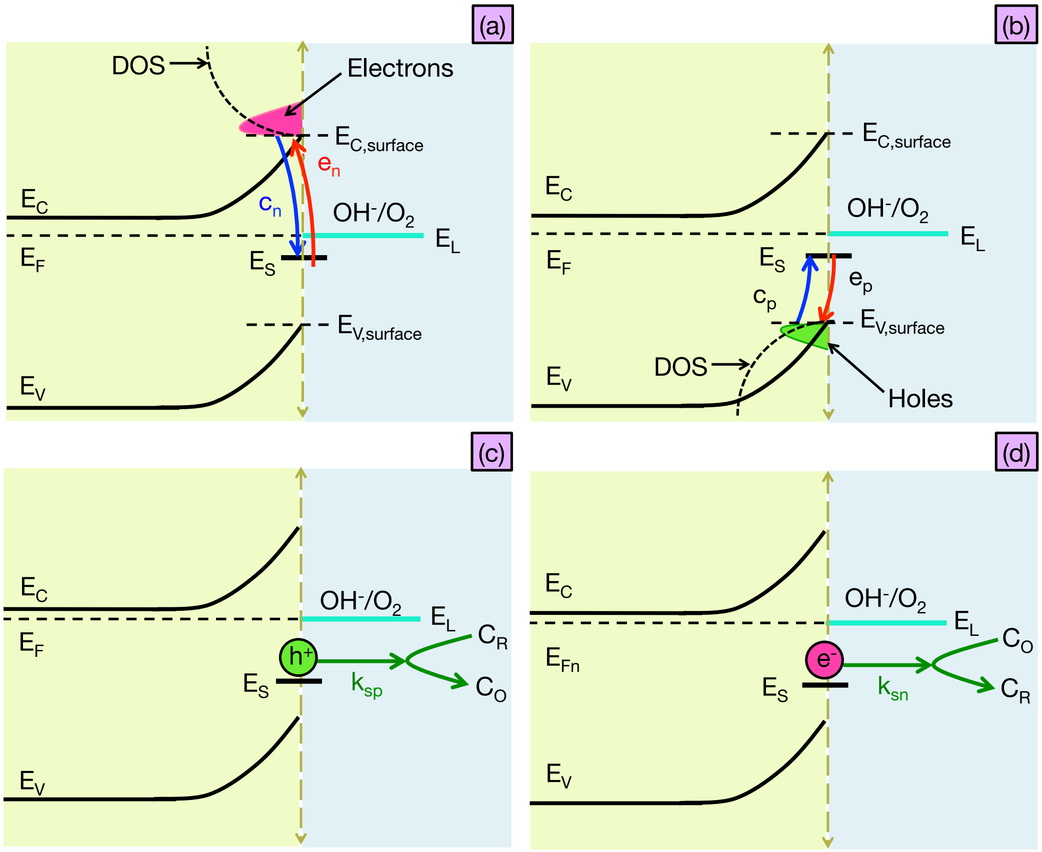

Figure 4.1: Various charge transfer processes involving surface states in a typical semiconductor photoanode. (a) Electron transfer between the conduction band and surface states with rate constants c_n and e_n. Free electrons occupy only a small portion of the available density of states (DOS) in conduction band close to E_C. (b) Hole transfer between the valence band and surface states with rate constants c_p and e_p. Most of the states in the valence band DOS are occupied by electrons and hence very few free holes, that posses an energy close to E_V, are available. (c) Transfer of a trapped hole from surface states to the reduced species (C_R) in the liquid with rate constant k_{sp} and (d) transfer of a trapped electron from the surface states to the oxidized species (C_O) in the liquid with rate constant k_{sn}. The schematic band diagrams are drawn under equilibrium in dark where all the Fermi levels are aligned.

SS-mediated semiconductor-liquid junction electrostatic and gives rise to interesting non-trivial trends previously observed in experiments, such as: non-linearity in the Mott-Schottky plot close to the flat-band potential, shifting of the Mott-Schottky plateau, and marked dips in the Mott-Schottky plots.[172–177]

4.2 Method

4.2.1 Charge Transfer Dynamics Involving Surface States

The various charge transfer processes involving surface states are illustrated in Fig. 4.1: (1) electron capture/emission with the conduction band (CB) (see Fig. 4.1a); (2) hole capture/emission with the valence band (VB) (see Fig. 4.1b); and (3) hole/electron transfer to the electroactive species in the liquid (see Fig. 4.1c and 4.1d). For simplicity, we consider only a single surface state located at energy E_s with spatial distribution density of N_s.[34, 124, 178] Capturing a distribution of surface states is left to future work. The occupation statistics of a single level SS can be expressed in terms of a Fermi-Dirac distribution of the form

$$f_s = \frac{1}{1 + exp\left[\frac{E_s - E_{Fs}}{k_B T}\right]} \tag{4.1}$$

where E_{Fs} is the SS Fermi level. Note that the expression "Fermi level" is often used interchangeably with the expression "electrochemical potential" in semiconductor device modeling.[33, 34] In this work we consider donor surface states, though similar trends hold for acceptor surface states. A filled donor SS is charge neutral, whereas an empty donor SS is positively charged.[143] This has an important impact on band bending at semiconductor-liquid interfaces, as we will show in Section 4.3. Therefore, it is important to know the type of surface states as well as their occupation statistics, in order to capture the charge contributed by surface states (ρ_{ss}). Moreover, to determine the occupation statistics of surface states as described by Eq. (4.1) we need to know E_{Fs}, which follows from a detailed consideration of all three SS charge transfer pathways shown in Fig. 4.1.

Electron Transfer Dynamics

To understand the electron transfer dynamics, let us first consider the process of electron capture by SS from the conduction band as shown in Fig. 4.1a. The rate of this process is given by

$$R_{n,CB\rightarrow SS} = \int_{E_C}^{\infty} N_s(1-f_s)c_n f(E)N(E)dE$$

where E_C is the conduction band minimum, $N(E)$ is the semiconductor density of states, c_n is the average probability per unit time of capturing a conduction band electron by a SS at energy E_s, and $f = 1/[1+exp(E-E_F)]$ is the Fermi distribution of the semiconductor anode with Fermi level E_F.[73] Since most of the conduction band electrons sit close to E_C, assuming a non-degenerate semiconductor, the above integral may be approximated as[33,73]

$$R_{n,CB\rightarrow SS} = N_s(1-f_s)c_n n_s \tag{4.2}$$

where n_s is the density of conduction band electrons at the surface. Similarly, the rate of electron emission from the SS to the conduction band can be defined via the corresponding emission probability per unit time e_n (see Fig. 4.1a) as

$$R_{n,SS\rightarrow CB} = \int_{E_C}^{\infty} N_s f_s e_n(1-f(E))N(E)dE$$

which can be reduced to[33,73]

$$R_{n,SS\rightarrow CB} = N_s f_s e_n N_C \tag{4.3}$$

Here, N_C is the effective density of states in the conduction band. Depending on the relative values of Eqs. (4.2) and (4.3), there will be a net capture or emission of electrons by surface states and equilibrium is characterized by a balance between these two processes as shown in Fig. 4.1a.[73]

Hole Transfer Dynamics

Likewise, hole transfer dynamics between the valence band and surface states can be captured as shown in Fig. 4.1b. In this case, the rate of capturing a hole in the valence band by SS is given by

$$R_{p,VB\rightarrow SS} = \int_{-\infty}^{E_V} N_s f_s c_p (1 - f(E)) N(E) dE$$

where c_p is the average probability per unit time of capturing a valence band hole by a SS at energy E_s and E_V is the valence band maximum. Furthermore, by assuming that all the free holes in the valence band reside close to E_V[33, 73]

$$R_{p,VB\rightarrow SS} = N_s f_s c_p p_s \tag{4.4}$$

where p_s is the density of valence band holes at the surface. Similarly, the hole backward emission rate is given by

$$R_{p,SS\rightarrow VB} = \int_{-\infty}^{E_V} N_s (1 - f_s) e_p f(E) N(E) dE$$

and can be approximated to[33, 73]

$$R_{p,SS\rightarrow VB} = N_s (1 - f_s) e_p N_V \tag{4.5}$$

Here, N_V is the effective density of states in valence band and e_p is the hole emission counterpart to c_p. Equilibrium is characterized by a balance between Eqs. (4.4) and (4.5) as shown in Fig. 4.1b.

Charge Transfer Dynamics Between Surface States and Liquid Species

To capture charge transfer between surface states and electrochemically active species in the liquid, we need to consider: (1) the transfer of holes to reduced species (C_R) in the liquid as shown in Fig. 4.1c; and (2) the transfer of electrons to oxidized species (C_O) as shown in Fig. 4.1d. Assuming the first order reaction kinetics, the rate of hole transfer from SS to reduced species in liquid may be expressed as

$$R_{p,SS\to R} = N_s(1-f_s)k_{sp}C_R \tag{4.6}$$

where k_{sp} is a rate constant characterizing hole transfer from surface states to reduced species. Similarly, the rate of electron transfer from surface states to oxidized species may be expressed as

$$R_{n,SS\to O} = N_s f_s k_{sn} C_O \tag{4.7}$$

where k_{sn} is a rate constant characterizing electron transfer from surface states to reduced species. Similarly, equilibrium is characterized by a balance between Eqs. (4.6) and (4.7) as shown in Figs. 4.1c and 4.1d.

4.2.2 Rate Equation of Surface State Charge Transfer

To describe how the charge transfer dynamics illustrated in Fig. 4.1 impacts the time dependent statistical occupation of surface states we can combine all of the rate constants in the form

$$\begin{aligned} N_s\frac{df_s}{dt} =& [R_{n,CB\to SS} - R_{n,SS\to CB}] + [R_{p,SS\to VB} - R_{p,VB\to SS}] + \\ & [R_{p,SS\to R} - R_{n,SS\to O}] \end{aligned} \tag{4.8}$$

and by further inserting Eqs. (4.2)-(4.7) into Eq. (4.8) we arrive at

$$\begin{aligned}\frac{df_s}{dt} =&(1-f_s)c_n n_s - f_s e_n N_C + (1-f_s)e_p N_V - f_s c_p p_s + \\ &(1-f_s)k_{sp}C_R - f_s k_{sn} C_O \end{aligned} \tag{4.9}$$

This generic expression can be applied to describe the overall rate of charge transfer to or from surface state in a typical semiconductor-water junction. Importantly, under steady state conditions surface state occupation remains constant such that $df_s/dt = 0$. Therefore the above expression simplifies to

$$\begin{aligned}(1-f_s)c_n n_s - f_s e_n N_C + (1-f_s)e_p N_V - f_s c_p p_s + \\ (1-f_s)k_{sp}C_R - f_s k_{sn} C_O = 0\end{aligned} \tag{4.10}$$

Typically, in a water splitting measurement one measures the long time-scale steady state response governed by Eq. (4.10). If short time scale transient techniques are applied, then Eq. (4.9) is more appropriate.[160] In this work we focus on the steady state response.

Steady State Rate Equation Under Equilibrium

To describe the steady state occupation of surface states, one may utilize the equilibrium balance relationships developed above for electrons, holes, and surface state mediated reactions.[73,178] For example, balancing electron capture and emission [Eqs. (4.2) and (4.3)] leads to

$$N_s(1-f_s)c_n n_s = N_s f_s e_n N_C$$

$$e_n = c_n exp\left[\frac{E_s - E_c}{k_B T}\right] \tag{4.11}$$

Here, the ratio of hole to electron occupation density $(1 - f_s)/f_s$ can be rewritten as $exp\left[(E_s - E_{Fs})/(k_B T)\right]$ using Eq. (4.1). Moreover at steady state, the density of conduction band electrons is $n_s = N_C exp\left[-(E_C - E_F)/(k_B T)\right]$ and under equilibrium all the Fermi levels of the system are aligned giving $E_F = E_{Fs}$.[33] Similarly, balancing the hole transfer dynamics between the valence band and surface states via Eqs. (4.4) and (4.5) gives

$$N_s f_s c_p p_s = N_s(1 - f_s) e_p N_V$$

$$e_p = c_p exp\left[\frac{E_V - E_s}{k_B T}\right] \tag{4.12}$$

utilizing the hole density given by $p_s = N_V exp\left[(E_V - E_F)/(k_B T)\right]$.[33] Finally, a similar equilibrium expression can be obtained for charge transfer between the surface states and the redox-active species, which via Eq. (4.6) and (4.7) results in

$$k_{sn} f_s C_O = k_{sp}(1 - f_s) C_R$$

$$C_O k_{sn} = C_R k_{sp} exp\left[\frac{E_s - E_L}{k_B T}\right] \tag{4.13}$$

where we have made use of the equilibration of the surface state (E_{Fs}) and liquid (E_L) Fermi levels under equilibrium $E_{Fs} = E_L$. Our goal is to utilize these expressions to describe the occupation statistics of a surface state under dark current conditions.

Steady State Rate Equation Under Non-Equilibrium

If we consider the non-equilibrium occupation of surface states under steady state conditions, then the master equation given by Eq. (4.10) leads to the following generic expression of f_s

$$f_s = \frac{c_n n_s + e_p N_V + C_R k_{sp}}{c_n n_s + e_n N_C + c_p p_s + e_p N_V + C_R k_{sp} + C_O k_{sn}}$$

or

$$f_s = \frac{1}{1 + \frac{e_n N_C + c_p p_s + C_O k_{sn}}{c_n n_s + e_p N_V + C_R k_{sp}}} \tag{4.14}$$

Now, from Eqs. (4.1) and (4.14), we can write

$$exp\left[\frac{E_s - E_{Fs}}{k_B T}\right] = \frac{e_n N_C + c_p p_s + C_O k_{sn}}{c_n n_s + e_p N_V + C_R k_{sp}} \tag{4.15}$$

The number of rate variables in Eq. (4.15) expression can be reduced by making use of Eqs. (4.11) and (4.12), as well as the expressions $n_s = N_C exp\left[-(E_C - E_F)/k_B T\right]$ and $p_s = N_V exp\left[(E_V - E_F)/k_B T\right]$, to write

$$e_n N_C = c_n n_s \left[exp\left(\frac{E_s - E_F}{k_B T}\right)\right]$$

$$p_s c_p = e_p N_V \left[exp\left(\frac{E_s - E_F}{k_B T}\right)\right]$$

which upon substitution in Eq. (4.15) provides

$$exp\left[\frac{E_s - E_{Fs}}{k_B T}\right] = \frac{\left(c_n n_s + e_p N_V\right) exp\left(\frac{E_s - E_F}{k_B T}\right) + C_R k_{sp} exp\left(\frac{E_s - E_L}{k_B T}\right)}{c_n n_s + e_p N_V + C_R k_{sp}} \tag{4.16}$$

With a rearrangement of variables the generic expression of surface state Fermi-level becomes

$$\begin{aligned} E_{Fs} &= E_s - k_B T ln\left(\Delta\right) \\ \Delta &= \left[\frac{\left(c_n n_s + e_p N_V\right) exp\left(\frac{E_s - E_F}{k_B T}\right) + C_R k_{sp} exp\left(\frac{E_s - E_L}{k_B T}\right)}{c_n n_s + e_p N_V + C_R k_{sp}}\right] \end{aligned} \tag{4.17}$$

Eq. (4.17) determines how the competing charge transfer dynamics interacting with surface states results in a Fermi level for surface states, distinct from that of the semiconductor or liquid, may arise under steady state conditions. Depending on the relative values of rate constants of these process, three different regimes can be identified:

Regime I (Fast Charge Transfer Between Semiconductor and the Surface State): When the SS to liquid (SS$\leftrightarrow$L) rate constants (k_{sn} and k_{sp}) are much less than the SS to semiconductor rate constants (c_n, c_p, e_n, and e_p), then Eq. (4.17) reduces to $E_{Fs} = E_F$. Meaning, in this regime the SS tends to equilibrate with the semiconductor Fermi level (E_F). In physical sense, this regime characterizes very sluggish SS$\leftrightarrow$L charge transfer, such that the SS occupation is mostly determined by considerably fast capture/emission dynamics between the semiconductor and SS.

Regime II (Fast Charge Transfer Between Surface State and the Liquid): Conversely, when the SS$\leftrightarrow$L rate constants (k_{sn} and k_{sp}) are much greater than the SS to semiconductor rate constants (c_n, c_p, e_n, and e_p), then Eq. (4.17) reduces to $E_{Fs} = E_L$. In this case, the SS prefers to equilibrate with the liquid Fermi level (E_L). This may arise when charge transfer between the semiconductor and SS becomes exceedingly sluggish, due to either low carrier concentrations or very low carrier mobility in the semiconductor (e.g. tightly bound small polaron hopping).[160]

Regime III (Intermediate Case): Between these two extreme cases, the SS$\leftrightarrow$L rate constants (k_{sn} and k_{sp}) and the SS to semiconductor rate constants (c_n, c_p, e_n, and e_p) are comparable in value. In this regime, E_{Fs} resides between the semiconductor and liquid Fermi-levels. This regime is the least explored and, as we shall see in Section 4.3, can arise easily when either the semiconductor carrier concentration becomes low or when a surface state resides far from the band edges well within the semiconductor band gap.

However, to model regime III proper estimates of n_s and p_s are needed [as described by Eq. (4.17)], which requires solving the band bending electrostatics present at the semiconductor-liquid interface as we shall explore next.

4.2.3 Band Bending Electrostatics

In the absence of surface states, an ideal interface between a semiconductor electrode and a liquid contains: a region of space charge in the semiconductor (ρ_{sc}), with an equal but opposite screening charge in the liquid (ρ_L). Taking into additional SS charges (ρ_{ss}), the overall charge balance for a semiconductor can be expressed as

$$\rho_{sc} + \rho_{ss} + \rho_L = 0. \tag{4.18}$$

The screening charge density inside the semiconductor under dark condition may be further broken down into[33]

$$\rho_{sc} = N_D^+ - N_A^- + p - n, \tag{4.19}$$

where N_D^+ and N_A^- are the density of ionized electron donors and acceptors, respectively, $n = N_C\ exp\left[-(E_C - E_F)/k_BT\right]$ refers to the electron density, and $p = N_V exp\left[-(E_F - E_V)/k_BT\right]$ refers to the hole density. Similarly, for the donor type surface states we consider the charge contributed is given by $\rho_{ss} = N_s(1 - f_s)$. Note that the surface state charge density expression is slightly modified when acceptor surface states are also present. Finally, the charge distribution inside the liquid can also be modelled semiclassically through a similar set of Boltzmann distributions dependent upon the electrostatic potential (ϕ) in the form

$$\rho_L = zn_+ - zn_- + c^0_{_{H^+}} e^{-\frac{q\phi}{k_BT}} - c^0_{_{OH^-}} e^{\frac{q\phi}{k_BT}}, \tag{4.20}$$

which is commonly known as the Gouy-Chapman model.[137] Here, $n_+ = c_{sup} exp\left[-zq\phi/k_BT\right]$ and $n_- = c_{sup} exp\left[zq\phi/k_BT\right]$ are the supporting electrolyte's cation and anion concentrations, where c_{sup} refers to their bulk concentration assumed to be 0.5 mol/L throughout – z denotes the charge number, k_B Boltzmann's constant, and T the temperature. Moreover, $c^0_{H^+}$ and $c^0_{OH^-}$ stand for the bulk concentration of H$^+$ and OH$^-$ species, respectively in the water splitting reaction.[25,34]

4.2.4 Electrostatics Across the Semiconductor-Liquid Interface

We can now begin to solve for the potential distribution across the semiconductor-liquid interface. Since the dielectric constant (ϵ) exhibits spatial dependence across the semiconductor-liquid junction, our starting point is the generic Gauss equation which has the 1D form

$$\frac{d}{dx}\left(\epsilon E_{field}\right) = \rho_{sc} + \rho_{ss} + \rho_L, \tag{4.21}$$

where the electric field is given by $E_{field} = -d\phi/dx$. This can be expanded into the non-linear form of Poisson's equation[122]

$$\epsilon\frac{d^2\phi}{dx^2} + \frac{d\phi}{dx}\frac{d\epsilon}{dx} = -\left[\rho_{sc} + \rho_{ss} + \rho_L\right] \tag{4.22}$$

which can be solved iteratively on a finite-difference numerical grid.[122] By adopting this approach, the potential distribution across the interface between two different dielectric media is maintained such that the differential form of Gauss's law is obeyed: $\epsilon_{sc}E_{field,sc} - \epsilon_L E_{field,L} = \rho_{ss}$, where $E_{field,sc}$ and $E_{field,L}$ are the semiconductor and liquid region electric fields just outside the interface, respectively. Hence, in the presence of charged surface states or adsorbed ions, the potential exhibits a jump at the interface.[129] Moreover, since the dielectric constant of the semiconductor region (ϵ_{sc}) can vary dramatically from that of water ($\epsilon_L \approx 80$),[129] it is crucial that the more general Gauss equation be applied when modelling the band bending at semiconductor-water interfaces semiclassically.

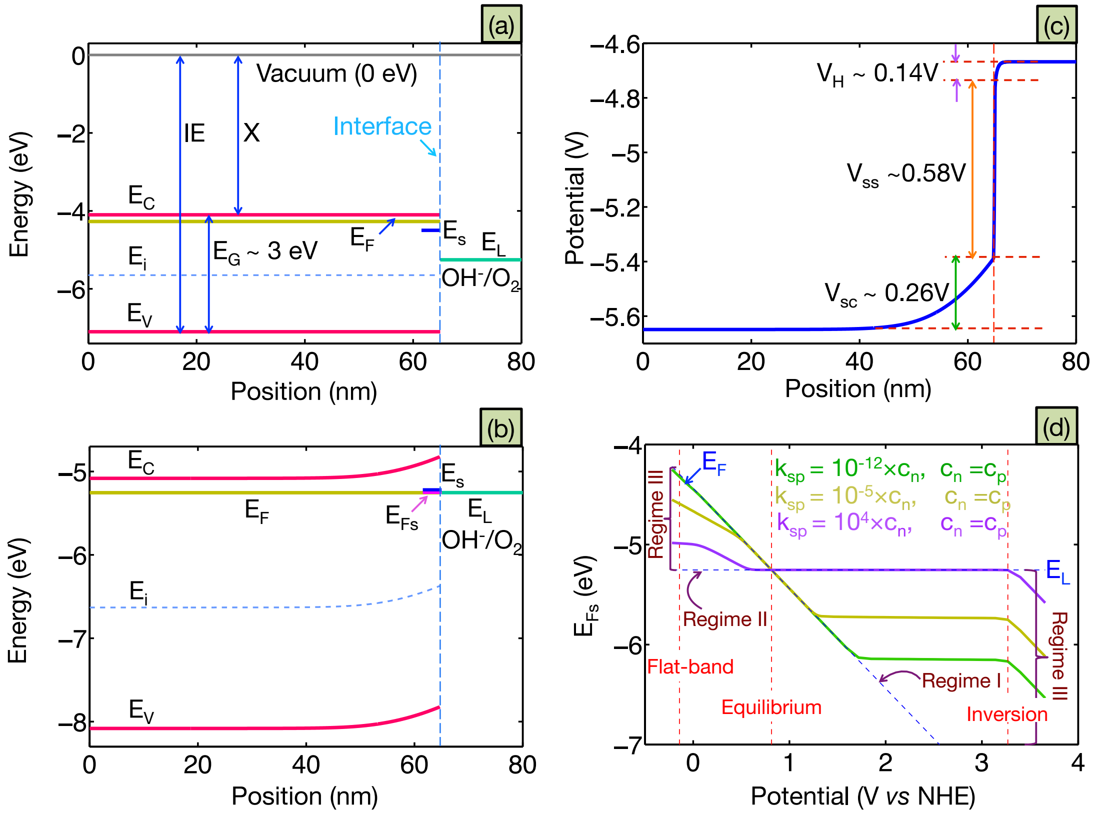

Figure 4.2: Calculated dark current energy band diagram of an n-type TiO_2-water junction under (a) flat-band (b) equilibrium conditions. A band gap of $\sim$ 3 eV is assumed. The junction in equilibrium demonstrates a flat Fermi level $E_F = E_L = E_{Fs}$. Due to the fact that E_{Fs} lies below E_s, donor-type surface states are ionized and hence positively charged ($\rho_{ss} > 0$). (c) Equilibrium potential distribution at the interface. The ionized surface states gives rise to the vertical potential jump at the interface (V_{ss}). Finally, most of the potential drop is accommodated by the semiconductor depletion region and SS region (V_{sc}+V_{ss}). (d) Calculated SS Fermi level (E_{Fs}) under an applied bias and using different sets of rate constants.

4.3 Results

We will now examine the impact of competing rate constants on the occupation statistics and charge transfer dynamics of surface states under an applied bias. As our model system, we have selected an n-type TiO_2 photoanode doped with niobium at a density of N_D= 10^{18} cm^{-3}, immersed in an aqueous solution of pH=7 (C_R = 1×10^{-7} mol/L), possessing a donor type surface state density of $\sim3\times10^{14}$ cm^{-2}.[172] To calculate the potential of this working electrode (TiO_2), we assumed Normal Hydrogen

Electrode (NHE) as the reference electrode, placed 4.44 eV below the liquid vacuum level.[1,129] However, the results of this study can be interpreted as applicable to semiconductor photoanodes in general (particularly those comprised of wide band gap materials). The discussion is split into two parts dedicated to shallow and deep surface states, respectively. Throughout the analysis an attempt made to correlate the occupation statistics of surface states with quantities observable via Mott-Schottky capacitance measurements.

4.3.1 Dynamics of Shallow Level Surface States

The first part of this analysis is aimed at exploring the dynamics of donor-type surface states that are located near to the conduction band edge (E_C) under dark current conditions. The precise positioning of shallow surface states is set at $E_C - E_s = 0.4$ eV as shown in Fig. 4.2a.[179,180] At the instant contact is made between the electrode and water, the respective bands remain flat and unaligned across the junction; the vacuum level however, remains flat throughout the whole junction. Both of these properties are illustrated in Fig. 4.2a. Charge transfer begins immediately in order to establish equilibrium alignment of the electrochemical potential on both sides ($E_F = E_{Fs} = E_L$); this is further accompanied by a balance between the anodic and cathodic currents at the interface ($J_{net} = 0$). The final equilibrium band diagram is shown in Fig. 4.2b.

Importantly, the equilibration process is accomplished by *direct* charge transfer from the semiconductor bands as well as *indirect* charge transfer via the surface states[82] — which in this case is characterized by a built-in potential of ~ 1 V across the interface (Fig. 4.2c). Due to the high concentration of supporting electrolyte carriers in the liquid (c_{sup}= 0.5 mol/L), only a small portion of the electrostatic potential (ϕ) drops across the liquid ($\sim$ 140 meV) as shown in Fig. 4.2c. The remainder of the potential drop occurs across the semiconductor depletion region and surface state region. In this system, equilibration of the electrochemical potential requires that the Fermi level fall below the surface states as shown in Fig. 4.2b, which results in $\sim 79\%$ ionization of the donor type surface states. This surface-exposed charge displaces the semiconductor bands, that are usually pinned, substantially contributing a vertical potential jump, $V_{ss} \sim 0.58$ V at the interface (see Fig. 4.2c).[30] Finally, to satisfy charge conservation, the semiconductor is depleted of majority carriers (ρ_{sc}) giving rise to the ~ 0.26 V potential drop within the electrode (denoted as V_{sc} in Fig. 4.2c). The important point here is that determining the equilibrium concentration of n_s, p_s, and ρ_{ss} (as dictated by band bending) requires an electrostatic consideration of all charges in the junction. The same holds out of equilibrium. We are concerned with these near surface charges because they directly impact upon the charge transfer rates as described by Eqs. (4.2) through to (4.17).

In equilibrium, surface states maintain a consistent Fermi level with that of the system and all of the three types of charge transfer kinetics involving them are balanced (as discussed in Section 4.2). Any shift from equilibrium causes a disturbance in the balance between individual processes. Thus, out of equilibrium one must solve Eq. (4.17) to determine the occupation statistics of surface states as described by E_{Fs}. We shall now explore how the competing rates interact to determine E_{Fs} for shallow traps under a dark current bias. When the charge transfer between the liquid and semiconductor is sluggish we generally reside in regime I, as discussed in Section 4.2, such that $E_{Fs} = E_F$ (marked as a diagonal dashed blue line in Fig. 4.2d). Conversely, when the exchange of charges between the surface state and bulk bands is very slow we generally reside in regime II, such that $E_{Fs} = E_L$ (marked as a horizontal dashed blue line in Fig. 4.2d). In shallow traps the rate of SS mediated charge transfer to the liquid is usually considerably smaller than the rate of capture/emission of trapped electron/hole between the SS and semiconductor bands, such that regime I is typically followed.[180]

To examine this assumption we systematically varied the relative charge transfer rates and calculated the resulting position of E_{Fs} under an applied bias as shown in Fig. 4.2d. In this analysis, we assume $e_p \propto \exp[-E_{A,p}/k_BT]$ and $e_n \propto \exp[-E_{A,n}/k_BT]$, where $E_{A,n} = E_C - E_s$ and $E_{A,p} = E_s - E_V$ are the respective activation energy or barrier energy for the emission processes.[181] Moreover, the capture constants are set equal ($c_p = c_n$) and k_{sp} is varied systematically with respect to c_p as dictated by Eq. (4.17). Typical sluggish charge transfer with the liquid ($k_{sp}/c_p = 10^{-12}$) is shown in green in Fig. 4.2d, where it can be seen that the surface state Fermi level (E_{Fs}) closely follows the semiconductor Fermi level (E_F) with a bias of approximately ±1 V about equilibrium (no bias). Note that the bias scale is taken with respect to NHE, as discussed earlier. However, as the semiconductor bands are bent closer to inversion the surface state Fermi level (E_{Fs}) begins to track the liquid Fermi level (E_L). This is marked by a flattened plateau in Fig. 4.2d (solid green line). This plateau occurs because the surface electron concentration is rapidly decreased by inversion directed band bending and the rate of hole exchange with shallow conduction band traps is quite low. Only when the inversion hole density becomes quite large does E_{Fs} again begin to track E_F at about 3.3 V (see solid green line in Fig. 4.2d). If the liquid rate constant transfer rate is increased to $k_{sp}/c_p = 10^{-5}$ and $k_{sp}/c_p = 10^4$, E_{Fs} begins to track E_L more and more closely (see solid yellow and solid purple lines in Fig. 4.2d, respectively). However, these higher rate constants do not represent physically achievable liquid charge transfer rates, but merely demonstrate the impact of increasing rate constants that will become more impactful when we examine deep level traps.

The question we wish to address next is: to what degree are the occupation statistics of shallow surface surface states observable experimentally? The most common method for characterizing surface state occupation involves some form of capacitance spectroscopy.[81,99,127] In this work we shall utilize Mott-Schottky analysis.[33,34] Let

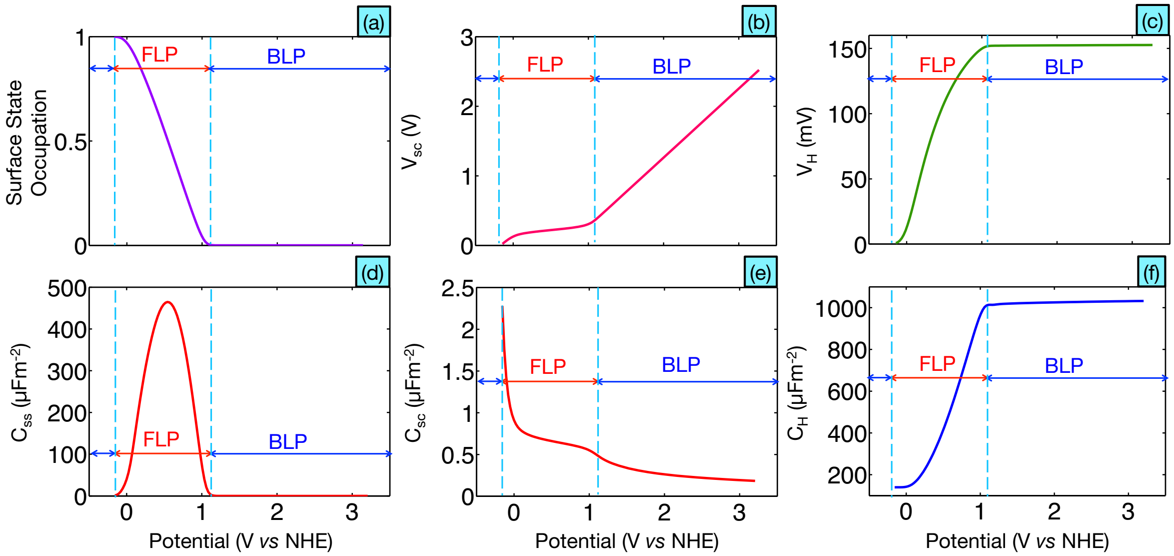

Figure 4.3: Electrostatics and occupation statistics of a TiO$_2$-water junction containing shallow level surface states with $\frac{k_{sp}}{c_n} \leq 10^{-12}$. (a) Normalized surface states occupation by electrons. Fermi level pinning (FLP) and band level pinning (BLP) regions are shown. FLP occurs due to surface state filling/emptying. (b)-(c) Variation of the potential across the semiconductor electrode and liquid with applied bias. When surface states are completely filled/empty, V$_{sc}$ follows a linear profile to accommodate the change in potential at the junction, whereas V$_H$ remains almost constant. However as the SS starts to participate in screening, V$_{sc}$ becomes nearly constant and V$_H$ starts to vary. (d)-(f) Plots of different junction capacitances C_{ss}, C_{sc} and C_H, respectively.

us begin by examining the calculated surface state electron occupation displayed in Fig. 4.3a for $k_{sp}/c_p = 10^{-12}$, where 1 represents a neutral donor surface state density and 0 represents an ionized donor surface state density.[143] While the surface state occupation changes under an applied bias the semiconductor bands undergo Fermi level pinning (FLP) as shown in Fig 4.3a. However, when the occupation is constant the semiconductor undergoes band level pinning (BLP) also shown in Fig 4.3a. The transition from Fermi level pinning to band level pinning appears in the potential drop across the semiconductor region (V_{sc} shown in Fig. 4.3b), with a plateaued region marking FLP and a linear slope during BLP. When the Fermi level is pinned the voltage drop across the liquid region (V_H) increases dramatically, however it remains relatively unchanged during BLP as shown in Fig. 4.3c.

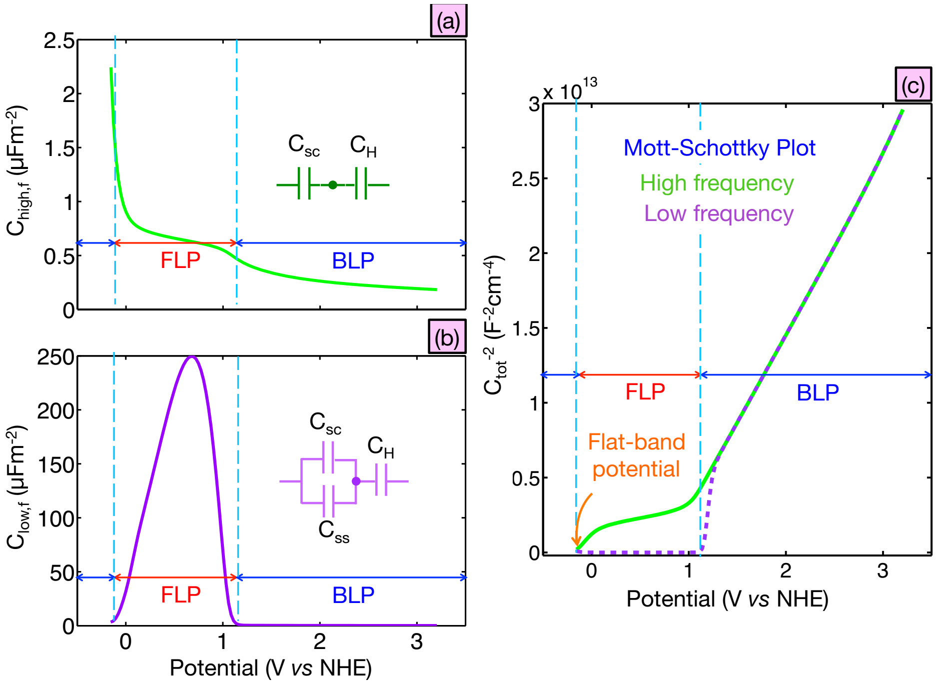

Figure 4.4: Electrostatics of a TiO_2-water junction containing shallow level surface states with $\frac{k_{sp}}{c_n} \leq 10^{-12}$. (a)-(b) Total junction capacitance in the high and low frequency regimes, respectively. The associated simple equivalent circuit models are also shown in the insets. (c) Calculated Mott-Schottky plots for high (green) and low (dashed puple) frequency regimes. The high frequency plot exhibits the classical plateauing effects. The low frequency plot exhibits non-linearly close to the flat-band potential that can be linked to the surface state capacitance.

The origin of Fermi level pinning resides in the high capacitance of the surface states (C_{ss}) shown in Fig. 4.3d. This surface state capacitance is often referred to as the "quantum capacitance" in the solid state literature and the "electrochemical capacitance" in the electrochemistry literature.[34,182] Because the surface state capacitance is so large and strongly localized about E_s it is unlikely that the high bias E_{Fs} plateauing features exhibited in Fig. 4.2d would be observable in the capacitance measurements of shallow surface states. Nevertheless, the occupation statistics of surface states does play an important role in the interpretation of capacitance measurements of semiconductor-liquid junctions, which also incorporates the semiconductor (C_{sc}) and Helmholtz/liquid (C_H) capacitances shown in Fig. 4.3e and 4.3f, respectively.

In a Mott-Schottky measurement of the junction capacitance, a small *ac* voltage signal is applied to the larger bias *dc* voltage signal.[33, 34] Depending on the rate of charge exchange between the semiconductor and surface states as described by Eqs. (4.2) through (4.5), the surface states may not be able to follow the alternating voltage signal.[131] If the surface states cannot follow the alternating voltage signal (i.e. at high frequencies), then only the semiconductor capacitance and Helmholtz/liquid capacitance are measured in series[131] as shown in green in Fig. 4.4a and Fig. 4.4c. The equivalent circuit then becomes $C_{tot} \rightarrow C_{high,f}{=}C_{sc}C_H/(C_{sc}+C_H)$ as shown in Fig. 4.4a, such that the surface state is observed as a plateau in the Mott-Schottky plot ($1/C_{tot}^2$) as shown in green in Fig. 4.4c.[30, 34, 36, 172] On the other hand, if the surface states can empty and fill in synchronization with the alternating voltage signal (i.e. at low frequencies), then the entire capacitance of the junction is measured including the surface state capacitance as shown in purple in Fig. 4.4b and dashed purple in Fig. 4.4c. In the low frequency regime the equivalent circuit then becomes $C_{tot} \rightarrow C_{low,f}{=}(C_{sc}+C_{ss})C_H/(C_{sc}+C_H+C_{ss})$ as shown in Fig. 4.4b, such that the surface state produces a marked non-linear dip in the Mott-Schottky plot as shown in dashed purple in Fig. 4.4c. Interestingly, this low frequency trend has been reported in different experimental results using various semiconductor electrodes used in artificial photosynthesis [TiO_2,[162, 172, 173, 183, 184] Fe_2O_3,[12, 163, 174] Si[175]]. Hence, from our present analysis, we can attribute surface state occupation statistics to the experimental trend of low frequency non-linearity in Mott-Schottky plots close to the flat-band potential.

However, the precise delineation between the high frequency regime and low frequency regime varies between systems, as it depends both on the semiconductor charge mobility and semiconductor-to-SS charge transfer rates. Nevertheless, it is important to note that the low frequency result follows directly from our self-consistent electrostatic calculation in the form of the total differential capacitance of the semiconductor-liquid junction by simply calculating $\delta Q_{tot}/\delta V$ – where δQ_{tot} is

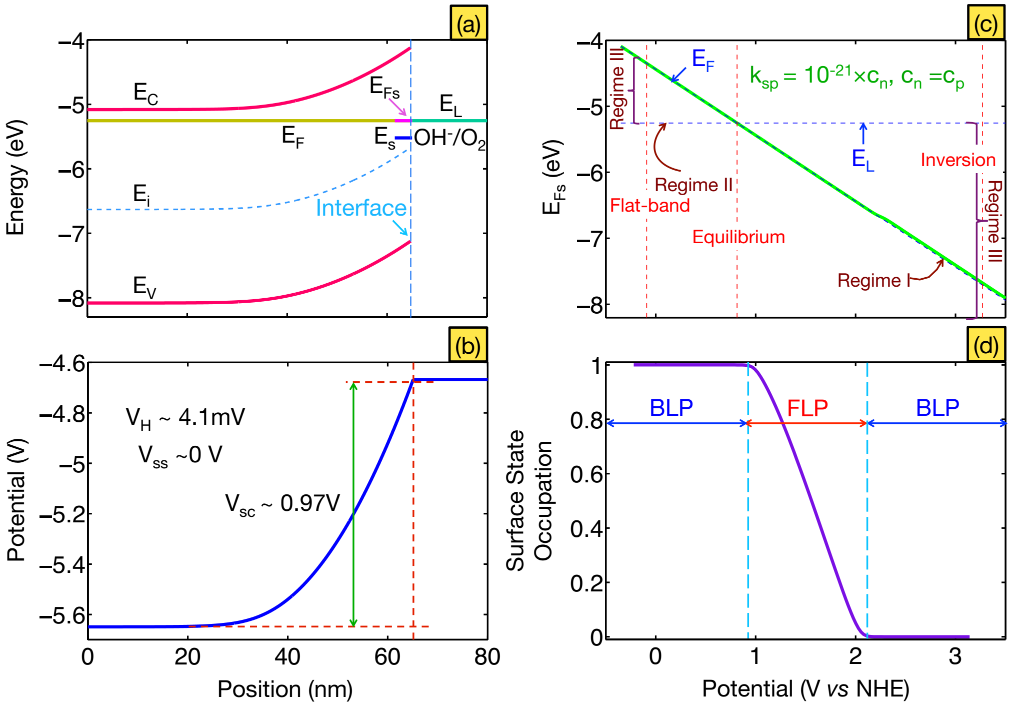

Figure 4.5: TiO_2-water junction under equilibrium, with a donor-type SS located deep inside the band gap. (a) Calculated equilibrium energy band diagram. The SS remains charge neutral, since E_{Fs} resides well above E_s. (b) Distribution of potential at the interface. Since $\rho_{ss} \sim 0$, semiconductor depletes further to compensate the counter charge in the liquid. (c) Plot of E_{Fs} at the maximum rate ($k_{sp}/c_p = 10^{-21}$) for which the SS remains in perfect equilibration with the semiconductor within the bias window. (d) Normalized surface states occupation by electrons. FLP and BLP regions are shown. SS charging takes place in deep depletion.

the differential charge added for a bias change δV. *Thus, it is a fundamental property which should be measurable at sufficiently low frequencies in any system.* In a similar manner, the semiconductor (C_{sc}), surface state (C_{ss}), and liquid/Helmholtz (C_H) capacitances in Fig. 4.3 are arrived at by examining the charge change in each region (δQ_{sc}, δQ_{ss} and δQ_H, respectively) with respect to the change in bias voltage (δV). The same approach is utilized in the analysis of deep level surface states discussed next.

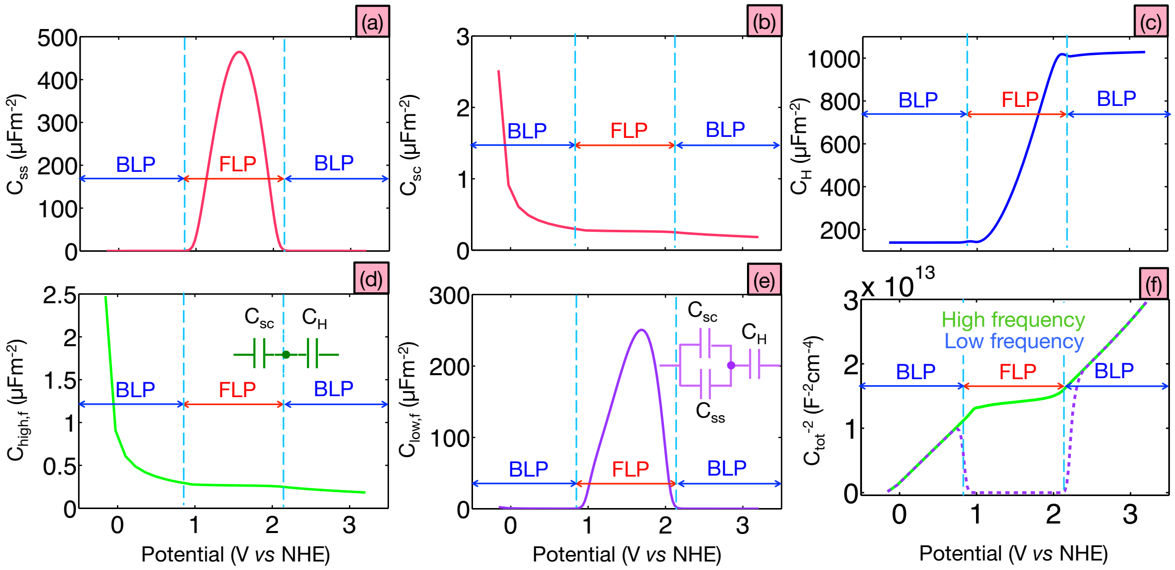

Figure 4.6: TiO$_2$-water junction with a donor-type SS located deep inside the band gap and $\frac{k_{sp}}{c_n} = 10^{-21}$. (a)-(c) Plots of different junction capacitance (C_{ss}, C_{sc} and C_H) respectively. (d)-(e) Total junction capacitance under high and low frequency approximation. The associated simple equivalent circuit models are also shown in the insets. (f) Calculated Mott-Schottky plots for the high (green) and low (blue) frequency approximations. High frequency plot exhibits the classical plateauing effects.[34,36] But the low frequency plot exhibits "U-shaped" non-linearly deep in depletion region that can be linked to the surface state capacitance.

4.3.2 Dynamics of Deep Level Surface States

Let us now study the occupation statistics of deep level surface states. Specifically, we shall examine a mono-energetic surface state located 0.1 eV above the semiconductor mid-gap, or 1.4 eV below E_C, as plotted in Fig. 4.5a.[185] The equilibrium band diagram shown in Fig. 4.5a reveals that the surface state is fully occupied, residing well below E_F. Thus, under equilibrium conditions, the deep level surface state is not ionized and does not contribute to the potential drop as shown in Fig. 4.5b. Since our primary aim is to examine the occupation statistics of deep level surface states, let us begin by examining the Mott-Schottky features (a direct capacitive measure of occupation statistics). If the relative ratio between rate constants is set at or below the extreme ratio $k_{sp}/c_p = 10^{-21}$, such that charge transfer to the liquid is exceptionally sluggish (regime I discussed in Section 4.2), then the deep level surface

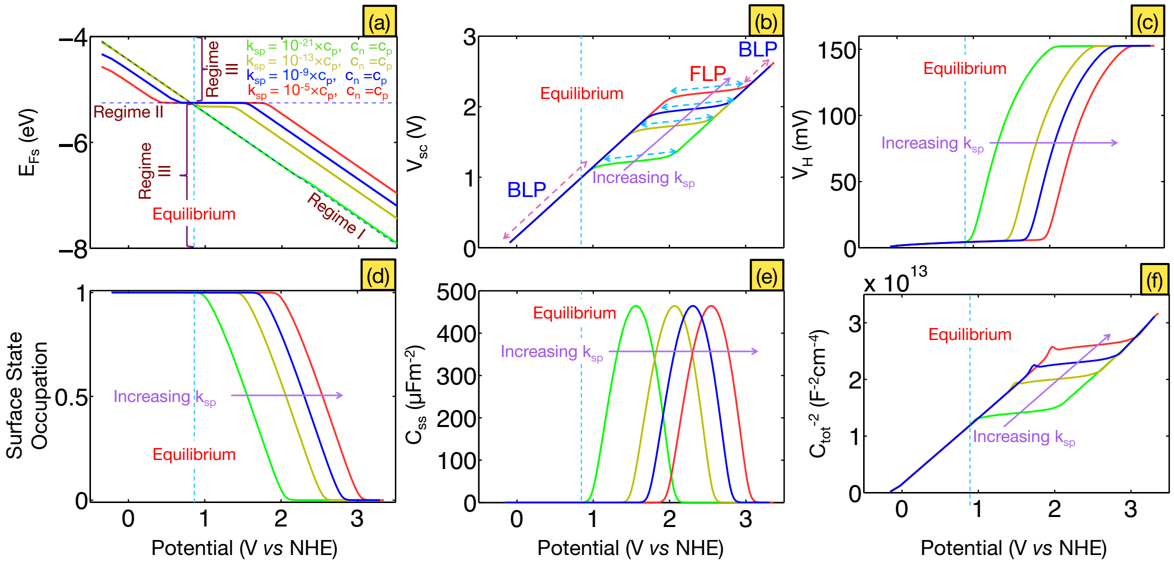

Figure 4.7: (a) Evolution of E_{Fs} under an applied bias for different hole transfer rate constants between the liquid and semiconductor. With increasing k_{sp}, E_{Fs} equilibrates more with E_L. (b)-(c) Variation of the potential across the semiconductor electrode and liquid under an applied bias. As k_{sp} increases, FLP region moves deeper into the depletion region. (d) Normalized surface state occupation by electrons. (e) Variation of C_{ss} with applied potential. Increasing k_{sp} shifts the peak of C_{ss} towards inversion region. (f) High frequency approximation of the Mott-Schottky plot, with its plateau driven deeper inside depletion region due to the increase in k_{sp}.

state Fermi level remains in equilibrium with the semiconductor across a wide range of biases as shown in Fig. 4.5c. The surface state occupation across this bias range is also plotted in Fig. 4.5d, where it can be seen the surface state induces FLP just beyond equilibrium up to biases midway towards inversion (compare Fig. 4.5c and Fig. 4.5d). Again, outside the bias window for FLP the surface state occupation is constant and BLP occurs (see Fig. 4.5d).

The capacitance of the deep surface state (C_{ss}) is shown as a peak in Fig. 4.6a, which may be compared with the semiconductor (C_{sc}) and liquid/Helmholtz (C_H) capacitances (see Figs. 4.6b and 4.6c, respectively). As described in the context of shallow surface states, if the *ac* capacitive measurement signal oscillates too fast then the deep level trap will not be able to empty/fill in synchronization with the applied signal and the measured capacitance will primarily contain the series combination

$C_{tot} \rightarrow C_{high,f}=C_{sc}C_H/(C_{sc}+C_H)$ (as shown in Fig. 4.6d).[131] This high frequency signal capacitance response produces the typical Mott-Schottky plateaued response about the surface state shown in green in Fig. 4.6f.[34,36] However, if the *ac* capacitive measurement signal is slow enough (as might be required for very low mobility semiconductors) then the surface state occupation statistics may be able to follow the *ac* signal. Thus, under sufficiently low frequencies, the total capacitance becomes $C_{tot} \rightarrow C_{low,f}=(C_{sc}+C_{ss})C_H/(C_{sc}+C_H+C_{ss})$ as shown in Fig. 4.6e. In the Mott-Schottky analysis, the participation of deep level surface state in the measured capacitance results in a marked non-linear "U-shaped" dip as shown in purple in Fig. 4.6f. To our current knowledge, the closest practical system that exhibits the above mentioned "U-shaped" Mott-Schottky plot at low frequencies would be the organic solar cells at low temperatures as reported in the literature.[176,177] In the case of organic semiconductors, the low temperature carrier mobility is very limited, requiring a very low frequency ac signal to experimentally obtain the Mott-Schottky plot.[33] However, similar low frequency features may be observable at water splitting electrodes possessing low carrier mobility.

Thus far our analysis of the Mott-Schottky measured variation in semiconductor occupation statistics of deep surface states has focused on regime I. Though regime II most likely remains unrealizable for water splitting reactions, regime III has particular relevance to deep surface states because of the increased difficulty of charge exchange with the semiconductor band edges. If we increase the ratio between rate constants (from $k_{sp}/c_p = 10^{-21}$ through to $k_{sp}/c_p = 10^{-13}$, $k_{sp}/c_p = 10^{-9}$, and $k_{sp}/c_p = 10^{-5}$) the surface state Fermi level [E_{Fs} as dictated by Eq. (4.17)] begins to deviate markedly from equilibration with the semiconductor as shown in Fig. 4.7a. Instead equilibration with liquid electrochemical potential (E_L) occurs over a mid-gap bias range (regime III) as the semiconductor is biased toward inversion (see yellow, blue and red lines in Fig. 4.7a, juxtaposed against full semiconductor equilibration in green). This occurs because the magnitude of the solution rate constant(s) multiplied by the solution reactant concentration(s), begins to exceed the semiconductor band edge rate constant(s) multiplied by the low carrier concentration present midway between surface accumulation and depletion [as described by Eqs. (4.2) through (4.13)]. For deep surface state traps the competition for liquid charge transfer is enchanced by the high electron and hole activation energies associated with the band edges. It is important to note that the liquid equilibration shown in Fig. 4.7a occurs at rate constant ratios that are comparable to those determined experimentally (i.e. $k_{sp}/c_p = 10^{-10}$).[99]

The tendency of the mid-gap surface states to partially follow the liquid electrochemical potential (E_L) at higher rate constants (as shown in Fig. 4.7a), leads to a delayed emptying of the surface states as the semiconductor is biased towards inversion (this is demonstrated in Fig. 4.7d). Meaning, the bias range over which the surface states follow the liquid electrochemical potential (E_L) in yellow, blue and red in Fig. 4.7a, leads to corresponding equivalent shift the emptying of surface state by the semiconductor electrochemical potential also shown in yellow, blue and red in Fig. 4.7d. Because the emptying of surface states is delayed when the liquid rate constant increases, the associated FLP pinning region is also delayed as demonstrated in the semiconductor (V_{sc}) and liquid/Helmholtz (V_H) potential profiles in Figs. 4.7b and 4.7c. Finally, since the emptying of the SS is delayed as the liquid rate constant is increased, the quantum capacitance peak associated with the surface state is also delayed until higher biases (and thus higher semiconductor charge transfer rates) are achieved. This is demonstrated in the transition from full semiconductor equilibration $k_{sp}/c_p = 10^{-21}$ (solid green in Fig.4.7e), through to higher rate constants $k_{sp}/c_p = 10^{-13}$ (solid yellow), $k_{sp}/c_p = 10^{-9}$ (solid blue) and $k_{sp}/c_p = 10^{-5}$ (solid red) lines in Fig. 4.7e. In terms of observable capacitive quantities, partial equilibration with the liquid leads to a shift in the high frequency Mott-Schottky plateau as shown in Fig. 4.7f.

The important point here is that the position of a Mott-Schottky plateau may not be directly associated with the precise position of a surface state inside the band gap. Taking our n-type TiO_2 model system as an example (displayed in Fig. 4.5a), based on the bias separation between the Mott-Schottky intercept and surface state plateau in Fig. 4.7f one could easily conclude that the surface state resides anywhere from mid-gap or towards the valence band edge depending on the relative rate constants – if this were a purely empirical measurement. Where, for the example given here in Fig. 4.5, the surface state always resides slightly above mid-gap (1.4 eV below E_C). Thus, it is imperative that capacitive measurements of surface states be accompanied with measures of both the liquid and semiconductor rate constants.[160,186] Such rate measurements may then be directly incorporated in self-consistent numerical models of the kind presented here to more accurately discern the nature, occupation statistics, and position of surface states in water splitting reactions. This problem is particularly acute with deep surface states, as the liquid rate constants can still influence occupation states when they are many orders of magnitude smaller than the semiconductor rate constants (as shown in Fig. 4.7).

4.4 Conclusion

To conclude, we have theoretically examined how the relative magnitude of rate constants at the interface determine surface state occupation statistics. This has been done utilizing the TiO_2-water junction as our model system. It was accomplished by coupling a semiclassical description of semiconductor-liquid charge transport and electrostatics, with the dynamics of surface state mediated electron/hole transfer. The primary result of this study was to demonstrate that surface state equilibration may occur with the liquid rather than the semiconductor (even with sluggish liquid electron/hole transfer). In particular, wide band gap oxide semiconductors with deep-level surface states can equilibrate with liquid, at least partially. This, in turn, impacts strongly upon the junction electrostatics contributed by surface states and the interpretation of capacitive measurements. In particular, if a deep-level surface states equilibrates partially/fully with the liquid then the location of the plateau in Mott-Schottky plot can exhibit a marked shift with respect to the applied potential – complicating the use of capacitive measurements to locate the position of surface states. It was also shown that non-linear trends in Mott-Schottky capacitive measurements close to the flat-band potential, can be correlated with the low frequency statistics of donor-type surface states located close to the conduction band edge. This appears to explain experimental observations in various semiconductor-liquid systems, such as: TiO_2,[162,172,173,183,184] Fe_2O_3,[12,163,174] and Si.[175] Similar non-linear trends might be observed in deep-level surface states.[176,177] In the future, further comparisons with experiment are needed to fully understand surface state equilibration with water under full light illumination for promising materials such as Fe_2O_3 and TiO_2 utilized in artificial photosynthesis.

4.5 Acknowledgement

The authors would like to acknowledge the financial support from NSERC of Canada and FQRNT of Québec, and the computational resources provided by the Canadian Foundation for Innovation, CalculQuebec and Compute-Canada. AI and KHB also graciously thank N. Kharche for engaging discussions on surface states.

Chapter 5

Simultaneously Solving the Photovoltage and Photocurrent at Semiconductor-Liquid Interfaces

---

This chapter presents a complete numerical description of the semiclassical transport equations at an archetypical semiconductor-liquid junction pertaining solar-assisted water splitting reactions. As demonstrated, the coupled Poisson-continuity equations must be solved in order to facilitate the simultaneous captures of the photovoltage and photocurrent. The solution of the majority carrier continuity equation is the key to capture the photovoltage, whereas the solution of the minority carrier continuity equation is the key to capture the photocurrent. The numerical results presented in this work manifested intriguing correlation with the experimental results reported in the literature. Furthermore, this technique provides a scope to theoretically probe the interfacial and bulk phenomena in a decoupled manner and thus can be utilized as a valuable tool in the design and optimization of the state-of-the-art photocatalytic devices.

This chapter is a reproduction of the article published in the *Journal of Physical Chemistry C*. The complete citation of the published article is:

Asif Iqbal and Kirk H. Bevan, Simultaneously Solving the Photovoltage and Photocurrent at Semiconductor–Liquid Interfaces, *The Journal of Physical Chemistry C*, 2018, 122 (1), 30–43.

Abstract

In this work, we present a general theoretical and numerical approach for simultaneously solving for the photovoltage and photocurrent at semiconductor-liquid interfaces. Our methodology extends drift-diffusion methods developed for metal-semiconductor Schottky contacts in the device physics community, into the domain of semiconductor-liquid 'pseudo-Schottky' contacts. This model is applied to the study of photoelectrochemical anodes, utilized in the oxidative splitting of water. To capture both the photovoltage and photocurrent at semiconductor-liquid interfaces we show that it is necessary to solve both the electron and hole current continuity equations simultaneously. The electron continuity equation is needed to primarily capture the photovoltage formation at photoanodes, whereas the hole continuity equation must be solved to obtain the photocurrent. Both continuity equations are solved through coupled recombination and generation terms. Moreover, to capture charge transfer at the semiconductor-liquid interface floating (Neumann) boundary conditions are applied to the electron and hole continuity equations. As a model system we have studied the illuminated hematite photoanode, where it is shown that our approach can capture band flattening during the formation of a photovoltage, as well as the photocurrent onset and saturation. Finally, the utility of this methodology is demonstrated by correlating our theoretical calculations with photocurrent measurements reported in the literature. In general, this work is intended to expand the scope of photocatalytic device design tools and thereby aid the optimization of solar fuel generation.

5.1 Introduction

Photoelectrochemical (PEC) devices capable of converting sunlight into solar fuels through water splitting hold out the possibility of a sustainable renewable energy economic paradigm.[1,4,54,160,187] Efficient solar harvesting using light-absorbing semiconductors provides one of the most promising routes towards unassisted solar water-splitting.[20] However, decades of extensive research have outlined several key scientific problems that must be resolved to achieve this goal, such as: (1) retarded on-set of the photocurrent[71]; (2) inefficient generation of the photovoltage[21]; (3) the recombination of carriers at surface states[22,81,85]; and (4) the role of electrocatalysts/spectators.[78,86,134] These problems must be addressed through combined theoretical and experimental efforts in order to improve the performance of PEC devices. Recent research has unequivocally attributed the aforementioned bottlenecks to the poor dynamics of carrier transport at semiconductor-liquid junctions, in particular, the interfacial region where electron-hole pairs are generated, separated and finally transferred to the liquid environment.[12,20,21,71] Thus an increased understanding of the mesoscopic charge transfer process at photocatalytic interfaces can provide both fundamental insights and enhanced PEC device designs.

In recent years, theoretical analysis and simulation of the semiconductor-liquid junction has gained a considerable amount of attention, with the aim of improving our understanding of the processes governing artificial photosynthesis. This includes, but is not limited to: the extraction of the steady-state band diagram electrostatics;[32] modeling of the surface states dynamics[188,189] and its impact on electrochemical measurements;[81,82,95,188,189] understanding the performance of electrocatalyst-coated photoelectrodes;[105,106] analyses of transient phenomena;[104,108] and a few studies using available commercial software.[107,109] It is also worthwhile to mention several key analytical[87,88,91–94] and numerical[72,100,101] approaches pioneered the development of carrier transport modeling at semiconductor-liquid junctions. In a nutshell, the standard approach towards numerically simulating charge transfer dynamics in semiconducting photodevices requires complete solution of the semiclassical drift-diffusion equations (more specifically, coupled Poisson-Continuity equations).[120–122] A comprehensive solution to the combined drift-diffusion equations in a photodevice should capture both the photovoltage (V_{ph})[21,36] and the photocurrent (J_{ph})[21,84] generation processes. Importantly, to capture both V_{ph} and J_{ph} in a drift-diffusion model appropriate boundary conditions must be applied and both the minority and majority carrier concentrations must be solved.[120–122] In earlier PEC device drift-diffusion modeling by Cendula *et al.*, band diagram electrostatics were extracted by only considering the minority carrier modulation under solar irradiation.[32] Later, Bisquert *et al.* explored the combined solution of electron and hole drift-diffusion equations to calculate the photocurrent at a photocatalytic interface.[82,103] However, the notion of photovoltage (as mentioned by Gratzel *et al.*[84] and Thorne *et al.*[71]) and the necessity of solving it in a coupled manner with the photocurrent, so far has not received proper attention under existing computational frameworks in the literature. Clearly, in order to simultaneously compute the photocurrent as well as the photovoltage in the semiclassical modeling of a photocatalytic interface, it is important to develop appropriate boundary conditions for both minority and majority carriers.

The typical procedure for simulating the photocurrent at a photocatalytic semiconductor-liquid (SL) junction assumes the presence of an interfacial pseudo-Schottky contact, similar to that which commonly occurs at metal-semiconductor (MS) junctions (see Fig. 5.1).[82,101,109,120–122] This assumption serves well due to the considerable similarities between the electrostatics of a MS junction and those of a SL junction.[34] To elaborate this point, let us consider the band alignments of a typical MS junction as well as a typical SL junction as shown in Figs. 5.1a and 5.1b. The barrier height of an ideal MS junction (denoted by $\Phi_m - \chi$ in Fig. 5.1a) remains constant irrespective of the applied external bias. Here, Φ_m is the metal

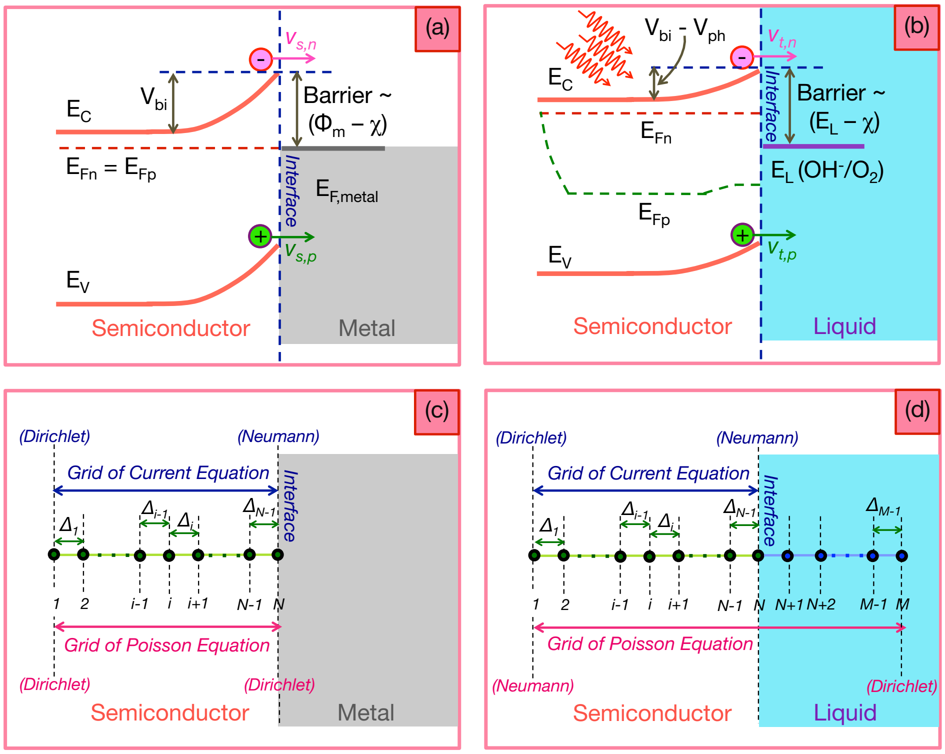

Figure 5.1: (a) Typical equilibrium band diagram alignment of a metal-semiconductor junction demonstrating perfect alignment of all the Fermi-levels ($E_{Fn} = E_{Fp} = E_{F,metal}$). Here E_C is the conduction band edge and E_V is the valence band edge. Formation of a Schottky contact is illustrated by a constant barrier height, whereas the electron and hole transfer over the barrier are modulated by $v_{s.n}$ and $v_{s.p}$, respectively. (b) Band diagram alignment of an illuminated semiconductor-liquid junction forming a pseudo-Schottky contact and demonstrating splitting between the quasi Fermi-levels. The generation of V_{ph} is marked by a reduction in band bending from the unbiased built-in potential (V_{bi}) under dark condition. (c)-(d) Illustration of the discretized spatial domains used in the simulation of the junctions shown in (a) and (b), respectively. All the boundary conditions are indicated as either Dirichlet or Neumann in character.

work-function and χ is the electron affinity of the semiconducting material. Likewise, the semiconductor band edges (E_C and E_V) at the surface should remain pinned when the semiconductor makes contact with the liquid[34,36] — a phenomenon known as the band edge/level pinning (BLP). BLP enforces a constant relative position of the liquid Fermi level (E_L) with respect to the semiconductor band edges (equivalent to the barrier at a MS contact). Thus one can assume the presence of a pseudo-Schottky contact at the semiconductor-liquid interface.[34] However, a photocatalytic interface can deviate from this ideal interfacial Schottky-type picture through unpinning of the semiconductor bands if the electrode begins to charge or discharge surface states.[188] In this case, an adaptive Schottky contact is required to represent the solid-liquid interface.[188]

Numerical solutions of a Schottky contact typically utilize the concept of 'effective recombination velocity', first introduced by Crowell and Sze in the wake of semiconductor device modeling development.[89, 190] By using separate recombination velocities for electrons and holes, the electron (J_n) and hole (J_p) currents at the contact can be expressed as[121, 158, 159]

$$J_n = -qv_{s,n}(n_s - n_{s0}), \tag{5.1}$$

$$J_p = qv_{s,p}(p_s - p_{s0}), \tag{5.2}$$

where $v_{s,n}$ and $v_{s,p}$ are the electron and hole surface recombination velocities (see Fig. 5.1a). Moreover, n_{s0} and p_{s0} are the equilibrium concentrations of electrons and holes at the interface and n_s and p_s are the non-equilibrium concentrations of electrons and holes at the interface, respectively. Here, Eqs. (5.1) and (5.2) constitute the boundary conditions for the current continuity equation and, as we will see later, the solution of these equations can effectively capture the electrostatics of both Schottky and Ohmic contacts.[89, 121, 158, 190]

Similarly, the assumption of pseudo-Schottky contact at the photocatalytic interface (by considering only first-order electron/hole transfer rates[32, 82, 101]) allows us to use expressions equivalent to Eqs. (5.1) and (5.2) to represent currents due to the electron and hole flow at the semiconductor-liquid junction, which are expressed as[34, 36]

$$J_n = -qv_{t,n}(n_s - n_{s0}), \tag{5.3}$$

$$J_p = qv_{t,p}(p_s - p_{s0}). \tag{5.4}$$

Here, $v_{t,n}$ and $v_{t,p}$ are the equivalent pseudo-Schottky contact terms of $v_{s,n}$ and $v_{s,p}$ and respectively represent the 'surface transfer velocities' of electron and hole from the semiconductor to the liquid (see Fig. 5.1b).[82, 101, 103] This pseudo-Schottky contact approximation works quite well in describing the current flow across SL junctions.[82, 103, 109] However, care must be taken in its implementation due to the key differences between a perfect metal-semiconductor Schottky contact and a pseudo semiconductor-liquid Schottky contact. In the case of an MS Schottky contact, the minority carrier population remains negligible and almost all of the current is carried by the transfer of majority carriers across the barrier.[89] In contrast, as the desired reaction at a SL interface takes place due to the minority carrier transfer, the current is primarily conveyed by minority carriers.[1, 34, 37, 186] Moreover, at SL junctions it is desirable to block the transfer of the majority carrier from the semiconductor side as this process can lead to the backward reaction and potentially degrade the water-splitting performance of a semiconducting electrode. Finally, different forms of generation and recombination processes at the photocatalytic interface and bulk can dramatically impact upon the overall performance and therefore, should be included in any comprehensive theoretical simulation approach.

In this work, we present a generic approach for solving both the minority carrier and majority carrier currents at photocatalytic SL electrodes, which leads directly to a simultaneous solution of both V_{ph} and J_{ph}. This is accomplished through the formulation of appropriate boundary conditions in the coupled Poisson-Continuity solution of an archetypal SL junction. Our approach directly extends the device modeling techniques developed for MS Schottky contacts,[89, 190] into the domain of SL pseudo-Schottky contacts. Moreover, the methodology we present includes all the key interfacial generation and recombination processes that might affect the overall charge transfer kinetics. In this manner, we demonstrate that the numerical solution of the coupled Poisson-Continuity equations can self-consistently capture the photocurrent as well as the photovoltage. Furthermore, we explore the scope of our method by revisiting the physics of photovoltage generation and semi-quantitatively correlating our computational photocurrent with experimental results reported in the literature.

5.2 Method

5.2.1 Discretization of the Semiconductor Continuity Equations

In order to develop a general approach for simultaneously solving for both V_{ph} and J_{ph} at SL junctions, let us begin by briefly revisiting the Scarfetter-Gummel (SG) discretization scheme developed for semiconductors.[157] Here, we will consider the problem of discretizing the electron and hole continuity equations inside the bulk of the semiconductor as shown in Fig. 5.1. The corresponding discretized domains used to solve the coupled Poisson-Continuity equations at a MS junction and a SL junction are shown in Figs. 5.1c and 5.1d, respectively. Numerically, the SG scheme allows us to write the discretized version of the current driven by electrons at the center of the mesh line connecting the grid points $i-1$ and i (see Figs. 5.1c and 5.1d) in the form of[120, 122]

$$J_{n|i-1/2} = \frac{qV_T}{\Delta_{i-1}}\mu_{n|i-1/2}\left[n_i B\left(\frac{\phi_i - \phi_{i-1}}{V_T}\right) - n_{i-1} B\left(\frac{\phi_{i-1} - \phi_i}{V_T}\right)\right], \tag{5.5}$$

where ϕ is the electrostatic potential, n is the electron concentration, μ_n is the electron mobility. Other parameters include the Boltzmann constant (k_B), temperature (T), $V_T = \frac{k_B T}{q}$, grid spacing (Δ) and Bernouli's function (B) given by $B(x) = \frac{x}{e^x - 1}$. Similarly, the electron current at the middle of the mesh line connecting the grid points $i+1$ and i can be expressed as

$$J_{n|i+1/2} = \frac{qV_T}{\Delta_i}\mu_{n|i+1/2}\left[n_{i+1}B\left(\frac{\phi_{i+1}-\phi_i}{V_T}\right) - n_i B\left(\frac{\phi_i-\phi_{i+1}}{V_T}\right)\right]. \tag{5.6}$$

Now the steady-state form of the electron continuity equation in 1D is written as[33, 122]

$$\frac{1}{q}\frac{dJ_n}{dx} + G_n - R_n = \frac{\partial n}{\partial t} = 0, \tag{5.7}$$

where G_n and R_n represent generation and recombination rates of electrons, respectively. This takes the following discretized form at grid point i[120, 122]

$$\frac{J_{n|i+1/2} - J_{n|i-1/2}}{\frac{\Delta_{i-1}+\Delta_i}{2}} = q(R_{n|i} - G_{n|i}). \tag{5.8}$$

Finally, by substituting Eqs. (5.5) - (5.6) into Eq. (5.8), we arrive at the discretized version of the electron current continuity equation as given by the SG scheme[120, 122]

$$\begin{aligned}
&\frac{\mu_{n|i-1/2}}{\Delta_{i-1}}\left[n_{i-1}B\left(\frac{\phi_{i-1}-\phi_i}{V_T}\right) - n_i B\left(\frac{\phi_i-\phi_{i-1}}{V_T}\right)\right]\\
&+\frac{\mu_{n|i+1/2}}{\Delta_i}\left[n_{i+1}B\left(\frac{\phi_{i+1}-\phi_i}{V_T}\right) - n_i B\left(\frac{\phi_i-\phi_{i+1}}{V_T}\right)\right]\\
&=\frac{(\Delta_{i-1}+\Delta_i)}{2V_T}\left(R_{n|i} - G_{n|i}\right).
\end{aligned} \tag{5.9}$$

Following a similar discretization procedure for the hole continuity equation leads to[120, 122]

$$\begin{aligned}
&\frac{\mu_{p|i-1/2}}{\Delta_{i-1}}\left[p_{i-1}B\left(\frac{\phi_i-\phi_{i-1}}{V_T}\right) - p_i B\left(\frac{\phi_{i-1}-\phi_i}{V_T}\right)\right]\\
&+\frac{\mu_{p|i+1/2}}{\Delta_i}\left[p_{i+1}B\left(\frac{\phi_i-\phi_{i+1}}{V_T}\right) - p_i B\left(\frac{\phi_{i+1}-\phi_i}{V_T}\right)\right]\\
&=\frac{(\Delta_{i-1}+\Delta_i)}{2V_T}\left(R_{p|i} - G_{p|i}\right),
\end{aligned} \tag{5.10}$$

where p is the hole concentration and μ_p is the hole mobility. Moreover, G_p and R_p represent generation and recombination rates of holes, respectively. It is important to understand that the standard Scharfetter-Gummel discretization scheme, resulting in Eqs. (5.9) and (5.10), can be directly applied to any grid point except those at boundaries. The boundaries should be solved by modifying the original SG approach, which we will now proceed to do for SL pseudo-Schottky contacts by building upon the techniques developed for MS Schottky contacts.[158]

5.2.2 Boundary Conditions at the Metal-Semiconductor Junction

To arrive at the discretized current equations due to electron and hole transport at a MS junction, one may utilize the SG scheme boundary condition extracted from the interface current expressions given in Eqs. (5.1) and (5.2). We begin here by considering the electron current arising from conduction band electron transfer at the MS junction as shown in Fig. 5.1a. At the contact grid point $i = N$, Eq. (5.1) takes the form of

$$J_{n|N} = -qv_{s,n}(n_N - n_{s0}). \tag{5.11}$$

In the original SG formulation, the current inside any interval $[i-1, i]$ is given as a truncated Taylor expansion about its value at the mid point $(i + \frac{1}{2})$ of that interval.[122] Using this well-defined numerical approximation, the electron current at the contact $(J_{n|N})$ can be approximated as the current value at the mid-point of the same interval $[N-1, N]$ or equivalently, $J_{n|N} \approx J_{n|N-1/2}$. Furthermore, $J_{n|N-1/2}$ can be determined from Eq. (5.5) as the case when $i = N$ and can be used to replace $J_{n|N}$ in Eq. (5.11). This procedure results in the discretized boundary condition representing the electron continuity equation at the interface and is given as[158]

$$\frac{qV_T}{\Delta_{N-1}}\mu_{n|N-1/2}\left[n_N B\left(\frac{\phi_N-\phi_{N-1}}{V_T}\right)-n_{N-1}B\left(\frac{\phi_{N-1}-\phi_N}{V_T}\right)\right]=-qv_{s,n}(n_N-n_{s0}). \tag{5.12}$$

This discretized form of the electron continuity equation at the contact has been widely used in the simulation of MS Schottky contacts.[158] By rearranging the terms in Eq. (5.12), the expression of the electron concentration at the boundary becomes

$$n_N=\frac{\left[\mu_{n|N-1/2}B(\frac{\phi_{N-1}-\phi_N}{V_T})\right]n_{N-1}+\frac{\Delta_{N-1}}{V_T}v_{s,n}n_{s0}}{\mu_{n|N-1/2}B(\frac{\phi_N-\phi_{N-1}}{V_T})+\frac{\Delta_{N-1}}{V_T}v_{s,n}}. \tag{5.13}$$

More insight can be obtained if Eq. (5.12) is rearranged and given a generic form similar to Eq. (5.9), or

$$\frac{\mu_{n|N-1/2}}{\Delta_{N-1}}\left[n_{N-1}B\left(\frac{\phi_{N-1}-\phi_N}{V_T}\right)-n_N B\left(\frac{\phi_N-\phi_{N-1}}{V_T}\right)\right]=\frac{\Delta_{N-1}}{V_T}\left[\frac{v_{s,n}(n_N-n_{s0})}{\Delta_{N-1}}\right]. \tag{5.14}$$

Interestingly, by comparing Eqs. (5.9) and (5.14), the transfer of conduction band electrons from the semiconductor to the metal ($\frac{v_{s,n}n_N}{\Delta_{N-1}}$) can be recognized as the interfacial electron recombination term ($R_{n|N}$). At the same time, the transfer of metal electrons to the semiconductor conduction band ($\frac{v_{s,n}n_{s0}}{\Delta_{N-1}}$) can be recognized as the interfacial electron generation term ($G_{n|N}$) — in the absence of any additional recombination or generation processes. In this sense $v_{s,n}$ can be interpreted as a 'recombination velocity' for electron transfer across a MS Schottky contact. Now if we introduce additional generation-recombination processes, which will be done in depth for a SL pseudo-Schottky contact, we can write the generic discretized form of the electron continuity equation boundary condition at the contact as

$$\frac{\mu_{n|N-1/2}}{\Delta_{N-1}}\left[n_{N-1}B\left(\frac{\phi_{N-1}-\phi_N}{V_T}\right)-n_N B\left(\frac{\phi_N-\phi_{N-1}}{V_T}\right)\right]=\frac{\Delta_{N-1}}{V_T}\left(R_{n|N}-G_{n|N}\right). \tag{5.15}$$

Here, $G_{n|N}$ and $R_{n|N}$ respectively take into account of all the interfacial electron generation and recombination processes, a concept that will be very useful for modeling the current flow at SL junctions. Following a similar approach, the discretization of the hole continuity equation at the contact ($i = N$) leads to

$$\frac{qV_T}{\Delta_{N-1}}\mu_{p|N-1/2}\left[p_{N-1}B\left(\frac{\phi_N-\phi_{N-1}}{V_T}\right)-p_N B\left(\frac{\phi_{N-1}-\phi_N}{V_T}\right)\right]=qv_{s,p}(p_N-p_{s0}), \tag{5.16}$$

and upon rearranging the terms in Eq. (5.16), the hole concentration at the boundary can be expressed as

$$p_N=\frac{\left[\mu_{p|N-1/2}B(\frac{\phi_N-\phi_{N-1}}{V_T})\right]p_{N-1}+\frac{\Delta_{N-1}}{V_T}v_{s,p}p_{s0}}{\mu_{p|N-1/2}B(\frac{\phi_{N-1}-\phi_N}{V_T})+\frac{\Delta_{N-1}}{V_T}v_{s,p}}. \tag{5.17}$$

Finally, by comparing Eqs. (5.10) and (5.16) one arrives at a similar generic discretized expression for the hole continuity equation interfacial boundary condition, with the form

$$\frac{\mu_{p|N-1/2}}{\Delta_{N-1}}\left[p_{N-1}B\left(\frac{\phi_N-\phi_{N-1}}{V_T}\right)-p_N B\left(\frac{\phi_{N-1}-\phi_N}{V_T}\right)\right]=\frac{\Delta_{N-1}}{V_T}\left(R_{p|N}-G_{p|N}\right), \tag{5.18}$$

where $G_{p|N}$ and $R_{p|N}$ respectively refer to all the interfacial hole generation and recombination processes. In this approach, recombination velocities ($v_{s,n}$ and $v_{s,p}$) play the pivotal role in capturing the electrostatics of MS Ohmic and Schottky contacts.[121,190] In general, Eqs. (5.15) and (5.18) constitute *Neumann*-type boundary conditions, where the concentrations of electrons and holes at the interface are allowed to float and the Schottky-type of character of the contact is revealed. For example, if $v_{s,n}$ and $v_{s,p}$ become significantly high in value, then $n_N \rightarrow n_{s0}$ and $p_N \rightarrow p_{s0}$ – as we can see from Eqs. (5.13) and (5.17). When framed in terms of a boundary condition problem, this extreme represents a *Dirichlet*-type condition where electron and hole concentrations take pre-defined constant values.[120] Physically, it represents an Ohmic contact.[190] This is due to the fact that an Ohmic contact tends to maintain its interfacial electron and hole concentrations equal to their equilibrium values. Therefore, according to the 'recombination velocity' approach, Ohmic contacts are often idealized by assuming infinite electron and hole recombination velocities at the interface.[121,190] Schottky contacts, on the other hand, do not maintain constant electron or hole concentrations and so must employ *Neumann* boundary conditions as shown above.

5.2.3 Boundary Condition at the Semiconductor-Liquid Junction

With general boundary conditions for the MS Schottky interface in hand, let us now extend this work to similarly formalize boundary conditions for the SL pseudo-Schottky interface — shown in Fig. 5.1d. The key additional criteria present at SL junctions, is that the electron and hole continuity equations must be coupled with Poisson's equation to capture both the photocurrent (J_{ph}) and the photovoltage (V_{ph}). Let us begin by developing boundary conditions for the electron and hole continuity equations, following a similar approach to that deployed for the MS junction in Section 5.2.2. Subsequently, revised boundary conditions for Poisson's equation, capable of capturing V_{ph}, will be introduced.

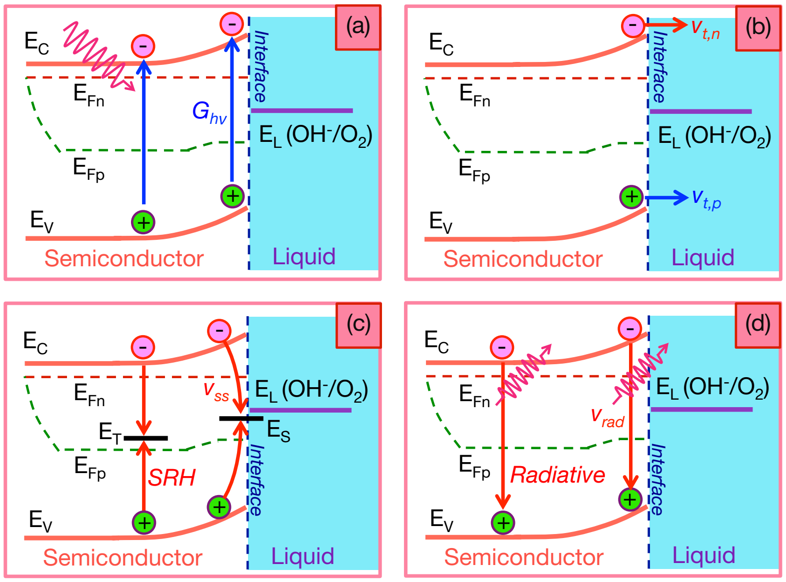

Figure 5.2: Various generation-recombination processes determining the interfacial/bulk charge transfer at an n-type photocatalytic semiconductor-liquid anode. Each process can be viewed as either beneficial (marked in blue) or detrimental (marked in red) in terms of the solar-to-chemical fuel conversion yield. (a) Photogeneration ($G_{h\nu}$) of electron-hole pairs under solar irradiation. (b) Transfer of conduction band electrons and valence band holes to reduce and oxidize species inside liquid, respectively. Here, hole transport is marked as the desired reaction, whereas electron transfer is the undesired backward reaction. (c) Non-radiative recombination in the semiconductor mediated by trap states and surface states. (d) Direct band-to-band radiative recombination.

Boundary Conditions of the Electron and Hole Continuity Equations

In principle, the transport of interfacial electrons and holes can be strongly modulated by the various generation-recombination processes present at the interface of a SL junction.[1, 109, 186] Therefore, it is crucial to explore and mathematically represent all of the basic generation-recombination processes (illustrated in Fig. 5.2), so that these effects can be taken into account when self-consistently solving the carrier transport properties of a SL interface.

Photogeneration of Electron-Hole Pairs. In a photocatalytic anode incident sunlight penetrates the semiconductor region, promoting the direct band-to-band photogeneration of electron-hole pairs (as shown in Fig. 5.2a). The photogeneration rate ($G_{h\nu}$) of electron-hole pairs, as a function of the penetration depth (x) into the semiconductor, can be calculated by the Lambert-Beer law as[32,109]

$$G_{h\nu}(x) = \int_{\lambda_{min}}^{\lambda_g} \eta\phi^0(\lambda)\alpha(\lambda)e^{-\alpha(\lambda)x}d\lambda, \tag{5.19}$$

where the incident photon flux density (ϕ^0) is related to the spectral power density (P) associated with the solar irradiation by $\phi^0(\lambda) = P(\lambda)\frac{\lambda}{hc}$. In a typical solar experiment under standard AM1.5G spectrum, P is usually specified along with other data. Here, η is the quantum efficiency of the generation process, α is the absorption coefficient, λ_g refers to the wavelength below which the semiconductor absorbs photons and λ_{min} is the lowest wavelength present in the incident solar spectrum.[32,109] It is important to note that $G_{h\nu}(x)$ serves as the photogeneration rate throughout the entire numerical grid of the semiconductor electrode including the photocatalytic interface.

Transport of Electrons and Holes to the Liquid. Just as with a MS Schottky contact, the transfer of holes across a SL pseudo-Schottky contact (depicted in Fig. 5.2b) can be treated as a recombination process modeled by $v_{t,p}$.[103,186] For MS junctions, this process physically represents the transfer of holes from the semiconductor side and their subsequent recombination with the electrons on the metal side (see Fig. 5.1a). However, the surface hole recombination velocity at an anodic SL junction physically represents the transfer of valence band holes leading to the desired reaction (oxidation of water at the photoanode as shown in Fig. 5.2a), thereby resulting in hole driven current flow as given by Eq. (5.4).[32,101,103] Furthermore, electron transfer at an anodic SL junction can be captured by $v_{t,n}$ (as given by Eq. (5.3)), and represents an undesirable counter back-reaction (reduction of O_2 by conduction band electrons) lowering the net water-splitting conversion yield of a PEC anode.[72,82,101] Whereas, the electron transfer across a MS Schottky contact is essential to device operation (as a diode). Hence, photocatalytic anodes are minority carrier devices (where one seeks to maximize J_p above J_n) and MS Schottky diodes are majority carrier devices (where one seeks to maximize J_n above J_p, for an n-type semiconductor).

Non-radiative Recombination of Carriers at the Interface. Interfacial trap states (and/or surface states) usually act as recombination centres, where electrons and holes recombine non-radiatively (as illustrated in Fig. 5.2c). The non-radiative dynamics of these states at the surface can be captured by additional surface recombination velocity terms for electrons ($v_{ss,n}$) and holes ($v_{ss,p}$). For example, $v_{ss,p}$ can be defined as[74–76, 186]

$$v_{ss,p} = \frac{R_{ss}}{p_s}, \tag{5.20}$$

where p_s is the surface hole concentration (per unit volume) and R_{ss} is the trap-assisted surface recombination rate per unit area. We can arrive at a definition for R_{ss} by starting with the non-radiative Schokley-Read-Hall (SRH) recombination expression[73, 74]

$$R_{SRH} = N_T \frac{\sigma_n \sigma_p v_{th,n} v_{th,p} \left(np - n_i^2\right)}{\sigma_n v_{th,n} \left(n + n_T\right) + \sigma_p v_{th,p} \left(p + p_T\right)}. \tag{5.21}$$

Here, N_T is the volume density of the trap states, $v_{th,n}$ and $v_{th,p}$ are the electron and hole thermal velocities, σ_n and σ_p are the electron and hole capture cross sections, and n_i is the intrinsic carrier concentration. Moreover, $n_T = n_i exp\left(\frac{E_T - E_i}{k_B T}\right)$ and $p_T = n_i exp\left(\frac{E_i - E_T}{k_B T}\right)$ respectively represent the concentrations of electrons and holes if the semiconductor Fermi-level falls at E_T, where E_T is the energy of the trap state and E_i is the intrinsic Fermi-level. Furthermore, electron and hole capture lifetimes can also be recognized as $\tau_{n0} = \frac{1}{N_T \sigma_n v_{th,n}}$ and $\tau_{p0} = \frac{1}{N_T \sigma_p v_{th,p}}$.[83] Now non-radiative recombination at the surface (R_{ss}) can be derived by modifying the SRH expression presented in Eq. (5.21).[74–77] This is accomplished by replacing n and p respectively with their surface quantities n_s and p_s and N_T with N_s. Here, N_s is the arial density of the trap states within a very short distance $\sim \Delta_x$ from the surface and taken as the mean value of $N_T\Delta_x$.[74] After these substitutions, R_{ss} takes the following form

$$R_{ss} = N_s \frac{\sigma_n \sigma_p v_{th,n} v_{th,p} \left(n_s p_s - n_i^2\right)}{\sigma_n v_{th,n} \left(n_s + n_T\right) + \sigma_p v_{th,p} \left(p_s + p_T\right)} = \Delta_x R_{s,SRH}, \tag{5.22}$$

where $R_{s,SRH}$ is the SRH recombination at the surface of the semiconductor. A full derivation of Eq. (5.22) can be found elsewhere.[74] Using the value of R_{ss} in Eq. (5.20), we arrive at

$$v_{ss,p} = \Delta_x \frac{R_{s,SRH}}{p_s}. \tag{5.23}$$

Likewise, the electron surface recombination velocity can be expressed as

$$v_{ss,n} = \Delta_x \frac{R_{s,SRH}}{n_s}. \tag{5.24}$$

Now, in our approach, we utilized Eqs. (5.23) and (5.24) to model the interfacial non-radiative recombination, whereas the non-radiative recombination at the bulk was modeled by Eq. (5.21).

Radiative Recombination of Carriers at the Interface. Finally, direct band-to-band recombination (see Fig. 5.2d) can also take place and reduce carrier concentrations at the surface, particularly if the semiconductor is a direct band-gap material.[83, 122] By utilizing a similar physical representation to that given by Eq. (5.23), for the non-radiative surface hole recombination process, we can also define the radiative recombination velocity for holes at the surface as

$$v_{rad,p} = \Delta_x \frac{R_{s,rad}}{p_s}. \tag{5.25}$$

Here $R_{s,rad}$ is the radiative recombination at the surface and is given by[32, 83, 103, 109]

$$R_{s,rad} = B_{rad} \left(n_s p_s - n_i^2\right), \tag{5.26}$$

where B_{rad} is the bimolecular recombination coefficient.[83,103] Similarly, radiative recombination velocity ($v_{rad,n}$) for electrons at the surface can be expressed as

$$v_{rad,n} = \Delta_x \frac{R_{s,rad}}{n_s}. \tag{5.27}$$

In this work, we used Eq. (5.25) and Eq. (5.27) to model the interfacial radiative recombination. On the other hand, bulk radiative recombination (R_{rad}) inside of the semiconductor is modeled in this work by $R_{rad} = B_{rad}\left(np - n_i^2\right)$ — which is the bulk form of Eq. (5.26).

Discretized Continuity Equations at the Semiconductor-Liquid Interface. We have now mathematically defined all the key interfacial generation-recombination processes that might impact upon interfacial charge flow at a SL junction. Our next step is to discretize Eqs. (5.3) and (5.4) by formulating boundary conditions for the electron and hole continuity equations at SL junctions, in a similar manner to what was done in Section 5.2.2 for MS junctions. To discretize Eq. (5.4) at the interface of a typical SL junction ($i = N$ in Fig 5.1d), one may utilize a similar analysis to that which provided Eq. (5.18) from Eq. (5.2) in the MS junction discretization. For the hole continuity equation, this would result in the discretized SL junction boundary condition of the form

$$\begin{aligned}
&\frac{\mu_{p|N-1/2}}{\Delta_{N-1}}\left[p_{N-1}B\left(\frac{\phi_N-\phi_{N-1}}{V_T}\right) - p_N B\left(\frac{\phi_{N-1}-\phi_N}{V_T}\right)\right] \\
&= \frac{\Delta_{N-1}}{V_T}\left[\frac{v_{t,p}(p_N - p_{s0}) + v_{ss,p}p_N + v_{rad,p}p_N}{\Delta_{N-1}} - G_{h\nu|N}\right] \\
&= \frac{\Delta_{N-1}}{V_T}\left[R_{p|N} - G_{p|N}\right],
\end{aligned} \tag{5.28}$$

where $G_{p|N}$ and $R_{p|N}$ respectively represent all the interfacial generation and recombination processes discussed so far. Finally, the surface hole concentration at steady-state is expressed as

$$p_N = \frac{\left[\mu_{p|N-1/2} B(\frac{\phi_N - \phi_{N-1}}{V_T})\right] p_{N-1} + \frac{\Delta_{N-1}}{V_T} v_{t,p} p_{s0} + \frac{\Delta_{N-1}^2}{V_T} G_{h\nu|_N}}{\mu_{p|N-1/2} B(\frac{\phi_{N-1} - \phi_N}{V_T}) + \frac{\Delta_{N-1}}{V_T} \left(v_{t,p} + v_{ss,p} + v_{rad,p}\right)}. \tag{5.29}$$

Now if a semiconductor-liquid junction simultaneously allows electrons and holes to be transferred to the liquid, which might be the case for a practical junction, we need allow the electron current continuity equation boundary condition to float as well. Following a similar analysis for electrons, we arrive at the below SL junction boundary condition for the discretized electron continuity equation

$$\begin{aligned} &\frac{\mu_{n|N-1/2}}{\Delta_{N-1}} \left[n_{N-1} B\left(\frac{\phi_{N-1} - \phi_N}{V_T}\right) - n_N B\left(\frac{\phi_N - \phi_{N-1}}{V_T}\right)\right] \\ &= \frac{\Delta_{N-1}}{V_T} \left[\frac{v_{t,n}(n_N - n_{s0}) + v_{ss,n} n_N + v_{rad,n} n_N}{\Delta_{N-1}} - G_{h\nu|N}\right]. \end{aligned} \tag{5.30}$$

Finally, the surface electron concentration at steady-state can be expressed as

$$n_N = \frac{\left[\mu_{n|N-1/2} B(\frac{\phi_{N-1} - \phi_N}{V_T})\right] n_{N-1} + \frac{\Delta_{N-1}}{V_T} v_{t,n} n_{s0} + \frac{\Delta_{N-1}^2}{V_T} G_{h\nu|_N}}{\mu_{n|N-1/2} B(\frac{\phi_N - \phi_{N-1}}{V_T}) + \frac{\Delta_{N-1}}{V_T} \left(v_{t,n} + v_{ss,n} + v_{rad,n}\right)}. \tag{5.31}$$

It is imperative to note that Eqs. (5.28) and (5.30) represent *Neumann*-type boundary conditions, allowing the interfacial concentrations of holes and electrons to float and thus revealing the pseudo-Schottky character of the photocatalytic interface.

Boundary Conditions for Modeling the Photovoltage

Origin of the Photovoltage. To correctly model the photovoltage (a thermodynamic quantity arising due to electron-hole pair generation), it is imperative that both the electron and hole continuity equations be solved simultaneously. To understand this, let us begin by considering the generation process of the open-circuit voltage (V_{oc}), also known as the photovoltage when no external bias is applied (V=0).[2,67] First consider an anodic SL junction under equilibrium (without any light illumination) as

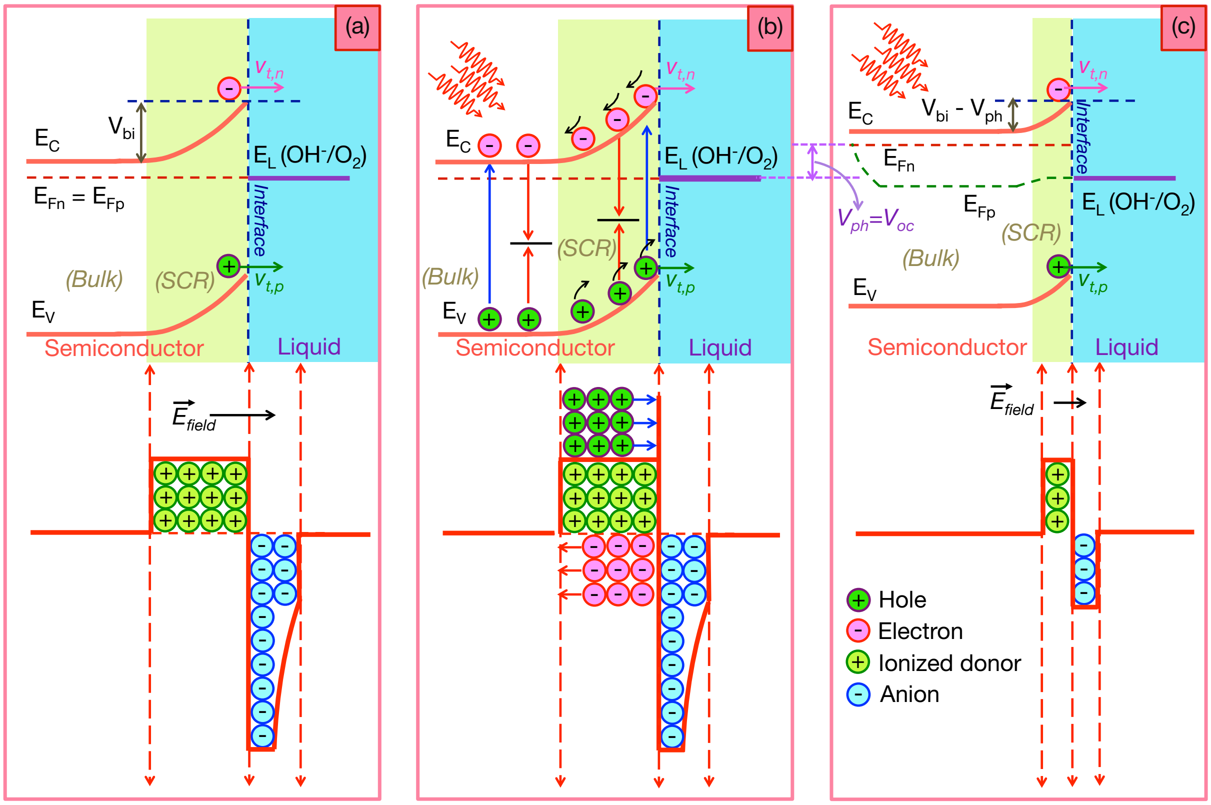

Figure 5.3: Photovoltage generation processes at a typical illuminated photoanode-liquid junction without any externally applied bias (V=0). (a) Equilibrium band alignment of the electrode, clearly illustrating the interface, SCR and bulk regions. Exposed ionized donors compensated by screening electrolyte ions in the SCR provide the depletion region electric field ($\vec{E}_{field}$). (b) Processes at the same photoanode occurring immediately after illumination, highlighting several interfacial and SCR generation-recombination processes. The photogenerated electrons and holes travel in opposite directions inside SCR due to the influence of $\vec{E}_{field}$. (c) Steady-state band diagram of the illuminated photoanode showing band flattening due to photovoltage generation and depicted by a reduction in the built-in potential (V_{bi}). Simultaneously, $\vec{E}_{field}$ weakens as the depletion region shortens.

shown in Fig. 5.3a. Here, we assumed that the photoanode is robust against corrosion and only exchanges electrons/holes with OH$^-$/O$_2$ redox species. Meaning, we assume the existence of an equilibrium condition where the Fermi-levels of electrons (E_{Fn}) and holes (E_{Fp}) are equivalent and aligned with the liquid Fermi-level (E_L), which is determined solely by OH$^-$/O$_2$ redox species.[32] However, a practical photocatalytic interface is prone to multiple possible electrochemical reactions including undesirable corrosion of the photoelectrode.[1,34] Therefore, future extensions of semiclassical modeling in this direction should include the impact of corrosion reactions on band alignments.

Now, under equilibrium as shown in Fig. 5.3a, the semiconductor space-charged-region (SCR) exhibits a net positive charge due to ionized donors (arising from downward band bending). The resulting electric-field ($\vec{E}_{field}$) within the SCR points toward the liquid (as marked in Fig. 5.3a). Immediately after the semiconductor is exposed to sunlight, electron-hole pairs are generated and driven in opposite directions by the electric-field. Electrons travel towards the Ohmic back contact, while holes travel towards the photocatalytic interface (see Fig. 5.3b). Thus both the electron and hole concentrations change substantially in the illuminated SCR, requiring that both the electron and hole continuity equations be solved simultaneously to capture the photovoltage. To accomplish this the bulk carrier concentrations are utilized as Dirichlet boundary conditions in the interior of the semiconductor, while the floating Neumann boundary conditions developed in Section 5.2.3 are utilized at the SL-interface as illustrated in Fig. 5.1b — for the electron and hole continuity equations. Importantly, this migration of photogenerated carriers, determined by their local concentrations and electrostatic fields (or quasi-Fermi levels), induces the photovoltage (which acts as an effective forward potential) on the semiconducting electrode.[33,36] The end result is a partial or even complete suppression of the electric-field in the SCR or equivalently the built-in voltage, V_{bi} (compare Figs. 5.3b and 5.3c).[36,130] This is shown in Fig. 5.3c, where our illuminated junction demonstrates a photovoltage (V_{ph}) and reduced band bending from $\sim V_{bi}$ under steady-state conditions.

Boundary Conditions for Poisson's Equation. We adopted a standard discretization technique for solving Poisson's equation to arrive at the electrostatic potential ϕ, and have incorporated a spatially varying dielectric constant across the SL junction as discussed in our earlier work.[188] In this manner, the potential drop inside the liquid (primarily comprised of the Helmholtz layer charges) is allowed to change as a function of surface state charging, semiconductor doping and the applied bias.[188] This enables one to capture both pinning and unpinning of the semiconductor band-edges at the solid-liquid interface. Now, in order to model the movement of semiconductor bands under illumination (compare Fig. 5.3a and Fig. 5.3c) and the generation of V_{ph}, it is imperative that one allow the conduction and the valence bands at the bulk of the electrode to float when self-consistently solving the Poisson equation. This can be implemented by setting a *Neumann*-type boundary condition on ϕ (defined as the potential of the local vacuum level) at the Ohmic back contact (see Fig. 5.1d), which also enforces $\vec{E}_{field} = 0$ in the bulk of the electrode. On the other hand, to guarantee a unique potential solution, a *Dirichlet*-type boundary condition on ϕ also needs to be implemented in the bulk of the liquid (at $i = M$ in Fig. 5.1d). This is accomplished by considering ϕ at $i = M$ of the grid to take some pre-defined reference value. In our case, we have assumed ϕ in the bulk of the liquid to be zero.

5.3 Results

5.3.1 Modeling a Metal-Semiconductor Schottky Junction

As stated in the introduction, it is the objective of this work to extend the device modeling techniques developed for MS Schottky junctions into the domain of SL pseudo-Schottky junctions. Thus we begin our analysis by briefly demonstrating that our methodology can capture the majority and minority carrier electrostatics of MS junctions, by numerically solving the complete drift-diffusion equations utilizing the boundary conditions derived in Section 5.2.2. The primary goal of this analysis is to verify that the implementation procedure discussed in our present work can capture the electrostatics and carrier transport of an MS Schottky junction – which has been well explored in the device physics literature.[89, 158, 159, 190, 191] Particular attention will

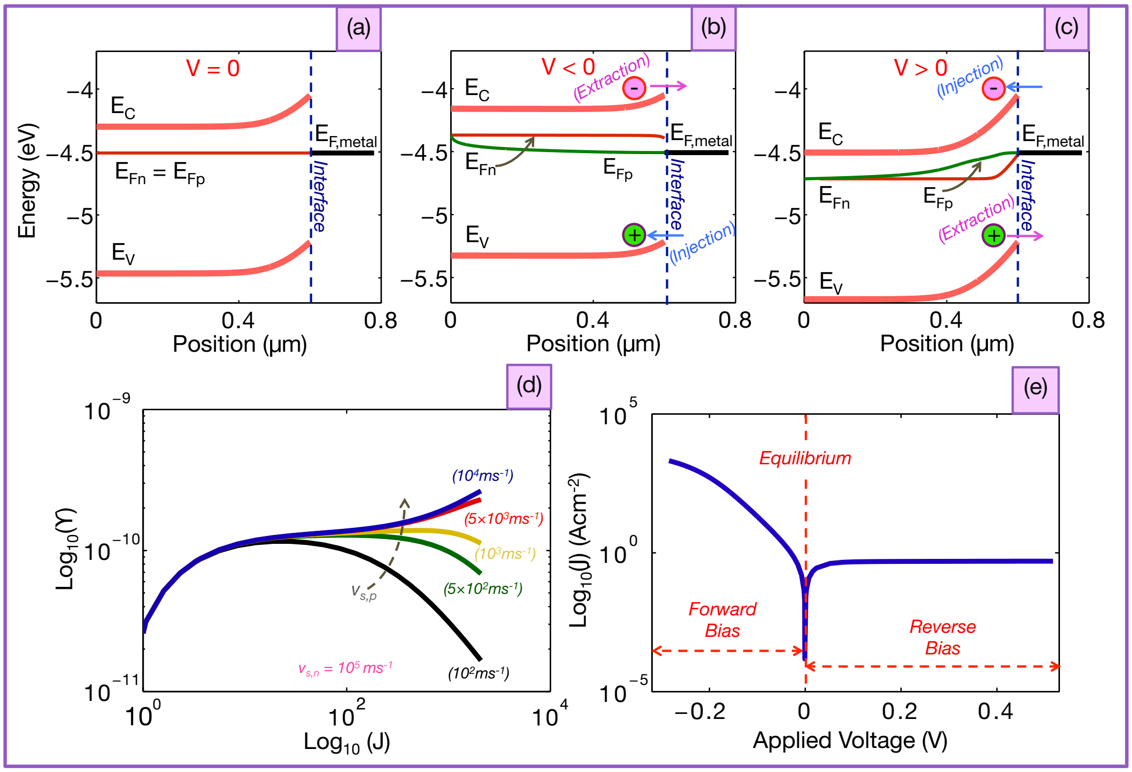

Figure 5.4: Self-consistently calculated electrostatics and charge transfer kinetics of an n-type Si-metal Schottky junction. (a) Unbiased ($V = 0$) band alignment with the demonstration of a flat Fermi-level ($E_{Fn} = E_{Fp} = E_{F,metal}$). The Si-metal interface is characterized by the formation of $\sim$ 0.45 eV Schottky barrier. (b) Band diagram under forward bias ($V < 0$) showing the extent of electron extraction and hole injection due to finite electron and hole recombination velocities. The quasi Fermi-level of electrons (E_{Fn}) moves away from E_C due to interfacial electron extraction, whereas the quasi Fermi-level of holes (E_{Fp}) equilibrates with $E_{F,metal}$ due to interfacial hole injection. (c) Band diagram under reverse bias ($V > 0$) illustrating injection of electrons into the conduction band and the extraction of valence band holes. (d) Calculated injection ratio defined as the hole current density over the total current density, drawn with respect to the forward bias current density. (e) Calculated total interfacial current density clearly showing the rectifying nature of a typical MS Schottky junction.

be given to modeling the transport of minority carriers due to its importance in photocatalytic semiconductor-liquid junctions, which is the ultimate goal of our present work.

As our model system, we have considered a Schottky junction between n-type Si, doped at a density of $N_D = 10^{16}$ cm^{-3}, and a corresponding metal contact with a work function (Φ_m) of $\sim$ 4.5 eV. The junction is situated in the dark and has no recombination or generation terms, apart from the interfacial electron transfer velocities across the MS junction as discussed in Section 5.2.2. All material dependent parameters were set at standard Si-based semiconductor simulation values as discussed in Ref.122. The calculated energy band diagram (presented in Fig. 5.4a) demonstrates equilibration between the electron quasi Fermi-level (E_{Fn}), hole quasi Fermi-level (E_{Fp}), and metal contact ($E_{F,metal}$) Fermi-level. From Fig. 5.4a we can see that the metal-Si junction forms a Schottky contact with a barrier height of $\sim$ 0.45 eV. To model the electron and hole transport across this junction, we have assumed initial interfacial transfer velocities of $v_{s,n} = 10^5$ ms^{-1} and $v_{s,p} = 10^4$ ms^{-1}, typical for Si.[192] Importantly, this equilibration process (unbiased) physically represents zero net electron (majority) transfer *via* the conduction band, as well as zero net hole (minority) transfer *via* the valence band, which is formally defined by both Eqs. (5.1) and (5.2) falling to zero. However, even for MS Schottky junctions the process of the interfacial charge transfer become rather complicated when the junction is biased from $V = 0$ to $|V| > 0$ — which we will explore next.

The concept of electron/hole extraction and injection at the metal-semiconductor interface is particularly helpful in order to understand the nature of carrier transport at a Schottky contact. In general, the extent of the electron/hole extraction and injection processes is such that the junction tends to work to restore the equilibrium carrier concentrations (n_{s0} and p_{s0}) even under applied bias. It is important to explore this for a MS Schottky contact, because similar processes are at work in SL pseudo-Schottky junctions. To understand what happens in a MS contact, let us consider the calculated band digram under forward bias condition ($V < 0$) as illustrated in Fig. 5.4b. Here V denotes the externally applied potential attached to the n-type Si electrode, whereas the metal electrode is assumed to be grounded (reference potential). However, as is customary in the device physics literature,[33] our MS Schottky junction band diagrams are drawn with respect to the vacuum level (0 eV). Now, the steady-state calculation with a non-zero electron recombination velocity, as presented in Fig. 5.4b, shows that the electron quasi Fermi-level (E_{Fn}) at the interface shifts downward or away from the conduction band edge (E_C) due to the transfer and subsequent relaxation of injected conduction band electrons on the metal side. In practice, E_{Fn} always tends to approach $E_{F,metal}$ with relatively small values of $v_{s,n}$ and the contact displays Schottky-type behavior. With a very high value of $v_{s,n}$, E_{Fn} perfectly restores its equilibrium with $E_{F,metal}$ even under forward bias and the contact becomes Ohmic in character. However, in the case of hole transfer, the contact behaves oppositely under forward bias ($V < 0$) by injecting holes to the semiconductor valence band from the metal side (see Fig. 5.4b) and eventually aligning the hole quasi Fermi-level (E_{Fp}) with $E_{F,metal}$ with moderate/high values of $v_{s,p}$. Likewise, by reversing the bias-direction ($V > 0$) n-type Si undergoes the injection of electrons and the extraction of holes as shown in Fig. 5.4c, which can be explained in a similar manner.

The results in Figs. 5.4a through 5.4c, showing the evolution of $E_{F,n}$ and $E_{F,p}$, match well with results from the device physics literature regarding minority carrier transport through a Schottky contact.[193–195] To further verify that our implementation captures the physics of minority carrier transport (a necessary property for modeling SL pseudo-Schottky contacts), we have calculated the injection ratio (Υ) in Fig. 5.4d. It is defined as the ratio of the hole current to the total current ($\Upsilon = |J_p|/|J_p + J_n|$) under forward bias.[196] In general, the injection ratio depends on the applied bias and the energy of the Schottky barrier. Under forward bias, Υ rises with the forward current.[196,197] Using practical values of $v_{s,n}$ and $v_{s,p}$ for Si,[192] our method reproduces uprising trend for Υ with respect to the total current as illustrated by the blue and red curves in Fig. 5.4d. Importantly, if one gradually reduces $v_{s,p}$ (while maintaining $v_{s,n}$ at a fixed value) the contact should become more ‘electron-selective’ resulting in a reduced injection ratio with increasing bias (or current flow). This is precisely what is demonstrated in Fig. 5.4d as $v_{s,p}$ is decreased from 10^4 m/s to 10^2 m/s. Thus, we have demonstrated that our approach captures the necessary minority carrier physics, an important prelude to evaluating SL pseudo-Schottky contacts which are dominated by minority carrier transport. Finally, the calculated current density (as shown in Fig. 5.4e) exhibits the rectifying character of a typical Schottky contact and can be compared with numerous current-voltage characteristics present in the device physics literature.[89,158,159,190,191]

5.3.2 Modeling a Semiconductor-Liquid pseudo-Schottky Junction

Let us now simultaneously solve for the photocurrent and photovoltage of a typical SL pseudo-Schottky junction, obtained by self-consistently solving the complete drift-diffusion equations with the boundary conditions derived in Section 5.2.3. As our model system, we have selected an n-type hematite ($\alpha-\mathrm{Fe_2O_3}$) photoanode performing water oxidation.[68] Hematite has been widely investigated for photocatalytic water splitting due to its inexpensive constituent elements and suitable band-gap that lies between 1.9 eV - 2.2 eV (absorbing wavelengths 560 nm - 660 nm or less in the solar spectrum).[1,60,198] However, its characteristic small-polaron carrier transport and sluggish hole transfer kinetics make hematite-based water splitting highly challenging.[62,69,199,200] Moreover, a practical hematite photoanode may undergo electronic band unpinning at the solid-liquid interface, due to surface charge accumulation through the formation of reaction intermediates.[127] Despite these practical challenges, recent theoretical studies have demonstrated the utility of semi-classical models in exploring hematite-based water splitting electrodes.[32,125] Thus, we also apply our semi-classical methodology to theoretically explore hematite photoanodes with the aim of extracting key electrostatics and charge transfer kinetics present in the

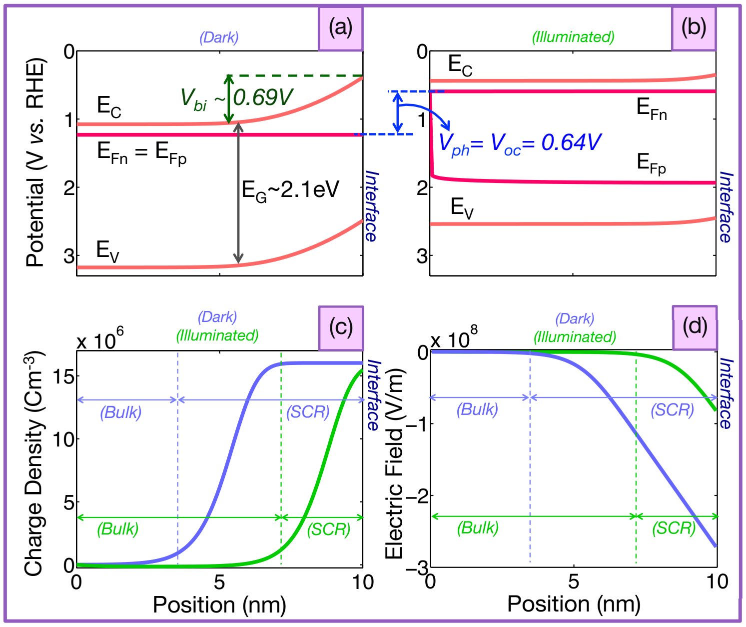

Figure 5.5: Self-consistent calculation of the photovoltage in an illuminated n-type hematite-water junction (pH=13.6). A band-gap of ∼ 2.1 eV is assumed. Calculated energy band diagram of an unbiased hematite photoanode under (a) dark and (b) 0.33 sun illumination. As can be seen, most of the built-in potential (∼ 0.69 V) is suppressed by the generated photovoltage (∼ 0.64 V). (c) Corresponding, depleted donor charge densities under dark (in blue) and 0.33 sun illumination (in green), where the illuminated hematite surface exhibits a dramatically shortened space-charged-region due to band-flattening by the induced photovoltage. (d) Calculated $\vec{E}_{field}$ inside hematite electrode under dark (blue) and solar irradiation (green).

literature.[68] Throughout our simulation, we considered a hematite photoanode with a band-gap (E_G) of ∼2.1 eV[32] and a doping density of $N_D \sim 10^{20}$ cm^{-3}[68, 115, 201–203] immersed in an aqueous solution of pH=13.6.[68] To calculate the potential of the working electrode, we assumed a reversible hydrogen electrode (RHE) as the reference electrode. This part of our discussion is split into two segments dedicated to the self-consistent calculation of the photovoltage and the calculation of the photocurrent, respectively.

Self-consistent Calculation of the Photovoltage

The first part of our analysis is aimed at verifying that the boundary conditions developed in Section 5.2.3 capture semiconductor band flattening due to the generation of a photovoltage.[20,21,36,71] Let us start by considering Fig. 5.5a, which displays the calculated equilibrium band diagram of the hematite photoanode. To enable a direct correlation between electrostatics and current-voltage properties, our calculated SL junction band diagrams are drawn with respect to RHE rather than the vacuum level – this involves a shift of -4.44 eV below the standard vacuum potential reference energy commonly found in the device physics literature.[32,33,129] Under equilibrium, the electrode is depleted of electrons (see also Figs. 5.5c and 5.6a), characterized by a built-in potential of $\sim$ 0.69 V and displayed a flat Fermi-level aligned at 1.23 V *vs.* RHE. Equivalently, our calculation corresponds to a flat-band potential (V_{fb}) of $\sim$ 0.54 V *vs.* RHE, which falls inside the experimentally determined flat-band potential (between 0.4 V - 0.55 V *vs.* RHE) for hematite photoanodes as reported in the literature.[70,147,202] Now, as discussed in Section 5.2.3, this simple picture of equilibration assumes the phototanode is only capable of exchanging electrons/holes with OH^-/O_2 redox species. Thus, this idealized situation should be replaced by a complicated non-equilibrium open-circuit condition if the electrode is prone to corrosion or allowed to exchange electrons/holes with other species present in the liquid.[1,34]

Now, if we begin from a depleted picture of the hematite surface under equilibrium (as presented in Fig. 5.5a), to maximize band flattening upon photoexcitation one would require good majority carrier conduction as well as a lengthened minority carrier lifetime.[1] However, both of these prerequisites are undermined by hematite due to: (1) its characteristic 'small polaronic' conduction mechanism[199]; and (2) high rates of non-radiative recombination.[204] In this regard, surface modification techniques (including nanostructuring of hematite electrodes) can improve the harvesting of photogenerated electrons and holes by partially suppressing detrimental recombination process and partially enhancing interfacial charge transfer kinetics.[17,21] However, the standard experimental procedure to analyze the performance of a photoanode is to probe the corresponding hole relaxation process by analyzing transient absorption (TA) spectra. For instance, the TA spectra of a nanostructured hematite electrode reported by Barroso *et al.*[69] suggest that the rapid electron-hole recombination in the bulk of the hematite photoanode can be assigned to the part of the spectra that decays at a scale of micro- to milli-seconds (known as 'fast-decay'). Nevertheless, other studies assigned the photogenerated hole relaxation time at the bulk of hematite in between 10ps - 100ps.[199,205] However, in accordance with Ref.70, we have adopted a carrier lifetime of $\tau_{p0} = \tau_{n0} = 1\mu$s to represent the trap-assisted bulk recombination of carriers. We also have assumed that all trap-states are located at the energy of the intrinsic Fermi-level ($E_T = E_i$), as well as $v_{th,p} = v_{th,n} = 10^5$ ms^{-1} and $\sigma_n = \sigma_p = 10^{-24}$ m^2.[74] On the other hand, to focus on the minority carrier physics, the electron transfer velocity ($v_{t,n}$) between the semiconductor and liquid was assumed to be zero. Whereas, the hole transfer velocity ($v_{t,p}$) was given the value $\sim 10^{-9}$ ms^{-1}, typical for hematite electrodes.[62,63,70,99] The value of $v_{t,p}$ can be estimated from the reported interfacial hole transfer rate (10-0.1 s^{-1})[62,70,99] and hole diffusion distance (2-4 nm)[63] at the surface of hematite photoanodes. In addition, we also assumed that the electron and hole transfer rates are mutually independent and remain constant irrespective of any external excitation (applied bias or light intersity).

Now, to produce a photovoltage the hematite electrode was theoretically set to $\sim$ 0.33 sun of solar irradiation ($\alpha \sim$ 1.5$\times$ 10^7 m^{-1}), for which the calculated band diagram is given in Fig. 5.5b.[68] As can be seen, the calculated band diagram under illumination exhibits almost complete flattening of the hematite bands by generating $V_{ph} \approx 0.64$ V. Moreover, the calculated exposed donor charge densities and electric-field inside the semiconductor depletion region under dark (marked in blue) and illuminated (marked in green) conditions are also shown in Fig. 5.5c- 5.5d, respectively. As expected from our earlier discussion, the SCR region under illumination shortens substantially, since V_{ph} effectively acts as a photo-induced forward potential.[21] This also underscores the importance of simultaneously solving both the electron and hole continuity equations to compute the photovoltage, as the exposed donor density is reduced through a photo-induced increase in the electron density in the SCR (see Fig. 5.6a).

Thus far we have only discussed the numerically computed electrostatics (band bending) associated with V_{ph} generation in the absence of any external bias. However, in practice, photovoltage generation also takes place under an externally applied bias[84] and can also be computed self-consistently using our approach. Next we wish to address to what degree can our approach capture: (1) the charge transfer kinetics (i.e. the dynamics of short- and long-lived holes,[68,70,99] the impact of the interfacial hole transfer rate,[62] etc.); and (2) the experimentally observable photocurrent (i.e. current on-set, saturation and the impact of the incident light intensity[20,68,71]).

Charge Transfer Kinetics and the Photocurrent

As discussed earlier, our approach is based on solving both the electron and hole continuity equations simultaneously. This means that we can capture the modulation of the majority carrier concentration along with the minority carrier concentration by solar irradiation in SL pseudo-Schottky junctions — a crucial physical ingredient often ignored[32] or not fully derived[82,103] in state-of-the-art photocatalytic interface simulations. In general, the majority carrier population of a depleted photoelectrode is modified under illumination and capturing this process is critical to the development of PEC device physics simulations.[36,37]

Fig. 5.6a juxtaposes the spatial distribution of electrons and holes under dark and illuminated conditions (with no external bias), calculated using the methodology discussed in this work. The dark carrier concentrations (marked in blue in Fig. 5.6a) indicate the presence of a strongly depleted semiconductor surface, with a long SCR and strong electric-field as shown in blue in Fig. 5.5d. We have already examined the

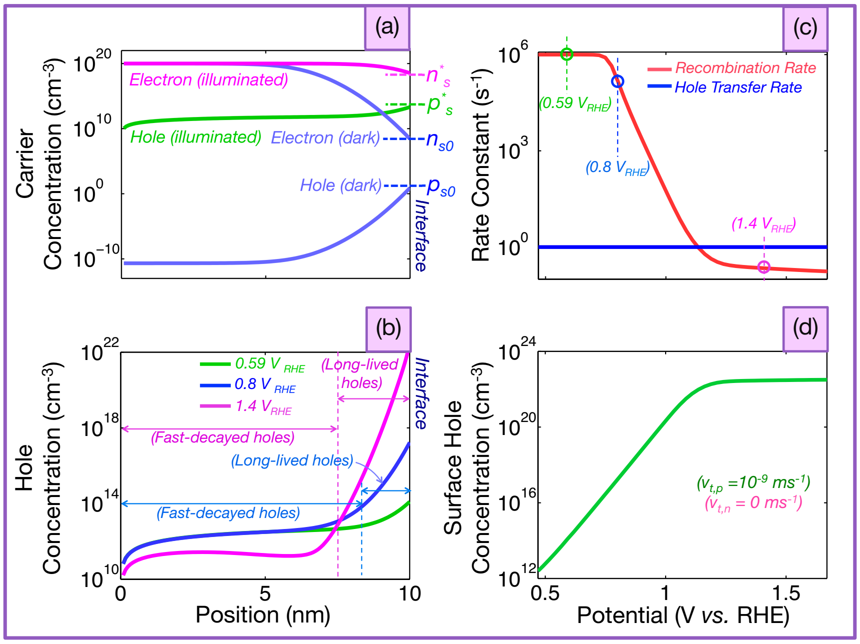

Figure 5.6: Calculated charge transfer kinetics of an n-type hematite-liquid junction. (a) Spatial distribution of the electron and hole densities of an unbiased junction under dark (marked in blue) and 0.33 sun illumination (pink and green, respectively). When dark, the hematite electrode demonstrates an electron-depleted surface, while under illumination both electron and hole concentrations are increased. (b) Calculated spatial distribution of holes inside an illuminated hematite photoanode under zero (0.59 V *vs.* RHE and in green), small (0.8 V *vs.* RHE and in blue) and large (1.4 V *vs.* RHE in pink) applied reverse potential. Photogenerated holes start to accumulate in the semiconductor SCR as the extent of the bias is increased. These holes with longer lifetimes are detected as 'long-lived' holes in practical TA experiments. (c) Comparison of rate of recombination (marked in red) and rate of interfacial hole transfer (marked in blue) with applied reverse bias demonstrating the suppression of hole SCR recombination. As the photogenerated holes become less vulnerable to recombination in the SCR, the photoanode exhibits higher yield of solar-to-chemical fuel conversion. (d) Evolution of the surface hole density under an applied reverse bias demonstrating the incremental trend (due to the gradual suppression of recombination) and saturation (due to the minimized recombination rate with respect to the interfacial hole transfer rate).

net SCR charge distribution under this particular operating condition in Fig. 5.5c. Now, upon illumination the hole concentration (marked in green) as well as the electron concentration (marked in pink) are spatially modulated as shown in Fig. 5.6a. In this case, the steady-state electron concentration at the illuminated junction is increased from its dark condition value, specifically near the interface. This is due to the strong initial electric-field (see Fig. 5.5d) that efficiently separates the photogenerated electron-hole pairs immediately after the electrode is illuminated. Throughout this simulation, the illuminated electron surface concentration (n_s^*) is optimized for the hole-driven water oxidation reaction by deliberately making the interface opaque to conduction band electron transfer to the liquid ($v_{t,n} = 0$). Fundamentally, these excess electrons now can either contribute constructively to V_{ph} by traveling towards the back Ohmic contact or degrade V_{ph} by participating in recombination with the available photogenerated holes.

Further degradation of V_{ph} can occur if the interface hole transfer velocity becomes sluggish enough (which is true for hematite) so that surface holes (p_s^*) are more likely to annihilate in recombination processes. In practice, the experimental procedure to probe this complex charge transfer kinetics requires analyzing standard TA spectra such as that reported in Refs. 69 and 70. The situation, as shown in Fig. 5.5b where hematite photoanode is operated close to the flat-band potential (precisely, at 0.59 V *vs.* RHE), corresponds to the 'fast-decay' portion of the TA spectrum due to the rapidly occuring trap-assisted recombination of phototgenerated holes. This can be verified in experiment by comparing the rate of recombination with the rate of interfacial hole transfer.[62, 70, 99] In this case, as the interfacial hole transfer in hematite is extraordinarily slow, the fate of the photogenerated holes is primarily decided by the bulk/SCR recombination process. Our calculation of recombination rate and interfacial hole transfer rate, as plotted in Fig. 5.6c, also demonstrates that a majority of the photogenerated holes undergo undesirable recombination with electrons at 0.59 V *vs.* RHE and as a consequence, the steady-state surface concentration of holes reaches as low as $\sim 6{\times}10^{12}$ cm^{-3} (see Fig. 5.6a and 5.6d).

However, the hole relaxation lifetime, from this nearly flat-band picture of the electrode, can be improved if the applied bias is increased in the reverse direction ($V > 0$). As our computation shows (see Fig. 5.6c), for electrode potential of 0.72 V *vs.* RHE

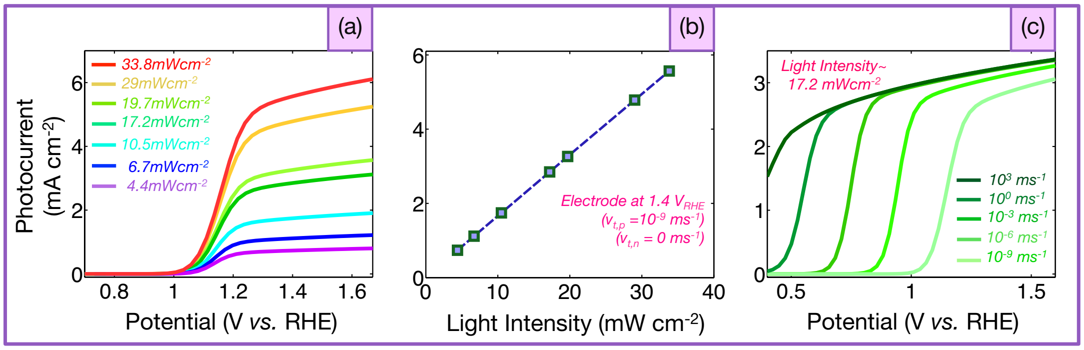

Figure 5.7: (a) Calculated photocurrents under different light intensities (4.4 $\text{mWcm}^{-2} \rightarrow 33.8\ \text{mWcm}^{-2}$), clearly demonstrating the experimental trend of photocurrent on-set, transition and saturation. The on-set potential of the photocurrents can be estimated to be slightly anodic to 1 V *vs.* RHE, whereas the saturation occurs at potential anodic to 1.3 V *vs.* RHE. (b) Photocurrent density with respect to the illumination intensity. In this case the linear dependency of the photocurrent with respect to illumination intensity is correlated with a slope of 0.170 mA mW^{-1}. (c) Impact of the interfacial hole transfer rate on the photocurrent. With faster hole transfer, the solar-to-chemical conversion yield improves by shifting the photocurrent in the cathodic direction.

and above, the reverse bias gradually suppresses interfacial recombination and restores the electric-field inside SCR. To gain further insights, we also have calculated (as shown in Fig. 5.6b) the evolution of spatial hole distribution under zero (0.59 V *vs.* RHE), small (0.8 V *vs.* RHE) and large (1.4 V *vs.* RHE) reverse potentials. As can be seen, photogenerated holes start to accumulate at the surface with increasing potential due to the gradual suppression of SCR recombination. These holes with a prolonged lifetime are commonly detected as 'long-lived' holes (τ_p = 0.1 - 10s) in TA measurements.[69, 70] Eventually, at a sufficiently strong reverse bias, as in our case ∼ 1.2 V *vs.* RHE and beyond, the hole recombination rate falls below the interfacial hole transfer rate (as shown in Fig. 5.6c). Afterwards the surface concentration of hole primarily depends on the hole transfer/extraction rate and becomes saturated if $v_{t,p}$ remains constant (see Fig. 5.6d). All of these results (Fig. 5.6b - 5.6d) are in agreement with the complex charge transfer kinetics observed in hematite-based PEC experiments.[62, 69, 70, 99]

Our final goal is to translate our calculated charge transfer kinetics into an interfacial photocurrent (J_{ph}), such as that commonly observed in hematite-based PEC experiments.[20, 60, 68, 70, 99] The photocurrent can be calculated directly from Eqs. (5.3) and (5.4) using the self-consistent solutions of carrier concentrations provided by Eqs. (5.28) and (5.30) and then compared with the literature. In this regard, we have selected the photocurrent measurement of a hematite photoanode by Le Formal *et al.*[68] to our benchmark results. As can be seen from Fig. 5.7a, the calculated photocurrents under different solar irradiation (ranging from 4.4 $\mathrm{mWcm^{-2}}$ to 33.8 $\mathrm{mWcm^{-2}}$) are comparable with reported experimental photocurrents for hematite.[68] The on-set of our self-consistently computed photocurrents fall close to the experimentally determined onsets of ~ 1 V *vs.* RHE. Furthermore, our calculated photocurrents saturate at ~ 1.3 V *vs.* RHE whereas the practical electrodes demonstrate saturation from 1.3 V - 1.4 V *vs.* RHE.[68] Fig. 5.7b shows the evolution of photocurrent with respect to light intensity, when the potential of the hematite photoanode is held at 1.4 V *vs.* RHE. Moreover, the calculated photocurrents clearly exhibit a linear increase with a slope of 0.170 $\mathrm{mA\ mW^{-1}}$ with respect to illumination intensity (which compares well to the experimental value of 0.177 $\mathrm{mA\ mW^{-1}}$ in Ref. 68).

Finally, impact of the interfacial hole transfer velocity on the calculated photocurrent is also computed (see Fig. 5.7c). In this case, we self-consistently solved the charge transport of an hematite photoanode under a solar irradiation intensity of 17.2 $\mathrm{mWcm^{-2}}$ and modulated the interfacial hole transfer velocity ($v_{t,p}$) from $10^3 \rightarrow 10^{-9}$ $\mathrm{ms^{-1}}$. We recognize that the higher values of $v_{t,p}$ considered in Fig. 5.7c are well above the values expected for sluggish hole transfer (as is commonly observed in practical hematite-based PEC devices). Nevertheless, with increasing $v_{t,p}$ the electrode shows significant improvement through a shift in the on-set of photocurrent towards lower potentials (in the cathodic direction as shown in Fig. 5.7c) and thus delineating the route towards unassisted solar water splitting as explained in Ref. 20. Importantly, this trend qualitatively matches with the experimental results presented by Thorne *et al.*[62] where the enhancement of the on-set (cathodic shift of the photocurrent) is correlated with the improvement in hole transfer velocity brought about by surface modification techniques. Therefore, the theoretical results for hematite-based photoanodes calculated from our approach are in agreement with the experimentally extracted kinetics reported in the literature.

However, the aim of this work is to derive a theoretical/numerical framework that can simultaneously capture both photovoltage and photocurrent properties of SL pseudo-Schottky junctions, by self-consistently solving the electron and hole drift-diffusion equations in the presence of recombination and generation processes. Therefore, we shall leave a detailed kinetics study of the process driving solar-assisted water splitting incorporating other key semiconductors and further experimental comparisons for future work.

5.4 Conclusion

In this work we have presented a general theoretical and numerical method for simultaneously calculating the photovoltage and photocurrent at semiconductor-liquid junctions. The method was developed by building upon Schottky junction modeling techniques within the device physics literature utilizing the concept of an 'effective recombination velocity'.[89,158,159,190,191] The recombination velocity concept was extended to capture both charge transfer and recombination physics present at semiconductor-liquid interfaces and applied to the pseudo-Schottky junction formed by an anodic water-splitting semiconductor. This approach was implemented through the introduction of *Neumann* boundary conditions within the electron and hole continuity equations at the semiconductor-liquid interface. Moreover, it was shown that both the electron and hole continuity equations must be simultaneously solved to capture both the photovoltage and the photocurrent at a semiconductor-liquid interface. The electron continuity equation must be solved primarily to capture dynamic screening in the space charge region under the active illumination (which gives rise to the photovoltage) and/or external bias. The hole continuity equation must be solved, in parallel, primarily to capture the hole concentration at the reacting semiconductor-liquid interface (which gives rise to the photocurrent). These equations are, of course, coupled and the dynamics of their interaction is influenced by the various recombination mechanisms present — which are included in our approach. We then theoretically explored photovoltage generation and the key charge transfer kinetics leading to the photocurrent at hematite photanodes. This, in turn, exhibited the capability of our self-consistent numerical treatment to address the various mesoscopic charge transfer processes present at practical photocatalytic interfaces. In particular, the method was demonstrated to exhibit the scope to correlate theoretical work with observable quantities in practical PEC experiments, including: the photovoltage, on-set and saturation of the photocurrent, interfacial hole transfer and bulk hole relaxation, interfacial recombination, space-charge-region screening processes, and the suppression of back reactions. Future work shall focus upon conducting exhaustive comparisons with experiments to address the charge transfer properties that impact upon the performance of water-splitting oxide semiconductors (hematite, TiO_2, etcetera). More importantly, since our methodology can decouple interfacial processes from the processes in the space-charged-region, future theoretical work in this direction should be able to elucidate possible routes to engineer both interfacial and space-charge-region processes.

5.5 Acknowledgement

The authors would like to acknowledge the financial support from NSERC of Canada and FQRNT of Québec, and the computational resources provided by the Canadian Foundation for Innovation, CalculQuebec and Compute-Canada.

Chapter 6

The Impact of Boundary Conditions on Calculated Photovoltages and Photocurrents at Photocatalytic Interfaces

---

The content of this chapter is designed to provide a scientific discussion on the impact of the boundary conditions on the computation of the complete solutions of the coupled Poisson-continuity equations at the photocatalytic semiconductor-liquid junctions. By utilizing the results from the numerical simulations, it has been shown that a floating boundary condition for the electrostatic potential, facilitating the band flattening in the bulk, is needed to capture the photovoltage. Furthermore, it has been also demonstrated that the capture of photovoltage with appropriate boundary conditions is pivotal to reliably replicate the practical photocurrent and realistic band diagrams of the photocatalytic junctions.

This chapter is a reproduction of the article published in *MRS Communications*. The complete citation of the published article is:

Asif Iqbal and Kirk H. Bevan, The Impact of Boundary Conditions on Calculated Photovoltages and Photocurrents at Photocatalytic Interfaces, *MRS Communications*, 2018, 8(2), 466–473.

Abstract

This work presents an in-depth study of how the choice of boundary conditions can impact upon the calculated photovoltage and photocurrent in photoelectrochemical (PEC) devices. Utilizing a floating boundary condition for the electrostatic potential and pseudo-Schottky boundary conditions for the interfacial electron/hole currents, we show simultaneous calculation of photovoltage and photocurrent. We also explore the significance of capturing the photovoltage, with proper boundary conditions, to accurately replicate practical photocurrent along with the realistic band-alignments. Finally, our results decouple the interfacial hole transfer from the recombination at the interface/space-charged-region and suggest possible methods to engineer the mesoscopic transfer process at PEC-electrodes.

6.1 Introduction

The rising societal and environmental costs of fossil fuels have driven a resurgence of intense research into artificial photosynthesis.[1,4,12,160,187] Solar-driven water splitting using light-absorbing semiconducting electrodes can delineate a possible route towards solar-to-chemical fuel conversion.[71] Extensive ongoing research in this direction has outlined critical scientific problems that entail urgent resolution through combined theoretical and experimental efforts.[21,81,86,105,188] Nevertheless, inadequate understanding of the complex processes governing semiconductor photocatalysis significantly impedes progress towards cost competitive unassisted solar water splitting.[105]

Thus, device models exploring the mesoscopic charge transfer processes driving photocatalysis at semiconductor-liquid (SL) junctions can deliver fundamental insights into these processes and may provide more efficient PEC device designs.

The modeling of mesoscopic phenomena at semiconductor-liquid junctions comprises an long standing problem in modern photoelectrochemistry.[91,100,101] In recent years, however, the development of numerical techniques, which provide an enhanced understanding of the photocatalytic process at SL junctions, has gained a considerable amount of attention. This includes, but is not limited to the calculation of steady-state band diagrams,[32] transient analysis of PEC device behavior,[104] modeling of surface-state dynamics,[188] complete solution of combined drift-diffusion equations,[206] and the simulation of electrocatalyst-coated photoelectrodes.[106] In general, mesoscopic charge transport in a SL junction can be self-consistently calculated by solving the coupled Poisson-continuity equations.[206] However, to capture the photocurrent (J_{ph}) and the photovoltage (V_{ph}) (two of the most commonly measured quantities in typical PEC experiments)[84] it is also imperative to that one set up appropriate boundary conditions. For instance, the interfacial photocurrent (J_{ph}) at a photocatalytic SL junction (a boundary point) is usually computed by assuming the presence of a pseudo-Schottky contact at the interface.[32,103,206] Yet, similar boundary conditions are needed for Poissons equation to capture V_{ph}, but this crucial issue has not received proper attention in the literature. As described by Thorne *et al.*[21] and Dotan *et al.*,[84] the photovoltage (V_{ph}) generated at a SL junction shifts the photocurrent toward cathodic direction (for a photoanode) or anodic direction (for a photocathode) to facilitate unassisted solar water splitting. Likewise, due to its tendency to flatten the bands of semiconducting electrodes, the accurate determination of V_{ph} is also important to precisely extract and understand the band-diagram electrostatics of PEC devices.[21,71,206]

As part of an ongoing effort to understand the mesoscopic phenomena occurring in photocatalytic SL junctions, we previously presented a comprehensive analysis of the discretized drift-diffusion equations to theoretically extract measurable quantities (such as the photovoltage, onset and saturation of photocurrent, etc.)[206] and a comprehensive analysis of the surface-state dynamics at SL junction under dark current conditions.[188] The purpose of our present work is to emphasize the significance/importance of choosing appropriate boundary conditions when modeling the photovoltage in PEC devices – a critical ingredient often ignored in the SL junction modeling literature. When combined with the governing drift-diffusion equations, these boundary conditions can self-consistently capture both the photocurrent and photovoltage. Special attention is given to outline how the typical theoretical results from our approach can be directly translated into experimental procedures and measurements. Furthermore, it is also demonstrated that our theoretical approach can be directly correlated with experimental transient absorption (TA) spectra analysis of semiconductor/metal oxide photoanodes performing solar-assisted water oxidation.

6.2 Method

To begin with, let us briefly revisit the standard band-diagram alignment of a typical PEC set-up (see Figure 6.1), where the photocatalytic interface between the semiconducting photoanode (n-type) and aqueous solution ($\mathrm{pH} > 7$) is utilized to perform the solar-assisted water oxidation reaction.[1,32] In addition, Figure 6.1 also demonstrates the basic configuration of a standard PEC experimental set-up.[1] As illustrated, a semiconductor electrode constitutes the working electrode (WE) whereas a metal counter electrode (CE) is required to complete the circuit.[1,129] All the relevant energy levels in the system are referred with respect to the energy of a reference electrode (E_{ref}). In our present work, we have considered a reversible hydrogen elec-

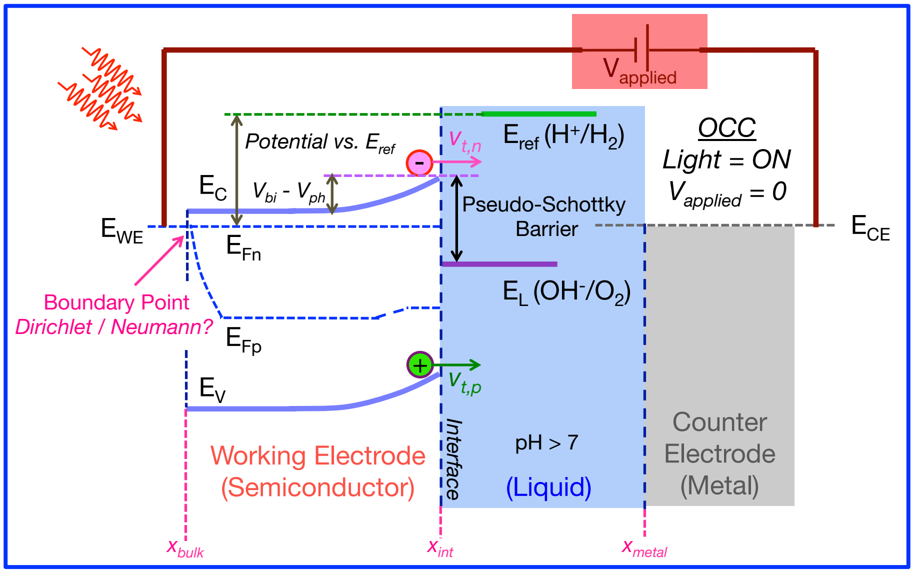

Figure 6.1: Typical band-diagram alignment of an illuminated semiconductor photoanode (n-type) in contact with an aqueous solution (pH > 7). All important energy levels are drawn for clarity. In this case, the energy of the reversible hydrogen electrode (RHE) is taken as the reference (E_{ref}). In PEC experiments, the potential of the working electrode (photoanode in our case) or E_{WE} is measured with respect to E_{ref}, whereas the metal counter electrode (operating at energy E_{CE}) is required to close the path of electron/hole flow. Under solar irradiation, the photoanode demonstrates splitting of electron (E_{Fn}) and hole (E_{Fp}) quasi-Fermi levels and the band bending is reduced by the amount of generated photovoltage (V_{ph}). The built-in potential at dark and the applied external bias are represented by V_{bi} and $V_{applied}$, respectively. Here, the PEC set-up is illustrated for $V_{applied} = 0$ with solar irradiation (illuminated OCC). A few important points along the space vector (x_{bulk}, x_{int} and x_{metal}) are also shown for convenience of the discussion.

trode (RHE) as the reference electrode.[1] Moreover, the PEC set-up in Figure 6.1 also allows the application of external excitation in the form of solar irradiation and/or externally applied potential source (denoted by $V_{applied}$).[32]

With the PEC set-up in hand, we now configure the governing equations with appropriate boundary conditions so that experimental trends of J_{ph} and V_{ph} can be reliably replicated in our calculations. Now, the electron and hole continuity equations inside of a semiconductor can be expressed as[33,120–122]

$$\frac{1}{q}\frac{dJ_n}{dx} + G_n - R_n = 0, \tag{6.1}$$

$$-\frac{1}{q}\frac{dJ_p}{dx} + G_p - R_p = 0, \tag{6.2}$$

Here, J_n and J_p respectively represent electron and hole currents throughout the semiconducting electrode. Other parameters include electron generation (G_n) and recombination (R_n) rates and hole generation (G_p) and recombination (R_p) rates, electron charge q and space vector x. At a SL junction, as presented in Figure 6.1, electronic conduction only exists inside of the semiconductor electrode, whereas the electrolyte is characterized by ionic conduction.[34,129] Thus, the pair of continuity equations (eqs. 6.1 and 6.2) are to be solved only inside the working electrode with boundary conditions located at $x = x_{bulk}$ and $x = x_{int}$. Now, the boundary conditions on continuity equations at the bulk of the photoanode ($x = x_{bulk}$) are merely set equal to the bulk concentrations of electrons (n_{bulk}) and holes (p_{bulk}) and thereby, are considered as Dirichlet type.[103,122,206] However, the appropriate boundary conditions for eqs. 6.1 and 6.2 at the SL interface ($x = x_{int}$) can be determined by comprehending that an ideal SL interface exhibits pinning of both the conduction band edge (E_C) and valence band edge (E_V) with respect to the liquid Fermi level (E_L).[34,36] Due to this characteristic band level pinning (BLP) of the semiconductor bands, it is customary to consider that an ideal SL interface closely mimics the properties of a conventional metal-semiconductor (MS) Schottky junction.[103,206] Consequently, the interfacial currents due hole ($J_{p|int}$) and electron ($J_{n|int}$) transfers at SL junctions can also be expressed similarly to those representing the interfacial currents at MS Schottky junctions and are given by[89,206]

$$J_{p|int} = qv_{t,p}\left(p_s - p_{s0}\right) \tag{6.3}$$

$$J_{n|int} = -qv_{t,n}\left(n_s - n_{s0}\right) \tag{6.4}$$

At an anodic SL junction, $v_{t,p}$ represents the transfer velocity of valence band holes to the liquid, leading to the desired oxidation reaction of OH^- species.[103,206]

Similarly, the conduction band electron transfer velocity is modeled by $v_{t,n}$, representing the undesired counter-reaction (reduction of O_2).[72,206] Here, n_{s0} and p_{s0} are the equilibrium concentrations of electrons and holes at the interface and n_s and p_s are the non-equilibrium concentrations of electrons and holes at the interface, respectively. However, an SL junction can deviate from the ideal Schottky-type behavior (constant height of the Schottky barrier) via unpinning the semiconductor bands if the charging/discharging process of surface states start to occur.[34,188] In this regard, an adaptive Schottky contact with varying barrier height, as presented in our earlier work,[206] is required to represent the SL interface. Finally, $J_{n|int}$ and $J_{p|int}$ (necessary to reliably capture the photocurrent) serve as the Neumann type boundary conditions for eqs. 6.1 and 6.2, respectively, at the photocatalytic SL interface ($x = x_{int}$).[103,206] The discretization technique of the continuity equations coupled with pseudo-Schottky type boundary conditions has already been presented in our earlier work to which the reader is referred.[206]

Now, to compute the electrostatic potential (ϕ) that spans over the entire SL junction, Poisson's equation must be solved together with the continuity equations (eqs. 6.1 and 6.2).[122,206] Fundamentally, ϕ arises due to exposed charges at the SL interface – denoted by the sum of the charge density in the semiconductor (ρ_{sc}) and liquid (ρ_L).[34,188] Here, we have incorporated a varying dielectric constant (ε) in Poisson's equation to solve for the electrostatic potential inside the entire span of the anodic SL junction, expressed as[188]

$$\varepsilon\frac{d^2\phi}{dx^2} + \frac{d\phi}{dx}\frac{d\varepsilon}{dx} = -\left[\rho_{sc} + \rho_L\right] \tag{6.5}$$

By solving the Poisson equation in this manner, we ensure that the potential drop inside the liquid (comprised mostly by the Helmholtz layer potential)[1,34] is allowed to evolve under the circumstances of surface state charging, applied external excitations and semiconductor doping.[188] Therefore, the SL contact is modeled as an adaptive Schottky contact capable of capturing both pinning and unpinning of semiconductor bands at the interface – an important prerequisite to simulate various oxide semiconductors (e.g., hematite, TiO_2, $BiVO_4$) used in photocatalysis.[206]

Now, our implementation of Poisson's equation assumes two boundary conditions located at $x = x_{bulk}$ and $x = x_{metal}$ (see Figure 6.1). The search for correct boundary conditions on ϕ is steered by: (1) the existence of the unique solution and (2) the band flattening process (under illumination) that occurs at the bulk of the semiconductor. To guarantee a unique potential solution, we set ϕ at $x = x_{metal}$ to some pre-defined value (for instance, the value of the local vacuum level), which imposes a Dirichlet boundary condition. Conversely, the appropriate boundary condition (Dirichlet/Neumann) at $x = x_{bulk}$ will be examined in this work by correlating theoretical calculations with the experimental procedures and trends.

6.3 Results

As a model system, we have considered an n-type hematite-based water splitting photoanode performing water oxidation.[68–70,201] Hematite (α-Fe_2O_3) has been widely investigated for solar-assisted water splitting due to its inexpensive elemental constituents and suitable band gap (1.9 eV - 2.2 eV).[1,60] In our simulation, we assumed a hematite photoanode with band gap (E_G) of $\sim$ 2.1 eV, immersed in an aqueous solution of pH = 13.6.[68] The donor concentration of the photoanode (N_D) is also set to $\sim 10^{20}$ cm^{-3} in accordance with values reported in the literature.[68,201] For convenience, our calculated energy band diagrams for the hematite photoanode are drawn with respect to reversible hydrogen electron (RHE), which is located -4.44 eV below the standard vacuum level reference commonly found in the device physics literature.[1,129]

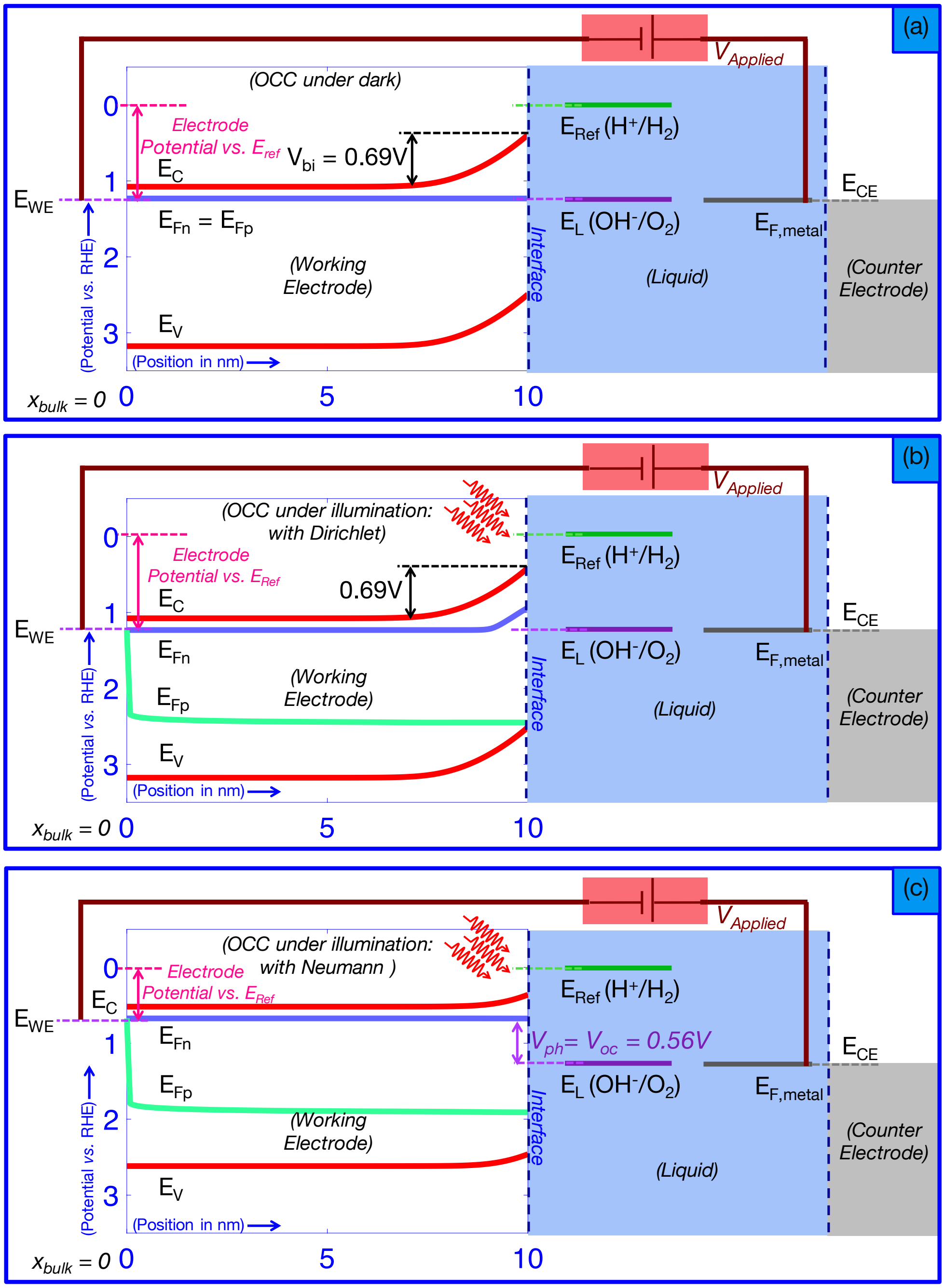

Figure 6.2: (a) Calculated band diagram of hematite photoanode at the dark OCC. The PEC system demonstrates perfect alignment of all the Fermi levels and thus illustrates the junction at equilibrium characterized by $V_{bi} \sim 0.69$ V. (b)-(c) Calculated band diagrams of the hematite photoanode under ~ 0.33 sun of solar irradiation. Depending on whether (b) Dirichlet- or (c) Neumann-type boundary condition is applied on the electrostatic potential at $x = x_{bulk}$, the band diagram may (Neumann) or may not (Dirichlet) capture the band flattening process brought by the illumination.

The first part of our analysis is aimed at numerically capturing the photovoltage at the illuminated hematite photoanode. This explores, as presented in the Method section, the impact of the chosen boundary condition (Dirichlet- or Neumann-type) for Poisson's equation at $x = x_{bulk}$, upon the band flattening process and charge transfer rates due to incident solar irradiation. That being said, the nature of this boundary condition should be such that the calculated electrostatics can effectively capture the evolution of ϕ (equivalent to semiconductor band bending) under any form of external excitation.[84] However, to analyze the band-diagram under dark and illumination, we only consider the open circuit condition (OCC) – characterized by a net zero current flow, within a dark or illuminated hematite photoanode.[36]

Figure 6.2a displays the calculated band diagram of the hematite photoanode at the dark OCC (also known as the 'equilibrium' condition). Importantly, the electrode considered in this study is assumed to be robust against corrosion and only allowed to exchange electrons/holes with OH^-/O_2 redox species.[72,206] This assumption, in other words, means that the liquid Fermi level (E_L) is solely determined by the energy of the OH^-/O_2 redox species.[32] Consequently, as clearly shown in Figure 6.2a, the electrode-electrolyte system, when situated in the dark, demonstrates equilibrium through perfectly aligning the electron (E_{Fn}) and hole (E_{Fp}) Fermi levels with E_L (at 1.23 V *vs.* RHE) when $V_{applied} = 0$.[206] Our results shows that under the dark OCC, the hematite surface is depleted from electrons (majority carrier) and characterized by a built-in potential (V_{bi}) of ~ 0.69 V. However, this OCC picture of the hematite photoanode when dark can be replaced by non-equilibrium OCC if the electrode is set to solar irradiation.[84] This, in turn, is regularly detected via different 'flat-band' experiments in the form of semiconductor band flattening due to V_{ph} generation.[130] Therefore, it is fundamentally imperative that any numerical technique applied to a SL junction correctly captures the band flattening process.

In order to self-consistently capture V_{ph} at the illuminated OCC, we separately used both Dirichlet- and Neumann-type boundary conditions on ϕ at $x = x_{bulk}$ and calculated the band alignments (shown in Figure 6.2b - Figure 6.2c, respectively). Here, the photoanode is theoretically set to $\sim$ 0.33 sun of solar irradiation, whereas the absorption coefficient (α) of hematite is considered to be $\sim 1.5 \times 10^{7}\text{m}^{-1}$.[32,68] We also considered the hole transfer velocity ($v_{t,p}$) $\sim 10^{-9}$ ms^{-1}, typical for hematite photoanode due to its extraordinarily sluggish hole transfer rate.[206] Moreover, to optimize the hole-driven oxidation reaction at the hematite interface, we deliberately made the hematite interface opaque to electron transfer by reducing the electron transfer velocity ($v_{t,n}$) to zero.[72] Utilizing this computational set-up, the calculated band diagram with a Dirichlet boundary condition imposed on ϕ at $x = x_{bulk}$ is unable to capture the band flattening process; this is demonstrated by the equal amount of band bending ($\sim$ 0.69 V) calculated for the hematite electrode under solar irradiation (see Figure 6.2b). Nevertheless the quasi-Fermi levels of electrons and holes are separated to accommodate photogenerated electron-hole pairs. As a consequence of the vanishing interfacial electron transfer, the electron quasi-Fermi level moves toward the conduction band and is depicted as a rise in interfacial electron concentration. As explained in Ref. [206], these photogenerated electrons (if not recombined in the space-charged region) should migrate toward the bulk of the electrode and induce V_{ph} that acts as a forward potential by flattening the semiconductor bands. However, the desired migration of the electrons (majority carrier) and thus the band flattening due to solar irradiation can only be captured when a Neumann-type boundary condition is imposed on ϕ at $x = x_{bulk}$ (see Figure 6.2c). In this case, the hematite photoanode generates a photovoltage of $\sim$ 0.56 V by efficiently separating the photogenerated electrons and holes created in the space-charged region (SCR). As expected, the quasi-Fermi level of electron remains flat at $\sim$ 0.67 V *vs.* RHE and is also elevated compared to the dark resting potential of the hematite photoanode ($\sim$ 1.23 V *vs.* RHE). Now, the band flattening due to solar irradiation is commonly measured/estimated as the amount of shift in OCC brought about by photoexcitation.[21] This has been well documented both theoretically (by Salvador[67]) and experimentally (by Wang and co-workers in a series of papers[21,71]) for hematite-based photoanodes. Following a similar procedure, our calculation of the band flattening (~ 0.56 V) is comparable to the experimentally determined range of band flattening (0.24 V - 0.8 V) exhibited by hematite photoanodes.[21,71] However, the numerical estimation of this band flattening process has not been captured in the existing SL junction simulation literature due to: (1) the consideration of the Dirichlet boundary condition on ϕ at $x = x_{bulk}$;[32,100,101,103] and (2) the assumption of only minority carrier modulation at the illuminated electrodes.[32] Nevertheless, the impact of different types of boundary conditions in simulating state-of-the-art solid-state devices constitutes an old problem, which has been explored thoroughly in the solid-state device physics literature.[120–122] However, this problem has not been well explored in the photocatalytic device literature. Importantly, capturing this critical band flattening process (equivalently, V_{ph}) profound impacts upon the computed photocurrent at the SL junctions – an issue that we will explore next.

A pivotal ingredient of our present work is the calculation of the photocurrent following the "standard" experimental steps albeit using a purely theoretical platform,[84] these steps include: (1) resting the electrode in the dark equilibrium (OCC under dark); (2) placing the electrode only under solar irradiation (illuminated OCC); and (3) imparting the electrode with both photoexcitation and an applied reverse bias ($V_{applied} > 0$). Up to now, we have discussed steps (1) and (2) and have determined that a Neumann boundary condition must be imposed on ϕ at $x = x_{bulk}$ to produce V_{ph} (or the band flattening, as shown in Figure 6.2). Now, the photocurrent can be computed as $J_{ph} = J_{n|int} + J_{p|int}$ (eqs. 6.3 and 6.4) using the self-consistent solution of the carrier concentrations obtained by solving the coupled Poisson-continuity equa-

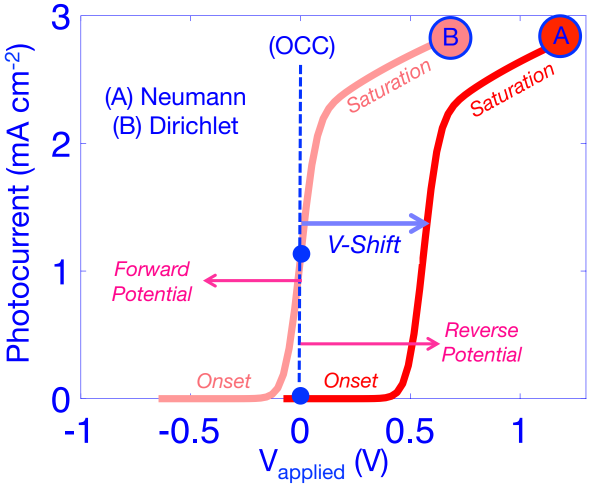

Figure 6.3: Calculated photocurrents using Neumann- (marked by A) and Dirichlet-type (marked by B) boundary conditions on ϕ at $x = x_{bulk}$. Here, J_{ph} is plotted as a function of the applied external potential, where $V_{applied} = 0$ denotes the open circuit potential (OCC). J_{ph} computed with a Neumann condition theoretically imitates the experimental procedure to generate practical current-voltage curve (dark OCC → illumination OCC → $V_{applied} > 0$) and hence, in accordance with the perception of hematite band bending and interfacial hole transport. However, J_{ph} computed with a Dirichlet condition fails to produce a photovoltage and is unable to provide a point-by-point match with experimental trend.

tions. Figure 6.3 presents calculations of the photocurrent at a hematite electrode and explicitly delineates the significance of placing appropriate boundary conditions on ϕ at the semiconductor bulk.

To understand, let us consider curve A in Figure 6.3, representing the photocurrent calculated using a Neumann boundary condition. At the illuminated OCC ($V_{applied} = 0$), J_{ph} is negligible ($\sim 6.2\times10^{-9}$ mAcm^{-2}) and essentially considered as zero. The reason J_{ph} becomes non-zero albeit very small in value, is directly linked with the extraordinary sluggish rate of interfacial hole transfer. However, with fast $v_{t,p}$, p_s approaches p_{s0} and can make $J_{p|int)} \rightarrow 0$ or $J_{ph} \rightarrow 0$. As discussed earlier (see Figure 6.2c), band flattening of the hematite electrode elevates the electron quasi-Fermi level ($\sim$ 0.67 V *vs.* RHE) and the electrode is operated close to the flat-band potential ($V_{FB} \sim 0.54$ V *vs.* RHE)[70] with a significantly low SCR electric field and high SCR/bulk recombination. At this point, in a practical PEC set-up, a reverse potential ($V_{applied} > 0$) is applied on the photoanode to gradually increase the SCR electric field in order to suppress the recombination.[84,206] In our simulation, the application of reverse potential on hematite electrode (operating in sub-onset region) also increases photocurrent by suppressing detrimental recombination processes. Critical operating points on J_{ph} can be marked as onset (small reverse bias), transition region (moderate reverse bias) and saturation (high reverse bias). Interestingly, curve A in Figure 6.3 depicts the photocurrent computed using an identical procedure to that applied in experiments. Here, photocurrent onset occurred at 0.4 V of reverse bias, transition region spans within a reverse bias from 0.4 V - 0.72 V and finally, saturation occurs at reverse bias > 0.72 V. Moreover, a photocurrent onset at 0.4 V of reverse bias ($V_{applied} = 0.4$ V) can be translated into an onset potential of ~ 1.07 V *vs.* RHE, which falls very close to the experimentally determined onset of hematite photoanode at 1.1 V *vs.* RHE.[68]

However, when the photocurrent is computed with a Dirichlet boundary condition on ϕ at $x = x_{bulk}$, one is unable to reproduce a step-by-step match with the practical J_{ph} curve. As presented in Figure 6.3, curve B produces a significantly high photocurrent (~ 1.1 mAcm^{-2}) at the illuminated OCC, such that OCC falls in the transition region of the photocurrent. This again can be linked with the absence of band flattening brought about by the solar irradiation when a Dirichlet boundary condition is applied. To tune the electrode inside the sub-onset region, in this case, the hematite photoanode requires a forwardly applied potential that can flatten the bands, which physically generated by the photoexcitation in a real system (not by a forward external bias).[21,36] Consequently, curve B results in the photocurrent onset at 0.18 V forward bias, the transition region from 0.18 V forward bias to 0.14 V reverse bias and saturation at a reverse bias of 0.14 V and beyond. Thus, despite the fact that the photocurrent presented by curve B appears to be similar to the experimental photocurrent, it nevertheless miscalculates the band bending demonstrated by an illuminated hematite electrode and fails to replicate the experimental procedure. It is also imperative to understand that practical electrodes can exhibit reduced/inefficient band flattening due to the detrimental events such as surface/bulk recombination,[21,71,81] which can impede the V_{ph} generation process. In addition, intermediate trap-states at the fluorine-doped-tin-oxide/hematite (FTO/hematite) interface can limit the practical band flattening at hematite electrodes.[18] The impact of surface/bulk recombination and the FTO/hematite interface on PEC performance, have both been experimentally investigated in the literature.[12,18,21,71,81] Nonetheless, while modeling these practical semiconducting electrodes utilized in PEC applications, one must consider floating boundary condition on ϕ at $x = x_{bulk}$. This is because a Dirichlet boundary condition is unable to capture the band flattening no matter how inefficient the V_{ph} generation process is. Moreover, the information regarding band bending is critical to the operation of PEC devices, as it is directly translated into mesoscopic charge transfer kinetics and provides valuable insights into SCR/bulk recombination and interfacial carrier transport. As our final goal, we now wish to address to what extent we can theoretically extract these charge transfer properties and correlate them with experimental results.

In PEC experiments, a common procedure for evaluating the complex charge transfer kinetics present is to probe the minority carrier (holes in n-type hematite) relaxation time via transient absorption (TA) spectra analysis.[68,69] For instance, TA spectra analysis of a hematite photoanode by Le Formal *et al.*,[70] suggests that the rapid (picosecond to millisecond) recombination of the photogenerated holes effectively limits the PEC performance and can be suppressed under anodic bias (bias applied toward reverse direction). This observation is also supported by Barroso *et al.*,[69] where part of the TA spectra demonstrates micro to millisecond decay and linked with the trap-assisted SCR recombination. In general,

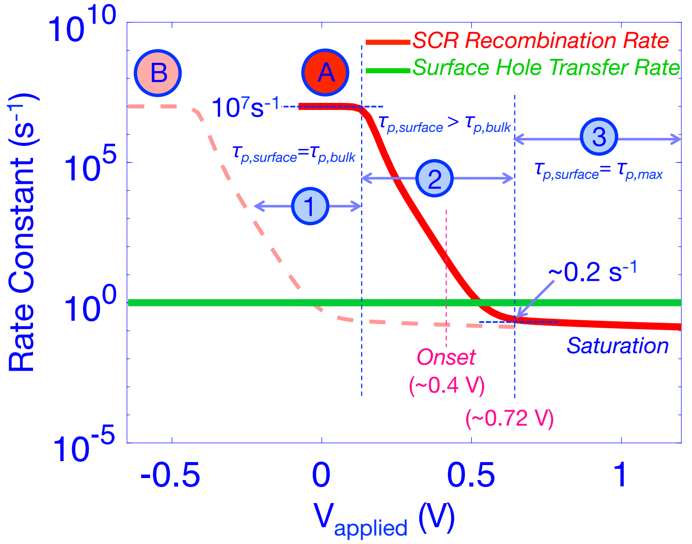

Figure 6.4: Comparison of the calculated rate of recombination and rate of interfacial hole transfer in an illuminated hematite photoanode with both Neumann (marked by A) and Dirichlet (marked by B) boundary conditions. For curve A, the entire region 1 and part of region 2 are situated in the sub-onset regime of the photocurrent (compare curve A in Figure 6.3). In this case, the interfacial hole transfer is suppressed by a high rate of recombination. These holes are detected experimentally as fast-decay hole in TA spectra analysis of hematite electrodes. Nevertheless, the lifetime of interfacial holes improves with the application of a reverse potential. It is only in region 3, where the interfacial hole transfer becomes comparable or outperforms the hole recombination process and the holes are detected as long-lived holes in TA spectra analysis. With improper Dirichlet condition (curve B), this entire process is unphysically shifted towards applied forward potentials and a direct correlation between theoretical and experimental results cannot be drawn.

rapidly occurring hole recombination is attributed to the 'fast-decay' portion of the TA spectrum.[70] In accordance with Ref. [68], we also considered that fast hole relaxation occurs at a lifetime ($\tau_{p,bulk}$) of 0.1 μs. Figure 6.4 shows the calculated rate of interfacial recombination (k_{rec}) with respect to the rate of interfacial hole transfer (k_{trans}) assuming both Neumann (curve A) and Dirichlet (curve B) boundary conditions on ϕ at $x = x_{bulk}$. In this computation, the rate of interfacial/SCR hole recombination is calculated as $k_{rec}(x) = \frac{R_p(x)}{p(x)}$ and the rate of interfacial hole transfer is assumed to be ~ 1 s^{-1}, which is in accordance with the literature[70,206] and can be computed using $k_{trans}(x_{int}) = \frac{L_{trans}}{v_{t,p}}$ [with a hole transfer distance (L_{trans})

of 1 nm]. Now, as presented by curve A (with Neumann boundary condition) in Figure 6.4, close to the illuminated OCC (when $V_{applied}$ is at a low reverse potential), the photocatalytic interface is characterized by extraordinarily high recombination (marked as region 1). In practice, this situation is directly correlated with a hematite photoanode operating close to the flat band condition and thereby unable to produce a sufficiently lengthened SCR that separates electrons and holes. This observation can be further supported by our simulated band diagram (see Figure 6.2c) and the negligible calculated photocurrent throughout the sub-onset portion of the photocurrent (see curve A in Figure Figure 6.3). Therefore, we can correlate region 1 of Figure 6.4 with the rapid recombination of the photogenerated holes giving rise to the fast-decay (≤ 0.1 μs) portion of the TA spectrum.[69, 70] In this region, interfacial recombination occurs at a timescale equal to the minority carrier lifetime ($\tau_{p,bulk}$).[69] As illustrated in Figure 6.4, if $\tau_{p,surface}$ represents the interfacial hole lifetime, subsequently region 1 is characterized by $\tau_{p,surface} = \tau_{p,bulk}$.

Now, starting from this sub-onset picture of photocatalytic hole transport, the interfacial hole lifetime at a hematite photoanode can be improved by applying potential in the reverse direction (marked as region 2).[68, 70] Nevertheless, the photocurrent will still remain small, as the photogenerated holes are being transferred too slowly that these carriers are still prone to interfacial/SCR recombination. However, under the application of large reverse bias, the effects of interfacial hole lifetime improvement start to translate into a photocurrent. This marks the situation in region 3 when the rate of interfacial/SCR recombination is substantially retarded by the comparable or superior interfacial hole transfer rate (due to the strong field separating carriers).[68, 69] Photogenerated holes under this condition are usually detected as 'long-lived' holes in an experimental TA analysis. As the photogenerated holes become less vulnerable to unwanted recombination, the photoanode exhibits a higher yield of solar-to-chemical fuel conversion, which is clearly revealed by the saturation of the photocurrent under high reverse bias in Figure 6.3.[69] All of these results were obtained with Neumann boundary conditions applied to ϕ at $x = x_{bulk}$ (curve A), when improper Dirichlet conditions are applied this entire process is unphysically shifted towards applied forward potentials (as shown in Figure 6.4, curve B) and again, a direct correlation between theoretical and experimental results (in this case, TA spectra analysis) cannot be made. Dirichlet conditions, therefore, incorrectly predict the applied potential needed to drive photocatalysis and miss the important physical interaction between the photovoltage and the applied potential in the practical operation of PEC devices.

6.4 Conclusion

In this work, we have presented a scientific discussion on the significance of utilizing appropriate boundary conditions in the mesoscopic modeling of photocatalytic semiconductor-liquid interfaces. Our approach considered the bulk semiconductor bands as floating (Neumann boundary condition) in order to respond to the band flattening process due to illumination. It was shown that to capture photovoltage formation, one must use a Neumann boundary condition for the electrostatic potential at the semiconductor bulk, when solving the coupled Poisson-continuity equations self-consistently. With the corollary, that if a Dirichlet boundary condition is assumed at the semiconductor bulk, then the photovoltage is not captured. From this comparison of electrostatic boundary conditions, with and without a photovoltage, it was further demonstrated that the incorporation of the appropriate boundary conditions is essential to obtaining a direct point-to-point match between the photocurrent observed practically and the photocurrent obtained theoretically (with meaningful applied external potentials). Moreover, use of the correct boundary conditions was also linked with obtaining an accurate band-diagram alignment (taking band flattening under illumination into account). Throughout this implementation, it was also imperative to assume that the prototype SL interface acted as a pseudo-Schottky contact for interfacial electron and hole transfer.[206] Finally, the intriguing scope of exploring the dynamics of interfacial/SCR recombination relative to the kinetics of interfacial charge transfer was also explored. This theoretical probing of interfacial charge transfer process was correlated with the practical hole relaxation experiments such as TA spectra analysis. Thereby, the method presented here offers intriguing results that provide improved ties to experimental methodologies. Overall, this work underscores importance of proper boundary conditions (and the consequence of improper boundary conditions) when modeling the mesoscopic phenomena at photocatalytic SL interfaces.

6.5 Acknowledgement

We acknowledge financial support from the NSERC of Canada and FQRNT of Québec and the computational resources provided by the Canadian Foundation for Innovation, CalculQuebec, and Compute-Canada.

Chapter 7

Impact of Bulk Trapping Phenomena on the Maximum Attainable Photovoltage of Semiconductor-Liquid Interfaces

---

This chapter presents the numerical simulations intended to unravel the impact of the bulk trap states in determining the interfacial photoelectrochemical performance at the semiconductor-aqueous junctions. This work incorporates the Shockley-Read-Hall description of the carrier capture and emission events by the trap states into the domain of photocatalytic semiconductor-liquid junctions. The impact of acceptor- and donor-type trap states have been assessed separately in the context of hematite-based PEC devices. In the case of the anodic oxidation reaction, acceptor trap states can lead to degradation of the maximum attainable photovoltage along with poor electron (majority carrier) conductivity. Conversely, donor trap are found to be merely beneficial with respect to an increase in the population of mobile electrons in the conduction band. Finally, with the aid of ab-initio calculations, the scope of this modeling has been extended to probe the detrimental influence of ‘small-polaronic’ conduction mechanism in metal-oxide semiconductors. Throughout the discussion, as presented in this chapter, a systematic effort has been made to link theoretical findings with commonly observable experimental results.

This chapter is a reproduction of the article published in the Journal of Physical Chemistry C. The complete citation of the published article is:

Asif Iqbal, Shuaishuai Yuan, Zi Wang and Kirk H. Bevan, Impact of Bulk Trapping Phenomena on the Maximum Attainable Photovoltage of Semiconductor-Liquid Interfaces, *The Journal of Physical Chemistry C*, 2018, 122, 42 23878–23889.

Abstract

In this work, we present a generic semiclassical approach for theoretically evaluating the impact of bulk trap states on the maximum attainable photovoltage in solar-assisted water splitting reactions. Our method explicitly considers the charge contribution due to the capture and emission of conduction band electrons and valence band holes by trap states situated in the bandgap, integrated within a self-consistent solution procedure for calculating electrostatic and charge transport properties. Utilizing the hematite photoanode as our model system, our approach reveals that bulk trap states may significantly degrade both the maximum attainable photovoltage and the concentration of mobile electrons (majority carriers) in the conduction band. These results, suggest that bulk trap states can have two primary consequences in photoanodes. First, they may limit the degree to which a favourable cathodic shift in the photocurrent can be achieved (by lowering the maximum attainable photovoltage). Second, they may impede the extraction of majority carriers at the bulk-electrode contact (by lowering the conduction band carrier concentration). Both of these phenomena are commonly observed in the state-of-the-art hematite photoanodes. Our semiclassical analysis is further supported by first-principles calculations of hematite, which

suggest that electron polarons impact adversely upon the maximum attainable photovoltage of oxide photoanodes. In general, this work underscores the importance of engineering the bulk electronic properties of photoelectrodes, and is intended to further assist the design of photoanodes en route to low cost unassisted solar water splitting.

7.1 Introduction

In recent years, there has been a resurgence of water splitting research seeking to convert intermittent solar energy into storable eco-friendly chemical fuels such as H_2.[1,4,160] By utilizing inexhaustible solar energy and earth-abundant materials, photocatalytic based water splitting aims to provide large-scale and economical green fuel production.[3,5] Consequently, photocatalytic semiconductor-liquid (SL) junctions comprised of earth-abundant metal-oxides capable of solar-assisted water splitting (*e.g.*, TiO_2, α-Fe_2O_3, $BiVO_4$, WO_3), are currently considered an important component en route to low-cost H_2 production.[13,54,57] In the same spirit, a large body of research has been directed towards understanding the key bottlenecks that impede the realization of efficient low-cost water splitting in such photoelectrodes.[1,13] It is now widely accepted that economical water splitting photoelectrodes can only be realized by combining experimental and theoretical efforts, with the aim of unraveling the fundamental processes governing artificial photosynthesis.[4]

Research work in this area has generally attributed several physical mechanisms to the limited photocatalytic performance of oxide photoanodes, including: (1) extraordinarily short minority carrier collection lengths (often on the order of few nm); (2) comparatively low light absorption coefficients; (3) high rates of electron-hole recombination at the surface and in the bulk; and (4) the sluggish rate of interfacial carrier transport/reactions.[20,21,54,57,71] Efforts to improve photoelectrochemical (PEC) performance have primarily focused on engineering the SL interfacial region of photoanodes – *i.e.*, where the photogenerated "minority" carriers are collected and subsequently transferred to the liquid environment.[12,17,207] This makes sense, since improved interfacial hole transfer in photoanodes translates into superior solar-to-chemical fuel production yields.[12,62] Conversely, the impact of bulk processes on the efficiency of photoanodes has not been as widely explored in the literature. However, as emphasized by Wang and co-workers,[20,21,71] the goal of economical unassisted solar water splitting can only be accomplished through the simultaneous enhancement of the photocurrent (through improved minority carrier collection and transfer) and the photovoltage (through efficient generation of the photogenerated majority and minority carriers in the semiconductor bulk). Interestingly, this key experimental observation is in agreement with results obtained from recent semiclassical modeling advances in the description of photocatalytic SL junctions.[32,106,206,208] Moreover, both of these conditions can only be achieved through minimal trapping, reduced recombination, and superior carrier extraction in the bulk.

The photovoltage (V_{ph}), a thermodynamic quantity arising due to electron-hole pair generation, is coupled with the photocurrent (J_{ph}) extracted from an anodic SL junction.[20,21,67,71,84,130] In practice, the maximum attainable photovoltage ($V_{ph|max}$) at an anodic SL junction is a highly important metric, since V_{ph} provides an essential cathodic shift in the onset of the anodic photocurrent.[20,21,71,84] This is important because a sufficiently large cathodic shift towards the H_2 evolution potential can enable unassisted water splitting.[20,21,71,84] Crucially, poor carrier transport properties in metal-oxide semiconductors (such as low bulk conductivity, trapping, and inefficient carrier extraction at the back contact) are often linked to a degradation in V_{ph}.[19,150,209,210] For example, experimental studies on hematite photoanodes have demonstrated that bulk trap states impact upon on the measured photocurrent density of photoanodes.[53,150] In extreme cases, the complete absence of a photocurrent coupled with a negligible or vanishing photovoltage has also been reported in the literature.[53] Others have associated the formation of a "dead-layer" near the back contact of photoanodes to defect states generated due to lattice mismatch between the photocatalytic material and the underlying substrate.[19] Likewise, small-polaron conduction properties, as well as the dynamics of the intermediate defect states inside the band gap, have been correlated with the poor electron transport properties often exhibited by metal-oxide semiconductors.[63, 115, 210–216] Additionally, the doping behavior of extrinsic impurities (*i.e.*, activation of the dopants)[19, 217] in metal oxides and the optimal structuring of nano-electrodes for the transport of carriers, remain pressing questions that impact upon bulk processes.[18, 150] All of these observations underscore the need for a deeper experimental and theoretical understanding of how bulk processes impact upon the performance of water splitting photoelectrodes.

In this work, we present a theoretical study aimed at understanding how bulk trap states may impact upon the maximum attainable photovoltage ($V_{ph|max}$) and the majority carrier transport properties of photoanodes. Our analysis extends the trapping/detrapping theoretical methodology developed for solid-state semiconductor devices[33, 73, 120, 122, 138, 218] into the domain of water-splitting photoanodes. From this we are able to theoretically explore how trap densities and distributions impact upon: band bending electrostatics, the populations of free and trapped carriers, the maximum achievable $V_{ph|max}$, etcetera. The role of both acceptor and donor type trap states state are evaluated in this manner. Using this methodology, it is shown that bulk trap states can significantly lower the maximum attainable photovoltage ($V_{ph|max}$) and therefore significantly impede a desirable cathodic shift in the photocurrent (for unassisted solar water splitting). It is also demonstrated that trap states can substantially lower the number of band carriers and thereby detrimentally impact upon bulk conductivity (a significant factor in limiting the overall photocurrent). These findings are further supported by first-principles calculations, which suggest that electron polarons may adversely impact upon the maximum attainable

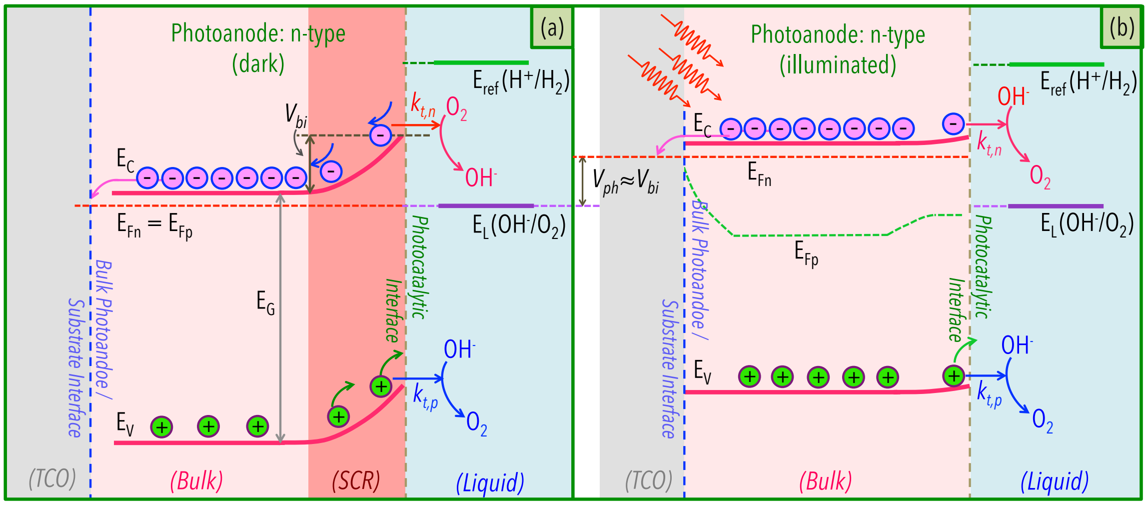

Figure 7.1: Idealized band-diagram alignments of a crystalline semiconducting photoanode-aqueous junction under (a) dark and (b) illuminated conditions, with no externally applied potential and in the absence of carrier trapping.[21, 130, 206] Schematic (a) represents the open-circuited SL junction at equilibrium (OCC dark) and therefore, $E_{Fn} = E_{Fp} = E_L$.[72, 206] Due to the electric-field in the SCR, photoexcited carriers are separated and driven in opposite directions. Schematic (b) displays the open-circuit SL junction under solar illumination (OCC under illumination). Here, the photoanode maximizes V_{ph}, which is achieved by suppressing V_{bi} and is characterized by a near complete flattening of the semiconductor bands. Quasi-Fermi level splitting also occurs under illumination.

photovoltage of oxide photoanodes, as well as experimental observations reported in the literature. In a nutshell, this work underscores the importance of bulk engineering of photoanodes, through the minimization of carrier trapping, when designing PEC devices.

7.2 Method

7.2.1 Idealized Semiconductor-Aqueous Junctions

To begin with, let us briefly revisit the ideal band diagram alignment of a photocatalytic SL junction as shown in Fig. 7.1 – consisting of a perfectly crystalline semiconductor (without any bandgap states) and an aqueous solution with pH > 7.[32, 206, 208] Here, the semiconductor is assumed to serve as a photoanode (n-type) performing solar-assisted water oxidation.[1,13] All photoelectrochemical reactions are assumed to occur at the semiconductor-aqueous interface, namely, the oxygen evolution reaction (OER) and oxygen reduction reaction (ORR).[29,37,72] To simplify our analysis, we have assumed that the photoanode is robust against corrosion and only electrochemically active to OH^-/O_2 species.[72,206] Therefore, in our model, the liquid Fermi-level (E_L) is solely determined by OH^-/O_2 species and is aligned with the electron (E_{Fn}) and hole (E_{Fp}) quasi-Fermi levels when the junction is resting in the dark, which is illustrated in Fig. 7.1a.[206,208] This is known as the open circuit condition or "OCC at dark" and characterized by zero interfacial current ($J = 0$). Throughout our discussion, we utilize the reversible hydrogen electrode (RHE) as the reference electrode (marked as E_{ref} in Fig. 7.1), which sets E_L at +1.23 V *vs.* RHE.[1,129] In addition, the SL junction is characterized by the formation of a built-in potential (V_{bi}) that is distributed throughout the span (L_{scr}) of the space charge region (SCR). Here, L_{scr} provides a rough estimate of the the hole collection distance in this PEC configuration. Conversely, the bulk of the electrode is characterized by a quasi-neutral region, and an interface between the photoanode and substrate [*e.g.*, transparent conductive oxide (TCO)].[12,53] Finally, $k_{t,p}$ and $k_{t,n}$ represent the rate of interfacial hole and electron transfer leading to the OER (desired water oxidation reaction) and ORR (undesired, backward reaction), respectively.[72,206]

Under solar illumination, as shown in Fig. 7.1b, the SL junction exhibits the photogeneration of electron-hole pairs (depicted by the splitting of E_{Fn} and E_{Fp}) and a photovoltage (a thermodynamic quantity, directly related with the Gibbs free energy of the photogenerated electron-hole pairs).[67] The photovoltage (V_{ph}) is usually detected experimentally *via* various "flatband" measurements related to semiconductor band flattening.[21,67,84,130] One of the essential design goals of unassisted solar-water splitting, as experimentally demonstrated by Wang and co-workers,[20,21,71] is to maximize V_{ph} under the open circuit condition (also known as the open circuit voltage or V_{oc}) – since a larger V_{ph} increases the cathodic shift in the onset of the photocurrent. However, the maximum value of V_{ph} is intrinsically limited by the magnitude of V_{bi}, which represents the offset between the flatband condition under illumination and band bending in the dark (compare Figs. 7.1a and 7.1b).[21,36,37,67,84,87,91,130] The schematic band alignment in Fig. 7.1b illustrates this particular situation (open circuit condition or 'OCC under illumination'), where the illuminated photoanode is operated at the flatband potential without any external bias source and the generated photovoltage approaches its maximum limit of $V_{ph|max} \approx V_{bi}$. Nevertheless, the generation of $V_{ph|max}$ (Fig. 7.1a $\rightarrow$ Fig. 7.1b) entails the efficient separation of the photogenerated electrons and holes by directing them oppositely inside the semiconductor.[36,206] Holes are collected at the anodic semiconductor-aqueous interface, whereas the electrons are collected at the substrate/electrode back contact in the bulk (see also Fig. 7.1).[209] Lastly, the photocurrent (J_{ph}) will depend on how quickly interfacial holes are transferred to reactants – a kinetic constraint where rapid hole transfer produces a high yield and sluggish hole transfer produces a low yield for solar-to-chemical conversion.[32,62,206,208] Importantly, the concept of $V_{ph|max} = V_{bi}$ is frequently mentioned in earlier work by considering photoelectrodes comprised of a crystalline semiconductor.[34,67,87,91] Crucially, carrier trapping by defect states inside the semiconductor bandgap can dramatically lower V_{bi} and consequently $V_{ph|max}$, thereby reducing the much needed cathodic shift in J_{ph} towards unassisted solar water splitting. Trap states can also dramatically lower the number of free carriers available to carry current from the SL interface into the bulk/electrode region (and thereby also limit J_{ph}). We shall explore both of these aspects in the next section.

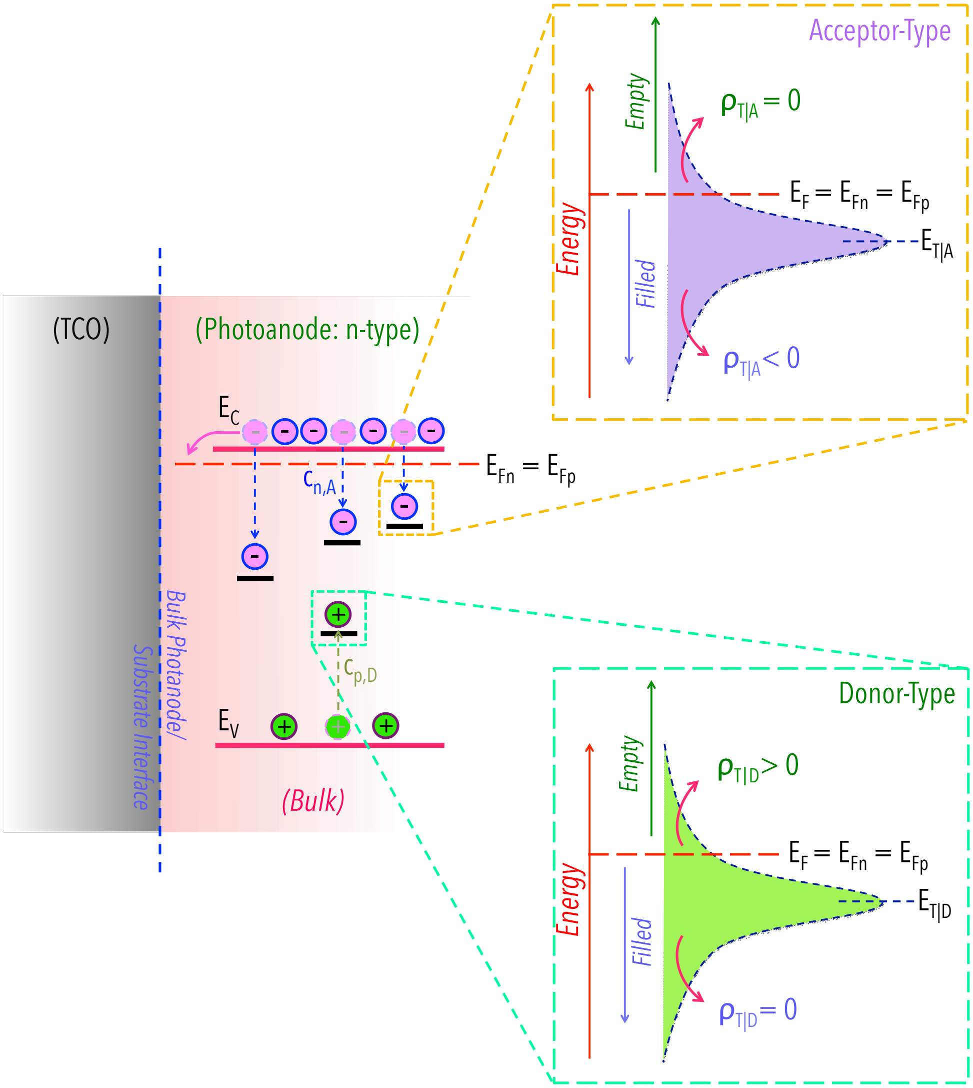

Figure 7.2: Electron and hole capture/emission by trap states distributed in a semiconductor. With the inclusion of trap states, electron and hole transport deviates from that of an idealized crystalline semiconductor.[73, 138, 218] This is illustrated by the capture of mobile electrons and holes, which should be separated and collected at the substrate/electrode and photocatalytic SL interfaces, respectively. Depending on the nature of the trap states and the types of carriers captured, the electrons/holes trapped by these states may or may not contribute to the overall charge balance.[143, 219] This is shown in the insets drawn for acceptor-type (upper) and donor-type (lower) states.

7.2.2 Semiconductor-Aqueous Junctions with Bulk Trapping

Modeling Charge Trapping inside Semiconductors

Up to now, in our discussion of semiconductor-liquid junctions in Sec. 7.2.1, we have assumed an idealized semiconducting photoanode that is perfectly crystalline and therefore free from any intermediate trap states lying in the bandgap. However, in practice, semiconductors may contain trap states inside the bandgap that capture electrons from the conduction band and/or holes from the valence band. In the case of metal-oxide semiconductors, as discussed in the introduction, these intermediate states originate from: lattice mismatch between the substrate and photoanode,[19,53,150] morphological defects,[210–212] polaronic bound states,[63,115,213–216] oxygen vacancies,[220,221] extrinsic impurities,[217,222] etcetera. To understand the impact of such trap states on photoanodes, we shall utilize a semiclassical model describing the trapping/detrapping dynamics of intermediate bandgap states. The approach we employ was originally developed to understand the operation of solid-state semiconductor devices prone to trapping.[73,74,218] A particular example would be the simulation of silicon heterojunction solar cells.[223–225] Now, Fig. 7.2 presents a generic picture of carrier trapping/detrapping events by intermediate states. Here, we show trap states with both acceptor and donor characteristics inside a bandgap. Acceptor states are considered to be negatively charged when filled by electrons and charge neutral when empty.[143] This is shown in the upper inset of Fig. 7.2, where the acceptor states located below the Fermi level are occupied by electrons and therefore, contribute negative charge ($\rho_{T|A} < 0$). Conversely, the empty acceptor states located above the Fermi level remain charge neutral ($\rho_{T|A} = 0$). On the other hand, donor-type states (see the lower inset of Fig. 7.2) are positively charged if they contain holes ($\rho_{T|D} > 0$) and are considered charge neutral when filled by electrons ($\rho_{T|D} = 0$).[143]

The exchange of carriers between bulk trap states and the semiconductor bands are represented by capture (trapping) and emission (detrapping) constants. These are respectively modeled by c_n and e_n for electrons, and c_p and e_p for holes.[73, 138, 218] In terms of water-splitting photoanodes, the trapping and detrapping of photogenerated carriers represents a significant deviation from the ideal picture of the crystalline photoanodes discussed in the previous section.[13, 209, 210] To understand the degree to which trapping removes us from the idealized photoanode picture, we need to formally describe the distribution of carriers in the semiconductor bands and trap states. From this we shall be able to calculate their impact on the electrostatic potential (ϕ) and V_{bi}, by utilizing standard self-consistent numerical techniques, while conserving charge neutrality along the entire photocatalytic SL junction.[188, 206] In this regard, the concentration of the mobile electrons in the conduction band (n_{cb}), by assuming non-degenerate carrier statistics, may be described by[33, 120, 122]

$$n_{cb}\left(x,\phi\right) = N_C \exp\left(-\left[\frac{E_C\left(x,\phi\right) - E_{Fn}\left(x\right)}{k_B T}\right]\right). \tag{7.1}$$

Similarly, p_{vb} represents the mobile holes in the valence band and is given by[33, 120, 122]

$$p_{vb}\left(x,\phi\right) = N_V \exp\left(\left[\frac{E_V\left(x,\phi\right) - E_{Fp}\left(x\right)}{k_B T}\right]\right). \tag{7.2}$$

Here, both n_{cb} and p_{vb} explicitly vary with ϕ and the space vector x. Moreover, E_C and E_V are the conduction and valence band edges, k_B is Boltzmann's constant, and T is the temperature. Finally, N_C and N_V represent the effective density of states in the conduction and valence bands, respectively. Here, we considered non-degenerate carrier statistics, which is a common assumption in the state-of-the-art semiclassical modeling of photocatalytic SL junctions.[32, 100, 101] Furthermore, we have also considered the presence of both acceptor ($g_{T|A}$) and donor ($g_{T|D}$) states that are distributed in energy (E) between the valance band maximum (E_V^+) and conduction band minimum (E_C^-).[138,218] Accordingly, by considering trap-assisted capture and emission processes leading to Shockley-Read-Hall (SRH) generation and recombination, the concentration of electrons captured by an acceptor state characterized by E, x and ϕ can be expressed as[73,138]

$$n_{T|A}\left(E,x,\phi\right)=g_{T|A}\left(E\right)\left[\frac{c_n n_{cb}\left(x,\phi\right)+c_p p_1\left(x,E\right)}{c_n\left[n_{cb}\left(x,\phi\right)+n_1\left(x,E\right)\right]+c_p\left[p_{vb}\left(x,\phi\right)+p_1\left(x,E\right)\right]}\right], \tag{7.3}$$

where,

$$n_1\left(x,E\right)=n_i\left(x\right)\exp\left[\frac{E-E_{Fi}\left(x\right)}{k_BT}\right] \tag{7.4}$$

and

$$p_1\left(x,E\right)=n_i\left(x\right)\exp\left[\frac{E_{Fi}\left(x\right)-E}{k_BT}\right] \tag{7.5}$$

respectively represent the concentrations of electrons and holes if the semiconductor Fermi-level falls at E. Where, E_{Fi} is the intrinsic Fermi level.

Thus, the total charge contribution from a distribution of acceptor states is[138,143,219]

$$\rho_{T|A}\left(x,\phi\right)=\int_{E_V^+}^{E_C^-}n_{T|A}\left(E,x,\phi\right)dE. \tag{7.6}$$

Similarly, the concentration of holes captured by a donor state located at energy E, position x and electrostatic potential ϕ is given by[73,138]

$$p_{T|D}\left(E,x,\phi\right)=g_{T|D}\left(E\right)\left[\frac{c_n n_1\left(x,E\right)+c_p p_{vb}\left(x,\phi\right)}{c_n\left[n_{cb}\left(x,\phi\right)+n_1\left(x,E\right)\right]+c_p\left[p_{vb}\left(x,\phi\right)+p_1\left(x,E\right)\right]}\right], \tag{7.7}$$

and the total charge provided by the distribution of donor states is expressed as

$$\rho_{T|D}\left(x,\phi\right)=\int_{E_V^+}^{E_C^-}p_{T|D}\left(E,x,\phi\right)dE. \tag{7.8}$$

Finally, the net charge contribution from the distribution of bulk trap states of both acceptor- and donor-type is computed as

$$\rho_T\left(x,\phi\right) = \rho_{T|D}\left(x,\phi\right) - \rho_{T|A}\left(x,\phi\right). \tag{7.9}$$

In our analysis of ρ_T, we have approximated $g_{T|A}$ and $g_{T|D}$ to take a normal distribution with respect to energy (see Fig. 7.2), following state-of-the-art modeling efforts regarding trap states inside disordered semiconductors by the device physics community (*e.g.*, amorphous silicon).[223–225] For instance, in our computation, $g_{T|A}$ is given by[225]

$$g_{T|A}\left(E\right) = \frac{\tilde{N}_{T|A}}{\sqrt{\pi}\,W_{T|A}} \exp\left[-\left(\frac{E - E_{T|A}}{W_{T|A}}\right)^2\right]. \tag{7.10}$$

Here, $E_{T|A}$ and $W_{T|A}/\sqrt{2}$ respectively are the location of the peak and the standard deviation of the distribution in eV, and $\tilde{N}_{T|A}$ is the total number of acceptor-type trap states in the bandgap in cm^{-3}.[225] Importantly, a normal distribution conserves the total number of states ($\tilde{N}_{T|A}$) even when the peak location and spread are altered. Consequently, this property allows us to investigate the impact of the same number of states as a function of their energetic location (shallow → deep) and/or spread (degree of localization). Similarly, $g_{T|D}$, denoting the distribution of the donor-states, is expressed as[225]

$$g_{T|D}\left(E\right) = \frac{\tilde{N}_{T|D}}{\sqrt{\pi}\,W_{T|D}} \exp\left[-\left(\frac{E - E_{T|D}}{W_{T|D}}\right)^2\right], \tag{7.11}$$

where, $E_{T|D}$ and $W_{T|D}/\sqrt{2}$ respectively are the location of the peak and the variance of the distribution in eV, and $\tilde{N}_{T|D}$ is the concentration of the donor-type trap states along the energy-axis. However, to systematically assess the influence of both acceptor-type and donor-type trap states on the photoelectrochemical performance of photoanodes, we have defined three parameters. Firstly, $\zeta = \frac{\tilde{N}_T}{N_D^+}$ denoting the ratio of the total number of trap states with respect to the ionized doping concentration, where $\tilde{N}_T = \tilde{N}_{T|A}$ or $\tilde{N}_T = \tilde{N}_{T|D}$ when acceptor or donor trap states are examined, respectively. Secondly, $f_{peak} = \frac{E_T - E_V}{E_G}$ representing the location of the peak of the distribution as a fraction of bandgap energy referred from the valence band edge, where $E_T = E_{T|A}$ or $E_T = E_{T|D}$ when acceptor or donor trap states are examined, respectively. Thirdly, σ_s to characterize the energetic distribution of trap states, where $W_{T|A} = W_{T|D} = \sigma_s \times k_B T$ and $k_B T \approx 25$ meV at room temperature.

Electrostatics of Photocatalytic SL Junctions with Bulk Trap States

By taking into account the net charge contribution from bulk trap states given by Eq. (7.9), the overall charge balance along the entire semiconductor-liquid junction can be expressed as

$$\rho_{sc} + \rho_T + \rho_L = 0. \tag{7.12}$$

Here, $\rho_{sc} = N_D^+ - N_A^- + p_{vb} - n_{cb}$ represents the charge contribution from the crystallinity of the semiconductor, where N_D^+ and N_A^- are respectively the concentrations of ionized impurities of donor and acceptor species (which always remain ionized due to their close proximity to the band edges).[33] Additionally, ρ_L is the charge in the liquid, balancing the charge in the semiconductor electrode and can be further broken down into[188]

$$\rho_L = zn_+ - zn_- + c_{H^+} - c_{OH^-}. \tag{7.13}$$

Eq. (7.13) is commonly known as the Gouy-Chapman model.[137,139,140] Here, $n_+ = c_{sup}^+ e^{[-z(\phi - \phi_b)/k_B T]}$ and $n_- = c_{sup}^- e^{[z(\phi - \phi_b)/k_B T]}$ are, respectively, the concentrations of the electrochemically inactive cations and anions forming the supporting electrolyte – where c_{sup}^+ and c_{sup}^- are their bulk concentrations and z denotes the charge number.[137,188] Furthemore, $c_{H^+} = c_{H^+}^0 e^{[-(\phi - \phi_b)/k_B T]}$ and $c_{OH^-} = c_{OH^-}^0 e^{[(\phi - \phi_b)/k_B T]}$, respectively, represent the concentrations of H$^+$ and OH$^-$ ions in the liquid – again, $c_{H^+}^0$

and $c^0_{OH^-}$ are their bulk concentrations. Finally, ϕ_b is the electrostatic potential in the bulk of the liquid that is arbitrarily chosen as our electrostatic reference potential. With the aid of Eq. (7.12), Poisson's equation for the SL junction can be written as[188]

$$\varepsilon\frac{d^2\phi}{dx^2} + \frac{d\varepsilon}{dx}\frac{d\phi}{dx} = -\left[\rho_{sc} + \rho_T + \rho_L\right]. \tag{7.14}$$

Where, ε is the dielectric constant that varies along the space vector x, since the semiconductor and liquid generally possess different values of ε.[1,129] Finally, the electrostatics of the SL junction under dark can be obtained by numerically solving Eq. (7.14) using standard self-consistent numerical techniques.[120,122,188] In particular, solving Poisson's equation (Eq. (7.14)) in this manner treats the SL junction as "adaptive Schottky contact", which allows the potential drop inside the liquid to change as a function of surface state charging, semiconductor doping and the applied bias. . Moreover, it enables one to capture both pinning and unpinning of the semiconductor band-edges at the solid-liquid interface.[188,206]

7.3 Results

7.3.1 Crystalline Hematite Photoanode-Aqueous Junction

As a model system, we have considered an n-type hematite photoanode performing the water oxidation reaction.[68–70,201,209,210] Hematite (α-Fe_2O_3) has been widely investigated for solar-assisted water splitting applications due to its inexpensive synthesis, suitable bandgap (1.9 eV - 2.2 eV) and superior chemical stability in aqueous solutions of pH $\geq$ 7.[1,13,54,57,60] In this part of our simulation, we have assumed a hematite photoanode with a bandgap (E_G) of $\sim$ 2.1 eV, immersed in an aqueous solution of pH = 13.6.[68] The extrinsic donor concentration is $N_D \sim 3.96\times10^{20}$ cm^{-3}, which is computed by assuming 1% of substitutional impurities and utilizing the

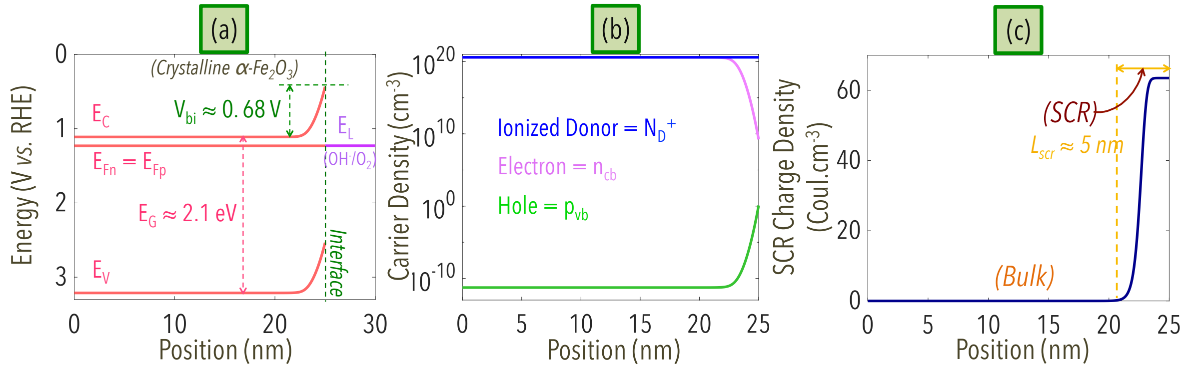

Figure 7.3: Calculated electrostatics of an idealized PEC junction between a perfectly crystalline hematite photoanode and an aqueous solution (pH = 13.6).[68] The computed band diagram in (a) exhibits the equilibration of Fermi levels on both sides of the SL interface. As can be seen from (b), the electron concentration in the bulk approaches the dopant concentration – expected for efficient n-type doping. Furthermore, with a span of ∼5 nm, the SCR region approximates the short minority carrier collection length commonly observed in hematite photoanodes.[57]

hematite lattice parameters.[226] Importantly, hematite photoanodes doped at this level (10^{20} cm^{-3}) remain “non-degenerate” due to its high effective density of states (N_C and N_V). This characteristic is commonly observed in metal oxide semiconductors (see the supporting information).[32,199,227] To maintain consistency with the photocatalysis literature, all the calculated energy band diagrams are drawn with respect to RHE, which is located -4.44 eV below the standard vacuum level reference commonly found in the device physics literature.[1,129,208]

Fig. 7.3 presents the computed electrostatics of an idealized crystalline hematite photoanode equilibrated with an aqueous solution (equivalently, OCC at dark). As can be seen in Fig. 7.3a, the calculated energy band diagram demonstrates a constant Fermi level ($E_{Fn} = E_{Fp} = E_L$) at +1.23 V *vs.* RHE. In addition, the photoanode exhibits V_{bi} ∼ 0.68 V, setting the maximum limit of the photovoltage ($V_{ph|max}$) extractable from this hematite-based PEC system (in the event of perfect flattening of the semiconductor bands upon illumination).[36] As expected, the hematite portion of the interface is depleted of electrons, within a SCR span of L_{scr} ∼5 nm, roughly correlating with the hole collection length reported in the literature (see Figs. 7.3b-c).[57,62] Interestingly, this idealized picture of a hematite photoanode demonstrates "satisfactory" electron conductivity due to efficient n-type doping. Meaning, all the excess electrons contributed by donor-impurities (*e.g.*, N_D^+: Ti^{4+}, Si^{4+}) are elevated to the conduction band and become mobile electrons (n_{cb}). This is evident from Fig. 7.3b, where the bulk is characterized by $N_D^+ \approx n_{cb}$ – delineating the complete ionization of extrinsic dopants. Importantly, efficient electron conduction in the bulk of a photoanode is needed to suppress electron-hole recombination in the photo-active SCR region, and therefore indirectly influences the interfacial electrochemical reaction.[1,210] Nevertheless, electron mobility and conductivity[115,215,216] (along with its extraction[12,210] at the substrate/electrode interface) is extraordinarily low in practical hematite-based photoanodes. This is often linked with the presence of intermediate defect trap states[19,53,148,210] and the 'small polaronic' nature of carrier conduction in hematite[115,214–216] – a topic we will explore next.

7.3.2 Impact of Bulk Trap States on the Photoelectrochemical Performance of Hematite Photoanodes

Impact of Acceptor-Type Trap States

We begin by analyzing the impact of acceptor-type trap states on hematite photoanodes, as summarized by the computed results in Figs. 7.4 and 7.5. The practical source of these trap states can be linked to the capture and localization of conduction band electrons (n_{cb}) by: (1) defect states at the TCO/hematite interface (forming the 'dead layer');[19,53,150] (2) intermediate trap states in the bulk of hematite;[210–212] and (3) Fe^{2+}-like polaronic states.[63,115,213–216] Electrons captured by these acceptor traps give rise to the net trapped charge $\rho_{T|A}$ as described by Eq. (7.6). Let us consider a distribution of acceptor traps that are gradually lowered deeper into the band gap, while fixing $\zeta = 1.48$ and $\sigma_s = 1$ (as shown in Fig. 7.4a). Specfically, we consider f_{peak} at

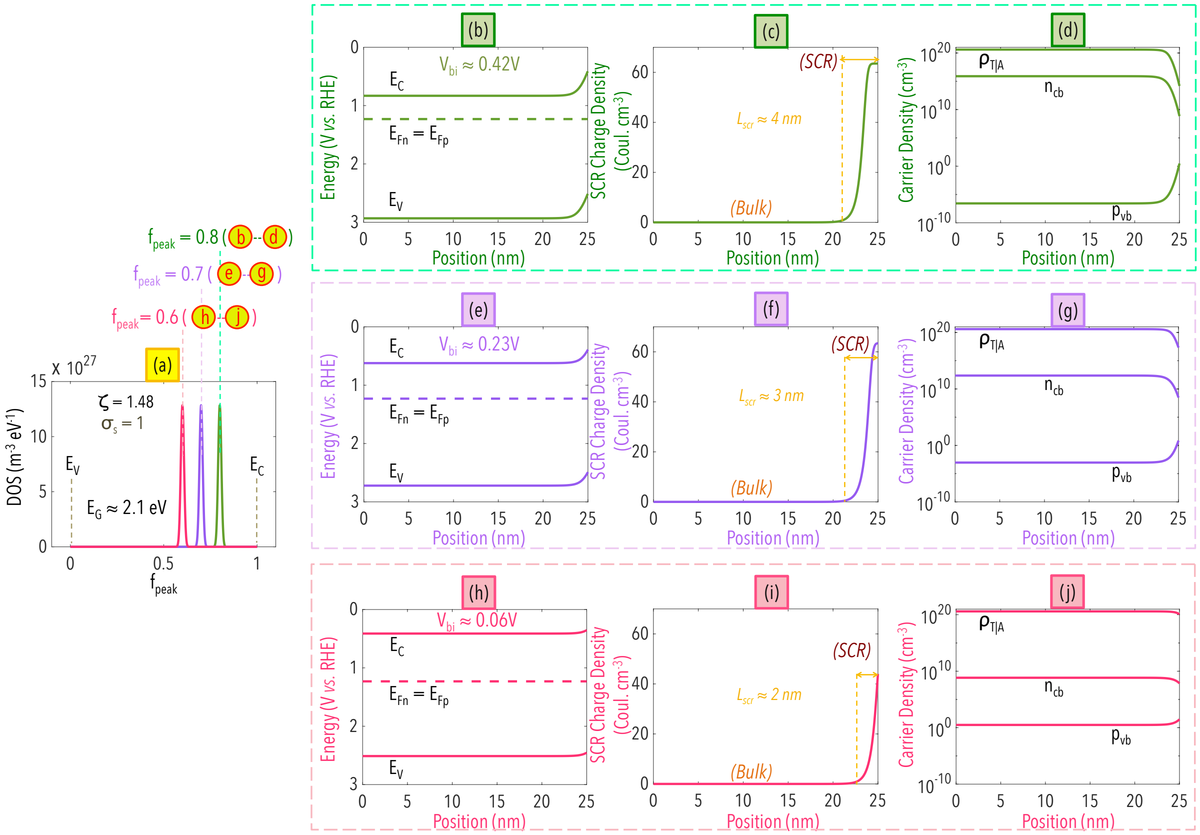

Figure 7.4: Calculated electrostatics of a hematite photoanode with a distribution of acceptor traps as expressed by Eq. (7.10), characterized by $\zeta = 1.48$ and $\sigma_s = 1$. The impact of shallow- to deep-level states are computed by varying f_{peak} from 0.8 (b-d, marked in green), through to 0.7 (e-g, marked in purple) and 0.6 (h-j, marked in red). As can be seen from the energy band diagrams in (b), (e) and (h), the built-in potential is gradually reduced, simultaneously decreasing the extent of $V_{ph|max}$. A reduction in L_{scr} (corresponding to the hole collection length) is also correlated with decreasing f_{peak} in (c), (f) and (i). The capture of conduction band electrons (n_{cb}) by acceptor traps ($n_{T|A}$) is also visible in (d), (g) and (j).

the values of 0.8 (green, Fig. 7.4b-d), 0.7 (purple, Fig. 7.4e-g) and 0.6 (red, Fig. 7.4h-j). This provides an excellent metric for studying the relative influence of shallow and deep level acceptor traps. In our estimate of ζ, we have assumed that 1.5% of the Fe^{3+} sites are replaced by lattice defects or equivalently, $\tilde{N}_{T|A} \approx 5.88 \times 10^{20}$ cm^{-3} (see the supporting information). From our calculated results in Fig. 7.4, the impact of the acceptor traps is found to be two-fold as their distribution is lowered deeper into the band gap: (1) the progressive reduction of available conduction band electrons (n_{cb}); (2) the gradual reduction of both V_{bi} (a measure of $V_{ph|max}$) and the span of the SCR (a rough measure of the hole collection length).

The progressive impact of deepening acceptor traps on n_{cb} can be seen in Figs. 7.4d, 7.4g and 7.4j. As acceptor states are placed further into the bandgap (f_{peak}: 0.8 → 0.6), the capture of the conduction band electrons becomes more prominent with n_{cb} in the bulk dropping from 7.87×10^{15} cm^{-3} to 6.92×10^{8} cm^{-3}. This can be compared with the idealized trap free value of 3.96×10^{20} cm^{-3} electrons in the conduction band (see Figs. 7.3b and 7.4d, 7.4g and 7.4j). Such low concentrations of electrons in the conduction band, due to trapping, can further contribute to the poor electron conductivity and inefficient doping observed in hematite samples.[115, 215, 216] It may even be that exceptionally high trap densities at the substrate/electrode interface significantly impede electron extraction (by lowering n_{cb}), thereby further enhancing electron-hole recombination in the bulk/SCR region and reducing the transfer of holes to the water oxidation reaction.[210]

Likewise, the progressive impact of deepening acceptor traps on $V_{ph|max}$ can be seen by comparing Fig. 7.3a with Figs. 7.4b, 7.4e and 7.4h. In the absence of trapping, the idealized hematite photoanode is predicted to have a maximum photovoltage of $V_{ph|max} \approx V_{bi} \approx 0.68$ V (see Fig. 7.3a). When acceptor traps are localized near the conduction band at $f_{peak} = 0.8$, this lowers to $V_{ph|max} \approx V_{bi} \approx 0.42$ V (see Fig. 7.4b). Moreover, as the trap states are lowered to $f_{peak} = 0.7$ and $f_{peak} = 0.6$, $V_{ph|max}$ falls further to ~ 0.23 V and ~ 0.06 V, respectively. This reduction in $V_{ph|max}$ and V_{bi} occurs because the hematite bulk Fermi level is forced to drop closer to the valance band maximum as the filled trap states drop lower. As the hematite Fermi level drops, it draws closer to the electrochemical potential of the aqueous solution (at +1.23 vs. RHE) and thereby lowers built-in voltage (V_{bi}) which is achieved through the equilibration between the hematite and liquid electrochemical potentials (see the discussion pertaining to Fig. 7.1). Importantly, this trapping driven collapse in V_{bi} severely limits the degree to which the photocurrent onset may be shifted cathodically by the photovoltage – a crucial and necessary component of unassisted solar water splitting.[20,21,71,84]

Similar trends have been observed in Mott-Schottky measurements of photoanodes,[20] where the flatband potential also moves towards the anodic direction and hinders the desired cathodic shift of the photocurrent onset. Overall, acceptor traps limit $V_{ph|max}$ far shy of its theoretical maximum (estimated from V_{bi} for an electrode without trapping), by capturing the conduction band electrons. Therefore, a photoanode prone to acceptor trapping is bound to operate at more anodic potential with respect to the H_2-evolution potential at 0 V *vs.* RHE. It is also important to note that acceptor traps may also lower the width of the SCR as shown in Figs. 7.4c, 7.4f and 7.4i. These results suggest SCR lengths in the range of 2-4 nm, in agreement with the extrodinarily short minority carrier collection lengths reported for hematite photoanodes in the literature.[1,57,62,217] This picture of the SCR/interfacial region suggests that acceptor trap states often mandate the application of large reverse potential to facilitate the interfacial hole collection/reaction – as is commonly supplied to practical hematite photoanodes (*e.g.* photocurrent saturation at 1.3 V *vs.* RHE and beyond).[68] The shift of the electrode flatband potential *vs.* RHE is summarized in Fig. 7.5a, where it is shown that significant acceptor trapping results in a marked

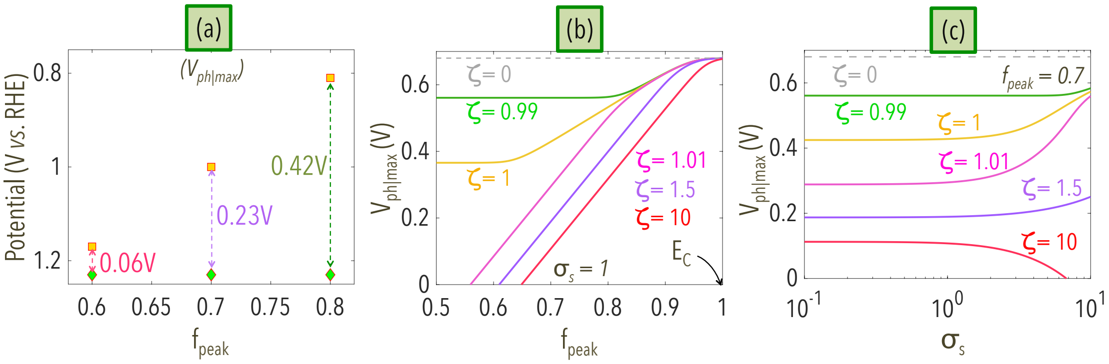

Figure 7.5: (a) Potential of the hematite photoanode *vs.* RHE, operating at the dark OCC (green diamond) and flatband condition (yellow square) drawn for the acceptor states as presented in Fig. 7.4. The flatband potential becomes increasingly anodic as the acceptor states are placed deep in the bandgap, leaving limited room for the desired cathodic shift of the photocurrent onset.[21] (b) Evolution of $V_{ph|max}$ as a function of the location of the peak of the distributed acceptor states. Here, we have assumed $\sigma_s = 1$ and ζ is allowed to change as 0 (grey), 0.99 (green), 1 (yellow), 1.01 (pink), 1.5 (purple) and 10 (red). (c) Evolution of $V_{ph|max}$ as a function of the spread of the distribution. In this case, f_{peak} is assumed to be fixed at 0.7 and ζ is allowed to take the same values as in the case of (b).

anodic shift upon illumination. Thus acceptor trapping can considerably impede the desirable cathodic shift in the onset of the photocurrent (by degrading $V_{ph|max}$).

Our analysis thus far is based upon acceptor traps with a fixed breadth ($\sigma_s = 1$) and fixed relative concentration ($\zeta = 1.48$). We will now further explore how varying these two parameters can alter the impact of acceptor traps. Fig. 7.5b presents the evolution of $V_{ph|max}$ as the peak position of acceptor traps is gradually lowered deeper into the bandgap ($f_{peak}: 1 \rightarrow 0.5$) for increasing values of ζ and a constant value of $\sigma_s = 1$. It can be seen that $V_{bi} \approx V_{ph|max}$ is dramatically lowered by acceptor traps located deep in the bandgap. The collapse in $V_{ph|max}$ proceeds quite rapidly when the concentration of acceptor traps exceeds the ionized dopant density ($\zeta \geq 1$). Consequently, when acceptor traps approach midgap ($f_{peak} \rightarrow 0.5$) and $\zeta \geq 1$, acceptor states can completely annihilate the built-in potential ($V_{bi} \rightarrow 0$, $V_{ph|max} \rightarrow 0$) resulting in a hematite photoanode that fails to produce a photovoltage and photocurrent of any significance. This theoretical insight provides a plausible explanation for the extremely low photocurrents observed in hematite photoanodes that are *not* annealed at high temperatures, supporting the hypothesis that high temperature annealing facilitates the removal of deep level traps.[53,60,228,229] It is also worthwhile to examine the evolution of $V_{ph|max}$ as a function of the trap-distribution breadth (σ_s) as presented in Fig. 7.5c. Here the peak location of the distribution is fixed at $f_{peak} = 0.7$ and ζ is allowed to vary from 0 to 10. Fig. 7.5c reveals that $V_{ph|max}$ is reduced substantially as the spread of the acceptor states gets narrower (becomes more localized in energy). This occurs because electrons in acceptor traps with narrower distributions are less easily promoted thermally to the conduction band, which in turn results in a lowering of the semiconductor Fermi level and a subsequent reduction in V_{bi} (as discussed earlier). Again, in Fig. 7.5c we see that $V_{ph|max}$ is substantially degraded when the acceptor trap concentration exceeds the ionized donor concentration ($\zeta \geq 1$) – though broadening in the trap distribution does help to some degree.

Impact of Donor-Type Trap States

Next, we shall theoretically analyze the impact of the donor traps on the photoelectrochemical performance of hematite photoanodes – assuming the absence of any acceptor traps. That being said, in this case, we have utilized Eq. (7.11) to model the distribution of donor traps. As discussed in the literature, donor traps in hematite can arise from oxygen vacancy defects (V_o).[220,221] Similar to our analysis of acceptor traps, we have evaluated the impact of donor traps on $V_{ph|max}$ as a function of both f_{peak} and σ_s (see Fig. 7.6). As can be seen in Fig. 7.6a, the influence of the donor states is negligible as f_{peak} is swept across the bandgap of an n-type hematite photoanode. This is because filled donor traps do not contribute to the overall charge balance of an n-type semiconductor.[143] Only if the donor traps are placed close to E_C, can they participate by beneficially donating further electrons to the conduction band (in the same manner as extrinsic dopants, as shown in Fig. 7.6b). This leads to a small in-

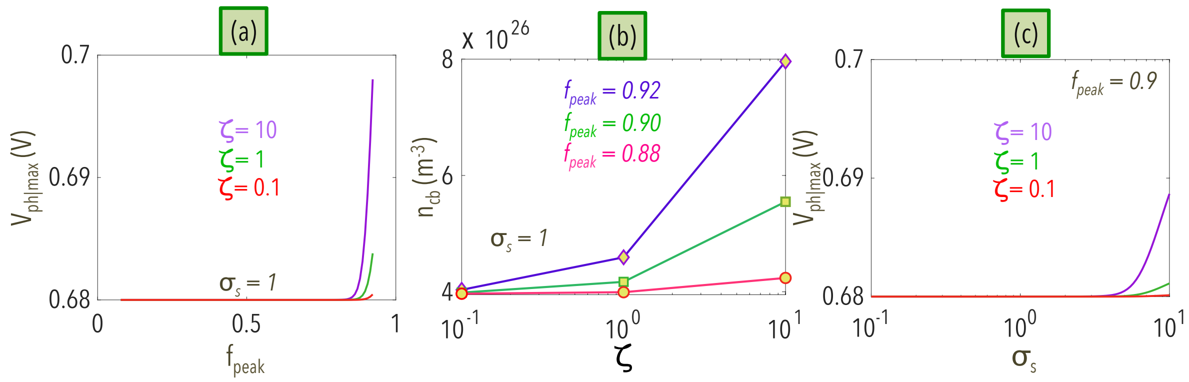

Figure 7.6: Calculated electrostatics of a hematite photoanode only with donor traps, as expressed by Eq. (7.11). Part (a) depicts the evolution of $V_{ph|max}$ with respect to the peak position of donor traps inside the bandgap (f_{peak}), assuming a fixed energetic breadth $\sigma_s = 1$ and varying the relative concentration (ζ) from 0.1 (red) to 1 (green) and 10 (purple). Whereas (b) depicts the electron doping activity of donor traps located close to the conduction band for various values of ζ and f_{peak}. This is also shown in (c), where enhanced broadening of σ_s results in an increase in $V_{ph|max}$ by raising the Fermi level slightly through the donation of electrons to the conduction band.

crease in $V_{ph|max}$ (or, equivalently, V_{bi}) by raising the Fermi level as shown in Fig. 7.6a. Similarly, donor traps with large spread can donate electrons to E_C and offer a small increase in $V_{ph|max}$ (as presented in Fig. 7.6c). Thus, bulk donor traps are generally benign or beneficial with respect to the carrier concentration and maximum achievable photovoltage of n-type photoanodes (as shown in Fig. 7.6a, c). This beneficial impact of "donor traps" on the electron concentration is in agreement with measurements in the literature, where conductivity improvements have been linked to donor-type oxygen vacancies and extrinsic dopants.[217, 220, 221, 230–232] In approximate agreement with the findings of Fig. 7.6, Mott-Schottky measurements have also exhibited roughly the same flatband potential (meaning negligible change in $V_{ph|max}$ or V_{bi}) and a lowered Mott-Schottky slope (implying increased conductivity) in the presence of such donor-type states.[230, 232]

Estimating the Impact of Polaronic States on the Maximum Attainable Photovoltage

In many oxide based anodes, electron polaron states are an intrinsic form of acceptor trapping.[57, 213, 233–235] They form due to strong electron-phonon coupling and therefore can be present even in a "perfect crystal".[213, 234] Thus, electron polarons can determine the true theoretical photovoltage maximum for even "perfectly synthesized" anodes and are the last topic of consideration in this study. They differ from other forms of acceptor trapping, in that their concentration can never exceed the total number of free electrons in a material – since they are a product of self-trapping. Such polarons are usually formed by electrons donated by intentionally introduced donor species. In the case of hematite, self-trapped electrons (polarons) are identifiable by temperature dependent electrical conduction measurements indicating thermally activated hopping between neighbouring Fe^{2+} and Fe^{3+} atoms.[63, 115, 213, 214]

To further refine our semiclassical parameters we have conducted first-principles electronic structure calculations of polaron trapping in hematite. More precisely, we have utilized the density functional theory (DFT+U) with additional on-site Hubbard corrections at Fe^{3+} ($U_{Fe^{3+}}$) and Fe^{2+} ($U_{Fe^{2+}}$) atoms to estimate the energetic location of polaronic states ($E_{T|A}$) inside the band gap of hematite.[213] To this end we have explored a range of U values on the polaron sites ($U_{Fe^{2+}}$) while keeping the U value on Fe^{3+} ions ($U_{Fe^{3+}}$) fixed at 4.3 eV as shown in Table 7.1. The details of our first-principles calculations may be found in the supporting information to this paper. Figs. 7.7a-b present the calculated electronic structure of α-Fe_2O_3 with $U_{Fe^{3+}} = U_{Fe^{2+}} = 4.3$ eV. The presence of an electron polaron state can be seen within the band gap at $E_{T|A} = 0.782$ eV below the conduction band (for a comparison to experimental values see the supporting information).[214] This corresponds to $f_{peak} = 0.64$ when considering a band gap of $E_G = 2.2$ eV as computed from our first-principles calculations.[213, 214] In general, we have found that the polaronic peak

Table 7.1: Energetic Location of Electron Polarons $(E_{T|A})$ from DFT+U Calculations and Corresponding Upper Bound Estimates of $V_{ph|max}$

$U_{Fe^{2+}}$ (eV)^a	$E_{T\|A}$ (eV)	f_{peak} (eV)	$V_{ph\|max}$ (V)^b
3.5	0.573	0.74	0.63 V
4.0	0.702	0.68	0.61 V
4.3	0.782	0.64	0.59 V

^{a} holding $U_{Fe^{3+}} = 4.3$ eV; ^{b} assuming $\sigma_s = 12.7$.

cannot be raised to much more than 0.573 eV from the conduction band minimum (corresponding to $U_{Fe^{2+}} = 3.5$ eV). Calculations with smaller values of $U_{Fe^{2+}}$ were attempted but convergence difficulties were encountered – indicating that the polaronic state might not be stable at much lower $U_{Fe^{2+}}$ values.

Let us continue with our semiclassical approach, as presented in Sec. 7.2, by considering the electrons localized at Fe^{2+}-like polaronic states in hematite as a distribution of acceptor-type states. Since the number of self-trapping electron polarons cannot exceed the number of donors (providing such electrons) we shall assume $\tilde{N}_{T|A} = N_D^+ \rightarrow \zeta = 1$. Now with $E_{T|A}$ and $\tilde{N}_{T|A}$ in hand, Eq. 7.10 can be utilized to explore the energetic distribution of polaron acceptor states by varying its spread (σ_s). A first-order estimation of σ_s for polaronic states can be performed by utilizing a first-principles derived two-site electron transfer model (discussed in the supporting information), resulting in a upper bound of approximately $\sigma_s \approx 12.7$ in hematite.[236]

Fig. 7.7c shows the refined band diagram of the idealized hematite-aqueous junctions considering $N_D^+ = 3.85\times10^{20}$ cm^{-3} and $E_G = 2.2$ eV (corresponding to the first-principles derived band gap). As depicted, the idealized hematite-aqueous junction exhibits $V_{bi} = 0.71$ V, elucidating the maximum attainable photovoltage or $V_{ph|max}$. This idealized electrostatic picture of the SL junction changes dramatically as electrons are self-trapped by polaronic states. Fig. 7.7d depicts the evolution of $V_{ph|max}$ as a function of the spread of the polaronic states (σ_s) for the first-principles derived f_{peak} values presented in Table 7.1. Clearly, the presence of the polaronic states de-

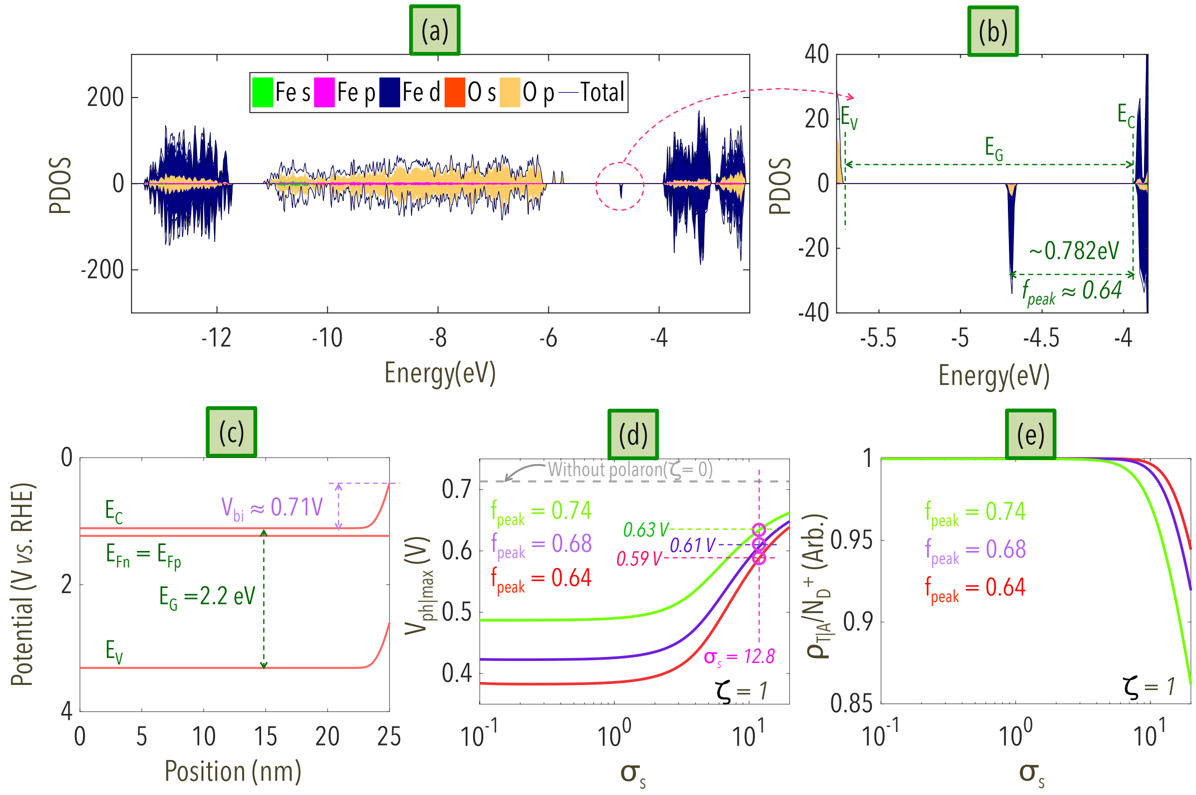

Figure 7.7: (a)-(b) α-Fe_2O_3 orbital projected density of states (PDOS) of the polaronic ground states as calculated from first-principles (with $U_{Fe^{3+}} = U_{Fe^{2+}} = 4.3$ eV). The electron polaron PDOS peak is more visible in (b) and is localized at $E_{T|A} = 0.782$ eV below the conduction band ($f_{peak} = 0.64$). (c) Calculated energy band diagram of the idealized α-Fe_2O_3-aqueous junction (using first-principles derived parameters). The photoelectrochemical junction is characterized by $V_{bi} = 0.71$ V. (d) Evolution of $V_{ph|max}$ as a function of σ_s for $f_{peak} = 0$ (dotted line), $f_{peak} = 0.64$ (red), 0.68 (purple) and $f_{peak} = 0.74$ (green). (e) Evolution of the concentration of the self-trapped electrons in polaronic states as a fraction of the total donated electron concentration and as a function of σ_s. We assume $\zeta = 1$ for all calculations in (d) and (e).

grades $V_{ph|max}$ from its idealized value, where the extent of the degradation becomes more severe with: (1) the degree of localization (low σ_s); and (2) the distance of these states from the conduction band edge (low f_{peak}). Both of these observations are in agreement with our earlier analysis in Sec. 7.3.2. Importantly, our upper bound estimate of $\sigma_s = 12.7$ in hematite, places a corresponding upper estimate on $V_{ph|max}$ between 0.59 V (at $f_{peak} = 0.63$) and 0.63 V (at $f_{peak} = 0.74$) for perfectly crystalline hematite anodes – as summarized in Table 7.1 and shown in Fig. 7.7d. These values correspond well with the photovoltage values reported in the literature.[20, 21, 53, 71] This is, in turn, directly limits the extent of the crucial cathodic shift of the photocurrent onset in hematite photoanodes in the absence of any further morphological defects.

Finally, let us explore the fraction of electrons self-trapped in polaronic states ($\rho_{T|A}$) as a function of σ_s with respect to the donor concentration N_D^+ as shown in Fig. 7.7e. In this case, $\rho_{T|A} \rightarrow 1$ corresponds to the drastic reduction of n_{cb}, in agreement with the practical observation of extraordinary low electron conductivity in hematite photoanodes.[115, 209, 210, 214] However, as the broadening of the polaronic state (σ_s) is increased, more electrons are able to gain enough energy to hop up to the conduction band reducing $\rho_{T|A} < 1$. Thus, it is plausible that enhanced polaron broadening can somewhat improve the conductivity of hematite photoanodes at exceptionally high doping concentrations. Nevertheless, it is important to note that our semi-classical model assumes a fixed polaron DOS distribution (at $\zeta = 1$) and does not account for the dynamical nature of electron self-trapping. Therefore it does not fully reflect the corresponding decrease in the polaron DOS when electrons are promoted to the conduction band in the regime $\rho_{T|A} < 1$. This dynamical impact is likely to be small for the system properties considered herein, a full consideration of dynamical trapping within this semi-classical model is left for future work.

7.4 Conclusion

We have presented a self-consistent numerical method for theoretically estimating the impact of bulk trapping phenomena on the maximum attainable photovoltage at semiconductor-liquid interfaces. This was accomplished by extending state-of-the-art descriptions of electron and hole trapping in semiconductors common to the solid-state device physics literature. By considering the concentration and energetic distribution of bulk trap states, our study revealed that: (1) acceptor-type bulk trap states can significantly lower the maximum attainable photovoltage and (2) may dramatically lower the number of free carriers. These effects were specifically investigated in hematite, where trapping induced lowering of the maximum photovoltage can be correlated with a reduced cathodic shift in the photocurrent onset. Likewise, lower concentrations of mobile electrons due to trapping can be linked to the extraordinarily low electron conductivity and mobility in hematite; particularly, non-polaronic trapping by high concentrations of crystalline defects that may arise at the interface between a photoanode and a conducting back electrode (*e.g.*, TCO). The negative impact of acceptor trap states were determined to intensify as they became more localized in energy and/or were lowered deeper below the conduction band minimum. Conversely, donor-type trap states were determined to have a negligible impact on heavily doped n-type photoanodes – and may even be a little beneficial, if raised close enough to the conduction band to donate electrons. Finally, we assessed the impact of electron polaron states, which can be viewed phenomenologically as an intrinsic form of acceptor trapping, with the aid of first-principles calculations. It was determined that electron polaron trap states likely further reduce the maximum achievable photovoltage of hematite photoanodes in a range that lies near experimentally reported photovoltages. In this study we have not evaluated the impact of surface trapping states on the photovoltage (as independent from the bulk distribution), nor have we examined the impact of specific surface modifications/heterostructures, this is left for future work.

7.5 Acknowledgement

The authors would like to acknowledge the financial support from NSERC of Canada and FQRNT of Québec, and the computational resources provided by the Canadian Foundation for Innovation, CalculQuebec and Compute-Canada.

7.6 Supporting Information

7.6.1 Calculation of the Modeling Parameters

Doping Concentration

Ref. [226] provides the lattice parameters of the hexagonal unit cell of a hematite sample: $a \approx 5.038$ Å, $c \approx 13.771$ Å, $Z = 6$ and space group: R$\bar{3}$c. Therefore, the atomic density can be determined as

$$N_{atom} = \frac{5 \times Z}{a^2 c \sin(60)}.$$

Consequently, 1% substitutional doping represents $N_D^+ = \frac{2N_{atom}}{3\times100} \approx 3.96\times10^{26}$ m^{-3}.

Non-Degeneracy of the Hematite Photoanode

In the case of non-degenerate n-type semiconductors, the Maxwell-Boltzmann approximation can be utilized to describe the occupational probability of electrons if $E_C - E_{Fn} \geq 3k_BT$.[33, 237] Accordingly, the non-degeneracy of hematite photoanodes utilized in this work can be validated as $E_C - E_{Fn} = 4.61 \times k_BT$ (Secs. 3.1, 3.2.1 and

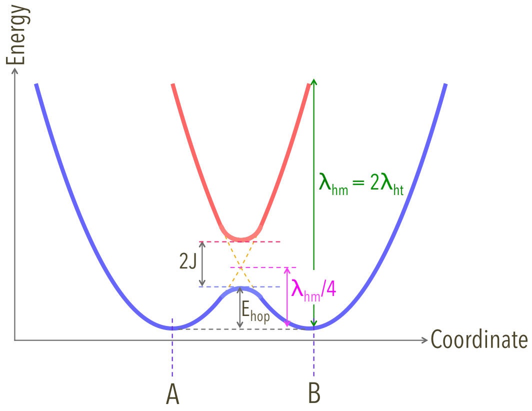

Figure 7.8: Two-site non-adiabatic electron transfer picture in the context of polaronic hopping in hematite. In this case, the localized electron hops between two neighbouring sites A and B by overcoming the barrier E_{hop}.

3.2.2) and $E_C - E_{Fn} = 4.64 \times k_B T$ (Sec 3.2.3). Here, $E_C - E_{Fn} = k_B T \times \ln\left[\frac{N_C}{n_{cb}}\right]$ and $N_C = 4 \times 10^{22}$ cm^{-3}.[32, 199, 227]

Calculation of ζ

Let us consider that 1.5% of the remaining Fe^{3+} sites host the lattice defects. Accordingly, $\tilde{N}_{T|A} = 0.015 \times \left[\frac{2}{3}N_{atom} - N_D^+\right] \approx 5.88 \times 10^{26}$ m^{-3}. Therefore, $\zeta = \frac{\tilde{N}_{T|A}}{N_D^+} \approx 1.48$.

Calculation of σ_s for Polaronic States in Hematite

In hematite, a Fe^{2+}-like polaronic state is formed when an electron becomes localized at a Fe^{3+} site. Now, the hopping of this localized electron (electrical conduction) is possible between two neighbouring sites (A and B) at the expense of a thermally activated process with an energetic barrier of E_{hop}. This electron transfer process is illustrated in Fig. 7.8 by utilizing the two-site non-adiabatic electron polaron picture.[213, 233, 236] Here, J is the electronic coupling between the polaronic sites A and B. In the non-adiabatic limit $J \ll k_B T$ – where k_B is Boltzmann's constant and T is the temperature. Moreover, λ_{hm} and λ_{ht} are the reorganization energies for homogenous and heterogenous electron transfer, respectively. The two are related by $\lambda_{ht} = \lambda_{hm}/2$.[236] Within the Gerischer-Hopfield electron-transfer picture, the reduced (*red*) polaronic state (Fe^{2+}) can be approximately described by a density of states (DOS) in the form of[233,236,238]

$$D_{red}\left(E\right) = \frac{1}{\sqrt{4\pi\lambda_{ht}k_BT}} \exp\left[-\frac{\left(E - E_{T|A}\right)^2}{4\lambda_{ht}k_BT}\right]. \tag{7.15}$$

where E is the single-particle energy (using the same notation as this manuscript). From existing first-principles calculations in the literature the magnitude of λ_{hm} can be estimated from the non-adiabatic hopping barrier $\lambda_{hm}/4 \approx 0.50$ eV between polaron sites in hematite.[214] The Gerischer-Hopfield DOS can be related to the distribution of the acceptor-type trap states by rewriting Eq. 7.15 as

$$D_{red}\left(E\right) = g_{T|A}\left(E\right) = \frac{g_{T|A}\left(E\right)}{N_{T|A}} = \frac{1}{\sqrt{\pi}\,W_{T|A}} \exp\left[-\left(\frac{E - E_{T|A}}{W_{T|A}}\right)^2\right]. \tag{7.16}$$

Comparing Eqs. 7.15 and 7.16, we obtain $\sigma_s = \sqrt{\frac{4\lambda_{ht}}{k_BT}} \approx 12.7$ (by utilizing $W_{T|A} = \sigma_s \times k_BT$, $k_BT = 24.8$ meV and $\lambda_{ht} = 1.00$ eV[214,236]). These equations assume that the hopping transitions are non-adiabatic. Since, many of the transitions in hematite are adiabatic ($J \gg k_BT$),[213,236] with a correspondingly lower activation barrier, this likely lies in the upper range of hematite polaron broadening.

7.6.2 Boundary Conditions for Poisson's Equation

Poisson's equation [Eq. (14)] for the semiconductor-liquid junction was solved by utilizing the standard Gummel iterative technique. Details regarding this numerical procedure can be found in the literature.[120,122,188,206,208] The unique solution of the potential in the bulk of the electrode satisfies charge neutrality ($\rho_{sc} + \rho_T + \rho_L = 0$) and can be obtained by either: (1) imposing a Neumann boundary condition on the potential; or (2) by numerically searching for the root of $\rho_{sc} + \rho_T + \rho_L = 0$ *via* a standard root-finding algorithm. On the other hand, the potential in the bulk of the liquid was set to some pre-defined value (such as the value of the local vacuum level), which numerically corresponds to a Dirichlet boundary condition.

Table 7.2: Parameters from the DFT+U calculation ($U_{Fe^{3+}} = U_{Fe^{2+}} = 4.3$ eV)

Parameters	Experiment	DFT (PBE + 4.3, Fe_pv)
Lattice parameter, a (Å)	5.035[a]	5.087
Lattice parameter, c (Å)	13.747 [a]	13.907
Fe – O bond (Å)	1.945 × 3, 2.113 × 3 [a]	1.972 × 3, 2.125 × 3
Bandgap (eV)	1.9–2.2 [b,c]	2.2
Energetic location of the polaronic state (eV)	0.82[d]	0.782
Saturated polaron concentration (cm^{-3})	—	3.8508×10^{22}

[a] Ref.[239]; [b] Ref.[1]; [c] Ref.[240]; [d] Ref.[214].

7.6.3 Details of the First-Principles Calculation

All first-principles calculations were performed within the Vienna Ab initio Simulation Package (VASP), utilizing the Perdew-Burke-Ernzerhof (PBE) generalized gradient approximation (GGA) with projector augmented wave (PAW) potentials.[241–247] The original antiferromagnetic α-Fe_2O_3 structure was obtained from Materials Project with a R$\bar{3}$c space group.[248] The structures were fully relaxed until all interatomic forces were converged to less than 0.02 eV/Å. A plane-wave cutoff energy 650 eV and a Gaussian smearing width 0.01 eV were used for all the simulations. Calculations of polaronic state were performed using a 120-atom-sized supercell. The 2×2×1 supercell were sampled with 2×2×2 k-point mesh. Due to exchange-correlation errors, standard density functional theory (DFT) functionals underestimate of the band gap and polaronic states of transition metal oxides.[213] In this study, we applied the DFT + U approach with effective Hubbard U parameter 4.3 eV for Fe 3d states and PAW potentials with valence $3p^6 3d^6 4s^2$ for Fe atoms.[249–251] The chosen U value and PAW potential were taken from ab initio piecewise linearity calculations found in the literature.[213]

Chapter 8

Conclusion

In this research, a comprehensive theoretical study has been performed to formulate the semiclassical modeling of the electrostatics and charge transport phenomena at the photocatalytic semiconductor-liquid interfaces. The scientific discussion presented in this work includes: (1) theory of the surface states occupation and equilibration; (2) theoretical extraction of various capacitive components at the SL junctions and their correlation with the capacitance spectroscopy measurements; (3) numerical formulation of the combined drift-diffusion equations at the SL junctions based on robust assumptions and appropriate boundary conditions; (4) self-consistent computations of the photovoltage and photocurrent (two of the most commonly measured quantities in PEC experiments); (5) numerical modeling of the charge captured by the bulk trap states and its impact on degrading the maximum of attainable photovoltage and majority carrier transportation; and (6) theoretical probing of the key processes influencing the performance of solar-assisted water splitting.

8.1 Global Conclusions

Conclusions from Chapter 3

1. Combined Poisson equation must be solved throughout the entire span of the semiconductor-liquid junctions, whereas the electron and hole continuity equations need to be solved only inside of the semiconducting electrode.

2. Section 3.5.3 provides a detailed documentation of the discretized version of the combined Poisson equation, which is particularly developed for the simulation of typical SL junctions.

3. Similarly, the derivations of the discretized electron and hole continuity equations are documented in Section 3.6.

Conclusions from Chapter 4

1. Relative values of the rate constants that characterize various charge transfer processes *via* surface states play the pivotal role in determining the overall surface states dynamics at a semiconductor-liquid interface. As an impact, the Fermi-level of the surface state can take values that falls within the respective Fermi-levels of the semiconductor and the liquid phases.

2. To predict the surface states equilibration process at a practical SL junction, it is imperative to determine the energetic location of the surface states within the bandgap of the semiconductor. This conclusion can be supported by the distinctive equilibration processes of the shallow- and deep-level surface states that are commonly observed in the experimental procedures.

3. In the case of the wide bandgap semiconductors, the shallow-level surface states most likely equilibrate entirely with the semiconducting electrode, whereas the

deep-level surface states most likely exhibit partial equilibration with the semiconductor and liquid electrolyte.

4. In practical capacitance spectroscopy, the charging/discharging of the shallow-level surface states in synchronization with the applied AC voltage is translated into non-linear trends in the Mott-Schottky plot. This characteristic non-linearity in Mott-Schottky plot usually appears very close to the flatband potential of the electrode and directly corresponds to the performance-degrading 'band level unpinning' event due to the gradual filling/emptying of surface states.

5. Deep-level surface states at the SL interfaces, however, usually appear as classical 'plateau' in the state-of-the-art capacitive measurements. More importantly, the location of this plateau strongly depends on the relative values of the rate constants. This, in turn, delineates that the location of the plateau does not necessarily correspond to the exact location of the deep-level surface states with respect to the semiconductor band edges.

Conclusions from Chapter 5

1. The results analysis in Section 5.3 has attributed the simultaneous captures of the photovoltage and photocurrent at the SL junctions to the complete numerical solutions of the coupled drift-diffusion equations. In this case, the minority carrier transport equation needs to be solved to capture the interfacial concentration of the minority carriers (which gives rise to the photocurrent). The majority carrier transport equation must be solved, in parallel, to capture the dynamic screening in the space charge region under the active illumination (which gives rise to the photovoltage).

2. The methodology deduced in Section 5.2 was demonstrated to exhibit its scope to correlate theoretical calculations with observable quantities from the practical PEC experiments. This includes the computations of the photovoltage, onset and saturation of the photocurrent, interfacial hole transfer and bulk hole relaxation, interfacial recombination, screening processes in the space charge region, and the suppression of back-reactions.

Conclusions from Chapter 6

1. The combined Poisson-continuity equations must be solved with appropriate boundary conditions to guarantee the self-consistent capture of both the photovoltage and photocurrent.

2. The incorporation of the appropriate boundary conditions is essential to obtain a direct point-to-point match between the photocurrent observed practically and the photocurrent obtained theoretically (with meaningful applied external potentials).

Conclusions from Chapter 7

1. Mobile carriers (electrons in the conduction band and holes in the valence band) can be captured by the trap states in the interior of the semiconductor. The bulk processes of this nature deteriorate the solar harvest of photogenerated carriers and indirectly reduce the interfacial transfer of the minority carrier.

2. The incorporation of charge contribution from the captured carriers by both the donor- and acceptor-types states should be considered for reliable computation of the band diagram electrostatics.

3. In the case of photoanode, the presence of acceptor-type trap states can degrade the maximum attainable photovoltage and limit the desired cathodic shift of the

on-set of the photocurrent. Simultaneously, electron extraction at the bulk contact is also impeded due to the low concentration of available mobile electrons. This can be linked with the extraordinarily low electron conductivity in the metal-oxide photoanodes, which is measured regularly *via* different electrode characterization experiments.

4. Conversely, the donor states, located close to the conduction band of the photoanodes, can enhance the electron extraction at the bulk contact by increasing the conduction band electron concentration. Nevertheless, the impact of donor states on the maximum achievable photovoltage and flatband potential are negligible.

8.2 Claims to Originality

The work presented in this thesis has resulted in several original contributions in the field of photoelectrolysis, photocatalysis and the modeling of semiconductor-liquid interfaces.

1. A complete numerical formulation of the coupled Poisson-continuity equations for the photocatalytic semiconductor-liquid interfaces has been developed in detail. This derivation is based on robust assumptions (see Section 3.3) in order to closely emulate the practical operations of the SL interfaces. The derivation also critically addresses many of the key limitations of the existing computational schemes (see Section 2.5.2 for details) and consequently extends the scope of semiclassical treatments in the domain of modeling of water splitting SL junctions.

2. The theoretical reproduction of various experimental parameters and characteristics, as presented in the published manuscripts from this work, can potentially

lead to an improved understanding of the fundamentals that govern artificial photosynthesis. The computational results presented throughout this thesis demonstrate accurate extraction of: the band diagram and potential distribution, carrier concentrations and their lifetimes, photovoltage, photocurrent, junction capacitance, Mott-Schottky plot, surface states occupations, impacts of the trap-assisted bulk processes, generation/recombination processes etc. A list of these parameters and characteristics is provided in Table 8.1.

3. This work has also demonstrated theoretical decoupling and probing of the key processes involving the solar-assisted water splitting reactions, which are often very difficult to perform *via* experimental procedures without the interference of other processes. For instance, Figures 5.6c and 6.4 present the calculations of the rate of interfacial minority carrier transfer (leading to the desired reaction) and rate of recombination (carrier loss) in a decoupled manner. Nevertheless, the numerical computation of this nature can quantitatively outline what would be the optimal values of different parameters, *e.g.*, lifetime of the carriers, rates of photogeneration and interfacial carrier transport, in order to maximize the photovoltage generation or to obtain a particular on-set of photocurrent.

4. This work manifests a theoretical platform to include the impact of the bulk trap states – one of the key determinants of the overall photoelectrochemical process at a typical SL junction. This numerical formulation can be utilized to theoretically probe various bulk processes including the transport of the majority carriers and the limit of the maximum attainable photovoltage.

5. The theory of surface states equilibration at the SL junctions in Chapter 4 has considered both of the detrimental (as recombination centre) and beneficial (indirect carrier transport to the liquid) roles of surface states, which aptly

Table 8.1: Theoretical extractions of the parameters and characteristics

Property	**Reference (in thesis)**
Energy-Levels and Potentials	
Electrostatic Potential	Figures 4.2c, 4.5b
Potential Drops	Figures 4.3b-c, 4.7b-c
Energy Band Diagram	Figures 4.2a-b, 4.5a, 5.5a-b, 6.2a-c, 7.3a, 7.4b, e, h, 7.7c
Carrier Concentrations and Occupations	
Electron Concentrations	Figures 5.6a, 7.3b, 7.4d, g, j, 7.6b
Hole Concentrations	Figures 5.6a-b, d, 7.3b, 7.4d, g, j
Charge Density	Figures 5.5c, 7.3c, 7.4c, f, i
Occupation of Surface States	Figures 4.3a, 4.5d, 4.7d
Charge Trapped in Bulk States	Figures 7.4d, g, j
Capacitances and Mott-Schottky Analysis	
Surface States Capacitance	Figures 4.3d, 4.6a, 4.7e
Semiconductor Capacitance	Figures 4.3e, 4.6b
Liquid Capacitance	Figures 4.3f, 4.6c
Junction Capacitance	Figures 4.4a-b, 4.6d-e
Mott-Schottky Plot	Figures 4.4c, 4.6f, 4.7f
Others	
Photovoltage	Figures 5.5a-b, 6.2c, 7.5, 7.6a, c, 7.7d, e
Photocurrent	Figures 5.7a-c, 6.3
Electric Field	Figure 5.5d
Generation	Figure B.1a
Recombination	Figure B.1a
Recombination Rate Constant	Figures 5.6c, 6.4
Lifetime of the Interfacial Holes	Figures B.1b

underscores the significance of this kind of analysis to explore the dual role played by surface states.

6. The choice of boundary conditions utilized in the numerical simulation plays a pivotal role in replicating practical photocurrent response along with the meaningful band diagram alignment – an important corollary deduced from Chapter 6.
7. A considerable amount of effort has been directed throughout this research with an aim to correlate experimentally observable quantities with the theoretical calculations. These results can allow one to theoretically determine and/or optimize the key electrostatics and charge transport properties at the SL junctions. The knowledge from the numerical analysis of this nature can set the guideline to engineer the performance of practical PEC devices.
8. The originality of this research work can be further supported by the quality of the journals that published the critical findings.

8.3 Future Work

1. As explained earlier in Section 3.3.5, the specific adsorption/desorption of the ions on the inner Helmholtz plane has not been explicitly considered in this numerical study. Undoubtedly, the inclusion of Stern layer dynamics, which gives rise to the adsorbed charges at the interface, remains one of the key challenges towards developing practical models for the combined photocatalytic SL junctions. One possible solution might come from the atomistic modeling of the Stern layer phenomena. It is also important to revisit relevant theories and analytical models reported in various fields of literature (metal-electrolyte junctions, ion-sensitive field-effect transistor or ISFET etc.) that addressed

similar adsorption/desorption phenomena occurring at different types of solid-liquid interfaces. Up to now, the calculation of the Stern layer charge (ρ_{ad}) in a self-consistent fashion remains largely unclear and thus it requires urgent theoretical effort in the near future.

2. A critical extension of the models presented in this thesis would be the incorporation of the possible mixed reactions at the photocatalytic interface. For example, at the water-oxidative photoanodes, we have considered OER/ORR as the only forward/reverse reactions (see Sections 3.3.3 and 3.3.4). However, if the semiconductor is able to transfer electrons to the liquid, the photoanode can exhibit reductions of both O_2 and H^+ species in the liquid. Consequently, the liquid Fermi-level will not be solely determined by the OH^-/O_2 species. This situation can be further complicated if the semiconductor is prone to corrosive reactions. Therefore, the inclusion of mixed reactions will allow one to compute a more realistic liquid Fermi-level along with the complex electrochemical activity of the interface. This improvement in the charge transport picture of the SL junction will offer better accuracy of the computed results from these models.

3. In the most simple picture of minority carriers transport to the liquid, the photoelectrochemical reaction is assumed to be a first-order reaction.[101] However, the recent experimental results have indicated the possibility of higher-order reaction at several oxide-semiconductor based photoanodes, such as Fe_2O_3,[68] $BiVO_4$[252] and TiO_2.[253] Therefore, an intriguing future extension would be the incorporation of the higher-order reaction dynamics into the domain of semi-classical approach.

4. Throughout the simulations, as presented in this work, the temperature is deliberately considered as constant. Nevertheless, it would be interesting to model the spatial variation of temperature along the photoelectrodes.

5. In addition of the basic PEC set-up (see Figure 2.3b), it would be equally important to model the complicated PEC configurations (as tandem cells) that are often fabricated in the state-of-the-art experimental studies. Furthermore, recent improvements of anodic PEC performance are often achieved by nanostructuring, surface coating and better geometry of the electrodes. Therefore, to make the SL junction modeling tools well-aligned with the up-to-date experimental set-ups, it is imperative to take these effects/modifications in account.

6. The numerical methodology to compute the impact of bulk trap states, as presented in Chapter 7, is developed for the SL junctions working under dark conditions. Future work in this direction need to implement the modified forms of the electrons and holes continuity equations so that the bulk processes at an illuminated photoelectrodes can also be captured.

Appendix A

Semiconductor Data

A.1 TiO_2

Table A.1: TiO_2 parameters

Parameter	Value
Bandgap (eV)[173]	3.0
Electron Effective Mass[254]	10
Hole Effective Mass[254]	0.8
Effective Density of States in Conduction Band (cm^{-3})[254]	7.92×10^{20}
Effective Density of States in Valence Band (cm^{-3})[254]	1.79×10^{19}
Dielectric Constant[254]	12
Location of the Shallow Level Surface States from E_C (eV)[179,180]	0.3-0.5
Location of the Deep Level Surface States from E_C (eV)[185]	1.4

A.2 Hematite (α-Fe$_2$O$_3$)

Table A.2: Hematite parameters

Parameter	Value
Bandgap (eV)[1]	2.1
Electron Affinity (eV)[10]	3.96
Electron Effective Mass[32]	137
Hole Effective Mass[32]	54.4
Effective Density of States in Conduction Band (cm^{-3})[32]	4×10^{22}
Effective Density of States in Valence Band (cm^{-3})[32]	10^{22}
Dielectric Constant[32]	32
pH[68]	13.6

Appendix B

Theoretical Extraction of Parameters and Characteristics

B.1 Numerical Results

Theoretical computations demonstrating the spatial evolutions of the generation and recombination rates are shown in Figure.B.1a. In this case, we have considered the

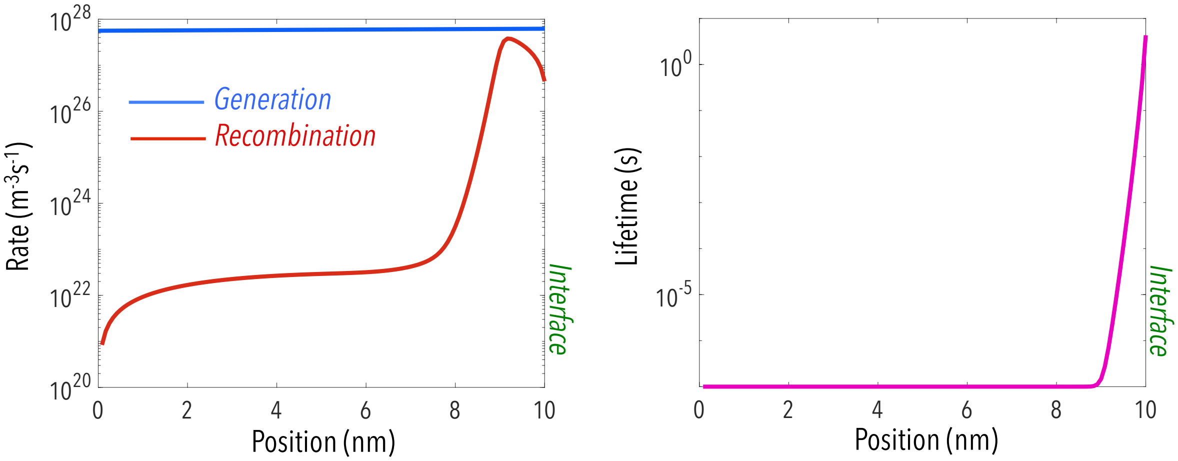

Figure B.1: (a) Calculated rates of generation (marked in blue) and recombination (marked in red) for the hematite photoanode in Chapter 6 operated at potential ~ 1.45 V *vs.* RHE. (b) Calculated hole lifetime for the same PEC set-up utilizing the hematite photoanode.

PEC set-up of Chapter 6 operated at an electrode potential of ~ 1.45 V *vs.* RHE. Furthermore, the spatial evolution of minority carrier lifetime for the same photoanode is also exhibited in Figure. B.1b.

Appendix C

List of Acronyms

Acronym	Full Format
PEC	Photoelectrochemical
OER	Oxygen Evolution Reaction
ORR	Oxygen Reduction Reaction
HER	Hydrogen Evolution Reaction
HOR	Hydrogen Oxidation Reaction
OCC	Open Circuit Condition
NHE	Normal Hydrogen Electrode
RHE	Reversible Hydrogen Electrode
EHP	Electron-Hole Pair
SCR	Space Charge Region
SRH	Shockley Read Hall
SL	Semiconductor-Liquid
MS	Metal-Semiconductor
SS	Surface State
SC	Semiconductor
L	Liquid
BLP	Band Level Pinning
FLP	Fermi-Level Pinning
VB	Valence Band
CB	Conduction Band
FTO	Fluorine-doped Tin Oxide
TCO	Transparent Conductive Oxide
IHP	Inner Helmholtz Plane
OHP	Outer Helmholtz Plane

Acronym	Full Format
GCS	Gouy-Chapman-Stern
DD	Drift-Diffusion
SG	Scharfetter-Gummel
DFT	Density Functional Theory
VASP	Vienna Ab initio Simulation Package
PBE	Perdew-Burke-Ernzerhof
GGA	Generalized Gradient Approximation
PAW	Projector Augmented Wave

Bibliography

[1] R. van de Krol and M. Grätzel, editors. *Photoelectrochemical hydrogen production.* Springer, 2012.

[2] M. G. Walter, E. L. Warren, J. R. McKone, S. W. Boettcher, Q. Mi, E. A. Santori, and N. S. Lewis. Solar water splitting cells. *Chemical Reviews*, 110:6446–6473, 2010.

[3] N. S. Lewis and D. G. Nocera. Powering the planet: Chemical challenges in solar energy utilization. *Proceedings of the National Academy of Sciences of the United States of America*, 103(43):15729–15735, 2006.

[4] J. Su and L. Vayssieres. A place in the sun for artificial photosynthesis. *ACS Energy Letters*, 1:121–135, May 2016.

[5] N. S. Lewis. Toward cost-effective solar energy use. *Science*, 315(5813):798–801, 2007.

[6] B. A. Pinaud, J. D. Benck, L. C. Seitz, A. J. Forman, Z. Chen, T. G. Deutsch, B. D. James, K. N. Baum, G. N. Baum, S. Ardo, H. Wang, E. Miller, and T. F. Jaramillo. Technical and economic feasibility of centralized facilities for solar hydrogen production via photocatalysis and photoelectrochemistry. *Energy and Environmental Science*, 6(7):1983–2002, 2013.

[7] M. Grätzel. Photoelectrochemical cells. *Nature*, 414:338–344, 2001.

[8] O. Khaselev and J. A. Turner. A monolithic photovoltaic-photoelectrochemical device for hydrogen production via water splitting. *Science*, 280:425–427, 1998.

[9] A. J. Bard and M. A. Fox. Artificial photosyntheis: Solar splitting of water to hyrdrogen and oxygen. *Accounts of Chemical Research*, 28:141–145, 1995.

[10] C. A. Grimes, O. K. Varghese, and S. Ranjan. *Light, Water, Hydrogen The Solar Generation of Hydrogen by water Photoelectrolysis.* Springer, 2008.

[11] K. Rajeshwar, R. McConnell, and S. Licht, editors. *Solar Hydrogen Generation–Toward a Renewable Energy Future.* Springer, New York, NY, 2008.

[12] O. Zandi and T. W. Hamann. The potential versus current state of water splitting with hematite. *Physical Chemistry Chemical Physics*, 17:22485, 2015.

[13] R. Van de Krol, Y. Q. Liang, and J. Schoonman. Solar hydrogen production with nanostructured metal oxides. *Journal of Materials Chemistry*, 18:2311–2320, 2008.

[14] M. G. Kibria and Z. Mi. Artificial photosynthesis using metal/nonmetal- nitride semiconductors: Current status, prospects, and challenges. *Journal of Materials Chemistry A*, 4:2801, 2016.

[15] I. Cesar, A. Kay, J. A. G. Martinez, and M. Grätzel. Translucent thin film Fe_2O_3 photoanodes for efficient water splitting by sunlight: nanostructure-directing effect of Si-doping. *Journal of the American Chemical Society*, 128(14):4582–4583, 2006.

[16] A. Kay, I. Cesar, and M. Grätzel. New benchmark for water photooxidation by nanostructured α-Fe_2O_3 films. *Journal of the American Chemical Society*, 128(49):15714–15721, 2006.

[17] N. Guijarro, M. S. Pre ́vot, and K. Sivula. Surface modification of semiconductor photoelectrodes. *Physical Chemistry Chemical Physics*, 17:15655, 2015.

[18] M. Rioult, H. Megnan, D. Stanescu, and A. Barbier. Single crystalline hematite films for solar water splitting: Ti-doping and thickness effects. *Journal of Physical Chemistry C*, 118(6):3007–3014, 2014.

[19] O. Zandi, B. Klahr, and T. W. Hamann. Highly photoactive Ti-doped α-Fe_2O_3 thin film electrodes: Resurrection of the dead layer. *Energy and Environmental Science*, 6:634, 2013.

[20] J. Jang, C. Du, Y. Ye, Y. Lin, X. Yao, J. E. Thorne, E. Liu, G. McMahon, J. Zhu, A. Javey, J. Guo, and D. Wang. Enabling unassisted solar water splitting by iron oxide and silicon. *Nature Communications*, 6:7447, 2015.

[21] J. E. Thorne, S. Li, C. Du, G. Qin, and D. Wang. Energetics at the surface of photoelectrodes and its influence on the photoelectrochemical properties. *Journal of Physical Chemistry Letters*, 6:4083–4088, 2015.

[22] O. Zandi and T. W. Hamann. Enhanced water splitting efficiency through selective surface state removal. *Journal of Physical Chemistry C*, 5:1522–1526, 2015.

[23] A. Fujishima and K. Honda. Electrochemical photolysis of water at a semiconductor electrode. *Nature*, 238:37, 1972.

[24] J. G. Mavroides, J. A. Kafalas, and D. F. Kolesar. Photoelectrolysis of water in cells with $SrTiO_3$. *Applied Physics Letters*, 28:241, 1976.

[25] A. Nozik and R. Memming. Physical chemistry of semiconductor-liquid interfaces. *Journal of Physical Chemistry*, 100:13061–13078, 1996.

[26] A. J. Nozik. P-n photoelectrolysis cells. *Applied Physics Letters*, 29:150, 1976.

[27] M. Grätzel. Mesoscopic solar cells for electricity and hydrogen production from sunlight. *Chemistry Letters*, 34:8–13, 2015.

[28] Y. J. Hwang, A. Boukai, and O. Yang. High density n-Si/n-TiO_2 core/shell nanowire arrays with enhanced photoactivity. *Nano Letters*, 9(1):410–415, 2009.

[29] J. Greeley and N. M. Markovic. The road from animal electricity to green energy: Combining experiment and theory in electrocatalysis. *Energy and Environmental Science*, 5:9246, 2012.

[30] J. O'M. Bockris, B. E. Conway, and White. R. E., editors. *Modern aspect of electrochemistry*, volume 22. Springer, 1992.

[31] A. J. Bard and L. R. Faulkner. *Electrochemical Methods Fundamentals and Applications*. John. Wiley and Sons, Inc., 2nd edition, 2001.

[32] P. Cendula, S.D. Tilley, S. Gimenez, J. Bisquert, M. Schmid, M. Grätzel, and J. O. Schumacher. Calculation of the energy band diagram of a photoelectrochemical water splitting cell. *Journal of Physical Chemistry C*, 118:29599–29607, 2014.

[33] R. F. Pierret. *Semiconductor Device Fundamentals*. Addison-Wesley, 1996.

[34] R. Memming. *Semicondcutor Electrochemistry*. Wiley-VCH, 2000.

[35] M. A. Butler. Photoelectrolysis and physical properties of the semiconducting electrode WO_2. *Journal of Applied Physics*, 48:1914, 1977.

[36] N. Sato. *Electrochemistry at metal and semiconductor electrodes*. Elsevier, 1998.

[37] S. Giménez and J. Bisquert, editors. *Photoelectrochemical Solar Fuel Production From Basic Principles to Advanced Devices*. Springer, 2016.

[38] M. M. Waegele, X. Chen, D. M. Herlihy, and T. Cuk. How surface potential determines the kinetics of the first hole transfer of photocatalytic water oxidation. *Journal of the American Chemical Society*, 136(30):10632–10639, 07 2014.

[39] N. M. Markovic and P. N. Ross Jr. Surface science studies of model fuel cell electrocatalysis. *Surface Science Reports*, 45(4-6):117–229, 2002.

[40] T. W. Hamann and N. S. Lewis. Control of the stability, electron-transfer kinetics, and ph-dependent energetics of Si/H_2O interfaces through methyl termination of Si(111) surfaces. *Journal of Physical Chemistry B*, 110(45):22291–22294, 2006.

[41] S. W. Boettcher, E. L. Warren, C. M. Putnam, E. A. Santori, D. Turner-Evans, M.D. Kelzenberg, M. G. Walter, J. R. McKone, B. S. Brunschwig, H. A. Atwater, and N. S. Lewis. Photoelectrochemical hydrogen evolution using Si microwire arrays. *Journal of the American Chemical Society*, 133(5):1216–1219, 2011.

[42] L. Ji, M. D. McDaniel, S. Wang, A. B. Posadas, X. Li, H. Huang, J. C. Lee, A. A. Demkov, A. J. Bard, J. G. Ekerdt, and E. T. Yu. A silicon-based photocathode for water reduction with an epitaxial $SrTiO_3$ protection layer and a nanostructured catalyst. *Nature Nanotechnology*, 10:84–90, 2015.

[43] D. Liu, L. Li, Y. Gao, C. Wang, J. Jiang, and Y. Xiong. The nature of photocatalytic"water splitting" on silicon nanowires. *Angewandte Chemie Internatioal Edition*, 54:2980–2985, 2015.

[44] S. Hu, M. R. Shaner, J. A. Beardslee, M. Lichterman, B. S. Brunschwig, and N. S. Lewis. Amorphous TiO_2 coatings stabilize Si, GaAs, and GaP photoanodes for efficient water oxidation. *Science*, 344(6187):1005–1009, 2014.

[45] Y. He, J. E. Thorne, C. H. Wu, P. Ma, Chun Du, Qi Dong, J. Guo, and D. Wang. What limits the performance of Ta_3N_5 for solar water splitting? *Chem*, 1(4):640–655, 2016.

[46] J. R. McKone, A. P. Pieterick, H. B. Gray, and N. S. Lewis. Hydrogen evolution from Pt/Ru-coated p-type WSe_2 photocathodes. *Journal of the American Chemical Society*, 135(1):223–231, 2013.

[47] F. Bozheyev, K. Harbauer, and K. Ellmer. Highly (001)-textured p-type WSe_2 thin films as efficient large-area photocathodes for solar hydrogen evolution. *Scientific Reports*, 7:16003, 2017.

[48] J. A. Baglio, G. S. Calabrese, D. J. Harrison, A. J. Ricco, M. S. Wrington, and G. D. Zoski. Previous article next article table of contents electrochemical characterization of p-type semiconducting tungsten disulfide photocathodes: efficient photoreduction processes at semiconductor/liquid electrolyte interfaces. *Journal of the American Chemical Society*, 105(8):2246–2256, 1983.

[49] B. AlOtaibi, H. P. T. Nguyen, S. Zhao, M. G. Kibria, S. Fan, and Z. Mi. Highly stable photoelectrochemical water splitting and hydrogen generation using a double-band InGaN/GaN core/shell nanowire photoanode. *Nano Letters*, 13(9):4356–4361, 2013.

[50] S. Yamane, N. Kato, S. Kojima, A. Imanishi, S. Ogawa, N. Yoshida, S. Nonomura, and Y. Nakato. Efficient solar water splitting with a composite "n-Si/p-Cui/n-i-p a-Si/n-p GaP/RuO_2" semiconductor electrode. *Journal of Physical Chemistry C*, 113(32):14575–14581, 2009.

[51] Y. J. Hwang, C. H. Wu, C. Hahn, H. E. Jeong, and P. Yang. Si/InGaN core/shell hierarchical nanowire arrays and their photoelectrochemical properties. *Nano Letters*, 12:1678–1682, 2012.

[52] M. G. Kibria, F. A. Chowdhury, S. Zhao, B. AlOtaibi, H. Trudeau, M. L. abd Guo, and Z. Mi. Visible light-driven efficient overall water splitting using p-type metal-nitride nanowire arrays. *Nature Communications*, 6:6797, 2015.

[53] K. Sivula, R. Zboril, F. Le Formal, R. Robert, A. Weidenkaff, J. Tucek, J. Frydrych, and M. Grätzel. Photoelectrochemical water splitting with mesoporous hematite prepared by a solution-based colloidal approach. *Journal of the American Chemical Society*, 132(21):7436–7444, 2010.

[54] C. X. Kronawitter, L. Vayssieres, S. Shen, L. Guo, D. A. Wheeler, J. Z. Zhang, B. R. Antoun, and S. S. Mao. A perspective on solar-driven water splitting with all-oxide hetero-nanostructures. *Energy and Environmental Science*, 4:3889–3899, 2011.

[55] T. W. Kim and Kyoung-Shin Choi. Nanoporous $BiVO_4$ photoanodes with dual-layer oxygen evolution catalysts for solar water splitting. *Science*, 343(6174):990–994, 2014.

[56] C. G. Morales-Guio, S. D. Tilley, H. Vrubel, M. Grätzel, and X. Hu. Hydrogen evolution from a copper(i) oxide photocathode coated with an amorphous molybdenum sulphide catalyst. *Nature Communications*, 5:3059 EP –, 2014.

[57] Z. Mi, L. Wang, and C. Jagadish, editors. *Semiconductors for Photocatalysis*, volume 97 of *Semiconductors and Semimetals*. Academic Press, 2017.

[58] A. Wahl, M. Ulmann, A. Carroy, B. Jermann, M. Dolata, P. Kedzierzawski, C. Chatelain, A. Monnier, and J. Augustynski. Phototelectrochemical studies peratining to the activity of TiO_2 towards photodegradation of organic compounds. *Journal of Electrochmical Society*, 396:41–51, 1995.

[59] A. B. Murphy, P. R. F. Barnes, L. K. Randeniya, I. C. Plumb, I. E. Grey, M. D. Horne, and J. A. Glasscock. Efficiency of solar water splitting using semiconductor electrodes. *International Journal of Hydrogen Energy*, 31:1999–2017, 2006.

[60] K. Sivula, F. Le Formal, and M. Grätzel. Solar water splitting: Progress using hematite (α-Fe_2O_3) photoelectrodes. *ChemSusChem*, 4:432–449, 2011.

[61] P. Salvador. Hole diffusion length in $nTiO_2$ single crystals and sintered electrodes: Photoelectrochemical determination and comparative analysis. *Journal of Applied Physics*, 55:2977, 1984.

[62] J. E. Thorne, J. Jang, E. Y. Liu, and D. Wang. Understanding the origin of photoelectrode performance enhancement by probing surface kinteics. *Chemical Science*, 7:3347, 2016.

[63] J. H. Kennedy and K. W. Frese. Photooxidation of water at $\alpha{-}Fe_2O_3$ electrodes. *Journal of Electrochmical Society*, 125:709–714, 1978.

[64] C. Santato, M. Ulmann, and J. Augustynski. Photoelectrochemical properties of nanostructured tungsten trioxide films. *Journal of Physical Chemistry B*, 105:936–940, 2001.

[65] C. Zachäus, F. Abdi, L. M. Peter, and R. Van de Krol. Photocurrent of $BiVO_4$ is limited by surface recombination, not surface catalysis. *Chemical Science*, 8:3712, 2017.

[66] L. M. Peter. Energetics and kinetics of light-driven oxygen evolution at semiconductor electrodes: the example of hematite. *Journal of Solid State Electrochemistry*, 17:315–326, 2013.

[67] P. Salvador. Semiconductors' photoelectrochemistry: A kinetic and thermodynamic analysis in the light of equilibrium and nonequilibrium models. *Journal of Physical Chemistry B*, 105:6128–6141, 2001.

[68] F. Le Formal, E. Pastor, S. D. Tilley, C. A. Mesa, S. R. Pendlebury, M. Grätzel, and J. R. Durrant. Rate law analysis of water oxidation on a hematite surface. *Journal of the American Chemical Society*, 137(20):6629–6637, 2015.

[69] M. Barroso, S. R. Pendlebury, A. J. Cowan, and J. R. Durrant. Charge carrier trapping, recombination and transfer in hematite (α-Fe_2O_3) water splitting photoanodes. *Chemical Science*, 4:2724, 2013.

[70] F. Le Formal, S. R. Pendlebury, M. Cornuz, S. D. Tilley, M. Grätzel, and J. R. Durrant. Back electron-hole recombination in hematite photoanodes for water splitting. *Journal of the American Chemical Society*, 136(6):2564–2574, 2014.

[71] C. Du, X. Yang, M. T. Mayer, H. Hoyt, J. Xie, G. McMahon, G. Bischoping, and D. Wang. Hematite-based water splitting with low turn-on voltages. *Angewandte Chemie Internatioal Edition*, 52:12692–12695, 2013.

[72] A. Kumar, P. G. Santangelo, and N. S. Lewis. Electrolysis of water at $SrTiO_3$ photoelectrodes: Distinguishing between the statistical and stochastic formalisms for electron-transfer processes in fuel-forming photoelectrochemical systems. *Journal of Physical Chemistry*, 96(2):834–842, 1992.

[73] W. Shockley and W. T. Read Jr. Statistics of the recombinations of holes and electrons. *Physical Review*, 87(5):835–842, 1952.

[74] D. E. Aspnes. Recombination at semiconductor surfaces and interfaces. *Surface Science*, 132:406–421, 1983.

[75] D. T. Stevenson and R. J. Keyes. Measurement of the recombination velocity at germanium surface. *Physica*, 20:1041, 1964.

[76] W. H. Brattain and J. Bardeen. Surface properties of germanium. *Bell System Tech. J.*, 32:1, 1953.

[77] D. J. Fitzgerald and A. S. Grove. Surface recombination in semiconductor. *Surface Science*, 9(347–369), 1968.

[78] M. Barroso, C. A. Mesa, S. R. Pendlebury, A. J. Cowan, T. Histomi, K. Sivula, M. Grätzel, D. R. Klug, and J. R. Durrant. Dynamics of photogenerated holes in surface modified $\alpha - Fe_2O_3$ photoanodes for solar water splitting. *Proceedings of the National Academy of Sciences of the United States of America*, 109(39):15640–15645, September 2012.

[79] F. Le Formal, Tétreault N., M. Cornuz, T. Moehl, M.l Grätzel, and K. Sivula. Passivating surface states on water splitting hematite photoanodes with alumina overlayers. *Chemical Science*, 2:737–743, 2011.

[80] M. S. Prévot, X. A. Jeanbourquin, W. S. Bouré, F. Abdi, D. Friedrich, R. Van de Krol, Néstor Guijarro, F. Le Formal, and K. Sivula. Evaluating charge carrier transport and surface states in CuFeO_2 photocathodes. *Chemistry of Materials*, 29:4952–4962, 2017.

[81] B. Klahr, S. Giménez, F. Fabregat-Santiago, T. W. Hamann, and J. Bisquert. Water oxidation at hematite photoelectrodes: The role of surface states. *Journal of the American Chemical Society*, 134:4294–4302, 2012.

[82] L. Bertoluzzi, P. Lopez-Varo, J. A. J. Tejada, and J. Bisquert. Charge transfer processes at the semiconductor/electrolyte interface for solar fuel production: insight from impedance spectroscopy. *Journal of Materials Chemistry A*, 4:2873, 2016.

[83] E. F. Schubert. *Light-Emitting Diodes*. Cambridge University Press, 2006.

[84] H. Dotan, N. Mathews, T. Hisatomi, M. Grätzel, and A. Rothschild. On the solar to hydrogen conversion efficiency of photoelectrodes for water splitting. *Journal of Physical Chemistry Letters*, 5(19):3330–3334, 2014.

[85] C. Du, M. Zhang, J. Jang, Y. Liu, G. Liu, and D. Wang. Observation and alteration of surface states of hematite photoelectrodes. *Journal of Physical Chemistry C*, 118(30):17054–17059, 2014.

[86] D. R. Gamelin. Catalyst or spectator? *Nature Chemistry*, 4:965 EP –, 11 2012.

[87] W. W. Gärtner. Depletion-layer photoeffects in semiconductors. *Physical Review*, 116(1):84–87, 1959.

[88] R. H. Wilson. A model for the current-voltage curve of photoexcited semiconductor electrodes. *Journal of Applied Physics*, 48(10):4292–4297, 1977.

[89] C.R. Crowell and S.M. Sze. Current transport in metal-semiconductor barriers. *Solid-State Electronics*, 9:1035–48, 1966.

[90] H. Reiss. Photocharacteristics for electrolyte-semiconductor junctions. *Journal of Electrochmical Society*, 125:937, 1978.

[91] J. Reichman. The current-volatge characteristics of semiconductor-electrolyte junction photovoltaic cells. *Applied Physics Letters*, 36(7):574–577, 1980.

[92] F. El. Guibaly and K. Colbow. Current-voltage characteristics of semiconductor-electrolyte junction solar cells. *Canadian Journal of Physics*, 59:1682, 1981.

[93] F. El. Guibaly and K. Colbow. Theory of photocurrent in semiconductor-electrolyte junction solar cells. *Journal of Applied Physics*, 53(3):1737–1740, 1982.

[94] F. El. Guibaly and K. Colbow. Current transport in semiconductor-electrolyte barriers: Surface recombination and photovoltaic applications. *Journal of Applied Physics*, 54(11):6488–6491, 1983.

[95] L. M. Peter and R. Peat. Surface recombination at semiconductor electrodes part I. transient and steady-state photocurrents. *Journal of Electroanalytical Chemistry*, 165:29–40, 1984.

[96] J. Li, R. Peat, and L. M. Peter. Surface recombination at semiconductor electrodes part II. photoinduced "near-surface" recombination centres in p-GaP. *Journal of Electroanalytical Chemistry*, 165:41–59, 1984.

[97] J. Li and L. M. Peter. Surface recombination at semiconductor electrodes part III. steady-state and intensity modulated photocurrent response. *Journal of Electroanalytical Chemistry*, 193:27–47, 1985.

[98] J. Li and L. M. Peter. Surface recombination at semiconductor electrodes part IV. steady-state and intensity modulated photocurrent response at n-GaAs electrodes. *Journal of Electroanalytical Chemistry*, 199:1–26, 1986.

[99] K. G. U. Wijayantha, S. Saremi-Yarahmadi, and L. M. Peter. Kinetics of oxygen evolution at α-Fe_2O_3 photoanodes: a study by photoelectrochemical impedance spectroscopy. *Physical Chemistry Chemical Physics*, 13:5264–5270, 2011.

[100] S. J. Anz and N. S. Lewis. Simulation of the steady-state current density vs potential characteristics of semiconducting electrodes. *Journal of Physical Chemistry B*, 103:3908–3915, 1999.

[101] M. J. Cass, W. Duffy, N, L. M. Peter, S. R. Pennock, S. Ushiroda, and A. B. Walker. Microwave reflectance studies of photoelectrochemical kinetics at semiconductor electrodes. 1. steday-state, transient, and periodic responses. *Journal of Physical Chemistry B*, 107:5857–5863, 2003.

[102] M. J. Cass, W. Duffy, N, L. M. Peter, S. R. Pennock, S. Ushiroda, and A. B. Walker. Microwave reflectance studies of photoelectrochemical kinetics at semiconductor electrodes. 1. hydrogen evolution at p-si in ammonium fluoride solution. *Journal of Physical Chemistry B*, 107:5864–5870, 2003.

[103] X. Shi, I. Herriaz-Cardona, L. Bertoluzzi, P. Lopez-Varo, J. Bisquert, J. H. Park, and S. Giménez. Understanding the synergistic effect of WO_3-$BiVO_4$ heterostructures by impedance spectroscopy. *Physical Chemistry Chemical Physics*, 18:9255, 2016.

[104] P. R. F. Barnes, A. Y. Anderson, J. R. Durrant, and B. C. O'Regan. Simulation and measurement of complete dye sensitised solar cells: Including the influence of trapping, electrolyte, oxidized dyes and light intensity on steady state and transient device behaviour. *Physical Chemistry Chemical Physics*, 13:5798–5816, 2011.

[105] M. R. Nellist, F. A. L. Laskowski, F. Lin, T. J. Mills, and S. W. Boettcher. Semiconductor-electrocatalyst interfaces: Theory, experiment, and applications in photoelectrochemical water splitting. *Accounts of Chemical Research*, 49:733–740, 2016.

[106] T. J. Mills, F. Lin, and S. W. Boettcher. Theory and simulations of electrocatalysts-coated semiconductor electrodes for solar water splitting. *Physical review Letters*, 112:148304, 2014.

[107] J. M. Foley, M. J. Price, J. I. Feldblyum, and S. Maldonado. Analysis of the operation of thin nanowire photoelectrodes for solar energy conversion. *Energy and Environmental Science*, 5:5203, 2012.

[108] M. Dumortier, T. Bosserez, J. Rongé, J. A. Martens, and S. Haussener. Combined experimental-numerical analysis of transient phenomena in photoelectrochemical water splitting cell. *Journal of Physical Chemistry C*, 120(7):3705–3714, 2016.

[109] Y. K. Gaudy and S. Haussener. Utilizing modeling, experiments, and statistics for the analysis of water-splitting photoelectrodes. *Journal of Materials Chemistry A*, 4:3100, 2016.

[110] Aron Walsh, Yanfa Yan, Muhammad N. Huda, Mowafak M. Al-Jassim, and Su-Huai Wei. Band edge electronic structure of BiVO4: Elucidating the role of the Bi s and V d orbitals. *Chemistry of Materials*, 21(3):547–551, 2009.

[111] J. K. Cooper, S. Gul, F. M. Toma, L. Chen, Per-Anders Glans, J. Guo, J. W. Ager, J. Yano, and I. D. Sharp. Electronic structure of monoclinic $BiVO_4$. *Chemistry of Materials*, 26(18):5365–5373, 2014.

[112] T. Das, X. Rocquefelte, R. Laskowski, L. Lajaunie, S. Jobic, P. Blaha, and K. Schwarz. Investigation of the optical and excitonic properties of the

visible light-driven photocatalytic $BiVO_4$ material. *Chemistry of Materials*, 29(8):3380–3386, 2017.

[113] Z. Zhou, P. Huo, L. Guo, and O. V. Prezhdo. Understanding hematite doping with group IV elements: A DFT+U study. *Journal of Physical Chemistry C*, 119(47):26303–26310, 2015.

[114] O. Neufeld and M. C. Toroker. Platinum-doped α-Fe_2O_3 for enhanced water splitting efficiency: A DFT+U study. *Journal of Physical Chemistry C*, 119(11):5836–5847, 03 2015.

[115] S. Chatman, C. I. Pearce, and K. M. Rosso. Charge transport at Ti-doped hematite (001)/aqeuous interfaces. *Chemistry of Materials*, 27(5):1665–1673, 03 2015.

[116] N. Kharche, J. T. Muckerman, and M. S. Hybertsen. First-principles approach to calculating energy level alignment at aqueous semiconductor interfaces. *Physical review Letters*, 113:176802, 2014.

[117] E. Watanabe, H. Ushiyama, and K. Yamashita. First-principles study of the band diagrams and schottky-type barrier heights of aqueous Ta_3N_5 interfaces. *ACS Applied Materials & Interfaces*, 9(11):9559–9566, 2017.

[118] E. Berardo and M. A. Zwijnenburg. Modeling the water splitting activity of a TiO_2 rutile nanoparticle. *Journal of Physical Chemistry C*, 119(24):13384–13393, 06 2015.

[119] M. G. Mavros, T. Tsuchimochi, T. Kowalczyk, A. McIsaac, Lee-Ping Wang, and T. V. Voorhis. What can density functional theory tell us about artificial catalytic water splitting? *Inorganic Chemistry*, 53(12):6386–6397, 07 2014.

[120] S. Selberherr. *Analysis and simulation of semiconductor devices.* Springer-Verlag Wien New York, 1984.

[121] D. Schroeder. *Modelling of interface carrier transport for device simulation.* Springer-Verlag Wien GmbH, 1994.

[122] D. Vasileska, S. M. Goodnick, and G. Klimeck. *Computational electronics: semiclassical and quantum device modelling and simulation.* UK: Taylor and Francis, 1st edition, 2010.

[123] J. Bisquert, F. Fabregat-Santiago, I. Mora-Seró, G. Garcia-Belmonte, and S. Giménez. Electron lifetime in dye-sensitized solar cells: Theory and interpretation of measurements. *Journal of Physical Chemistry C*, 113:17278–17290, 2009.

[124] L. Bertoluzzi and J. Bisquert. Equivalent circuit of electrons and holes in thin semiconductor films for photoelectrochemical water splitting applications. *Journal of Physical Chemistry Letters*, 3:2517–2522, 2012.

[125] L. Bertoluzzi, L. Badia-Bou, F. Fabregat-Santiago, S. Giménez, and J. Bisquert. Interpretation of cyclic voltammetry measurements of thin semiconductor films for solar fuel application. *Journal of Physical Chemistry Letters*, 4:1334–1339, 2013.

[126] F. Fabregat-Santiago, I. Mora-Seró, G. Garcia-Belmonte, and J. Bisquert. Cyclic voltammetry studies of nanoporous semiconductors. capacitive and reactive properties of nanocrystalline TiO_2 electrodes in aqueous electrolyte. *Journal of Physical Chemistry B*, 107:758–768, 2003.

[127] B. Klahr, S. Gimenez, F. Fabregat-Santiago, J. Bisquert, and T. W. Hamann. Electrochemical and photoelectrochemical investigation of water oxidation with hematite electrodes. *Energy and Environmental Science*, 6:7626, 2012.

[128] J. A. Glasscock, P. R. F. Barnes, I. C. Plumb, A. Bendavid, and P. J. Martin. Structural, optical and electrical properties of undoped polycrystalline hematite thin films produced using filtered arc deposition. *Thin Solid Films*, 516:1716–1724, 2008.

[129] J. O'M. Bockris, A. K. N. Reddy, and M. E. Galboa-Aldeco. *Modern Electrochemistry 2A*. Springer US, 2nd edition, 2000.

[130] Z. Chen, H. N. Dinh, and E. Miller. *Photoelectrochemical water splitting standards, experimental methods and protocols*. Springer, 2013.

[131] K. W. Frese Jr. and S. R. Morrison. Electrochemical measurements of interface states at the GaAs/oxide interafce. *Journal of Electrochmical Society*, 126(7):1235–1241, 1979.

[132] I. Mora-Seró and J. Bisquert. Fermi level of surface states in TiO_2 nanoparticles. *Nano Letters*, 3(7):945–949, 2003.

[133] J. Y. Kim, D. H. Youn, J. H. Kim, H. G. Kim, and J. S. Lee. Nanostructure-preserved hematite thin film for efficient solar water splitting. *ACS Applied Materials & Interfaces*, 7(25):14123–14129, 2015.

[134] B. Klahr, S. Giménez, F. Fabregat-Santiago, J. Bisquert, and T. W. Hamann. Photoelectrochemical and impedance spectroscopic investigation of water oxidation with "Co-Pi"-coated hematite electrodes. *Journal of the American Chemical Society*, 134:16693–16700, 2012.

[135] H. Wang and L. Pilon. Accurate simulations of electric double layer capacitance of ultramicroelectrodes. *Journal of Physical Chemistry C*, 115(33):16711–16719, 2011.

[136] J. Lyklema. *3 - Electric Double Layers*, volume 2 of *Fundamentals of Interface and Colloid Science*, chapter 3. Academic Press, 1995.

[137] W. Schmickler and E. Santos. *Interfacial Electrochemistry.* Springer-Verlag Berlin Heidelberg, 2nd edition, 2010.

[138] R. F. Pierret. *Advanced Semiconductor Fundamentals*, volume 6 of *Modular Series on Solid State Devices*. Addison-Wesley, 2nd edition, 1987.

[139] G. Gouy. Constitution of the electric charge at the surface of an electrolyte. *Journal of Theoretical and Applied Physics*, 9:457–468, 1910.

[140] D. Chapman. A contribution to the theory of electrocapillarity. *Philosophical Magazine*, 25:475–481, 1913.

[141] H. von Helmholtz. Studien *Ü*ber electrische grenzchichten. *Annals of Physics*, 243:337–382, 1879.

[142] O. Stern. The theory of the electrolyte double layer. *Z. Elecktrochem. Angew. Phys. Chem.*, 20:508–516, 1924.

[143] W. Mönch. *Semiconductor Surfaces and Interfaces.* Springer-Verlag Berlin Heidelberg GmbH, 3rd edition, 2001.

[144] W. C. Ellis, N. D. McDaniel, S. Bernhard, and T. J. Collins. Fast water oxidation using iron. *Journal of the American Chemical Society*, 132(32):10990–10991, 08 2010.

[145] S. Sch*ä*fer, A. H. R. Koch, A. Cavallini, M. Stutzmann, and I. D. Sharp. Charge transfer across the n-type GaN–electrolyte interface. *Journal of Physical Chemistry C*, 116(42):22281–22286, 10 2012.

[146] P. Zhang, T. Wang, and J. Gong. Passivation of surface states by ALD-grown TiO_2 overlayers on Ta_3N_5 anodes for photoelectrochemical water oxidation. *Chemical Communications*, 52(57):8806–8809, 2016.

[147] I. Cesar, K. Sivula, A. Kay, R. Zboril, and M. Grätzel. Influence of feature size, film thickness, and silicon doping on the performance of nanostructured hematite photoanodes for solar water splitting. *Journal of Physical Chemistry C*, 113:772–782, 2009.

[148] F. Le Formal, M. Grätzel, and K. Sivula. Controlling photoactivity in ultrathin hematite films for solar water-splitting. *Advanced Functional Materials*, 20:1099–1107, 2010.

[149] T. Hisatomi, J. Brillet, M. Cornuz, F. Le Formal, N. Tetreault, K. Sivula, and M. Gratzel. A Ga_2O_3 underlayer as an isomorphic template for ultrathin hematite films toward efficient photoelectrochemical water splitting. *Faraday Discussions*, 155(0):223–232, 2012.

[150] F. L. Souza, K. P. Lopes, E. Longo, and E. R. Leite. The influence of the film thickness of nanostructured α-Fe_2O_3 on water photooxidation. *Physical Chemistry Chemical Physics*, 11(8):1215–1219, 2009.

[151] L. M. Peter. *CHAPTER 2 Kinetics and Mechanisms of Light-Driven Reactions at Semiconductor Electrodes: Principles and Techniques*, chapter 2, pages 19–51. The Royal Society of Chemistry, 2013.

[152] A. G. Tamirat, J. Rick, A. A. Dubale, Wei-Nien Su, and Bing-Joe Hwang. Using hematite for photoelectrochemical water splitting: a review of current progress and challenges. *Nanoscale Horizons*, 1(4):243–267, 2016.

[153] M. S. Kilic, M. Z. Bazant, and A. Ajdari. Steric effects in the dynamics of electrolytes at large applied voltages. I. double-layer charging. *Physical Review E*, 75:021502, 2007.

[154] M. Z. Bazant, M. S. Kilic, and A. Ajdari. Towards an understanding of induced-charge electrokinetics at large applied voltages in concentrated solutions. *Advances in Colloid and Interface Science*, 152:48–88, 2009.

[155] W. L. Masterton, D. Bolocofsky, and T. P. Lee. Ionic radii from scaled particle theory of the salt effect. *Journal of Physical Chemistry*, 75(18):2809–2815, 09 1971.

[156] H. K. Gummel. A self-consistent iterative scheme for one-dimensional steady state transistor calculation. *IEEE Transactions on Electron Devices*, 11:455–465, 1964.

[157] D. L. Scharfetter and H. K. Gummel. Large signal analysis of a silicon read diode oscillator. *IEEE Transactions on Electron Devices*, 16(1):64–77, 1969.

[158] J.O. Nylander, F. Masszi, S. Selberherr, and S. Berg. Computer simulation of schottky contacts with a non-constant recombination velocity. *Solid-State Electronics*, 32(5):363–367, 1989.

[159] J. Racko, D. Donoval, M. Barus, V. Nagl, and A. Grmanova. Revised theory of current transport through the schottky structure. *Solid-State Electronics*, 35(7):913–919, 1992.

[160] L. M. Peter and K. G. U. Wijayantha. Photoelectrochemical water splitting at semiconductor electrodes: fundamental problems and new perspectives. *ChemPhysChem*, 15:1983–1995, 2014.

[161] Y. Tachibana, L. Vayssieres, and J. R. Durrant. Artificial photosynthesis for solar water-splitting. *Nature Photonics*, 6:511–518, 2012.

[162] P. Sudhagar, Anitha Devadoss, K. Nakata, C. Terashima, and A. Fujishima. Enhanced photoelectrocatalytic water splitting at hierarchical Gd^{3+}:TiO_2 nanostructures through amplifying light reception and surface states passivation. *Journal of Electrochmical Society*, 162(3):H108–H114, 2015.

[163] Jen-Chun Chou, Szu-An Lin, Chi-Young Lee, and Jon-Yiew Gan. Effect of bulk doping and surface-trapped states on water splitting with hematite photoanodes. *Journal of Materials Chemistry A*, 1:5908, 2013.

[164] S. George, S. Pokhrel, Z. Ji, B. L. Henderson, T. Xia, L. Li, J. I. Zink, A. E. Nel, and L. Mädler. Role of Fe doping in tuning the band gap of TiO_2 for the photo-oxidation induced cytotoxicity paradigm. *Journal of the American Chemical Society*, 133:11270–11278, 2011.

[165] Z. Yao, F. Jia, Shujun Tian, C. Li, Z. Jiang, and X. Bai. Microporous Ni-doped TiO_2 film photocatalyst by plasma electrolytic oxidation. *ACS Applied Materials & Interfaces*, 2(9):2617–2622, 2010.

[166] H. Jie, H. Park, Kon-Bae Lee, Hye-Jung Chang, Ahn Jae-Pyoung, and Jong-Ku Park. A new absorption band and visible absorption properties in V-doped Tio_2 nanopowder. *Surface and Interface Analysis*, 44:1449–1452, 2012.

[167] H. Zhu, J. Tao, and X. Dong. Preparation and photoelectrochemical activity of Cr-doped TiO_2 nanorods with nanocavities. *Journal of Physical Chemistry C*, 114:2873–2879, 2010.

[168] J. H. Park, S. Kim, and A. J. Bard. Novel carbon-doped TiO_2 nanotube arrays with high aspect ratios for efficient solar water splitting. *Nano Letters*, 6(1):24–28, 2006.

[169] P. Sudhagar, K. Asokan, E. Ito, and Y. S. Kang. N-Ion-implanted TiO_2 photoanodes in quantum dot-sensitized solar cells. *Nanoscale*, 4:2416, 2012.

[170] Q. Sun, J. Zhang, P. Wang, J. Zheng, X. Zhang, Y. Cui, J. Feng, and Y. Zhu. Sulfur-doped TiO_2 nanocrystalline photoanodes for dye-sensitized solar cells. *Journal Renewable Sustainable Energy*, 4:023104, 2012.

[171] J. Cheng, J. VandeVondele, and M. Sprik. Identifying trapped electronic holes at the aqueous TiO_2 interface. *Journal of Physical Chemistry C*, 118:5437–5444, 2014.

[172] S. Takata, Y. Miura, and Y. Matsumoto. Evidence for the intrinsic nature of band-gap states electrochemically observed on atomically flat $TiO_2(110)$ surfaces. *Physical Chemistry Chemical Physics*, 16:24784, 2014.

[173] L. Li, J. Yan, T. Wang, Z Zhao, J. Zhang, J. Gong, and N. Guan. Sub-10 nm rutile titanium dioxide nanoparticles for efficient visible-light-driven photocatalytic hydrogen production. *Nature Communications*, 6:5881, 2015.

[174] P. S. Shinde, S. H. Choi, Y. Kim, J. Ryu, and J. S. Jang. Onset potential behavior in $\alpha - Fe_2O_3$ photoanodes: the influence of surface and diffusion Sn doping on the surface states. *Physical Chemistry Chemical Physics*, 18:2495, 2016.

[175] T. Cottineau, M. Morin, and D. Bélanger. Surface band structure of aryldiazonium modified p-Si electrodes determined by x-ray photoelectron spectroscopy and electrochemical measurements. *RSC Advances*, 3:23649, 2013.

[176] B. Qi, Zhi-Guo Zhang, and J. Wang. Uncovering the role of cathode buffer layer in organic solar cells. *Scientific Reports*, 5:7803, 2015.

[177] B. Qi, Q. Zhou, and J. Wang. Exploring the Open-Circuit Voltage of Organic Solar Cells Under Low Temperature. *Scientific Reports*, 5:11363, 2015.

[178] J. Bisquert. Theory of the impedance of charge transfer via surface states in dye-sensitized solar cells. *Journal of Electroanalytical Chemistry*, 646(1-2):43–51, July 2010.

[179] F. Nunzi, E. Mosconi, L. Storchi, E. Ronca, A. Selloni, M. Grätzel, and F. Angelis De. Inherent electronic trap states in TiO_2 nanocrystals: effect of saturation and sintering. *Energy and Environmental Science*, 6:1221, 2013.

[180] L. Bertoluzzi, I. Herriaz-Cardona, R. Gottesman, A. Zaban, and J. Bisquert. Realaxation of electron carriers in the density of states of nanocrystalline TiO_2. *Journal of Physical Chemistry Letters*, 5:689–694, 2014.

[181] V. F. Gantmakher. *Electrons and disorder in solids*. Oxford Science Publications, 2005.

[182] S. Datta. *Quantum transport: atom to transistor*. Cambridge University Press, 2005.

[183] Dan-Ni Pei, L. Gong, Ai-Yong Zhang, X. Zhang, Jie-Jie Chen, Y. Mu, and Han-Qing Yu. Defective titanium dioxide single crystals exposed by high-energy 001 facets for efficient oxygen reduction. *Nature Communications*, 6:8696, 2015.

[184] M. Han, J. Jia, L. Yu, and G. Yi. Fabrication and photoelectrochemical characteristics of $CuInS_2$ and PbS quantum dots co-sensitized TiO_2 nanorods photoelectrodes. *RSC Advances*, 5:51493, 2015.

[185] K. Schwanitz, U. Weiler, R. Hunger, T. Mayer, and W. Jaegermann. Synchrotron-induced photoelectron spectroscopy of the dye-sensitized Nanocrystalline TiO_2/Electrolyte interface: Band gap states and their interaction with dye and solvent molecules. *Journal of Physical Chemistry C*, 111:849–854, 2007.

[186] Hanz-Joachim Lewerenz and L. M. Peter, editors. *Photoelectrochemical water splitting: materials, processes and architectures*. RSC Publishing, 2013.

[187] D. Wang, A. Pierre, Md G. Kibria, K. Cui, X. Han, K. H. Bevan, H. Guo, S. Paradis, A. Hakima, and Z. Mi. Wafer-level photocatalytic water splitting on GaN nanowire arrays grown by molecular beam epitaxy. *Nano Letters*, 11(6):2353–2357, 2011.

[188] A. Iqbal, M. S. Hossain, and K. H. Bevan. The role of relative rate constants in determining surface state phenomena at semiconductor–liquid interfaces. *Physical Chemistry Chemical Physics*, 18:29466, 2016.

[189] T. J. Mills, F. A. L. Laskowski, C. Dette, M. R. Nellist, F. Lin, and S. W. Boettcher. The role of surface states in electrocatalyst-modified semiconductor photoelectrodes: Theory and simulation. *arXiv:1707.03112*, 2017.

[190] W. L. Engl, H. K. Dirks, and B. Meinerzhagen. Device modeling. *Proceedings of the IEEE*, 71(1):10–33, 1983.

[191] D. Donoval, C. M. Snowden, M. Barus, J. Racko, and M. Bedlek. Critical analysis of the schottky boundary condition for numerical simulation of schottky and mesfet structure. *Physica Scripta*, 50:432–436, 1994.

[192] H. M. Bath and M. Culter. Measurement of surface recombination velocity in silicon by steady-state photoconductance. *Journal of Physics and Chemistry of Solids*, 5:171–179, 1958.

[193] E. Demoulin and F. van de Wiele. Inversion layer at the interface of schottky diodes. *Solid-State Electronics*, 17:825–833, 1974.

[194] L. F. Wagner. Advanced concepts in vlsi schottky-barrier diode modeling. *International Electron Devices Meeting*, pages 676–679, 1982.

[195] S. C. Choo. Theory of surface photovoltage in a semiconductor with a schottky contact. *Solid-State Electronics*, 38(12):2085–2093, 1995.

[196] D. L. Scharfetter. Minority carrier injection and charge storage in epitaxial schottky barrier diodes. *Solid-State Electronics*, 8:299–311, 1965.

[197] M. A. Green and J. Shewchun. Minority carrier effects upon the small signal and steady-state properties of schottky diodes. *Solid-State Electronics*, 16:1141–1150, 1973.

[198] T. Lindgren, L. Vayssieres, H. Wang, and S. Lindquist. *Chemical Physics of Nanostructured Semiconductors, Chapter: Photo-oxidation of Water at Hematite Electrodes*, chapter 3, pages 83–110. VSP, 2003.

[199] A. Bosman and H. van Daal. Small-polaron versus band conduction in some transition-metal oxides. *Advances in Physics*, 19:1–117, 1970.

[200] Y. Lin, G. Yuan, S. Sheehan, S. Zhou, and D. Wang. Hematite-based solar water splitting: Challenges and opportunities. *Energy and Environmental Science*, 4:4862–4869, 2011.

[201] S. D. Tilley, M. Cornuz, K. Sivula, and M. Grätzel. Light-induced water splitting with hematite: Improved nanostructure and iridium oxide catalysis. *Angewandte Chemie Internatioal Edition*, 49:6405–6408, 2010.

[202] H. Dontan, K. Sivula, M. Grätzel, A. Rothschild, and S. C. Warren. Probing the photoelectrochemical properties of hematite (α-Fe_2O_3) electrodes using hydrogen peroxide as a hole scavenger. *Energy and Environmental Science*, 4:958–964, 2011.

[203] Y. Fu, C. Dong, Z. Zhou, W. Lee, J. Chen, P. Guo, L. Zhao, and S. Shen. Solution growth of Ta-doped hematite nanorods for efficient photoelectrochemcial water splitting: A tradeoff between electronic structure and nanaostructure evolution. *Physical Chemistry Chemical Physics*, 18:3846, 2016.

[204] A. G. Joly, J. R. Williams, S. A. Chambers, G. Xiong, W. P. Hess, and D. M. Laman. Carrier dynamics in alpha-Fe_2O_3 (0001) thin films and single crystal probed by femtosecond transient absorption and reflectivity. *Journal of Applied Physics*, 99:053521, 2006.

[205] N. J. Cherepy, D. B. Liston, J. A. Lovejoy, H. M. Deng, and J. Z. Zhang. Ultrafast studies of photoexcited electron dynamics in gamma- and alpha-Fe_2O_3 semiconducor nanoparticles. *Journal of Physical Chemistry B*, 102:770, 1998.

[206] A. Iqbal and K. H. Bevan. Simultaneously solving the photovoltage and photocurrent at semiconductor–liquid interfaces. *Journal of Physical Chemistry C*, 122(1):30–43, 2018.

[207] R. Liu, Z. Zheng, J. Spurgeon, and X. Yang. Enhanced photoelectrochemical water-splitting performance of semiconductors by surface passivation layers. *Energy & Environmental Science*, 7(8):2504–2517, 2014.

[208] A. Iqbal and K. H. Bevan. The impact of boundary conditions on calculated photovoltages and photocurrents at photocatalytic interfaces. *MRS Communications*, pages 1–8, 2018.

[209] S. R. Pendlebury, A. J. Cowan, M. Barroso, K. Sivula, J. Ye, M. Gratzel, D. R. Klug, J. Tang, and J. R. Durrant. Correlating long-lived photogenerated hole populations with photocurrent densities in hematite water oxidation photoanodes. *Energy & Environmental Science*, 5(4):6304–6312, 2012.

[210] C. X. Kronawitter, I. Zegkinoglou, C. Rogero, J. H. Guo, S. S. Mao, F. J. Himpsel, and L. Vayssieres. On the interfacial electronic structure origin of efficiency enhancement in hematite photoanodes. *Journal of Physical Chemistry C*, 116(43):22780–22785, 11 2012.

[211] G. Horowitz. Capacitance-voltage measurements and flat-band potential determination on Zr-doped α-Fe_2O_3 single-crystal electrodes. *Journal of Electroanalytical Chemistry*, 159(2):421–436, 1983.

[212] S. M. Ahmed, J. Leduc, and S. F. Haller. Photoelectrochemical and impedance characteristics of specular hematite. 1. photoelectrochemical parallel conductance, and trap rate studies. *Journal of Physical Chemistry*, 92(23):6655–6660, 11 1988.

[213] Z. Wang, C. Brock, A. Matt, and K. H. Bevan. Implications of the DFT+U method on polaron properties in energy materials. *Physical Review B*, 96(12):125150–, 09 2017.

[214] N. Adelstein, J. B. Neaton, M. Asta, and L. C. De Jonghe. Density functional theory based calculation of small-polaron mobility in hematite. *Physical Review B*, 89(24):245115–, 2014.

[215] B. Zhao, T. C. Kaspar, T. C. Droubay, J. McCloy, M. E. Bowden, V. Shutthanandan, S. M. Heald, and S. A. Chambers. Electrical transport properties of Ti-doped Fe_2O_3(0001) epitaxial films. *Physical Review B*, 84(24):245325–, 12 2011.

[216] H. J. Van Daal and A. J. Bosman. Hall effect in CoO, NiO and α-Fe_2O_3. *Physical Review*, 158(3):736–747, 06 1967.

[217] C. D. Bohn, A. K. Agrawal, E. C. Walter, M. D. Vaudin, A. A. Herzing, P. M. Haney, A. A. Talin, and V. A. Szalai. Effect of tin doping on α-Fe_2O_3 photoanodes for water splitting. *Journal of Physcial Chemistry C*, 116(29):15290–15296, 07 2012.

[218] J. G. Simmons and G. W. Taylor. Nonequilibrium steady-state statistics and associated effects for insulators and semiconductors containing an arbitrary distribution of traps. *Physical Review B*, 4(2):502–511, 07 1971.

[219] W. E. Spear, P. G. Le Comber, and A. J. Snell. An investigation of the amorphous-silicon barrier and p-n junction. *Philosophical Magazine B*, 38(3):303–317, 09 1978.

[220] Y. Ling, G. Wang, J. Reddy, C. Wang, J. Z. Zhang, and Y. Li. The influence of oxygen content on the thermal activation of hematite nanowires. *Angewandte Chemie Internatioal Edition*, 51(17):4074–4079, 2012.

[221] X. Yang, R. Liu, Y. Lei, P. Li, K. Wang, Z. Zheng, and D. Wang. Dual influence of reduction annealing on diffused hematite/fto junction for enhanced photoelectrochemical water oxidation. *ACS Applied Materials & Interfaces*, 8(25):16476–16485, 06 2016.

[222] P. Liao, M. C. Toroker, and E. A. Carter. Electron transport in pure and doped hematite. *Nano Letters*, 11(4):1775–1781, 04 2011.

[223] M. Mikolášek, J. Racko, L. Harmatha, P. Gašpierik, and P. Šutta. Influence of the broken symmetry of defect state distribution at the a-si:h/c-si interface on the performance of hetero-junction solar cells. *Applied Surface Science*, 256(18):5662–5666, 2010.

[224] A. Froitzheim, R. Stangl, L. Elstner, M. Schmidt, and W. Fuhs. Interface recombination in amorphous/crystalline silicon solar cells, a simulation study.

In *Proceedings of the 29th IEEE Photovoltaic Specialist Conference*, pages 1238–1241, New Orleans, USA, 2002.

[225] R. E. I. Schropp and M. Zeman. *Amorphous and Microcrystalline Silicon Solar Cells: Modeling, Materials and Device Technology*. Springer, Boston, MA, 1998.

[226] R. L. Blake, R. E. Hessevick, T. Zoltai, and L. W. Finger. Refinement of the hematite structure. *Americal Mineralogist*, 51:123–129, 1966.

[227] F. J. Morin. Electrical properties of Fe_2O_3. *Physical Review*, 93(6):1195, 1954.

[228] J. Y. Kim, G. Magesh, D. H. Youn, J. Jang, J. Kubota, K. Domen, and J. S. Lee. Single-crystalline, wormlike hematite photoanodes for efficient solar water splitting. *Scientific Reports*, 3:2681 EP –, 09 2013.

[229] Y. Ling, G. Wang, D. A. Wheeler, J. Z. Zhang, and Y. Li. Sn-doped hematite nanostructures for photoelectrochemical water splitting. *Nano Letters*, 11(5):2119–2125, 05 2011.

[230] X. Zhao, J. Feng, S. Chen, Y. Huang, T. C. Sum, and Z. Chen. New insight into the roles of oxygen vacancies in hematite for solar water splitting. *Physical Chemistry Chemical Physics*, 19(2):1074–1082, 2017.

[231] T.-Y. Yang, H.-Y. Kang, U. Sim, Y.-J. Lee, J.-H. Lee, B. Koo, K. T. Nam, and Y.-C. Joo. A new hematite photoanode doping strategy for solar water splitting: oxygen vacancy generation. *Physical Chemistry Chemical Physics*, 15(6):2117–2124, 2013.

[232] A. Pu, J. Deng, M. Li, J. Gao, H. Zhang, Y. Hao, J. Zhong, and X. Sun. Coupling Ti-doping and oxygen vacancies in hematite nanostructures for solar water oxidation with high efficiency. *Journal of Materials Chemistry A*, 2(8):2491–2497, 2014.

[233] Z. Wang and K. H. Bevan. Exploring the impact of semicore level electronic relaxation on polaron dynamics: An adiabatic ab initio study of ${\mathrm{fepo}}_{4}$. *Physical Review B*, 93(2):024303–, 01 2016.

[234] A. M. Stoneham, J. Gavartin, A. L. Shluger, A. V. Kimmel, D. M. Ramo, H. M. Rønnow, G. Aeppli, and C. Renner. Trapping, self-trapping and the polaron family. *Journal of Physics: Condensed Matter*, 19:255208, 2007.

[235] I. G. Austin and N. F. Mott. Polarons in crytalline and non-crystalline materials. *Advances in Physics*, 18(71):41–102, 1969.

[236] K. H. Bevan. Electron transfer from the perspective of electron transmission: Biased non-adiabatic intermolecular reactions in the single-particle picture. *J. Chem. Phys.*, 146:134106, 2017.

[237] D. A Neaman. *Semiconductor Physics and Devices: Basic Principles*. McGraw-Hill, New York, 3rd edition, 2003.

[238] K. H. Bevan, Md. S. Hossain, A. Iqbal, and Z. Wang. Exploring bridges between quantum transport and electrochemistry. i. *Journal of Physical Chemistry C*, 120(1):179–187, 01 2016.

[239] M. Catti, G. Valerio, and R. Dovesi. Theoretical study of electronic, magnetic, and structural properties of α-Fe_2O_3 (hematite). *Physical Review B*, 51(12):7441–7450, 03 1995.

[240] P. Merchant, R. Collins, R. kershaw, K. Dwight, and A. Wold. The electrical, optical and photoconducting properties of $Fe_{2-x}Cr_xo_3$ (0≥x≥0.47). *Journal of Solid State Chemistry*, 27(3):307–315, 1979.

[241] G. Kresse and J. Furthm*ü*ller. Efficient iterative schemes for ab initio total-energy calculations using a plane-wave basis set. *Physical Review B*, 54(16):11169–11186, 1996.

[242] G. Kresse and J. Furthm*ü*ller. Efficiency of ab-initio total energy calculations for metals and semiconductors using a plane-wave basis set. *Computational Materials Science*, 6(1):15–50, 1996.

[243] G. Kresse and J. Hafner. Ab initio molecular-dynamics simulation of the liquid-metal–amorphous-semiconductor transition in germanium. *Physical Review B*, 49(20):14251–14269, 1994.

[244] G. Kresse and J. Hafner. Ab initio molecular dynamics for liquid metals. *Physical Review B*, 47(1):558–561, 01 1993.

[245] J. P. Perdew, K. Burke, and M. Ernzerhof. Generalized gradient approximation made simple. *Physical Review Letters*, 77(18):3865–3868, 10 1996.

[246] P. E. Bl*ö*chl. Projector augmented-wave method. *Physical Review B*, 50(24):17953–17979, 12 1994.

[247] G. Kresse and D. Joubert. From ultrasoft pseudopotentials to the projector augmented-wave method. *Physical Review B*, 59(3):1758–1775, 01 1999.

[248] A. Jain, S. P. Ong, G. Hautier, W. Chen, W. D. RIchards, S. Dacek, S. Cholia, D. Gunter, D. Skinner, G. Ceder, and K. A. Persson. Commentary: The materials project: A materials genome approach to accelerating materials innovation. *APL Materials*, 1:011002, 2013.

[249] A. I. Liechtenstein, V. I. Anisimov, and J. Zaanen. Density-functional theory and strong interactions: Orbital ordering in mott-hubbard insulators. *Physical Review B*, 52(8):R5467–R5470, 08 1995.

[250] V. I. Anisimov, J. Zaanen, and O. K. Andersen. Band theory and mott insulators: Hubbard u instead of stoner i. *Physical Review B*, 44(3):943–954, 07 1991.

[251] V. I. Anisimov and O. Gunnarsson. Density-functional calculation of effective coulomb interactions in metals. *Physical Review B*, 43(10):7570–7574, 04 1991.

[252] Y. Ma, C. A. Mesa, E. Pastor, A. Kafizas, L. Francàs, F. Le Formal, S. R. Pendlebury, and J. R. Durrant. Rate law analysis of water oxidation and hole scavenging on a bivo4 photoanode. *ACS Energy Letters*, 1(3):618–623, 09 2016.

[253] A. Kafizas, Y. Ma, E. Pastor, S. R. Pendlebury, C. Mesa, L. Francàs, F. Le Formal, N. Noor, M. Ling, C. Sotelo-Vazquez, C. J. Carmalt, I. P. Parkin, and J. R. Durrant. Water oxidation kinetics of accumulated holes on the surface of a TiO_2 photoanode: A rate law analysis. *ACS Catalysis*, 7(7):4896–4903, 07 2017.

[254] B. Enright and D. Fitzmaurice. Spectroscopic determination of electron and hole effective masses in a nanocrystalline semiconductor film. *Journal of Physical Chemistry*, 100(3):1027–1035, 01 1996.